ODESA ASTRONOMICAL PUBLICATIONS

Volume 37
(2024)

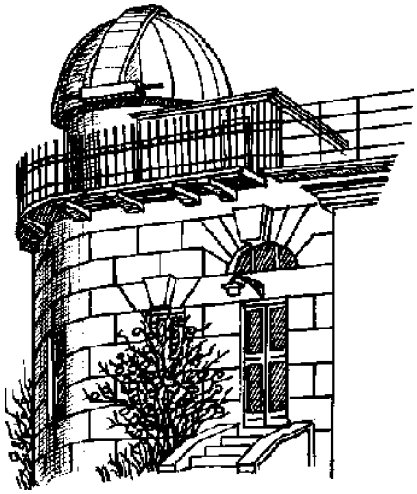

Astronomical Observatory
of Odesa I. I. Mechnikov National University

ODESA ASTRONOMICAL PUBLICATIONS

Volume 37
(2024)

Address:
Astronomical Observatory, Odesa National University,
T. G. Shevchenko Park, Odesa, 65014, UKRAINE
Tel.: + 38 048 722-03-96
E-mail: astronomical_observatory@onu.edu.ua
http://www.astro-observ-odessa0.1gb.ua

The electronic version of the journal is available at the website: http://oap.onu.edu.ua

Одеські Астрономічні Публікації
Видається з 1946 року (видання відновлено в 1993 р., № 6)

As per Resolution of the National Council on Television and Radio Broadcasting of Ukraine No 36 dated 11.01.2024 the journal is registered as a print media with identifier R30-02636.
As per Order of the Ministry of Education and Science of Ukraine No 1643 dated 28.12.2019, the journal is included in the List of Specialist Scientific Publiications of Ukraine (Category B).

Printed as per the Resolution of the Academic Council of the RI "Astronomical Observatory" of Odesa I. I. Mechnikov National University: Minutes No 4 dated 14 November 2024.

Printed in UKRAINE
"ONU" PUBLISHING COMPANY

ISSN 1810-4215

CONTENTS

Cosmology, gravitation, astroparticle physics, high energy physics

Astrophysics (stellar atmospheres, interacting binary systems, variable stars)

Solar system and space environment

Radioastronomy

Sun, solar activity, solar-terrestrial relations and astrobiology

Memorial

COSMOLOGY, GRAVITATION, ASTROPARTICLE PHYSICS, HIGH ENERGY PHYSICS

https://doi.org/10.18524/1810-4215.2024.37.312680

SPECTRA OF LIGHTNING IN SOME WINDOWS OF TRANSPARENCY OF X-RAY AND γ-RADIATION

Doikov D.N.[1,2], Doikov M.D.[3]

[1] Department of Physics, Medical Laboratory, the North Medical Center, Poria, Israel

[2] Department of Mathematics, Physics and Astronomy, Odesa National Maritime University, Ukraine, *dmitro.doikov@gmail.com*

[3] Faculty of Physics and Technology, Plovdiv University "Paisii Hilendarski", Plovdiv, Bulgaria *marik.doikov@gmail.com*

ABSTRACT. The processes associated with the formation of lightning and their spectra during atmospheric and volcanic phenomena were considered as a means of studying the atmospheric plasma in the X-ray and soft γ-ray bands. It was found that the time intervals, power of the processes, and their energy make it possible to develop new generation equipment. The lightning spectra cover the X-ray and gamma-ray bands. Hard radiation detectors have been developed and proposed for their registration. It is shown that in a physical system of emitter (lightning), absorber (medium between lightning and detector), and the detector itself, the spectral structure on the detector depends on the distance to the source and the chemical composition of the environment around thunderstorms and volcanoes. Therefore, we have calculated and found the intervals of quanta energies in which the absorber response is small. Such spectral regions are called transparency windows and are necessary for the design of appropriate detectors. In the transparency windows, the original spectra of lightning discharges are observed. To conduct field work and reduce the influence of the atmosphere during a thunderstorm, the percentage contribution of air and water extrusion in atmospheric thunderstorms was found. For volcanic discharges, silicates and Al_2O_3 particles were taken. The parameters of the previously designed high-speed electrical interface suitable for operation under high voltage conditions, which is supplied to the $CsPbBr_3$ or $Lu(SiO)_5$ detector-crystal, were obtained and described. The main economic and operational advantages of the proposed spectroscopic equipment in the field are emphasized. The operation of the high-speed spectrograph in outer space was modeled in the absence of the need for its operation without deep cooling. The transparency windows and the structure of the radiation field in the X-ray and γ-ray bands were calculated and systematized.

Keywords: hard radiation detectors, lightning, radiation deposition, X-ray transparent windows, diffusion emission, thunderstorm aerosol.

АНОТАЦІЯ. Процеси, пов'язані з утворенням блискавок та їх спектрів під час атмосферних та вулканічних явищ були розглянути як засіб вивчення атмосферної плазми у рентгенівському та м'якому γ-діапазонах. Отримано, що інтервали часу, потужність процесів та їх енергетика дає можливість розробляти обладнання нового покоління. Спектри блискавок охоплюють рентгенівський та гамма-діапазон. Для їх реєстрації розроблено та запропоновано детектори жорсткого випромінювання. Отримано, що у фізичної системі Випромінювач (блискавка), Поглинач (середовище між блискавкою та детектором) та сам Детектор структура спектру на Детекторі залежить від відстані до джерела і хімічного складу середовища навколо гроз і вулканів. Тому у роботі проведено розрахунки та знайдено інтервали енергій квантів, у яких відгук Поглинача малий. Такі ділянки спектрів є вікнами прозорості і необхідні для проектування відповідних детекторів. У вікнах прозорості спостерігаються вихідні спектри грозових розрядів. Для проведення польових робіт та зменшення впливу атмосфери в процесі грози було знайдено відсотковий внесок екстинкції повітря та води в атмосферних грозах. Для вулканічних розрядів бралися силікати та частки Al_2O_3. Отримані та описані параметри раніше спроектованого високошвидкісного електричного інтерфейсу, придатного для роботи умовах високої напруги, що подається на кристал-детектор $CsPbBr_3$ або $Lu(SiO)_5$. Підкреслено основні економічні та експлуатаційні переваги запропонованого спектроскопічного обладнання у польових умовах. Проведено моделювання роботи високошвидкісного спектрографа в умовах відкритого космосу за відсутності необхідності його експлуатації без глибокого охолодження. Розраховані та систематизовані вікна прозорості та структура радіаційного поля в рентгені та γ-діапазоні.

Ключові слова: детектори жорсткого випромінювання, блискавка, радіаційні втрати, рентгенівські вікна прозорості, дифузійне випромінювання, грозовий аерозоль.

1. Introduction

During the motion of quanta from the Emitter towards the Detector the processes of photoabsorption, incoherent Compton and coherent Rayleigh scattering are noticeable. As a result of photo absorption, there is also induced (characteristic) radiation. To register the latter, it is necessary to take into account that according to the presented graphs in the long-wave wing of the X-ray spectrum photo absorption

prevails. Photo absorption and corresponding resonance radiation are directly proportional. A part of quanta with energies not falling on the resonant K-lines of carbon, nitrogen and oxygen can go beyond the Absorber. The exception is the transparency window in the energy range of 280 eV (atomic oxygen), 380 eV (atomic nitrogen) and 440 eV (atomic carbon). Strong resonant scattering is observed near the marked characteristic lines. Therefore, the soft X-ray field at wavelengths of 2 nm – 4 nm is used to study microscopic particles and biological structures. To accomplish such a task, the incoming or diffuse radiation field must be sufficiently powerful. In X-ray microscopy, the role of the Emitter is played by a source of powerful cyclotron radiation. The absence of such sources can be compensated by the registration of resonance scattering near the indicated lines. Let us also note that even primitive photographic and visual observations of lightning show the stepwise character of the current motion. Such curvilinear motion of relativistic electrons leads to flashes of synchrotron radiation in the specified wavelength interval in microsecond time intervals. In other words, our designed detector should have high sensitivity in the indicated intervals of the X-ray and gamma spectrum.

2. The energy resource of lightning

Lightning discharges of thunderstorm and volcanic origin are formed in the zone of high potential difference $\Delta\varphi$=100 MV, electric field strength E=1000 V/m. In thunderstorm clouds, the cloud potential is formed by friction and collision of microscopic aerosols, mainly consisting of water. Initial inoculum charges can form showers and individual cosmic rays. In volcanic lightning, the main potential and inoculum charges are formed by solid particles. Mechanism of lightning formation presented in (Gurevich & Zybin, 2001; Petrov, 2021).

The Earth's atmosphere during storms and volcanic phenomena a possible to study the state of atmospheric plasma, including various aerosols. For elements with small atomic numbers the characteristic lines are in soft X-ray. The present work takes water vapor as the main aerosol component. Between the clouds pure water together with atmospheric gas are in a strong electric field with potential difference $\Delta\varphi \approx (10^6 – 10^8)$ V. It has been shown that the hard radiation flux generated by lightning is the result of transforming the initial braking spectrum of relativistic electrons and collisions of protons, ions of C, N, and O elements with resting atoms of the medium. Both currents consisting of ions and electrons are directed in opposite directions.

The gamma and X-ray radiation of lightning reaches the detectors with strongly attenuated long-wave part. At energies less than 1 keV, practically all energy of long-wavelength X-ray quanta is spent in photo-ionization of surrounding water vapor. However, in the wavelength range (2.34 – 4.4) nm we have bound energies (530 – 280) eV. There is a transparency window with characteristic K-lines of C, N, O atoms. We propose a method and compose a model for registration of radiation fluxes in the window of water transparency. This allows us to study the plasma in which intensive ionization processes occur by the joint action of photons and impact ionization of atoms by electrons and protons. The protons and electrons experience collisions with target atoms – C, N, O. It was obtained that at sufficiently high saturation with water vapor around the lightning. Its long-wave part is cut off in the X-ray spectrum. The relationship between water vapor content and radiation intensity at the receiver is described. The concurrence of the processes of scattering, absorption of X-ray quanta and formation of induced secondary quanta (characteristic emission of C, N, O elements) is responsible for the formation of the observed diffuse (bulk) X-ray fluorescence (Kozirev et al., 2011), (Doikov & Doikov, 2023).

For simulation of the process of nucleation of electron and hadronic (p, α-particles + C, N, O - ions) currents was carried out in the framework of the Geant4 DNA code (Inserti et. al., 2010). Concurrently, the formation of X-ray and UV fluorescence was monitored. All necessary spectroscopic constants for the media in which the processes under consideration took place above described processes took place in a strong electric field with a potential difference of $\Delta\varphi = (10^6 – 10^8)$V, which leads to the intensity E=$(10^3 – 10^5)$V/m. A comparison with the laboratory experiments in (Kozirev et al., 2011) has been made. On the basis of modeling of various types of lightning using spectra of lightning in the X-ray range are constructed and conclusions are drawn concerning the application of this method in the study of explosive processes on the surface of White Dwarfs (WD).

3. X-ray transport in thunderstorm clouds

Lightning generates X-ray and gamma radiation in a wide range of the spectrum. It is caused by braking of fast (in some cases relativistic) electrons. Appearing inside the current cylinder, the quanta cross its surface and are directed to the detector. Further quanta experience random multiple acts of Compton and Rayleigh scattering, or experience photo absorption. In this case, the radiation field is determined by the elemental composition of air (in the used codes it is macro command G4_Air) and the fraction of water vapor (G4_Water). If lightning is formed in volcanic clouds, it is necessary to specify the distribution of silicon and phosphorus along the propagation of quanta. In rain clouds, the inoculum of free ions is formed as a result of CR ionization losses. In volcanic ones as a result of mutual friction of the solid fraction.

3.1. Formation of radiation in lightning

The current discharge in lightning has a powerful transient, mile-microsecond pulse character. The electronic component of the current at the specified values of $\Delta\varphi$ has velocities sufficient for the formation of braking radiation. This leads to the formation of a continuous spectrum of hard radiation. This spectrum is limited on the short wavelength side by soft γ-radiation. The target atoms for fast electrons are C-N-O elements, the maximum of the spectral distribution of the braking radiation of which is more likely to fall in the entire X-ray range.

The electron kinetic energy spectrum W(λ) is essentially relativistic. The external electric field has a strength $E \cong 10^2 - 10^3$ V/m. The maximum current amplitude at the peak of discharge reaches $3 \cdot 10^4 A$. During discharge, $\Delta\varphi$ drops to zero. According to (Gurevich & Zybin, 2001) and

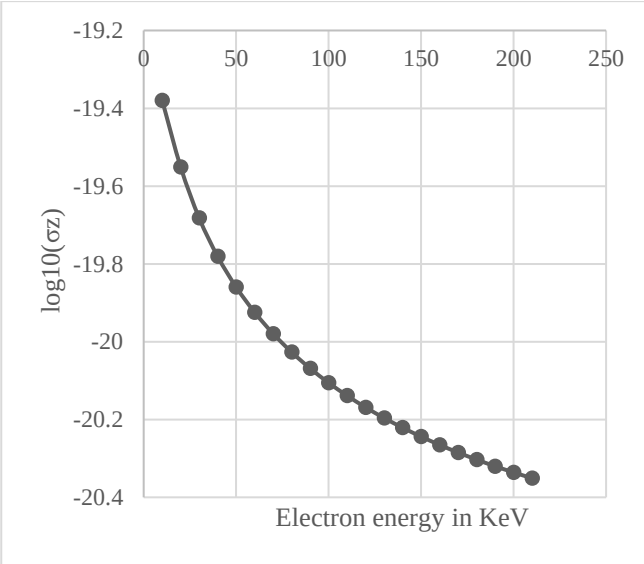

Figure 1: Impact ionization cross section σ_Z

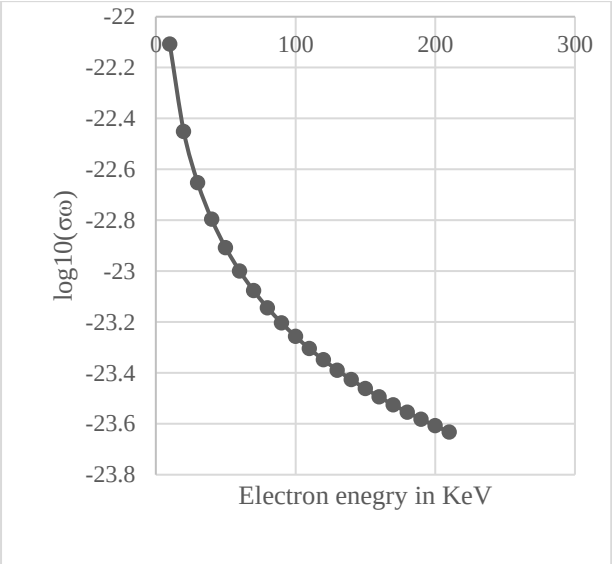

Figure 2: Bremsstrahlung cross section σ_ω

(Petrov, 2023) the formation of the current pulse is determined by "fleeing" electrons. A δ-shaped peak appears in the spectrum W(λ) at this moment. To determine the time evolution of W(λ), it is necessary to take into account all channels of energy acquisition and loss by fast electrons. As an initial approximation, we choose the Maxwell velocity distribution. Then let us apply the corresponding potential difference Δφ to the cylinder in which the lightning nucleates. Among the main channels of energy losses, we note the losses on Bremsstrahlung radiation with cross section σ_ω and the cross section of ionization of K-level C-N-O atoms is σ_Z.

$$\sigma_\omega = \frac{16\pi e^2}{3hc^2}\left(\frac{Ze^2}{mV_0}\right)^2 ln^2\left(\frac{2mV_0^2}{\gamma Ze^2\omega_{mn}}\right) \quad (1)$$

$$\sigma_Z \cong \frac{10^{-24}cm^2}{I_Z E(E+2)}\left\{2+(E+1)^2 ln\sqrt{\frac{E(E+1)}{I_Z}} - \frac{I_Z}{E}\left[(E+2)^2 + \right.\right.$$
$$\left.\left. +2(2E+1)ln\frac{E}{E_Z} - 2\right]\right\} \quad (2)$$

Here $I_Z = \frac{E_Z}{mc^2}, E = \frac{mV_0^2}{2mc^2}, E_O = 537$ eV, $E_N = 405$ eV. At a quantum energy of 10 keV, the characteristic cross section value is $\sigma_Z \cong 5\cdot 10^{-20}cm^2$, a $\sigma_\omega/\sigma_Z \cong 10^{-3}$. Fig. 1 and Fig. 2 show the cross sections σ_ω, σ_Z in logarithmic scale normalized to the electron scattering cross section σ_T.

Diffuse X-ray emission. The initial spectrum of hard radiation undergoes further evolution during the discharge process. For this purpose, the macro commands of Weber G codes (see Weber G link) are addressed to cross sections of characteristic processes of interaction of quanta with matter. The structure of the nonlinear behavior of cross sections of all energy loss channels leads to a shift of the maximum of the spectral distribution of their energy towards longer wavelengths. Modeling of X-ray quantum beams shows that their spectrum is gradually filled with a diffuse X-ray component.

A similar effect occurs in observations of the intrinsic diffuse radiation of planets caused by the Sun's radiation. The calculations of the spectrum of hard radiation coming from lightning suggest that its quanta at the initial moment of time cross the walls of the current cylinder. At this moment the mechanisms of coherent and incoherent scattering of hard radiation are switched on. Rayleigh scattering of sunlight on molecules is replaced by the scattering of hard radiation on atomic structures.

In this case the extinction cross section k is defined through the cross sections of Compton scattering $\sigma_c^\gamma(\varepsilon)$ and atomic photo effect $\sigma_{af}^\gamma(\varepsilon)$. Similarly to formulas (1) and (2) for the energy of quanta we substitute $\varepsilon = E_\gamma/m_e c^2$. E_γ is the energy of a hard radiation photon. $m_e c^2$ is the rest energy of the electron. Let us denote by $\sigma_T = 6.65\cdot 10^{-25}$см^2 the cross section of elastic, Thomson scattering of photons on electrons. Then we have

$$k = \sigma_{af}^\gamma(\varepsilon) + \sigma_c^\gamma(\varepsilon)\,. \quad (3)$$

In the framework of the adopted notations, we will write down:

$$\sigma_{af}^\gamma(\varepsilon) = \left(\frac{32}{\varepsilon}\right)^{3/2}\alpha^4 Z^5\sigma_T\,, \quad (4)$$

$$\sigma_c^\gamma(\varepsilon) = 2\sigma_T\left[\frac{1+\varepsilon}{\varepsilon^2}\left(\frac{2(1+\varepsilon)}{1+2\varepsilon} - \frac{1}{\varepsilon}\ln(1+2\varepsilon)\right) - \frac{1}{2\varepsilon}\ln(1+\right.$$
$$\left. +2\varepsilon) - \frac{(1+3\varepsilon)}{(1+2\varepsilon)^2}\right]. \quad (5)$$

For each individual quantum within the free path length all its characteristics and trajectory are tracked by the Monte Carlo method. Such quanta form secondary electrons, which in turn ionize the medium along their trajectory. The flux of quanta and particles formed in this way arrives at the detector crystal. The calculation results are presented in Fig. 3 and Fig. 4.

It follows from the results shown in Fig. 6 that in the conditions of thunderstorm clouds Compton scattering takes the highest values in the long-wave part of the spectrum.

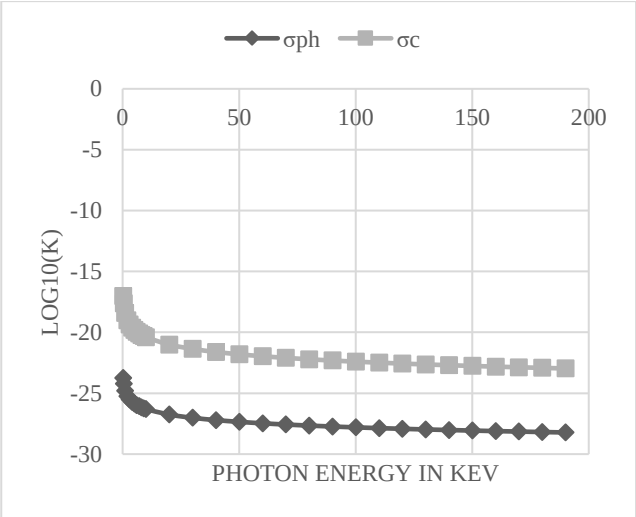

Figure 3: Diffuse photoelectric σph and Compton scattering σc

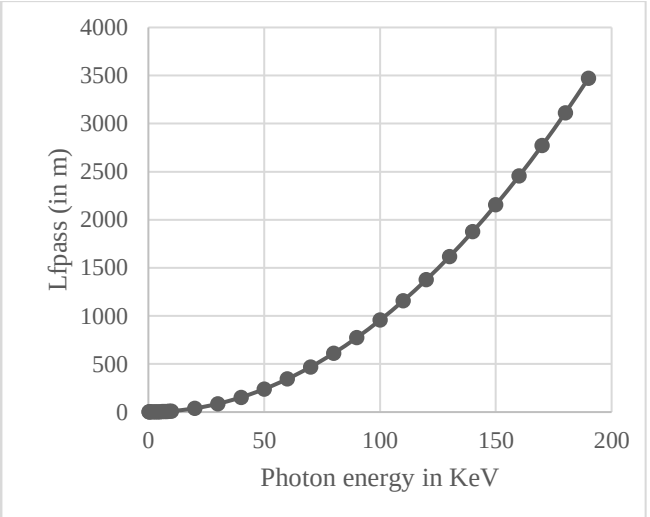

Figure 4: Free path lengths X-, γ-rays photon in pure air (G4_Air)

It follows from the results shown in Fig. 6 that in the conditions of thunderstorm clouds Compton scattering takes the highest values in the long-wave part of the spectrum. The short-wave part of the X-ray spectrum of lightning is practically undistorted up to energies of 50 keV. If we consider the cloud as a fog with relative humidity, the free path length of X-ray quanta between two acts of Coulomb scattering takes the values shown in Fig. 5. During rain, it is necessary to take into account the percentage of drops in the thunderstorm cloud.

Let us take into account that the average concentration of water in raindrops is three orders of magnitude higher, then the obtained values of fpass should be on average 10^3 times higher and, accordingly, fpass is the same number of times smaller. It follows from Fig. 3 – Fig. 5 that the main type of X-ray scattering is the incoherent Compton scattering given by the formula. Moreover, at each act of scattering it is necessary to recalculate the wavelength of the quantum after scattering – λ' . If before scattering we have a wavelength λ and a scattering angle θ, then the relation is satisfied:

$$\lambda' = \lambda + \frac{h}{mc^2}(1 - cos\theta) = \lambda + 2{,}4 \cdot 10^{-3}\text{нм} \cdot (1 - cos\theta) \quad (6)$$

At the wavelength interval from 0.12 to 0.06 nm, the peak of Compton scattering in water is noticeable and a rapid decrease in photo absorption begins. In this interval, the appearance of X-rays scattered mostly by oxygen and nitrogen is expected. The quantum beam attenuation coefficients due to photo absorption, Compton and Rayleigh scattering are presented in Fig. 6. In the presented resources we calculated scattering angles θ were set by the Monte Carlo method in the range from 0 to π radians. The results of averaging cross sections of beams containing 100 X-ray quanta each are presented in Fig. 7. The calculations were performed for the thickness of the equivalent water layer of 1 cm. The modeling results show general trends in the dependence of attenuation coefficients on the energy of quanta predicted by the formulas. However, for spectral analysis of the investigated objects the results of accurate "ab initio" The calculations in Fig. 6 are applicable. In the future, we will use them for quantitative analysis of X-ray spectra of lightning to determine the content of elements in lightning during lightning discharge (Kozirev et al., 2011).

3.2 *Characteristic radiation*

Quanta of soft X-ray radiation occupy wavelengths of 0.01 nm – 10 nm. In this interval all quanta from electron transitions to the free K-level of atoms, which are part of air and water droplets, occur.

If the energies of the quanta are adjacent to the edge of the lines arising in the photo effect, strong resonance scattering is observed, and inside the absorption lines. Along with elastic scattering, X-ray quanta also experience incoherent scattering in the form of Compton scattering.

The process of photo ionization of aerosol represented by water droplets of carbon, nitrogen and oxygen, which are part of air. Scattered quanta is mainly determined by photo ionization of K-shells of atoms. Near these lines we have resonant scattering of diffuse radiation.

Next, for air under normal conditions and for a given concentration of raindrops, we estimate the number of such collision acts on the path of the X-ray quantum to the detector. We need to trace the shift of the X-ray spectrum in the region of the "transparency window" of water.

4. Detector construction

The design of detectors-spectrographs of hard radiations requires fulfillment of a number of requirements to their operation. In particular, for diagnostics of the described processes in thunderstorm and volcanic lightning requires the closest possible placement of equipment to the object of study. In high mountain conditions at altitudes higher than 1 km the distance from the Detector to the Emitter can reach 1 km on average. The thunderstorm cloud aerosol at such scales completely absorbs the long-wave part of X-ray radiation. Quanta with energies up to 100 keV experience complete Compton scattering. In this range we have diffuse

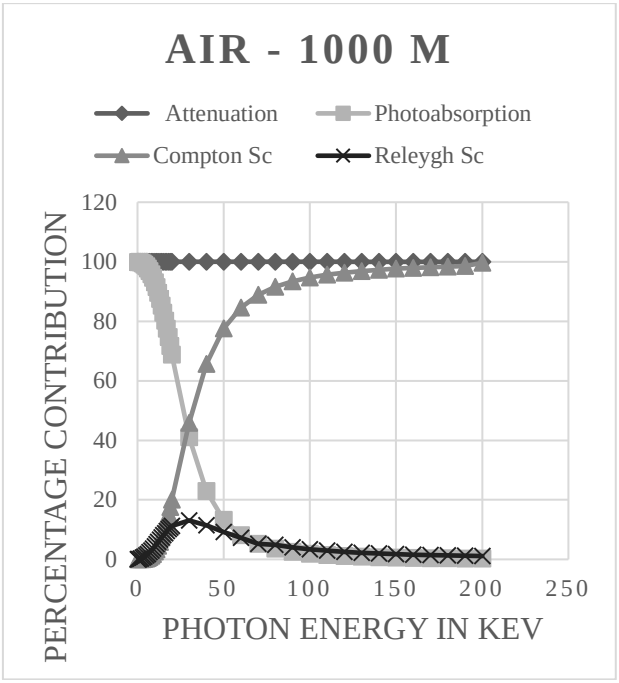

Figure 5: Radiation field after crossing 1 km of pure air

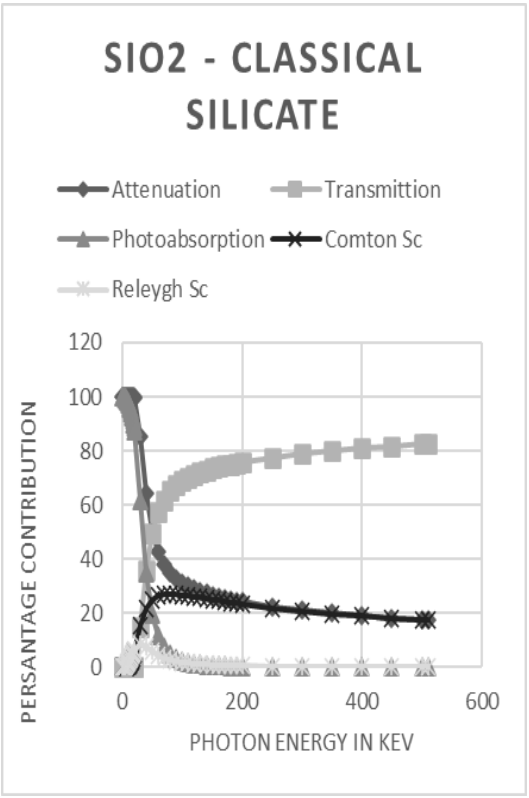

Figure 7: Ibid after crossing of 1cm classical silicate

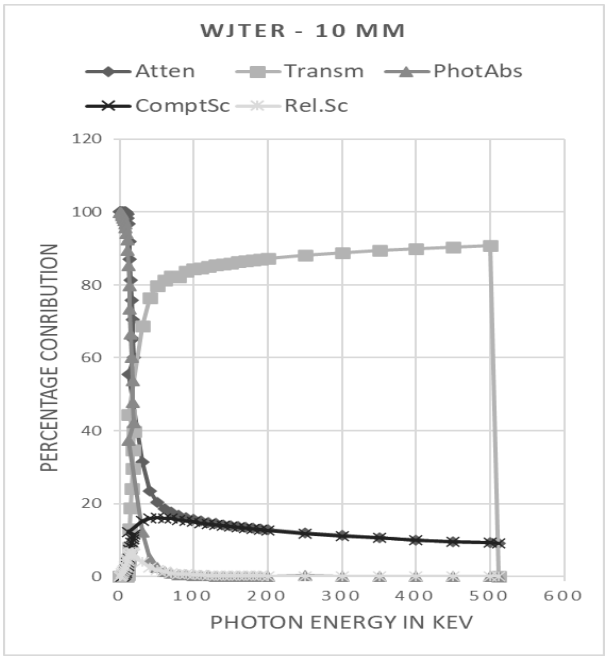

Figure 6: Radiation field spectra after crossing 1 cm of pure water

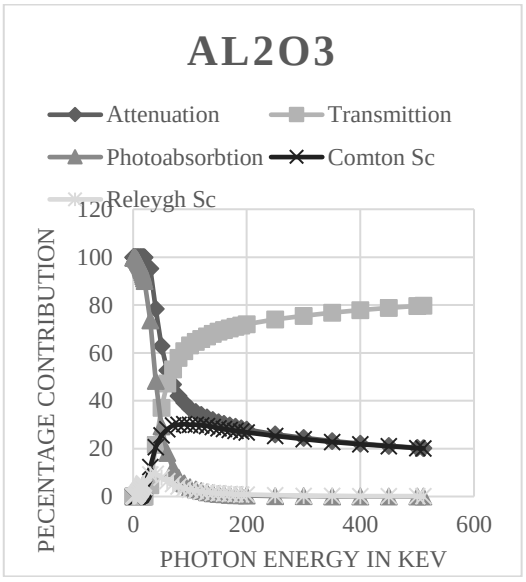

Figure 8: Ibid after crossing of 1cm Al_2O_3

X-ray luminescence. The directional flux of gamma ray quanta is expectedly registered by the detector. The calculated shape of the lightning detector includes a thin quartz plate and a cube with an edge of 0.5 cm – 1 cm. This geometry allows for guaranteed registration of lightning radiation in the range of 0.01 MeV – 1 MeV. Semiconductor crystals have been widely studied for this purpose $CsPbBr_3$ и $Lu(SiO)_5$. The obtained results on design and modeling of detectors are presented in Fig. 9 and Fig. 10. The number of quanta in the flux is assumed to be 50. The flux defocusing is carried out by incoherent Compton scattering. A part of quanta is reflected back (by 180^o). Visualization of particle trajectories is described in (Inserti et. al., 2010). To determine the efficiency of the crystal, the fraction of the flux energy spent on the actual ionization of the crystal substance was determined. A detailed study of these issues in (Doikov, 2022) allows us to obtain the values of the current pulse amplitude (1 nA – 10 nA) and the time scale of its formation (1 μs – 100 μs).

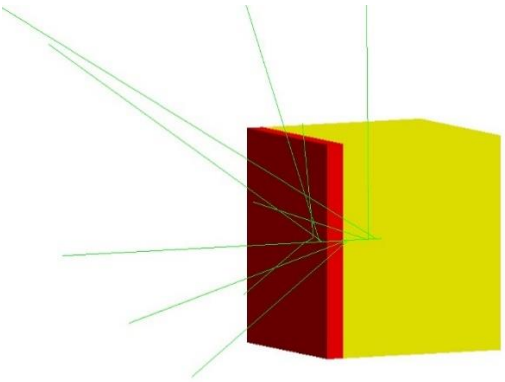

Figure 9: SiO2 0.1 mm and $CsPbBr_3$ 10 mm target length. Eγ = 511 keV

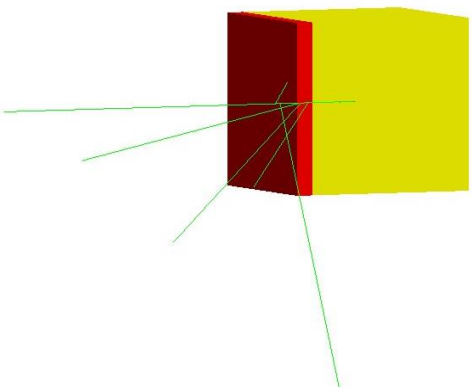

Figure 10: SiO2 0.1 mm and $Lu(SiO)_5$ 10 mm target length. Eγ = 100 keV

5. Discussion

The transfer of hard radiation formed by lightning is accompanied by a noticeable change in its shape. The most informative results are obtained with high-speed X-ray and gamma-ray spectrographs at the flash peak. This means that the equipment we are developing should operate in the monitoring mode. This means that the electronic interface should only be triggered when a sufficiently powerful pulse is received that the signal-to-noise ratio is maximized. The convenience in carrying out mass in-situ measurements of lightning spectra and images from stationary high-altitude observatories significantly increases the chances of obtaining high-quality results.

6. Conclusion

In the present work we obtained original results necessary for diagnostics of hard radiations formed at fast thermonuclear processes. The energy resource of lightning in sounder stomps and volcano causes a whole chain of thermonuclear processes and their accompanying bursts of hard radiation. Presented in Fig. 5 – Fig. 8 predicted the presence of an intense component in the spectrum of scattered X-rays and the presence of strong self-absorption near the spectral windows of transparency. Multiple scattering of hard radiation quanta creates specific images of lightning and requires a separate approach to their visualization.

Acknowledgements. D.D., would like to thank Tsafon Medical Center for material support in writing this paper. M.D. and D.D. thank the Geant4-DNA project (Inserti et al., 2010) and Dr. G. Weber for the opportunity to use the open-source code of their programs.

Athor contribution: DD: sections 2; MD: sections 3,4.5. In sections 1, 6 of the article the authors' contributions are the same.

References

Doikov D.N., Doikov M.D.: 2023, *OAP*, **36**, 51-58.
Doikov M.D.: 2022, *OAP*, **35**, 24-29.
Gurevich A.V., Zybin K.P.: 2001, *Usp. Phys. Nauk,* **171**, № 11, p. 1177.
Inserti S., Balanchino G., Bernal M. et al.: 2010, *Int. J. of Modeling, Simulation, and Scientific Computing*. 01, 02, 157-178. DOI: 10.1142/ S179396231000012
Kozirev A.V., Tarasenko V.F., Baksht E.H. et al.: 2011, *Letter in JTF*, **37**, 22.
Petrov N.I.: 2021, *Scientific Report* **11:19824**, *https://doi.org/10.1038/s41598-021-99336-3.*
Weber G. *https://web-docs.gsi.de/~stoe_exp/web_programs/x_ray_absorption/index.php*

https://doi.org/10.18524/1810-4215.2024.37.312675

THE DESIGN AND MODELING OF HARD-RADIATION SPECTROGRAPHS FOR RECORDING OF THE FAST-FLOWING PROCESSES

Marko D. Doikov

Faculty of Physics and Technologies, Plovdiv University "Paisii Hilendarski",

Plovdiv, Bulgaria, *marik.doikov@gmail.com*

ABSTRACT. Hard radiation spectra are associated with fast-flowing thermonuclear processes. For the registration of hard radiation spectra, a new generation of semiconductor detectors is developed and modeled. Their main difference is the presence in their composition of chemical elements with large atomic numbers. In particular, Pb and Lu, which are part of $CsPbBr_3$ and $Lu(SiO)_5$ crystals. The calculations of the detector design were performed using Giant4 open-source codes (Geant4 – School, 2024), which is an integrated engineering and physics constructor. The energy range of particles and quanta accompanying lightning flashes has been preliminarily determined. It was obtained that the totality of mechanisms of energy losses of quanta and particles in lightning discharges points to the energy interval (0.001 – 2) MeV. The necessary calculations have been carried out in order to select affordable, minimize the size and structure of the detection systems planned for operation. The detailed tracks of quanta, the values of energy losses, and their relation to the amplitudes of current pulses delivered to the high-voltage preamplifier are determined. The detailed tracks and quanta, energy loss values, and their relation to the amplitudes of current pulses delivered to the high-voltage preamplifier have been determined. The selection of a suitable electronic interface has been carried out, demonstrating the cost-effectiveness of fabrication and operation of the obtained detector-spectrograph. In particular, the possibility of its operation under normal conditions, which does not require deep cooling, was revealed. Two varieties of detectors were modeled and constructed. A two-layer one, with a silicon wafer of 1 mm x 1 cm x 1 cm, and either a $CsPbBr_3$ or a $Lu(SiO)_5$ crystal. The source of modulation of current pulses of the detector is chosen to be a directed radiation beam consisting of 50 X- or gamma-quanta. The detector efficiency is estimated. All basic elementary processes were taken into account on the basis of the Monte Carlo method. The energy of the beam entering the detector was set in the range from 1 kev to 1 MeV. At given time intervals, elementary scattering acts are visualized and tracks inside a given detector are plotted. A detailed relationship between the absorbed energy and the current pulse of a given detector is constructed.

Keywords: perovskite; total ionizing dose; CsPbBr3; detector; X-ray, gamma-irradiation of lightnings.

АНОТАЦІЯ. Зростання необхідності реєстрації спектрів жорсткого випромінювання, пов'язаного з швидкоплинними термоядерними процесами, вимагає розробки та моделювання нового покоління напівпровідникових детекторів. У обраних нами пристроїв спостерігається присутність у хімічному складі елементів з великими атомними номерами. Зокрема, розглядаються включення атомів Pb та Lu. Це є напівпровідники-кристали $CsPbBr_3$ та $Lu(SiO)_5$. Запропонована задача була вирішена за допомогою відкритих кодів Giant4-DNA версії 11.2 (Geant4 – School, 2024) у вигляді використання інтегрованого інженерно-фізичного конструктора. Зроблено моделювання рентгенівських та γ-спектрографів в інтервалі енергій (0,001 – 10) МеВ. Відмічено доступність у придбанні, мінімізації розмірів та структури, експлуатації детектуючих систем. Отримано детальні треки частинок та квантів, визначенні енергетичні втрати, їх зв'язок з амплітудами струмових імпульсів, що надходять на високовольтний підсилювач. На основі отриманих результатів зроблено вибір відповідного електронного інтерфейсу. Перевага запропонованої конструкції детектора-спектрографа полягає в експлуатації за нормальними умовами і не потребує глибокого охолодження. У роботі змодельовано детектор, який складається із двох шарів. Перший шар є силікатною пластиною для поглинання рентгенівського спектра розміром 1 х 10 х 10 мм. Другий детектор $CsPbBr_3$ або $Lu(SiO)_5$ має розміри 1 см х 1 см х 1 см і поглинає жорсткий рентген та м'яке γ-випромінювання. Між детекторами немає проміжку. Зроблено висновок, що у більшості випадків оптимальна геометрія детектора складається з 5 шарів $CsPbBr_3$ та 5 шарів кремнієвого ізолятора високої напруги. У наведеному прикладі всі шари мають однакові розміри, що пов'язано з необхідністю високоточного калібрування енергії падаючих на них квантів і частинок. Для модуляції ми обрали потік, що складається з 20 частинок рентгенівських або гамма-променів. Було змодельовано сценарій взаємодії цих квантів з матеріалом детектора. Враховано всі основні елементарні процеси з урахуванням методу Монте-Карло. Для певності розглянута енергія пучка, що входить у детектор в межах від 10 кеВ до 1 МеВ. На обраних інтервалах часу за допомогою

даного методу візуалізовано елементарні акти розсіювання та побудовано треки всередині заданого детектора. Даний метод дозволив побудувати детальний зв'язок між поглинутою енергією та струмовим імпульсом даного шару детектора. Візуалізація всіх процесів та їх спектрів є на візуальних 3D малюнках.

Ключові слова: перовськіт; сумарна іонізуюча доза; $CsPbBr_3$; детектор; рентгенівське та гамма-випромінювання, блискавки.

1. Introduction

Design features of hard radiation detectors depend on the range of energies received by the receiver (hereinafter referred to as the Detector) and its physical and chemical structure. Depending on the tasks to be solved, the geometry and types of compositions of different materials have to be taken into account. This leads to the complication of the design of the Detector body itself and its electronic interface. There is also a qualitative dependence of the radiation spectrum conversion processes inside the Detector (Doikov, 2022; 2023). The calculations of the spectroscopic response of various crystals to incident hard radiation were previously carried out using the codes G. Weber (see link) and test tasks in (Geant4-School, 2024). The calculations showed that the entire long-wavelength wing of X-ray radiation is effectively absorbed due to photo absorption in a 1 mm thick layer of silicon semiconductors in the energy range $E_\gamma \leq 10$ keV. Semiconductor crystals CsPbBr3 and $Lu(SiO)_5$ were used to register photons up to 1 MeV.

2. Energy transport in Absorber and Detector

Increasing the efficiency of the Detector required introduction of additional layers with the necessary materials into its construction. Until recently, silicon semiconductors were used in computed tomography (CT). Their widespread use in such tasks was due to their availability, the history of the development of semiconductor device research. The results of my X-ray transport calculations for silicon semiconductors are shown in Fig. 1 – Fig. 4. As can be seen from the presented results, taking into account multiple scattering and geometry of the Detectors (e.g., their thickness) significantly changes the percentage contribution of the scattering and absorption mechanisms. Despite the significant photoabsorption of the long-wavelength wing of X-rays, a transparency window convenient for obtaining lightning spectra is located in the wavelength interval 2.2 nm – 4.4 nm. For this purpose, the Detector must be in sufficient proximity to the lightning. In these “windows” the extinction is many times less than in the adjacent wavelength intervals. Let's call the source object whose spectrum is recorded by the Emitter. The medium between the Detector and the Radiator is further called the Absorber. Photon beams from the Emitter are separated in this energy range. Taking into account miniaturization possibilities and dielectric properties of silicon semiconductors, the first layer of the Detector is a receiver of soft X-ray radiation – Fig. 5 or Fig. 6. The rest of the Detector is a combination of insulator layers and detector material. For simplicity, this paper presents vari-

.

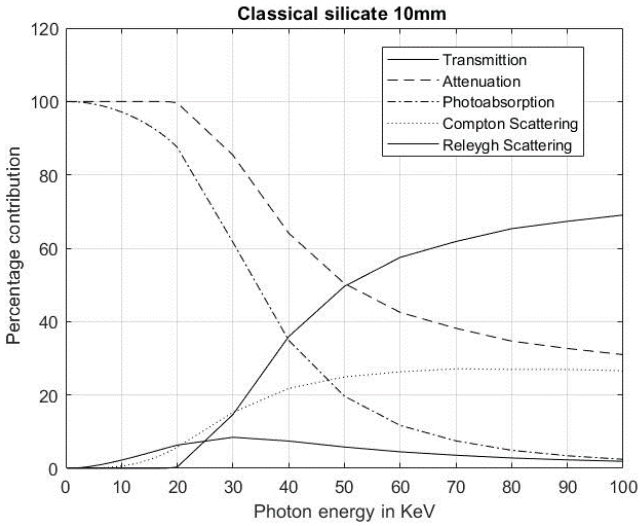

Figure 1: Radiation transport in SiO_2. Target length 10 mm in different scales across axis of energies.

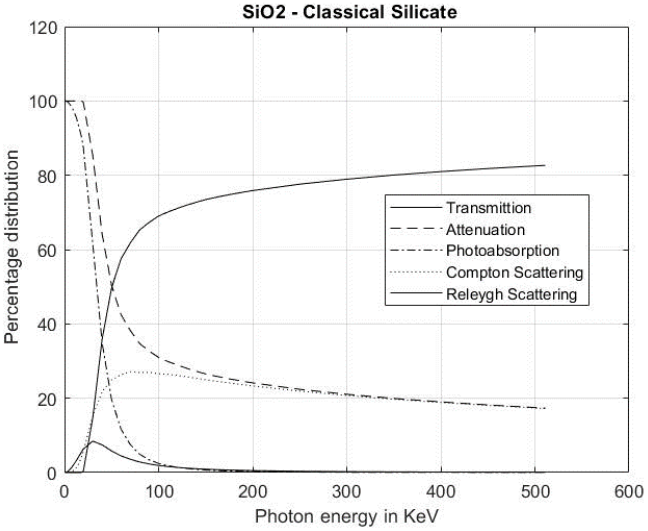

Figure 2: Ibid. At a four times greater energy scale

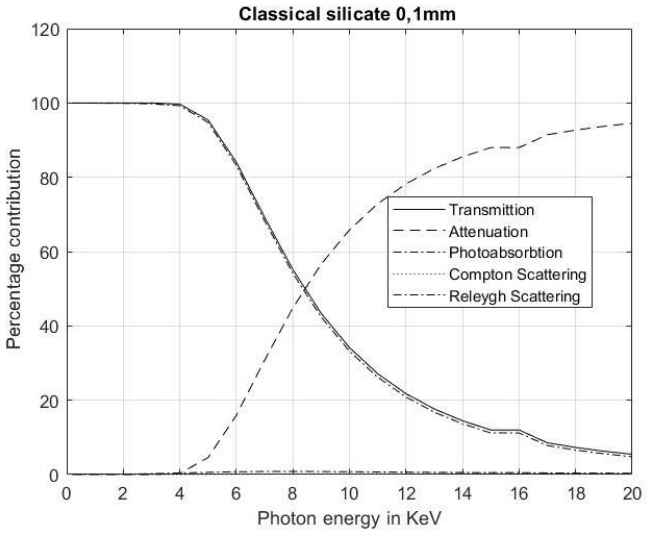

Figure 3: Ibid. Target length 0.1 mm

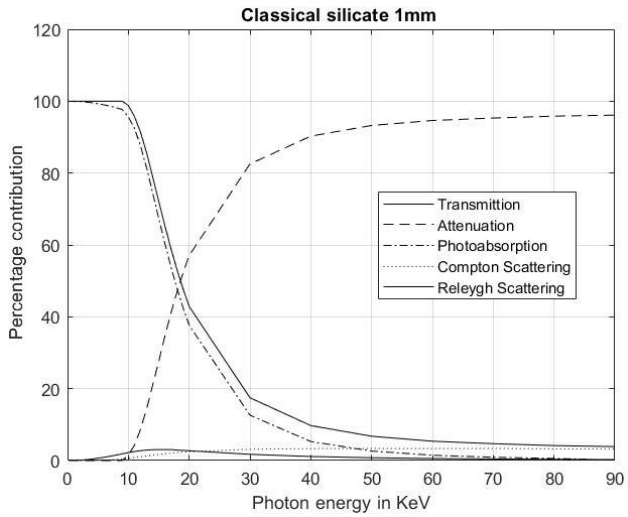

Figure 4: Ibid. Target length 1 mm

ants of the detector in 2 layers. Their design, physical and chemical structure, and geometry are such that efficient signal processing is possible in the energy range 10 keV≤Eγ≤1.3 MeV. This is due to the specificity of the flow of thermonuclear reactions in the objects under consideration and the formation of their own spectrum of hard radiation.

3. Modeling of detectors. Objects of study

Lightning in thunderstorm and volcanic clouds. The main processes occur in millisecond time intervals. The energy resource in the peak of discharge reaches 200 MeV. The main reactions can proceed with effective energies up to 10 MeV. The rest of the energy of relativistic electrons is spent on impact ionization and braking radiation. Photo visual observations confirmed the step character of the lightning trajectory. The observed numerous local bends of the trajectory of relativistic electrons leads to the formation of cyclotron radiation. Depending on the conditions of discharge flow in the spectrum of the Emitter we have a combination of braking, and in some cases synchrotron. Thus, Following X-ray radiation transformation by the Absorber, we obtain the spectrum of the quantum flux entering the Detector. It follows from the obtained results that on such geometrical scales the extinction of the directed flux of quanta is due to Compton incoherent scattering. In this case the detector registers a wide range of continuous X-ray spectrum. The probability of registration of X-ray and gamma pulses increases.

X-ray and possible gamma-ray bursts in double star systems may be rarer and shorter. Some white dwarfs have a companion star nearby. If matter from the companion star falls out in proper amounts, a hydrogen-helium mixture in a degenerate state form on the surface of the white dwarf. The explosive burning of this mixture results in a prominent flare in all ranges of the spectrum. For the most part, this is a rare event. However, monitoring such flares is important for understanding the conditions for the origin of type I supernova explosions. Flares are most common in some double systems where the magnetic field of the white dwarf reaches 10^3T or more. Observations show that several times a year there is a powerful flare in the optical range. Our previous calculations showed that if we take into account protons and helium nuclei, which make up the bulk of the matter falling along the magnetic column, the formation of X-ray and gamma-ray flares during the near-surface explosion is expected.

In the previously proposed binary detector (Doikov, 2022; 2023), the combined use of monitoring equipment was based on the operation of two separate detectors. In the present work, a multilayer detector of X-ray and gamma radiation emitted in such explosions is proposed. Since the proposed detector consists of several, sequentially alternating layers, the current pulses coming from these layers are processed within a single electronic interface. The height of each unit pulse is determined by the quantum contribution of the corresponding energy. The percentage quantum contribution is determined by the absorbed energy of a given layer. The parameter of such estimation is the percentage contribution to the total extinction called “Attenuation” and is presented in Fig. 1 – Fig. 4.The calculation of the time interval of soft gamma-ray and hard X-ray flares is microseconds. At the same time, its optical component lasts about a week. At the peak of the flare, the flux of X-ray and gamma-ray quanta from the AM Her double system on the near-Earth detector can be 10 – 100 quanta/cm^2·s. This is noticeably above its sensitivity limit.

4. Layout modeling of detectors

Thus, the use of semiconductors based on heavy elements-perovskites allows us to solve two problems at once. The first detector must efficiently absorb gamma and X-ray quanta and convert the energy into a current pulse. The presented figures Fig. 5 and Fig. 6 show the layout modeling and individual trajectories of quanta during their motion in the Detector. The use of new engineering and physical methods of modeling detectors accelerates their fabrication and reduces the cost of their bench testing. The following tasks were set and solved during modeling and prototyping:

1. Size and geometry, chemistry composition and emission spectrum of the incoming radiation detector.
2. Graphical interface tracked each individual trajectory.
3. During the motion of the quanta, its trajectories are generated and then its average characteristics are determined as shown in the figures.
4. In this work, the part of energy loss that forms the current pulse of the high voltage preamplifier is highlighted.

The obtained results of modeling and prototyping of detectors are presented in Fig. 5 and Fig. 6 allowed to select the optimal size, shape and chemical composition of detectors. Quanta with energy higher than 10 keV cross the silicon substrate and are trapped by the second layer of the detector up to 200 keV. Multiple scattering in the range from 200 keV to 511 keV leads to defocusing of the directed beam of quanta passing through the spectrograph aperture. Fig. 5 and Fig. 6 show the results of such scattering.

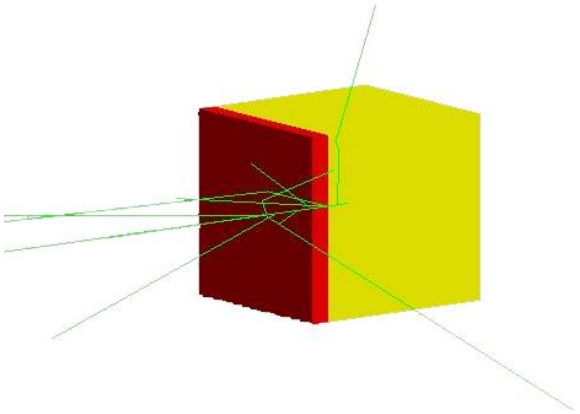

Figure 5: Model of bilayer detector $CsPbBr_3$ 1 x 1 x 1cm and SiO_2 0.1 x 1 x 1 cm. Eγ=511 KeV

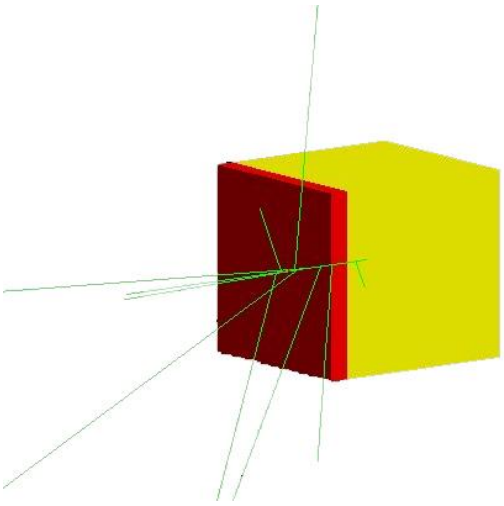

Figure 6: Model of bilayer detector $Lu(SiO)_5$ 1 x 1 x 1 cm and SiO_2 0.1 x 1 x 1 cm. E_γ=511 KeV

5. Discussion

Long-term operation of detectors under normal conditions requires elimination of surface degradation of these crystals. Therefore, they are placed in an isolation volume in which the air is evacuated and the high-voltage preamplifier can be operated. However, this leads to energy losses in the long-wavelength X-ray wing. In an open space environment, there is no need to resort to such procedures (Ma et al., 2023).

6. Conclusion

In the present work, the detector parameters necessary for their design are calculated. The method of selection of geometrical and physicochemical characteristics of used semiconductor crystals including chemical elements with large atomic numbers is proposed. Their operation does not require deep cooling and the signal-to-noise ratio is insensitive to changes in ambient temperatures. All major elements of the detector and electronic interface are publicly available.

Acknowledgements. I express my gratitude to the speakers of the Giant4 School in Pavia, Italy and their help in implementing the codes in solving the present problem. Prof. Gotsulskiy V.Y. and Senior Researcher INFN, Italy Pandola L. for productive discussion.

References

Doikov M.D.: 2022, *OAP*, **35**, 24.
Doikov M.D.: 2023, *OAP*, **36**, 42.
Geant4 – School: 2024, January 13-19, Pavia University, Italy.
Ma W. et al.: 2023, *Sensors*, **23**, 2017.
Weber G. *https://web-docs.gsi.de/~stoe_exp/web_programs/x_ray_absorption/index.php*

https://doi.org/10.18524/1810-4215.2024.37.314109

THE INNER STRUCTURE OF GALAXY CLUSTERS IN THE TRIPLETS

E.A. Panko[1], S.I. Yemelianov[2]

[1] Odesa I. I. Mechnikov National University, Odesa, Ukraine, *panko.elena@gmail.com*

[2] V.O. Sukhomlinsky Mykolaiv National University, Mykolaiv, Ukraine, *sviatoslavem@gmail.com*

ABSTRACT. The inner structure of galaxy clusters is determined by the interaction of baryon matter with the surrounding structures and the influence of the underlying dark matter. For the search of the results of such interaction, we select the 18 triplets (11 elongated and 7 rounded ones) of galaxy clusters from the triplets founded in the PF Catalogue of Galaxy Clusters and Groups (Panko & Flin). The shape of the all founded triplets vary from practically regular triangle to straight chain, i.e., the ellipticity of the best-fitted ellipse of the triplets ranged from 0.12 to 0.92. We select the triplets with ellipticities in the range $0.8 - 1.0$ as the first subset and with the ellipticities in the range $0.1 - 0.4$ as the second one.

The comparison the results obtained for two subsets allowed to conclude the elongated triplets arise along the filament. Binggeli effect was detected in a major part of clusters. In the linear substructure L11 in PF 0369–7499 galaxies show also perpendicular alignment in contrast to other galaxies of this cluster. We suppose the substructures in the galaxy clusters of our data set must be connected with the influence of other triplet members.

Keywords: galaxy clusters: morphology: inner structure; galaxies: orientations; data analysis

АНОТАЦІЯ. Внутрішня структура скупчень галактик визначається взаємодією баріонної матерії з навколишніми структурами та впливом підстилаючої темної матерії. Для пошуку результатів такої взаємодії ми обрали 18 триплетів (11 витягнутих і 7 округлих) скупчень галактик із списку триплетів, що було знайдено у Каталозі скупчень і груп галактик PF (Panko & Flin,2006). Форма всіх триплетів, що було знайдено, варіюється від майже правильного трикутника до практично прямого ланцюжка, тобто еліптичність найкращого еліпсу для триплетів скупчень галактик знаходиться у межах від 0,12 до 0,92. Ми обрали триплети скупчень з еліптичностями в діапазоні $0{,}8 - 1{,}0$ в якості першого набору даних та з еліптичностями в діапазоні $0{,}1 - 0{,}4$ в якості другого набору.

Порівняння результатів, отриманих для двох наборів, дозволило дійти до висновку, що витягнуті триплети виникають уздовж філаменту, що збігається з ідеєю еволюції елементів великомасштабної структури Всесвіту. Ефект Бінггелі був виявлений у більшої частини скупчень. Особливо розглянуто PF 0369–7499, що має дуже вузьку лінійну підструктуру L11. Галактики у лінійній підструктурі цього скупчення показують перпендикулярне вирівнювання відносно напряму на найближчого сусіда, на відміну від інших галактик цього скупчення. Ми припускаємо, що підструктури в скупченнях галактик нашого набору даних мають бути пов'язані з впливом інших членів триплету.

Ключові слова: скупчення галактик: морфологія: внутрішня структура; галактики: орієнтація; аналіз даних.

1. Introduction

The different elements of the Large Scale Structure of Universe (LSS) evolve in the interaction with surround. From the base theoretical works like Silk (1968), Peebles (1969), Peebles & Yu (1970), Zeldovich (1970), and latest it is considered the LSS elements as co-evolved objects. The fluctuations of the gravitational field and Hubble flow produce the different kinds of LSS elements, namely, $3D$ contraction gives spherical or ellipsoidal structures, $2D$ leads to filaments, and the walls are formed due to $1D$ contraction. Some additional overdense regions in the filaments can evolve to groups of small galaxy clusters which form elongated higher-level structures having two, three and more galaxy clusters. In another case – in the walls higher-level structures can obtain rounded shapes. The triplets of galaxy clusters can be good examples of both the first and second cases of the contraction, and must be reflected in the inner structure of the galaxy clusters belonging to

corresponding type of the triplet.

Our approach takes into consideration the result of the modern observations (Wen et al., 2009, Dietrich et al., 2012, Parekh et al., 2020) as well as numerical simulations from the first (Klypin & Shandarin, 1983) to latest (Springel et al., 2005, Vogelsberger et al., 2014, Artale et al., 2017, Cui et al., 2018, Tomoaki et al., 2021), where the massive gravitational bounded objects, galaxy clusters can arise on the cross of filaments or the cross of filament and wall. We suppose the footprints of such interactions we can detect as substructures in the galaxy clusters for all components, namely DM, hot gas and galaxies. The correspondence of the DM, hot intracluster gas and galaxies distribution in galaxy clusters was studied (for example, Dietrich et al., 2012) and it was shown the difference in the distributions of the cluster components arises in the collisions (Markevitch et al., 2004). The features of the distribution of galaxies give us good image for other components – hot gas and DM for non-collided, but for evolved clusters.

Our previous studies were directed to the detection of substructures in galaxy clusters in fields with different densities, from the richest regions (Panko et al., 2021) to isolated galaxy clusters (Panko et al., 2022). In all cases, we detected the different kinds of regular substructures, such as linear ones from wide bands to thin filaments, crosses and semi-crosses, and short dense curve stripes.

The next key question is the alignment of galaxies in the clusters or substructures. The Binggeli effect (Binggeli, 1982) was confirmed in a lot of works on both galaxies and galaxy clusters (Godlowski et al., 2010; Biernacka et al., 2015; Pajowska et al., 2019).

The goals of the present study are based on the following points:

- the galaxy clusters are evolved objects, and the general direction is:
- from open structure to cluster having a distinct concentration of galaxies in the center of gravity;
- from open structure to structure having some kinds of substructures and the final stage will be the same distinct concentration of galaxies in the center of gravity;
- the substructures can arise due to the gravity of the neighbor;
- the alignment of galaxies is not random;
- the substructures in the galaxy clusters belonging to elongated triplets the nonrandom alignment must be seen.

We select galaxy clusters belonging to elongated and rounded triplets as an object for present study.

2. Observational Data

The main base of our study is the list of galaxies obtained from 216 digitized plates of the Muenster Red Sky Survey (Ungrue et al., 2003), hereafter MRSS and the Catalogue of Galaxy Clusters and Groups (Panko & Flin, 2006), hereafter PF, created on the MRSS. Both catalogs cover about 5000 square degrees of sky with galactic latitudes $b < -45^o$ and completeness limit in red magnitude $r_F = 18.3^m$. For each galaxy in MRSS, the next parameters are shown: equatorial coordinates, r_F magnitude, the size of axes of the galaxy image in best-fitted ellipse approximation (in *arcsec*), ellipticity, and the position angle of the major axis of a galaxy image. Unfortunately, MRSS is the last photographic sky survey with corresponding weaknesses, and their galaxies have no redshifts.

The estimated redshifts for PF galaxy clusters were obtained from the comparison of PF catalog with ACO (Abell, 1989) and APM (Dalton et al., 1997) catalogs according to $logz$ vs. m_{10} relation (Biernacka et al. 2009), following Dalton et al. (1997). 1711 PF galaxy clusters with $z_{est} < 0.15$ and richness over 50 galaxies allowed to create the list of galaxy superclusters (Panko, 2011) using *FoF* method in Zeldovich et al. (1982) form. Simultaneously, for each of these clusters, the distance to the nearest neighbor was determined. It allows to create also the separate lists of isolated galaxy clusters, pairs of clusters, and triplets of clusters (TCl).

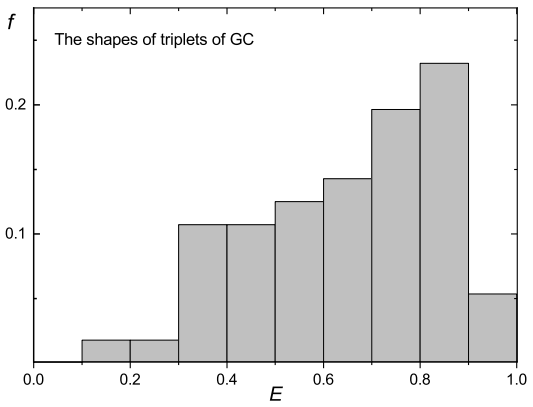

Figure 1: The distribution of the estimated shaped of triplets of galaxy clusters

The full list of triplets contains 56 records with TCl identifier, the equatorial coordinates of their centers, redshif, the full number of galaxies, the maximal size of the triplet, and the estimated shape (ellipticity), calculated using the seconds statistical moments. The distribution of the shapes is shown in Fig. 1. One can see the main part of the triplets are elongated objects like

the straight chain, nevertheless, the rounded triplets with small ellipticity are present too.

The data set for the present study contains 58 galaxy clusters belonging to 18 triplets: 11 triplets are elongated structures with ellipticities in the range $0.8 - 1.0$ and 7 ones are rounded with the ellipticities in the range $0.1 - 0.4$. We supposed two subsets must have the difference in the galaxy substructures kinds. The estimated redshifts for our data set are from 0.06 to 0.114.

3. Cluster Mapping and Substructures Detection

We used the advanced version of the "Clusters Cartography", hereafter CC (Yemelyanov & Panko, 2021), for this study. The new Web version of CC was created in JavaScript to implement dynamic data visualization in a web environment. The Web version of the CC code includes functions for processing data, calculating statistics, and plotting maps, histograms, and graphics, which are built using different parameters, such as the radii and widths of the rings in determining the degree of the concentration to the center, the widths of the bands in determining of the degree of the concentration in the linear substructures etc. we also added to the code the possibility to study the Bunggeli effect both for all galaxies and separated substructure. We conserved in the new version the base functions: the search for the position of the greatest density of galaxies in the cluster field, the detection of the regular linear and cross-type substructures, the analysis of the shape of the members of the cluster (Yemelyanov & Panko, 2021). All CC maps in the new version also have the same size $4000 \times 4000\, arcsec$. The size, shape, and orientation of symbols for galaxies correspond to MRSS data: magnitude m, ellipticity E, and positional angle of the major axis PA of the galaxy image in the best-fitted ellipse. The size of the symbol m' is calculated from the magnitude as

$$m' = 3 \cdot 2^{0.6(18.5-m)} + 6,$$

And the axes A and B of the ellipse having the same square, as:

$$A = \frac{m'}{\sqrt[4]{(1 - 2E + E^2)}}, \quad B = \frac{(m')^2}{A}.$$

The results of the analysis are based on the correspondent distribution of the selected parameter, so, they are statistically significant.

We studied the next parameters for 54 galaxy clusters: the cluster type according to the advanced morphological scheme (Panko, 2013), the presence of the regular substructures, the distribution of the ellipticities of the cluster's members, the appearances of the Binggeli effect both all galaxies in the clusters field and galaxies included in substructures.

Table 1: The morphology of galaxies in elongated and rounded triplets

Type	Elongated triplets				Rounded triplets			
	Main	L	Y	BG	Main	L	Y	BG
O	25(8)	3	4	1	16(4)	4		
I	7(1)	3	1	2	4			1
C	1				1			1
	33(9)	6	5	3	21(4)	4		2

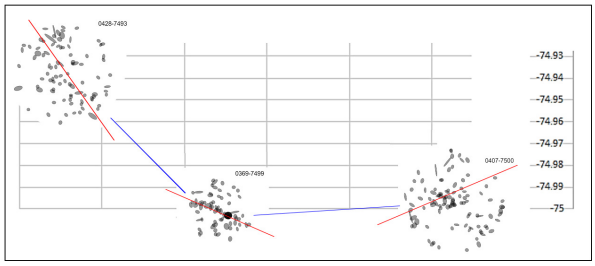

Figure 2: The triplet TCl 040-750 unites galaxy clusters PF 0369-7499, PF 0407-7500, PF 0428-7493. Red lines illustrate the detected substructure direction, and blue ones correspond od the direction of the neighbor. The position of the centers of the clusters are in the scale, at the same time the cluster images are enlarged for clarity.

4. Results and Discussion

The common results for the studied 33 galaxy clusters, belonging to elongated triplets and 21 galaxy clusters belonging to rounded ones are presented in Table 1. The values in brackets in Table 1 indicate the number of clusters with some uncertain classification of the degree of concentration toward the center. That is, for the first subset of 25 clusters of type O from the first subset, 8 ones showed a slightly pronounced concentration that can be described as OI. Similarly, in the second subset the analogical situation: OI type of cluster was detected for 4 clusters from 16. For I type in the first subset we detected only one cluster which can be classified as IC. In our previous studies pronounced OI, IO, or IC types were extremely rare.

We did not detect X-type substructures in 58 selected clusters, Y-type substructures are present only in clusters belonging to elongated triples. The correspondence between the direction of the substructure and the direction of the neighbor is seen (Fig. 2). Corresponded acute angles are small, we can suppose the inner substructures trace the parent filament direction.

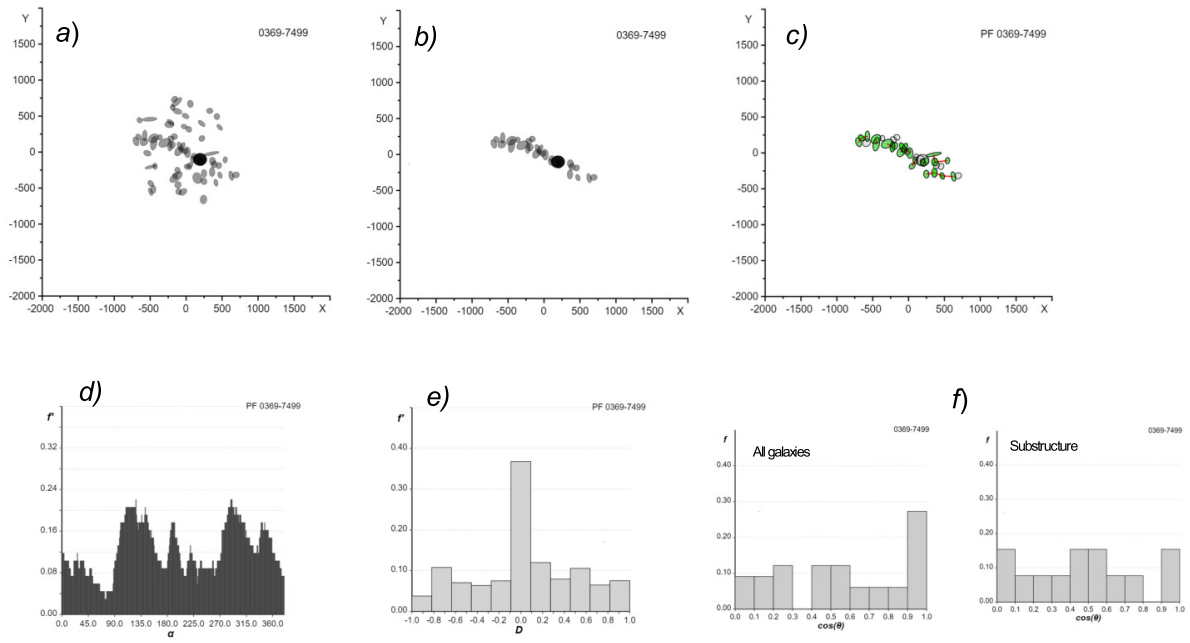

Figure 3: PF 0407-7500 cluster and its L11 substructure. In the upper panel, the maps are shown: a – the cluster, b – substructure, and c – the alignment of galaxies with E¿0.2 (green) in the substructure. the brightest cluster member is shows as black symbol. In the bottom panel: d – LHB diagram with four peaks, e – normalized galaxy densities in 11 bands, and f – alignment of galaxies as according to Binggeli effect presence

The cluster PF 0407-7500 (OL11 type) has so interesting and perspective substructure (Fig. 3a). Light-Houses Beam diagram, LHB regime in CC (fig. 3d) notes to powerful linear substructure (two wide peaks) as well as allows us to suppose the presence of the small short chain (two thin peaks). The crossing points of these substructures have the brightest galaxy, which is shown as black in Fig. 3a,b. The linear substructure is detected not only using LHB. Linear mode in CC (Fig. 3e) demonstrates a significant peak in the middle band, corresponding to the L11 type. Only galaxies in the linear substructure are shown in Fig. 3b and the example of Binggeli effect analysis for this substructure is shown in Fig. 3c. The alignment of galaxies in the L11 substructure on common is in the perpendicular direction to the direction of the neighbor galaxy. In contrast, all galaxies of the PF 0407-7500 show the Biggeli effect in classical form (Fig. 3f). The galaxies having an ellipticity less than 0.2 were.

Other triplets show similar peculiarities for linear and Y-type substructures.

5. Conclusion

We analyzed the inner structure of galaxies in both elongated and rounded triplets. About half of the clusters in both subsets are open clusters without features. For round triplets, we did not detect crosses or semi-crosses. There are linear substructures on O type that, are present only in four cases. Clusters of I and O types in this subset have no regular substructures.

For elongated triplets the part of clusters having the regular substructures, linear or semi-cross, are present in about 30% for O-type clusters and in 57% for I-type clusters.

The Binggeli effect was detected in a major part of the clusters. In the linear substructure in PF 0369-7499 galaxies show also perpendicular alignment in contrast to other galaxies of this cluster.

Acknowledgements. This research has made use of NASA's Astrophysics Data System.

References

Abell G. O., Corwin H.!G. & Olowin R. P.: 1989, *ApJS*, **70**, 1.

Artale M. C., Pedrosa S. E., Trayford J., et al.: 2017, *MNRAS*, **470**, 1771.

Biernacka M., Flin P. A. & Panko E., 2009, *ApJ*, **696**, 1689.

Biernacka M., Panko E. Bajan K., et al.: 2015, *ApJ*, **813**, 20.

Binggeli B.: 1982, *A&A*, **107**, 338.

Cui W., Knebe A., Yepes G., et al.: 2018, *MNRAS*, **473**, 68.
Dalton G. B., Maddox S. J., Sutherland W. J. & Efstathiou G.: 1997, *MNRAS*, **289**, 263.
Dietrich J. P., Werner N., Clowe D., et al.: 2012, *Nature*, **487**, 202.
Godlowski W., Piwowarska P., Panko E., el al.: 2010, *ApJ*, **723**, 985.
Klypin A. A. & Shandarin S. F.: 1983, *MNRAS*, **204**, 891.
Markevitch M., Gonzalez A. H., Clowe D., et al.: 2004, *ApJ*, **606**, 819.
Pajowska P., Godlowski W., Zong-Hong Zhu, et al.: 2019, *JCAP*, **02**, art.id 005, 1.
Panko E. A. & Flin P.: 2006, JAD, **12**, 1.
Panko E.: 2011, *BaltA*, **20**, 313.
Panko E.: 2013, *OAP*, **26**, 90.
Panko E.,Yemelianov S., Korshunov V., et al.: 2021, *ARep*, **65**, 1002.
Panko E A., Yemelianov S., Sirginava A., & Pysarevskyi Z.: 2022, *CoBAO*, **69**, 256.
Parekh V., Lagana T. F., Tho K., et al.: 2020, *MNRAS*, **491**, 2605.
Peebles P.: 1969, *AJ*, **155**, 393.
Peebles P. J. E. & Yu J. T.: 1970, *ApJ*, **162**, 815.
Silk J.: 1968, *ApJ*, **151**, 459.
Springel V., White S. D., Jenkins A., et al.: 2005, *Nature*, **435**, 629.
Tomoaki A. A., Francisco P., Klypin A. A., et al.: 2021, *MNRAS*, **506**, 4210.
Ungrue R., Seitter W. C., Duerbeck H. W.: 2003, *JAD*, **9**, 1.
Vogelsberger M., Genel S., Springel V., et al.: 2014, *MNRAS*, **444**, 1518.
Wen Z. L., Han J. L. & Liu A. C.: 2009, *ApJSS*, **183**, 197.
Yemelyanov S. I. & Panko E. A.: 2021, *OAP*, **34**, 35.
Zeldovich Y. B.: 1970, *A&A*, **5**, 84.
Zeldovich Y., Einasto J. & Shandarin S.: 1982, *Nature*, **300**, 407.

https://doi.org/10.18524/1810-4215.2024.37.311727

THE EINSTEIN-PODOLSKY-ROSEN PARADOX: FALSE SUPERLUMINAL INFORMATION TRANSFER

S.L. Parnovsky

Taras Shevchenko National University of Kyiv,
Kyiv, Ukraine, *parnovsky@knu.ua*

ABSTRACT. The paradox about the supposedly instantaneous transfer of information associated with the determination of the parameters of one of the particles included in a quantum entangled pair is considered. It is shown that this conclusion is drawn on the basis of not quite correctly formulated conditions of the thought experiment underlying the imaginary paradox.

Keywords: quantum entanglement, special relativity, superluminal transmission of information.

АНОТАЦІЯ. Розглянуто парадокс Айнштайна-Подольського-Розена про нібито миттєву передачу інформації, пов'язану з визначенням параметрів однієї з частинок, що входять до квантової заплутаної пари. Ці дві частинки поєднуються певним чином, незалежно від відстані між ними, якщо їхній стан залишається незмінним. Явище квантової заплутаності підтверджено експериментами.

У найпростішої версії парадоксу пара заплутаних фотонів народжується десь у космосі. Один із них прилітає на Землю, де фізики вимірюють його спіральність. Це дає змогу дізнатися спіральність другого фотона, який у цей момент знаходиться десь у туманності Андромеди. Виникає питання про можливість отримати інформацію зі швидкістю вище світлової.

Запропоновано неквантову аналогію парадокса, що виникає через можливу зміну проекції спіну або спіральності при взаємодію з частинками або полями. Продемонстровано, що спроби уникнути такої зміни призводять до впливу на величину, що вимірюється. Перша з можливостей є ілюстрація відомого твердження квантової механіки про вплив процесу вимірювання, в даному випадку спостереження, на стан спостережуваної системи. Друга, пов'язана зі оточенням частинки непрозорою оболонкою призводить до зміни стану частинки через ефект Казимира та зміну поляризації вакууму.

Висновок про можливість миттєвої передачі інформації зроблено на основі не зовсім коректно сформульованих умов уявного експерименту, що лежить в основі нібито парадоксу. Запропоновано поняття часткової квантової заплутаності та параметр, пов'язаний із зменшенням кореляції станів частинок, які спочатку були заплутані.

Ключові слова: квантова заплутаність, спеціальна теорія відносності, надсвітлове передавання інформації.

1. Introduction

The discussion between Einstein and Bohr played a important role in the process of understanding the concepts of quantum mechanics, which was being created at that time. Einstein proposed a number of thought (gedanken) experiments that were supposed to disprove the foundations of quantum mechanics, for example, the Heisenberg uncertainty principle. However, Bohr was able to show the falsity of these attempts in all cases. A kind of continuation of this series of thought experiments was the article (Einstein et al, 1935). Its ideas subsequently led to the emergence of the concept of quantum entanglement, when two particles link together in a certain way no matter how far apart they are in space. Their state remains the same.

The existence of quantum entanglement has been confirmed in numerous experiments and is not questioned. The experiments described in (Storz et al, 2023) are an important stage in the study of this quantum mechanical phenomenon in which the quantum states of two or more objects are interdependent. For example, one can get a pair of photons in an entangled state, and measure the spin of the one of the photons. If its helicity turns out to be positive, then the helicity of the second should be negative, and vice versa.

In this paper I want to discuss some aspects related to the paradox usually associated with this concept. I do not go into details related to Bell's inequality (Bell, 1964), etc., limiting myself to a discussion and analysis of simple thought experiments.

The paradox associated with the existence of a pair

of quantum entangled objects is connected with the fact that a measurement of a parameter of one particle is related to an instantaneous termination of the entangled state of the other. In the simplest example, a pair of entangled photons is born somewhere in space. One of them arrives on Earth, where physicists measure its helicity. This makes it possible to know the helicity of the second photon, which is somewhere in the Andromeda Nebula at that moment. Is this a transmission of information at faster than the speed of light in a vacuum? This is forbidden by the special theory of relativity. I am going to show that the paradoxicality of this situation has much to do with its formulation.

2. Analysis of the paradox

2.1. Preliminary analysis of the paradox

The presence of non-trivial and somewhat mysterious quantum entanglement may hinder understanding of the paradox. Therefore, we start by considering the EPR paradox counterpart for the non-quantum classical world. This is possible for many paradoxes related to quantum mechanics, including the famous Schrödinger's cat (Parnovsky, 2023).

In the case of a pair of entangled photons we can also present a thought experiment that is close in essence and not related to the world of quanta. We take out two playing cards from the deck, for example, the king of spades and the seven of clubs. We put them in two envelopes and randomly write two recipients on them. One of the recipients receives a letter with the king of spades in Glasgow and realizes that the second recipient in Sydney received a letter with a seven of clubs. The situation resembles a paradox with quantum entangled photons, but without the halo of mystery.

Let's not discuss how long it takes the addressee to draw a conclusion and compare it with the time it takes light to travel from Sydney to Glasgow through the globe. This is not important when analyzing a situation that has become plain and simple. The key question is how accurate is the conclusion about the card inside the envelope in Sydney.

In reality, all that the addressee from Glasgow sees is an envelope with the king of spades inside. The final conclusion is also based on additional information, which is the result of assumptions and descriptions of the organization of our thought experiment. It is implicitly assumed that two envelopes were sent with the specified playing cards inside, with the second addressee being a participant in the experiment from Sydney. The letters are not lost and not be replaced along the way. For the EPL paradox, the entangled particles must not interact with anything and retain spin or helicity.

I want to add a more general remark. There is a difference between obtaining real information and using the results of the estimates and calculations that underlie the paradox under discussion. A predicting the helicity of a distant photon or the projection of the spin of a massive distant particle is like the situation with a rocket sent to Alpha Centauri carrying a time bomb. Observers on Earth may believe that the bomb has exploded at a calculated point in time, but they will not receive direct information about the explosion until more than 4 years later. Up to this point, it is not information, but just a guess. You never know what could happen to the rocket, the bomb and the clockwork.

The production of a pair of quantum entangled particles is provided by the laws of physics, including quantum mechanics and the law of conservation of angular momentum of particles. But the requirement that the state of the particle must not change during its journey is very important. This is implicitly assumed in the conditions of the gedanken experiment, but how much is it admissible in reality? If an elementary particle moves in space, it can change the projection of its spin on a given axis while interacting with another particle or in an external field. For example, during interaction with photons of CMB radiation (see the Greisen–Zatsepin–Kuzmin cutoff (Greisen, 1966; Zatsepin, Kuz'min, 1966)).

2.2. The need for observation and its impact on particles

In order to be sure that the emitted particle has not changed helicity or projection of spin, one must know that it has not interacted with anything during the motion. Here it is worth remembering that in quantum mechanics the measurement process and the observation process as a special case affects the state of the system. This has been repeatedly illustrated by various examples.

Say an observer wants to know if there is a black cat in a dark room. He can use a flashlight, but this would cause the pressure of the torch's light to affect the cat, naturally if it is in the room, and would change its momentum as a result. From this it is not difficult to obtain a constraint related to the Heisenberg uncertainty principle. Corresponding estimates are given, for example, in the book (Parnovsky, 2023).

If we place observers in space along its trajectory, armed with torches or other means of gaining information about the world around it, to make sure that a receding entangled particle does not interact with other particles, the particle may change its helicity or spin projection due to interaction with the light from these torches.

Let's try to break the deadlock in another way, making our thought experiment much more complicated. We surround the massive particle with a sphere of

strong opaque material, which do not let photons or other particles near it. It flies at the same speed, escorting the particle and protecting it from unwanted interactions. However, this would not solve the problem. The mere existence of the shell changes the oscillations of the physical fields within it, including the electromagnetic one. This leads to a change of polarization of the vacuum, i.e. to the manifestation of the Casimir effect (Casimir, 1948; DeWitt, 2022).Its influence can change the projection of a particle's spin on a chosen axis.

So, it is quite possible that the spin or helicity of a particle moving in this medium may change. Some mechanisms of such a change are related to the very fundamentals of quantum mechanics, such as the effect of a measurement process on the object being measured. Therefore, they always work. I note that the particle, whose state is supposedly determined remotely, may simply not be present at the point in space-time, where it should be according to calculations.

3. Partial quantum entanglement

The above is sufficient to show that when using a pair of quantum entangled particles and having received information about the spin or helicity of one of them, we can determine the position or the very fact of the existence and spin or helicity of the second one only with a certain probability different from unity. This is sufficient to consider the obtained estimate not information, but merely an assumption.

To obtain quantitative characteristics, an approach somewhat similar to the concept of partially coherent light (Born and Wolf, 1999) can be used. Let us indicate the basic approach. Consider the motion of one of the particles produced as an entangled pair at distance $x = 0$. Let it be a fermion with spin 1/2, having two projections on the selected axis: 'spin up' and 'spin down', or a photon with positive or negative helicity. The pair was born from the initial configuration with zero angular momentum, so that the projections or helicities of the two produced particles are initially opposite.

The quantities $p_+(x)$ and $p_-(x)$ show the probabilities that the particle will show positive and negative spin projection or helicity when measuring at distance $x < 0$ from the point of birth of the pair. These quantities can change due to interaction with particles and fields during the particle's motion, but their sum is equal to 1.

$$p_+(x) + p_-(x) = 1. \qquad (1)$$

Let us assume that the effect of external factors is random and isotropic. Let the particle, having traveled the path dx, change the direction of its spin with equal probability from 'spin down' to 'spin up' or vice versa:

$$\frac{dp_+(x)}{dx} = -\frac{dp_-(x)}{dx} = \alpha(p_-(x) - p_+(x)). \qquad (2)$$

The quantity $\alpha \geq 0$ characterizes the rate of change of the spin component during the motion of the particle. It does not take into account the possibility of annihilation or transformation of the particle by interaction or by scattering. For simplicity, we assume that this quantity is constant. The solution to the system of equations has the form

$$p_+(x) = p_+(0)\exp(-2\alpha x) + \frac{1 - exp(-2\alpha x)}{2}. \qquad (3)$$

If $\alpha = 0$, as is implicitly implied in the standard formulation of the paradox, then $p_+(x) = p_+(0)$. But for any small non-zero value of $\alpha > 0$, this value changes. For $x \ll \alpha^{-1}$, we get $p_+(x) \approx p_+(0)$, and for $x \gg \alpha^{-1}$, we get $p_+(x) \to 1/2$.

The latter is related to the used assumption of isotropy of interaction. In reality, it can be anisotropic with distinguished directions determined by the direction of the fields, say, the galactic or intergalactic magnetic field and the speed of the used frame of reference relative to the one in which the dipole component of the relic radiation is zeroed. Note that in the process of interaction with the CMB, the energy and speed of fermions can decrease [5,6].

Any value of $\alpha > 0$ makes the connection between $p_+(x)$ and $p_+(0)$, and hence between the spin projections of two partially entangled particles, not uniquely defined but probabilistic with a correlation that decreases as the particles move away. The actual experiments [2] were conducted at $x \ll \alpha^{-1}$, and the formulation of the paradox not only assumes $x \gg \alpha^{-1}$, but also requires obtaining information rather than an estimate, albeit a very probable one.

So, if the particles have to travel huge interstellar or even intergalactic distances, then the probability that they remain entangled is greatly reduced. As a result, for this reason alone, registration of the state parameters of one of the particles does not guarantee knowledge of the state parameters of the second particle. Accordingly, it is impossible to speak about the transfer of information about it with superluminal speed.

4. Conclusions

The phenomenon of quantum entanglement has been confirmed by experiments. However, a paradox about the supposedly instantaneous transmission of information is associated with it. The analysis carried out showed that in reality this paradox does not exist. The conclusion about the possibility of instantaneous transmission of information was made on the basis

of not quite correctly formulated conditions of the gedanken experiment that underlay the imaginary paradox. An essential detail of the analysis is the well-known statement of quantum mechanics about the influence of the process of measurement, in this case, observation, on the state of the observed system.

Acknowledgements. The work was supported by the Ministry of Education and Science of Ukraine under Project No. 0122U001865.

References

Bell J.S.: 1964, *Physics Physique Fizika*, **1**, 195.

Born M., Wolf E.: 1999, Principles of optics: electromagnetic theory of propagation, interference and diffraction of light (7th expanded ed.) (Cambridge: Cambridge University Press).

Casimir H.B.G.: 1948, Proc. of the Koninklijke Nederlandse Akademie van Wetenschappen, **B51**, 793.

DeWitt B.S.: 1975, *PhR*, **19**, 295.

Einstein A., Podolsky B., Rosen N.: 1935, *PhR*, **47**, 777.

Greisen K.: 1966, *PhRvL*, **16**, 748.

Parnovsky S.: 2023, About the Biggest, the Smallest, and Everything Else: Travelling Through the Universe with a Physicist Guide. (Singapore: World Scientific)

Storz S., Schär J., Kulikov A., et al.: 2023, *Nature*, **617**, 265.

Zatsepin G.T., Kuz'min V.A.: 1966, *JETPL*, **4**, 78.

https://doi.org/10.18524/1810-4215.2024.37.313462

IMPLICATIONS OF PHOTON–AXION OSCILLATIONS ON X-RAY OBSERVATIONS OF THE COMA CLUSTER

Y.Sahai[1], L.Zadorozhna[1,2], O.Prikhodko[1], D.Malyshev[3], A.Tugay[1], N.Pulatova[4,5]
[1] Faculty of Physics, Taras Shevchenko National University of Kyiv, Ukraine
[2] Niels Bohr Institute, University of Copenhagen, Denmark
[3] Institut für Astronomie und Astrophysik Tübingen, Universität Tübingen, Germany
[4] Main Astronomical Observatory of the NAS of Ukraine, Kyiv, Ukraine
[5] Max-Planck-Institut für Astronomie, Heidelberg, Germany
e-mail: lidiia.zadorozhna@knu.ua

ABSTRACT. Axion-like particles (ALPs) emerge as predictions from various extensions of the Standard Model, standing out as plausible candidates for dark matter. Axions are thought to be produced when light passes through regions of magnetic fields. This positions astrophysical environments as prime sites for their production and subsequent detection. However, establishing precise constraints on axion parameters remains challenging, primarily due to the limited understanding of astrophysical magnetic fields. The Coma cluster is notable for being the sole cluster where the profile of magnetic field strength has been relatively accurately determined using Faraday Rotation Measures. We examined the X-ray spectrum of the Coma galaxy cluster using data from the XMM-Newton observatory. We combined data from eight XMM-Newton observations conducted between 2000 and 2005, spanning a $40' \times 40'$ area centered on the Coma cluster, totaling 343.8 ks. The X-ray spectrum of the ICM was characterized by modeling it with emissions from a single-temperature hot plasma. Furthermore, we explored the potential impact of photon-to-ALP conversion on the spectrum of the Coma cluster. Our investigation encompassed a range of parameters – the coupling constant and the axion mass, focusing on regions that have not yet been excluded. For the selected axion parameters, the primary impact on the spectrum could occur at high energies exceeding 5 keV. Analysis of the limited statistics gathered in this study indicates that the excluded parameter space for ALPs, based on X-ray observations of the Coma cluster, lies above the following values: $g_{a\gamma} < 5 \cdot 10^{-13}\,\mathrm{GeV}^{-1}$, $m_a < 1 \cdot 10^{-12}\,\mathrm{eV}$ with 95% probability.

Keywords: axion, clusters of galaxies, intergalactic plasma, X-ray radiation.

АНОТАЦІЯ. Аксіоноподібні частинки виникають як передбачення розширень Стандартної моделі, виокремлюючись як потенційні кандидати на роль темної матерії. Вважається, що аксіони формуються під час проходження світла через магнітні поля, що робить астрофізичне середовище ключовим місцем для їхнього утворення та можливого виявлення. Однак точне встановлення обмежень на параметри аксіонів залишається складною задачею, переважно через обмежене розуміння астрофізичних магнітних полів. Скупчення Кома привертає увагу тим, що воно єдине, де профіль напруженості магнітного поля відносно точно визначений за допомогою вимірювань обертання Фарадея. Ми дослідили рентгенівський спектр скупчення галактик Кома, використовуючи дані обсерваторії XMM-Newton. Для цього об'єднали дані 8 спостережень XMM-Newton з області розміром $40' \times 40'$ із центром у скупченні Кома, проведених у період з 2000 по 2005 рік, із загальною тривалістю 343,8 кс. Рентгенівський спектр внутрішньокластерного середовища був змодельований як випромінюваня однотемпературної гарячої плазми. Ми вивчали можливий вплив фотон-аксіонної конверсії на спектр кластера Кома. Ми розглянули параметри — константу зв'язку та масу аксіону, зосереджуючись зокрема на тих їх величинах, які досі залишалися невиключені. Для вибраних параметрів аксіонів їхній основний внесок у спектр може спостерігатися при високих енергіях, що перевищують 5 кеВ. Аналіз обмеженої статистики, зібраної у цьому дослідженні, показує, що простір параметрів для аксіоноподібних частинок, який є виключеним на підставі рентгенівських спостережень скупчення Коми, лежить вище за наступні значення: $g_{a\gamma} < 5 \cdot 10^{-13}\,\mathrm{ГеВ}^{-1}$, $m_a < 1 \cdot 10^{-12}$ еВ з ймовірністю 95%.

Ключові слова: аксіон, скупчення галактик, міжгалактична плазма, рентгенівське випромінювання

1. Introduction

1.1. Exploring ALPs in astrophysics

Axions are hypothetical particles originally proposed as a solution to the strong CP-problem (Peccei, 1977a; Peccei, 1977b). Almost immediately, these particles were identified as prime candidates for dark matter (Weinberg, 1978; Wilczek, 1978). Today, we discuss a wider family of axion-like particles (ALPs) that share the main properties of axions: they are very light (much lighter than even a neutrino) and interact with photons when traversing regions of magnetic fields, via the term (Malyshev, 2018; Raffelt, 1988):

$$\mathcal{L}_{\gamma a} = -\frac{1}{4} g_{\gamma a} F_{\mu\nu} \tilde{F}^{\mu\nu}\, a = g_{\gamma a} \mathbf{E}\cdot\mathbf{B}\, a\,, \qquad (1)$$

where a is a pseudo-scalar axion field, $F_{\mu\nu}$ is the electromagnetic field strength, $\tilde{F}_{\mu\nu} \equiv \frac{1}{2}\varepsilon_{\mu\nu\rho\sigma}F^{\rho\sigma}$ is the electromagnetic dual, $\mathbf{E}$ and $\mathbf{B}$ are the electric and magnetic field strengths, respectively, and $g_{\gamma a}$ is the photon-axion coupling. Natural Lorentz-Heaviside units with $\hbar = c = 1$ are used throughout this article.

A variety of search strategies can be used depending on the ALP mass. ALPs can be detected through astrophysical observations or laboratory experiments, where photon-ALP oscillations occur in the presence of a magnetic field. These oscillations generate distinct features in the spectra of astrophysical objects. Photon-to-ALP conversion is expected to cause detectable energy-dependent distortions in the X-ray or γ-ray spectra of sources within or behind galaxy clusters (Conlon, 2016; Davies, 2023; Hochmuth, 2007; Malyshev, 2018; Meyer, 2013; Mirizzi, 2008; Reynolds, 2020). The absence of ALP imprints on photon signals from astronomical sources has been crucial in establishing constraints on the axion mass and coupling constant (O'Hare, 2020).

1.2. X-ray-ALP conversion in the cluster magnetic field

The propagation of a photon (A_x, A_y) with energy E along z-axis is described by (Hochmuth, 2007; Malyshev, 2018)

$$[E - i\partial_z - M(m_a, g_{\gamma a}, B_\perp)]\,\mathbf{A} = \mathbf{0}, \qquad (2)$$

where

$$\mathbf{A} \equiv \begin{pmatrix} A_x \\ A_y \\ a \end{pmatrix},$$

and $M(m_a, g_{a\gamma}, B_\perp)$ is the mixing matrix. The primary components of the mixing matrix, concerning keV photons traveling through the galaxy cluster environment are:

$$M = \begin{pmatrix} \Delta_{pl} & 0 & \Delta_{a\gamma}\cos\phi \\ 0 & \Delta_{pl} & \Delta_{a\gamma}\sin\phi \\ \Delta_{a\gamma}\cos\phi & \Delta_{a\gamma}\sin\phi & \Delta_a \end{pmatrix}, \qquad (3)$$

where $\cos\phi = \mathbf{B}_\perp \cdot \mathbf{e}_x / B_\perp = \sqrt{1-\sin^2\phi}$. Elements of the matrix Eq. (3) are given by:

$$\Delta_{a\gamma} = \frac{1}{2} g_{a\gamma} B_\perp \simeq$$

$$\simeq 7.6\cdot 10^{-7} \left(\frac{g_{a\gamma}}{5\cdot 10^{-13}\mathrm{GeV}^{-1}}\right)\left(\frac{B_\perp}{\mu\mathrm{G}}\right)\mathrm{pc}^{-1},$$

$$\Delta_a = -\frac{m_a^2}{2E} \simeq$$

$$\simeq -1.95\cdot 10^{-3} \left(\frac{m_a}{5\cdot 10^{-12}\mathrm{eV}}\right)^2 \left(\frac{E}{\mathrm{keV}}\right)^{-1} \mathrm{pc}^{-1},$$

$$\Delta_{\mathrm{pl}} = -\frac{\omega_{\mathrm{pl}}^2}{2E} \simeq$$

$$\simeq -1.1\cdot 10^{-4} \left(\frac{E}{\mathrm{keV}}\right)^{-1} \left(\frac{n_e}{10^{-3}\,\mathrm{cm}^{-3}}\right)\mathrm{pc}^{-1},$$

where $\omega_{\mathrm{pl}}^2 = 4\pi\alpha n_e/m_e$ is the plasma frequency of the medium, n_e is the electron density and $\alpha \equiv e^2/(4\pi) = 1/137$ the fine-structure constant with e the electron charge.

$$\omega_{\mathrm{pl}} = e\left(\frac{n_e}{m_e}\right)^{1/2} = 1.17\cdot 10^{-12}\left(\frac{n_e}{10^{-3}cm^{-3}}\right)^{1/2}\ \mathrm{eV}.$$

If axions exist, magnetic fields cause photons to convert into them with the strength of the interaction, controlled by $g_{a\gamma}$.

The probability of the photon-axion conversion is proportional to the magnetic field, perpendicular to the line of sight:

$$P_{\gamma a} \approx 3\cdot 10^{-5}\left(\frac{B_\perp}{\mu\mathrm{G}}\frac{L}{10\,\mathrm{kpc}}\frac{g_{a\gamma}}{5\cdot 10^{-13}\,\mathrm{GeV}^{-1}}\right)^2,$$

where L is the magnetic field coherent length. Here we have normalized the quantities to typical parameters relevant to the galaxy cluster.

1.3. Coma cluster

The Coma cluster (Abell 1656) has been extensively studied across various wavelengths as a galaxy cluster with a hot gas composition. Located approximately 99 Mpc from the observer, with a redshift of $z = 0.0231$, the Coma cluster consists of over 10^3 galaxies. This virialized structure possesses a mass ranging from 10^{14} to 10^{15} $M_\odot$ and extends over spatial scales of more than 1 Mpc (Bower, 2013). The

intracluster medium (ICM) within the Coma cluster emits diffuse X-ray radiation primarily through thermal bremsstrahlung, with a typical temperature of $T \sim 10^8$ K and a number density in the range of $n_e \sim 10^{-1} - 10^{-3}\,\mathrm{cm}^{-3}$ (Chen, 2007).

The celestial size of the Coma cluster extends over more than 2° in the sky, with its ICM being an extended X-ray source larger than 45′.

Both radio and X-ray observations suggest turbulence and disruption within the intergalactic plasma (Churazov, 2012; Schuecker, 2004). Moreover, the behavior of transport processes is closely linked to the configuration of local magnetic field. The presence of substructures within the Coma ICM, particularly gas fluctuations arising from galaxy cluster collisions, highlights the intricate nature of the ICM.

The Coma cluster stands out as one of the few clusters whose magnetic field strength profile has been measured. The primary method for probing a cluster's magnetic fields is through Faraday rotation measure (RM). These fields are intimately connected with the plasma and can pervade its internal structure. Their properties often indicate a stochastic and turbulent nature. Generally, the beta-profile is employed for gas density, with a corresponding profile for the magnetic field. The radial distribution of electrons in the Coma cluster is described by $n_e(r) = n_0[1 + (r/r_c)^2]^{-3\beta/2}$, where $n_0 = 3.44 \cdot 10^{-3}\,\mathrm{cm}^{-3}$, $r_c = 291\,\mathrm{kpc}$, and $\beta = 0.75$ (Bonafede, 2010; Łokas, 2003), while the magnetic field profile follows $B(r) = B_0[n_e(r)/n_0]^\eta$, where $B_0 = 5.2\,\mu\mathrm{G}$ and $\eta = 0.67$ (Bonafede, 2010).

2. Data analysis

2.1. XMM-Newton X-ray spectrum

We analyzed observation data files for the Coma cluster from the XMM-Newton X-ray observatory. The observations included the following ObsIDs: 0124711401, 0153750101, 0300530101, 0300530301, 0300530401, 0300530501, 0300530601, and 0300530701, with a total exposure time of 343.8 ksec. We studied the combined MOS1/MOS2 spectra from the central region $40' \times 40'$ using the `Xspec` package. In our spectral analysis, we did not perform background subtraction because the object's size exceeds the field of view, making it impossible to select an appropriate region for background spectrum estimation. To account for residual calibration uncertainties in XMM-Newton observations, we added 1% systematic error.

The resulting **base model fit** (see Table 1) consists of the thermal radiation from the plasma `apec_3` within the Coma cluster, along with various astrophysical components such as Solar System plasma `apec_1`, hot interstellar plasma `apec_2`, and the cosmic X-ray background `powerlaw_1`. Additionally, it includes the hydrogen column density for absorption `phabs`, as well as instrumental backgrounds featuring a smooth continuum `powerlaw` and line-like `gaussian` features. Refs. (Malyshev, 2022; Zadorozhna, 2023) provide comprehensive lists of the most significant instrumental and astrophysical lines essential for modeling the XMM-Newton background.

2.2. Photon-to-ALP conversion simulation

We used the publicly available `AlPro` (Axion-Like PROpagation) (Matthews, 2022) code in Python designed to solve the equations of motion for a photon-ALP beam, accounting for the mixing between photon and ALP states.

We assumed that most of the X-ray photons that travel a sufficient distance and in a strong enough magnetic field to oscillate into axions are born in the central region of the cluster. The initial parameters for running the code were chosen as follows: the magnetic field profile and amplitude as described in subsection *1.3*, and the cluster radius was set to 1.5 Mpc. We divided the cluster into 50 randomly distributed domains, with sizes ranging from 2 to 32 kpc. The magnetic field's orientation varied randomly in the photon polarization plane within each domain, while the magnetic field amplitude remained constant in each domain. Each run of the code generated a curve depicting the probability of photon survival as it travels from the center of the Coma cluster (see Figures 1, 2). Significant contributions from conversions at the given ALP parameters occur at energies higher than 5 keV.

For the ALP parameters $g_{a\gamma} = 5 \cdot 10^{-13}\,\mathrm{GeV}^{-1}$ and $m_a = 5 \cdot 10^{-12}\,\mathrm{eV}$, the conversion probability does not exceed 1% as can be seen from Figure 1. Each curve was transformed into a multiplicative ALPs model and then multiplied by the **base model** (see Table 1). The fitting results for curves with these parameters are summarized in Table 2. In Table 1, the columns **fit 1**, **fit 3**, **fit 5**, and **fit 11** present the detailed fitting results as examples. For the ALP parameters $g_{a\gamma} = 6 \cdot 10^{-13}\,\mathrm{GeV}^{-1}$ and $m_a = 3 \cdot 10^{-12}\,\mathrm{eV}$, the conversion probability remains below 10%, as illustrated in Figure 2.

Figure 3 presents the spectrum with various model fits. The line colors in Figure 3 match the curve colors in Figure 2. These colored curves were used as a multiplicative ALPs model to fit the data and construct the correspondingly colored lines in Figure 3.

2.3. Bounds on ALPs

Detecting photon-axion oscillations in the X-ray thermal spectrum of a cluster is challenging due to the presence of spectral lines and complexities in background modeling. Our analysis found no significant

No	Model Comp.	Parameter Unit	**Value** **base model** **fit**	**Value** **base model+ALPs** **fit 1**	**Value** **base model+ALPs** **fit 3**	**Value** **base model+ALPs** **fit 5**	**Value** **base model+ALPs** **fit 11**
1	apec_1	kT, keV	0.307 ± 0.018	0.307 ± 0.018	0.307 ± 0.018	0.307 ± 0.018	0.307 ± 0.0182
2	apec_1	Abundance	1.000 frozen	1.000 frozen	1.000 frozen	1.000 frozen	1.000 frozen
4	apec_1	Redshift	0.0 frozen	0.0 frozen	0.0 frozen	0.0 frozen	0.0 frozen
5	apec_1	norm, cm^{-3}	$(8.278 \pm 1.941) \cdot 10^{-4}$	$(8.282 \pm 2.010) \cdot 10^{-4}$	$(8.285 \pm 1.941) \cdot 10^{-4}$	$(8.29 \pm 1.941) \cdot 10^{-4}$	$(8.278 \pm 1.942) \cdot 10^{-4}$
6	phabs	n_H, $10^{22}\,\mathrm{atoms\,cm}^{-2}$	$(1.502 \pm 0.491) \cdot 10^{-2}$	$(1.502 \pm 0.491) \cdot 10^{-2}$	$(1.502 \pm 0.492) \cdot 10^{-2}$	$(1.502 \pm 0.492) \cdot 10^{-2}$	$(1.502 \pm 0.492) \cdot 10^{-2}$
7	pl_1	PhoIndex	1.478 ± 0.021	1.478 ± 0.021	1.478 ± 0.022	1.478 ± 0.022	1.478 ± 0.022
8	pl_1	$\mathrm{ph\,cm}^{-2}\,\mathrm{s}^{-1}\,\mathrm{sr}^{-1}\,\mathrm{keV}^{-1}$	$(2.450 \pm 0.249) \cdot 10^{-2}$	$(2.450 \pm 0.249) \cdot 10^{-2}$	$(2.450 \pm 0.249) \cdot 10^{-2}$	$(2.450 \pm 0.249) \cdot 10^{-2}$	$(2.450 \pm 0.249) \cdot 10^{-2}$
9	apec_2	kT, keV	1.002 ± 0.040	1.002 ± 0.040	1.002 ± 0.040	1.002 ± 0.040	1.002 ± 0.040
10	apec_2	Abundance	1.000 frozen	1.000 frozen	1.000 frozen	1.000 frozen	1.000 frozen
11	apec_2	Redshift	0.0 frozen	0.0 frozen	0.0 frozen	0.0 frozen	0.0 frozen
12	apec_2	norm, cm^{-3}	$(6.333 \pm 1.282) \cdot 10^{-4}$	$(6.333 \pm 1.282) \cdot 10^{-4}$	$(6.331 \pm 1.282) \cdot 10^{-4}$	$(6.335 \pm 1.282) \cdot 10^{-4}$	$(6.333 \pm 1.283) \cdot 10^{-4}$
13	apec_3	kT, keV	7.658 ± 0.140	7.671 ± 0.140	7.675 ± 0.140	7.678 ± 0.140	7.664 ± 0.139
14	apec_3	Abundance	0.542 ± 0.063	0.542 ± 0.063	0.544 ± 0.064	0.542 ± 0.064	0.542 ± 0.063
15	apec_3	Redshift	0.0231 frozen	0.0231 frozen	0.0231 frozen	0.0231 frozen	0.0231 frozen
16	apec_3	norm, cm^{-3}	$(7.658 \pm 0.908) \cdot 10^{-2}$	$(7.658 \pm 0.908) \cdot 10^{-2}$	$(7.658 \pm 0.908) \cdot 10^{-2}$	$(7.658 \pm 0.908) \cdot 10^{-2}$	$(7.658 \pm 0.908) \cdot 10^{-2}$
17	ALPs_1	$g_{a\gamma}$, GeV^{-1}	–	$5 \cdot 10^{-13}$	$5 \cdot 10^{-13}$	$5 \cdot 10^{-13}$	$5 \cdot 10^{-13}$
18	ALPs_1	m_a, eV	–	$5 \cdot 10^{-12}$	$5 \cdot 10^{-12}$	$5 \cdot 10^{-12}$	$5 \cdot 10^{-12}$
		$\chi^2/d.o.f.$	1926.78/1936	1928.97/1936	1924.78/1939	1921.19/1936	1926.78/1939
		P(H0)	30.0%	28.8%	31.1%	33.2%	30.0%

Table 1: Model parameters of the combined MOS1/MOS2 spectrum extracted from the central region of the Coma cluster. The column labeled **Value base model fit** displays a set of parameters for the complex model `apec_1 + phabs*(powerlaw_1+apec_2+apec_3)` with the addition of an instrumental background. The columns labeled **Value base model+ALPs fit 1**, **Value base model+ALPs fit 3**, **Value base model+ALPs fit 5**, and **Value base model+ALPs fit 11** present parameters from the previous model with an additional ALPs component (apec_1 + phabs*(powerlaw_1+apec_2+apec_3))*ALPs, including the contribution of instrumental background.

Table 2: Summary of the fitting results. The Fit column denotes the number of attempts made to approximate the spectrum using the complex model with the previously generated ALP model incorporated, corresponding to the curves in Figure 1. Columns labeled χ^2/d.o.f. and P(H0) show the chi-squared test results and the null hypothesis probability, respectively.

Fit	χ^2/d.o.f.	P(H0)
1	1928.97/1936	28.8%
2	1925.07/1939	31.0%
3	1924.78/1939	31.1%
4	1926.44/1939	30.2%
5	1921.19/1939	33.2%
6	1924.68/1939	31.2%
7	1927.34/1939	29.7%
8	1927.82/1939	29.4%
9	1928.08/1939	29.3%
10	1924.03/1939	31.6%
11-19	1926.78/1939	30.0%
20	1924.35/1939	31.1%

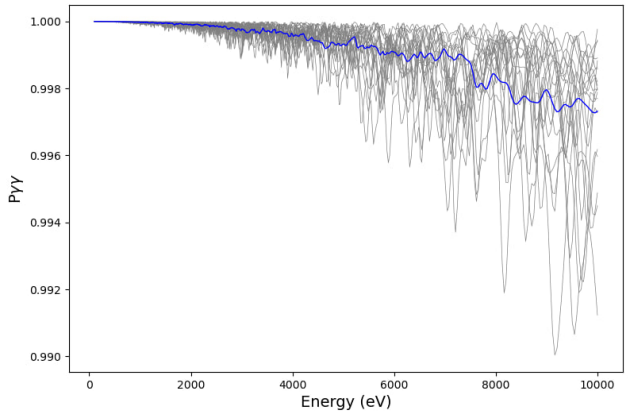

Figure 1: The photon survival probability when traversing the Coma cluster is shown for 20 different realizations of the cluster's magnetic field in **gray lines**. All realizations maintain the same amplitude and radial profile of the magnetic field. They differ only in the random orientation of the magnetic field to the photon polarization plane and the sizes of the domains in which the field remains constant. The gray curves fluctuate to such an extent that they nearly merge into a continuous area. The **blue line** illustrates the conversion probability averaged over these 20 realizations. The ALP parameters used are $g_{a\gamma} = 5 \cdot 10^{-13}\,\mathrm{GeV}^{-1}$ and $m_a = 5 \cdot 10^{-12}\,\mathrm{eV}$ for all curves.

deviations from the thermal spectrum, thus constraining the ALP parameter space. We scanned the parameter area for the axion-photon coupling constant $g_{a\gamma} \in [5 \cdot 10^{-13}\ \mathrm{GeV}^{-1}; 3 \cdot 10^{-12}\ \mathrm{GeV}^{-1}]$ and ALPs mass $m_a \in [1 \cdot 10^{-12}\ \mathrm{eV}; 5 \cdot 10^{-12}\ \mathrm{eV}]$ with a 10% step for each parameter and conducted 20 trials for each

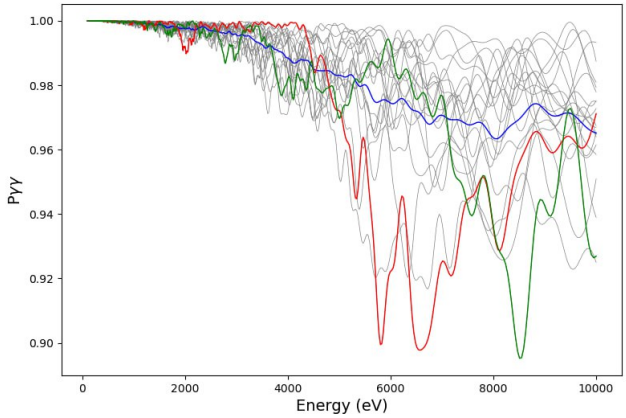

Figure 2: The photon survival probability through the Coma cluster is shown for 20 magnetic field realizations (**gray lines, green line, red line**), which differ in magnetic field orientation and domain sizes but share the same amplitude and radial profile. The average over these 20 realizations conversion probability is depicted by the **blue line**. The ALP parameters used are $g_{a\gamma} = 6 \cdot 10^{-13}\,\mathrm{GeV}^{-1}$ and $m_a = 3 \cdot 10^{-12}\,\mathrm{eV}$ for all curves.

parameter pair. The results are represented by a color gradient in Figure 4: white indicates a 0% probability of exclusion, while blue indicates a 100% probability of exclusion. A parameter pair is excluded with 95% probability if 19 out of 20 tests show degradation of the baseline spectrum.

Our assessment is limited by a 1% systematic error from residual calibration uncertainties in XMM-Newton observations. We did not take into account statistical errors due to limited observation time. Additionally, our limits may be overestimated because of the modest attempts for each pair of parameters, which we plan to address in future work. Nonetheless, our results are consistent with existing bounds and even improve upon them. It is important to note, however, that existing analyses are not optimized for ALP searches.

Notably, within the above parameter range, a significant increase in the null hypothesis probability was observed in one of the random realizations of the magnetic field for the ALP parameters $g_{a\gamma} = 6 \cdot 10^{-13}\,\mathrm{GeV}^{-1}$ and $m_a = 3 \cdot 10^{-12}\,\mathrm{eV}$. The probability rose to 88% from the base model's 30%. The photon survival probability curve corresponding to this fit is shown in Figure 2 as a red line. Additionally, Figure 2 also includes a green line representing the photon survival curve for which the fit has the lowest null hypothesis probability of just 0.08%.

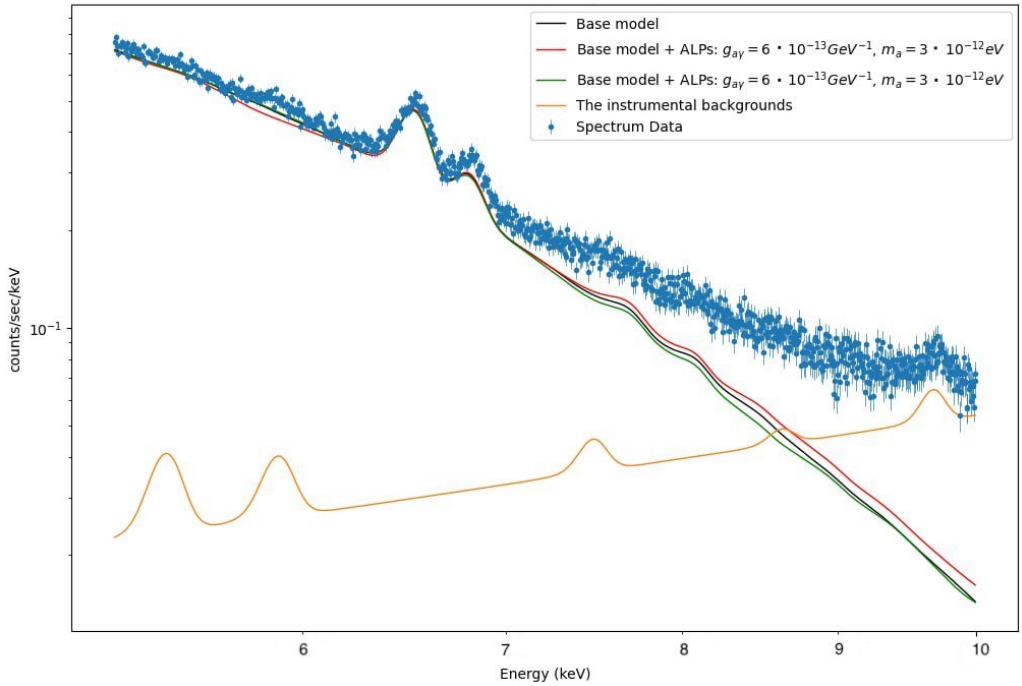

Figure 3: XMM-Newtom/MOS spectrum extracted from Coma cluster central region. The fitting using the base model is represented by a **black** line. The base model + ALPs with parameters $g_{a\gamma} = 6 \cdot 10^{-13}\,\mathrm{GeV}^{-1}$ and $m_a = 3 \cdot 10^{-12}\,\mathrm{eV}$, and the magnetic field realization that yields the highest null hypothesis probability 88% from our trials, is shown in **red**. The fit using the base model + ALPs with the same parameters, but with the realization that gives the lowest null hypothesis probability 0.08%, is depicted in **green**. The instrumental backgrounds (smooth continuum powerlaw and line-like gaussian features) is illustrated by the **yellow** line.

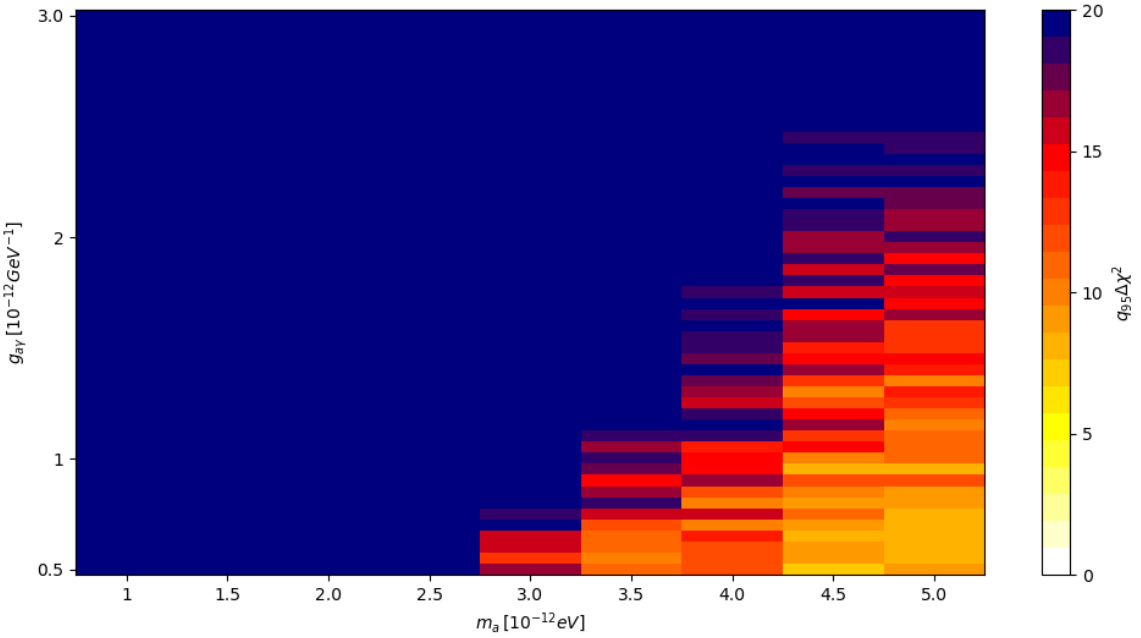

Figure 4: χ^2 change and ALP exclusion regions. The colors illustrate the difference between the best-fit χ^2 for the base model and the base + ALPs model for the Coma cluster XMM-Newton/MOS spectrum fit.

3. Conclusion

Based on X-ray observations of the Coma cluster, the excluded parameter space for ALPs is constrained to $g_{a\gamma} < 5 \cdot 10^{-13}\,\mathrm{GeV}^{-1}$ for $m_a < 1 \cdot 10^{-12}\,\mathrm{eV}$.

The study of X-ray emission from clusters and its connection to axions is promising, as data from space missions continue to improve. The first observational data from XRISM (The X-Ray Imaging and Spectroscopy Mission) has been published, offering greater precision with the Resolve Soft X-ray Spectrometer's 7 eV resolution. Additionally, new radio observations and the increased number of radio sources will enhance Faraday rotation measurements of galaxy clusters' magnetic fields, providing better constraints on ALP parameters.

Acknowledgements. Lidiia Zadorozhna's work is supported by a Scholars at Risk Denmark Fellowship for Scholars from Ukrainian Universities (SARU Fellowship) at the University of Copenhagen.

This research was made with the support of the Center for the Collective Use of Scientific Equipment "Laboratory of High Energy Physics and Astrophysics" of Taras Shevchenko National University of Kyiv.

References

Bonafede A. et al.: 2010, *A&A*, **513**, A30, 1002.0594.

Bower R.: 2013, Clusters of Galaxies. In: Oswalt, T.D., Keel, W.C. (eds) Planets, Stars and Stellar Systems, (Springer, Dordrecht).

Chen Y. et al.: 2007, *A & A*, **466**, 805.

Churazov E. et al.: 2012, *MNRAS*, **421**, 1123.

Conlon J.P., Powell A.J., & Marsh M.C.D.: 2016, *PhysRevD*, **93**, 123526.

Davies J., Meyer M., & Cotter G.: 2023, *PhysRevD*, **107**, 083027.

Hochmuth K.A. & Sigl G.: 2007, *PhysRevD*, **76**, 123011.

Łokas E.L. & Mamon G.A.: 2003, *MNRAS*, **343**, 401.

Malyshev D. et al.: 2018, *arXiv e-prints*, arXiv: 1805.04388.

Malyshev D., Moulin E., & Santangelo A.: 2022, *PhysRevD*, **106**, 123020.

Matthews J.H. et al.: 2022, *ApJ*, **930**, 90.

Meyer M., Horns D., & Raue M.: 2013, *PhysRevD*, **87**, 035027.

Mirizzi A., Raffelt G.G., & Serpico P.D.: 2008, *Axions,* **741**, 115.

O'Hare C.: 2020, Zenodo, https://cajohare. github.io/ AxionLimits/.

Peccei R.D. & Quinn H.R.: 1977a, *PhysRevD*, **16**, 1791.

Peccei R.D. & Quinn H.R.: 1977b, *PhysRevL*, **38**, 1440.

Raffelt G. & Stodolsky L.: 1988, *PhysRevD*, **37**, 1237.

Reynolds C.S. et al.: 2020, *ApJ*, **890**, 59.

Schuecker P. et al.: 2004, *A&A*, **426**, 387.

Weinberg S.: 1978, *PhysRevL*, **40**, 223.

Wilczek F.: 1978, *PhysRevL*, **40**, 279.

Zadorozhna L. et al: 2023, *OAP*, **36**, 36.

ASTROPHYSICS

(stellar atmospheres, interacting binary systems, variable stars)

https://doi.org/10.18524/1810-4215.2024.37.313467

DETERMINATION OF THE ZANSTRA TEMPERATURES OF THE CENTRAL STARS OF NGC 246 AND NGC 7293 PLANETARY NEBULAE

A.H.Alili, Kh.M.Mikailov, K.I.Alisheva

Baku State University, Baku, Azerbaijan

aynuraalili@bsu.edu.az, kamalaalisheva@bsu.edu.az

ABSTRACT. In this work from processed the spectra of the NGC 246 and NGC 7293 planetary nebulae we have determined the fluxes in the H_β and HeII emission lines. Spectra of these planetary nebulae were taken from the archive of the European Southern Observatory. From the determined fluxes we calculated Zanstra temperatures according to the HI and HeII lines of the central stars of planetary nebulae. Respectively, the temperatures of 53723.14 K and 100871.43K were found for the central stars of NGC 246, the temperatures of 51072K and 89073.4K were found for the central stars of NGC 7293. The results obtained were also compared with results of other authors.

Keywords: central star, temperature, flux in the H_β emission line, flux in the HeII emission line.

АНОТАЦІЯ. Планетарні туманності є ідеальною лабораторією для дослідження взаємодії між випромінюванням і речовиною. Вся енергія, яку отримує планетарна туманність, надходить від центральної зорі. Частина випромінювання поглинається туманністю. Центральна зоря планетарної туманності є продуктом еволюції зір малої і помірної маси. Такі зорі проходять через стадію зорі асимптотичної гілки гігантів. Температура центральної зорі є важливим параметром від якого залежать характеристики самої планетарної туманності. Він зумовлює ступінь збудження та іонізації атомів речовини туманності. У цій роботі зі спектрів планетарних туманностей NGC 246 і NGC 7293, які попередньо були нами оброблені, ми визначили потоки в лініях випромінювання H_β і HeII. Спектри цих планетарних туманностей були взяті з архіву Європейської Південної Обсерваторії. З визначених потоків в лініях ми розрахували температури за методом Занстра відповідно по вищевказаних ліній центральних зір планетарних туманностей. Відповідно для центральної зорі туманності NGC 246 були знайденні значення температур 53723.14 K і 53723,14 K, а для центральної зорі туманності NGC 7293 − 51072 K і 89073,4 K. Отримані результати порівнюються з результатами інших авторів.

Ключові слова: центральні зорі, температура, потоки в емісійних лініях Гідрогену і Гелію.

1. Introduction

Planetary nebulae (PNe) are an ideal laboratory for the study of the interaction between radiation and matter. All the energy of a nebula is derived from a single source, the central star. Radiation emitted by the star is absorbed and processed by the nebula. Central stars of planetary nebulae (CSPN) are the final products of the evolution of low- and intermediate-mass stars, the stars that most likely go through the asymptotic giant branch (AGB) phase. By the time, a star departs the AGB, it loses most of its outer envelope, and if the remnant core evolves to high temperature before the ejected envelope disperses it will be visible as a PN for the rather short ≈ 10000 yrs time.

As known, the temperature of the CSPN is essential parameter for studying the evolution of these stars. The nebula characteristics are related to the stellar temperature, especially the level of excitation and ionization of the nebula, and intensity of some nebular lines. Studying the CSPN is difficult, and the standard methods for the temperature determination cannot be applied.

We report here on the determination of the fluxes in the H_β and HeII emission lines and the temperature determination for NGC 246 and NGC 7293 by using the Zanstra method based on HI and on a single ionized HeII lines. We discuss our results and compare these values to temperatures (Pottash, 1992; Phillips, 2003; Montez et al., 2015; Frew et al., 2016) reported by various authors.

2. Determination of the Zanstra hydrogen $T_Z(H)$ and helium $T_Z(HeII)$ temperatures

Zanstra (1927) developed the method to derive the central star temperature by comparing the nebular recombination flux with the stellar continuum magnitude. This method is based

on the assumption that the number of Lyman continuum photons absorbed in the nebula is equal to the total number of recombinations to all levels excluding the ground state.

Both of Zanstra methods can only be applied to nebulae that are optically thick in L_c. In optically thick nebulae all L_c quanta are radiated by the star that absorbed by the nebula (Gleizes et al., 1989). At this time, it is assumed that the star radiates as a black body. It is assumed that the HI and He++ ions in the nebula absorb all radiation in the λ<912 Å and λ<228 Å regions from the star. Each L_c quantum emitted by the core in the Lyman series limit of hydrogen being swallowed up in the nebula produces one L_α quantum and one Balmer series quantum. When each L_c quantum is absorbed in the limit of Layman series, during the L_c quantum recombination of HeII, it can produce the L_α quanta and Balmer continuum quantum of ionized helium.

The number of Balmer quanta emitted by the nebula defines the number of quanta emitted by the star in the ultraviolet region of the spectrum. The temperature of the star can be determined by comparing these quanta with quanta emitted in the visible region of the spectrum. In a practice, the HeII λ4686 Å line is used for determination Tz(HeII).

If we assume that a star with radius R_s and temperature T radiates as a black body, the luminosity in the $d\nu$ interval will be $L_\nu d\nu$

$$L_\nu = 4\pi^2 R_s^2 B_\nu(T) \qquad (1)$$

Here, B_ν is the Planck function. $\nu \geq \nu_i$ the number of stellar quanta will be:

$$Q_i = \int_{\nu_i}^{\infty} (L_\nu / h\nu)\, d\nu = \frac{8\pi^2 R_s^2}{c^2} \left(\frac{kT}{h}\right)^3 G_i(T) \qquad (2)$$

ν_1 – is a limit of Lyman series, the energy of this quantum is sufficient to ionize hydrogen. ν_4 – is a limit of the main series of HeII, the energy of this quantum is sufficient for ionizing singly ionized helium.
Here,

$$G_i(T) = \int_{h\nu_i/kT}^{\infty} x^2 (e^x - 1)^{-1}\, dx. \qquad (3)$$

For determination of the temperature we first replaced the integral $G_i(T)$ by the sum (Alili et al. 2023):

$$\int_{x_0}^{\infty} \frac{x^2 dx}{e^{x_i} - 1} = \sum_{n=0}^{\infty} \int_{x_0}^{\infty} e^{-(n+1)x} x^2 dx\,. \qquad (4)$$

ν_0 – is the boundary of the main serieses of HI and HeII. It is enough to add up to the value n=3, even the temperatures obtained from n=3 with n=2, they differ from each other only by 0.01. The observed $F(H_\beta)$ and $F(4686)$ radiation fluxes of the nebula will be as follows:

$$4\pi d^2 F(H_\beta) = h\nu(H_\beta) \int n_e\, n(H^+) \alpha(H_\beta) dv \qquad (5)$$

and

$$4\pi d^2 F(4686) = h\nu(4686) \int n_e\, n(He^{++}) \alpha(4686)\, dv \qquad (6)$$

Here, the frequency of the $\nu(H_\beta)$ – H_β line is the effective recombination coefficient related to the generation of $\alpha(H_\beta)$ – H_β quanta. $\alpha(4686)$ – He^{++} is the effective recombination coefficient related to the generation of quanta. Considering $(L_\nu = 4\pi d^2 F_\nu)$, (5) and (6) in L/L_0 expression (L_0 is the luminosity of the Sun) of luminosity in terms of the stars' radiation fluxes F_ν we get the following expressions:

$$\frac{F(H_\beta)}{F_\lambda} = 3.95 \cdot 10^{-11} T^3 G_1(T) \left[e^{26650/T} - 1\right] \qquad (7)$$

and

$$\frac{F(4686)}{F_{\lambda(vis)}} = 8.49 \cdot 10^{-11} T^3 G_4(T) \left[e^{26650/T} - 1\right]. \qquad (8)$$

$F_{\lambda(vis)}$– m_v is the radiation flux in the visible region of the spectrum is determined by the size of the visible star:

$$F_\lambda = 3.68 \cdot 10^{-9} \cdot 10^{-m_v/2{,}5} \left[erg/(cm^2 \cdot s \cdot Å)\right] \qquad (9)$$

m_v – is the visual magnitude. In each of the fluxes on the left side of (7) and (8) equality absorption in the interstellar medium was taken into account as follows:

$$lg \frac{F_{\lambda(theor.)}}{F_{\lambda(obs.)}} = \frac{A_{5450}\ E_{B-V}}{2{,}5} \qquad (10)$$

$$lg \frac{F(H_\beta)_{(theor.)}}{F(H_\beta)_{(obs.)}} = \frac{A_{4861}\ E_{B-V}}{2{,}5} \qquad (11)$$

$$lg \frac{F_{4686(theor.)}}{F_{4686(obs.)}} = \frac{A_{4686}\ E_{B-V}}{2{,}5} \qquad (12)$$

Here, A is the absorption coefficient in the interstellar medium, and E_{B-V} is the extinction. $F(H_\beta)_{(obs.)}$ and $F_{4686(obs.)}$ were determined from the processing of the spectra of the 2 planetary nebulae that we have studied. We have determined the temperatures of the central stars by the method of successive approximation from equations (7) and (8), and the results are given in Table 3.

3. Determination of the fluxes F(H_β) and F(4686)

The fluxes $F(H_\beta)$ and F(4686) in the expression (7) and (8) are determined from processing the spectra for each planetary nebula. For this purpose, we studied the spectra of nebulae. We took them from the Southern Observatory (ESO) website. These spectra were observed in 2016, ESO-VLT-U2 (8-meter) and ESO-3P6 (3.6-meter) telescopes. The spectra were processed using the DECH 30 software package (Galazutdinov, priv. comm.). According to the magnitudes of the studied nebulae in different filters (UBVR) energy distribution curves were constructed in absolute flux units $\left[erg \cdot cm^{-2} s^{-1} Å^{-1}\right]$. Using the energy distribution curve and spectrum it is possible to estimate the flux in any spectral line. So, the value of the flux in the continuum near the spectral line given by multiplying the value of the equivalent width of the line, a flux is definitely found in any spectral line in the sphere. The flux in the spectral line is given in $[erg \cdot cm^{-2} s^{-1}]$. In the figures you can see the HI and HeII lines profiles of each nebula.

Table 1:

PN	V	W (Å)	$F(H_c) \times 10^{-13}$	$lgF_{\lambda(obs.)}$	$lgF_{obs}(H_\beta)$	E(B–V)	Referens
NGC 246	11.76	980.5	0.35	–13.138	–9.6	0.02	(Frew, 2016), SIMBAD
NGC 7293	13.52	7.18	57.85	–13.844	–10.38	0.02	(Frew, 2016), SIMBAD

H_β in $erg \cdot cm^{-2}s^{-1}$.

Table 2:

PN	W (Å)	$F(HeII_c) \times 10^{-13}$	$lgF_{obs}(4686)$	A(5450)	A(4861)	A(4686)	Referens
NGC 246	259.6	12.3	–10.47	3.14	3.63	3.8	(Pottash, 1992)
NGC 7293	569	0.289	–10.78	3.14	3.63	3,8	(Pottash, 1992)

Table 3:

PN	T_z(HI)	T_z(HeII)	T(HI)	T(HeII)	T(HeII)	Ref.
NGC 246	53723	100871	42000	88600	140000	(Pottash, 1992), (Phillips, 2003), (Montez, 2015)
NGC 7293	51072	89073		107000	110000	(Phillips, 2003), (Frew, 2016)

The obtained results are given in the table 1 and in the table 2. In the 2nd column of the table 1, we give the visual stellar magnitudes of the nebulae, in the 3rd column, H_β line equivalent widths in each nebulae, in the 4th column, H fluxes in the continuum (H_c), in the 5th column, the stars' radiation fluxes, in the 6th column, the observed fluxes of the H_β and in the 7th column, the extinctions. In the 2nd column of the table 2, we give HeII line equivalent widths in each nebulae in the 3rd column, He fluxes in the continuum ($HeII_c$), in the 4th, 5th and 6th columns, the coefficients.

In the 2nd and 3rd column of the table 3, we show the Zanstra temperature calculated with lines HI and HeII by us, in the 4th, 5th and 6th column of the table 3, the Zanstra temperature calculated witrh line HeII by other authors are given.

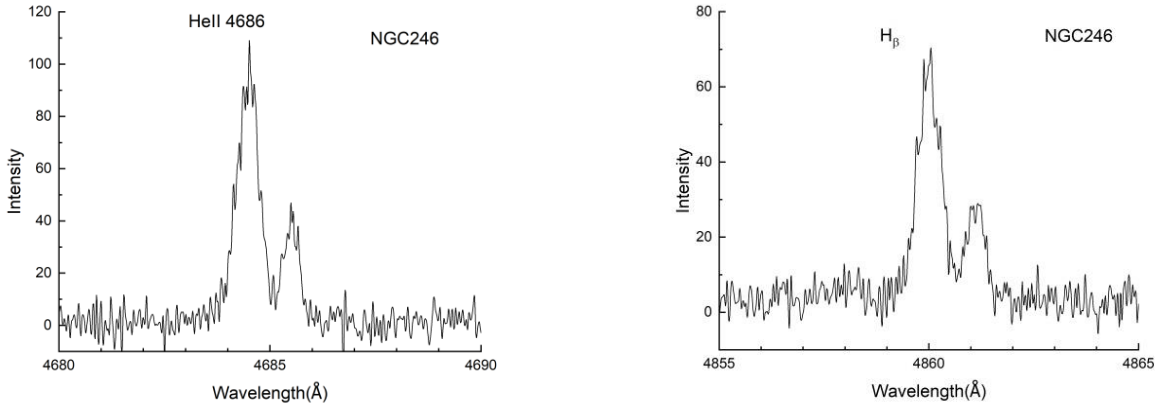

Figure 1: Profiles of the line HeII and H_β in planetary nebula NGC 246

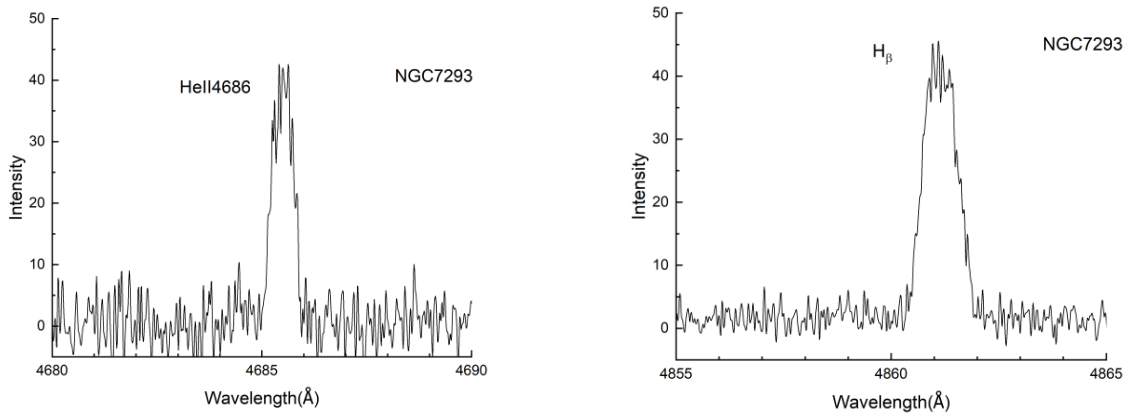

Figure 2: Profiles of the line HeII and H_β in planetary nebula NGC 7293

4. Conclusion

So, as it can be seen from the table 3, the temperatures we determined by the Zanstra method are differs a little bit from the temperatures determined by other authors before us by this method. The reason for this is that the processed spectra are obtained on telescopes with different resolution in different years. The temperatures we determined according to the HI and HeII lines of the central stars also differ from each other. Since the Zanstra method could be applied if the nebula is optically thick in hydrogen (respectively, helium) in the Lyman continuum, PN change from optically thin in H and He at different times (Kwok, 2000). The fact that stellar atmosphere are not well approximated by blackbodies can also contribute to the errors in the Zanstra temperatures.

Acknowledgements. This research has made use of the SIMBAD database, operated at CDS, Strasbourg, France.

References

Alili A.H., Alisheva K.I., Mikailov Kh.M.: 2003, *OAP*, **36**, 96.
ESOwebsite: http://archive.eso.org/cms.html
Frew D.J., Parker Q.A., Bojicic I.C.: 2016, *MNRAS*, **455**, 1459.
Gleizes F., Acker A., Stenholm B.: 1989, *A&A*, **222**, 237.
Kwok S.: 2000, *CAS*, **33**, 243.
Montez R.Jr., Kastner J.H., Balick B. et al.: 2015, *AJ*, 800:8 (19pp).
Phillips J.P.: 2003, *MNRAS*, **344**, 501.
Pottash S.R.: 1992, *A&Arv*, **4**, 215.
Zanstra H.: 1927, *ApJ*, **65**, 50.

https://doi.org/10.18524/1810-4215.2024.37.313706

THE R-BAND OBSERVATIONS AND COMPARISON WITH RESULTS IN THE V-BAND OF FI Sge

L. Keir[1], S. Udovichenko[2]

[1] Department of Physics and Astronomy, Odesa I. I. Mechnikov National University, Ukraine, *partneroae@gmail.com*

[2] Research Institute "Astronomical Observatory", Odesa I. I. Mechnikov National University, Ukraine, *s.udovichenko@onu.edu.ua*

ABSTRACT. We present the result of the processing of our observations of the FI Sge, the pulsating RR Lyrae type variable with the Blazhko effect in the R-band. The data were obtained during 36 nights in 2018 as well as during 13 nights in 2021. We used the period and initial epoch obtained from our observations in V-band. We confirmed the presence of the Blazhko effect, the bi-cyclicity effect, and also the effect of discrete displacement of the light curves along the phase curve detected firstly in the V-band. We detect some differences in the dynamic of the light curve variability in different photometrical bands, possibly related to the Blazhko effect.

Keywords: stars: variables: RR Lyr: individual: FI Sge.

АНОТАЦІЯ. Нами викладені результати обробки спостережень у фільтрі R пульсуючої змінної зорі типу RR Ліри з ефектом Блажко FI Sge за 36 ночей у 2018 році та 13 ночей у 2021 році. Ми використовували період та початкову епоху для цієї зорі, які були вже визначені за спостереженнями у V фільтрі. Наші спостереження у фільтрі R підтверджують наявність у FI Sge двох періодів модуляції амплітуди всередині циклу Блажко, виявлених за спостереженнями у фільтрі V раніше. Аналіз зміщень кривих блиску вздовж фазової кривої за 2021 рік у фільтрі R призводить до висновку, що значення величини дискретного зміщення для зорі FI Sge потрібно змінити з 0,043 фази подвійного періоду (0,50500*2 дні) на кратне їй значення 0,01075. Нові спостереження 2021 року у фільтрі R дозволяють припустити, що час зміни напрямку зміщень кривих блиску вздовж фазової кривої становить півтора року, а приблизний період цих змін становить три роки. Порівняння кривих блиску у фільтрі R та фільтрі V показує, що існує деяке запізнення часу моментів зміщень у фільтрі V по відношенню до фільтру R. Його значення не менше ніж 12 діб. Зміна показника кольору (V–R) вказує на ймовірне підвищення температури зорі, або в момент зміщення кривої блиску, або відразу після цього.

Спостереження у фільтрі R підтверджують наявність у зорі FI Sge ефекту Блажко, ефекту бі-циклічності та ефекту зміщення моментів максимумів до початкової епохи вздовж фазової кривої.

Ключові слова: зорі: змінні: RR Lyr: індивідуальні: FI Sge.

1. Introduction

FI Sge is a pulsating variable star of the RR Lyrae type with the Blazhko effect. In the GCVS (Samus et al., 2017) this star ($RA_{2000.0} = 20^h13^m16.2^s$, $Dec_{2000.0} = +17°30'37''$) is described as RRab type variable, Sp=A2, the magnitude variations are in the range from 13.2^m to 14.3^m, $JDmax = (2428333.441 + 0.5047545E)^d$, and period of the Blazhko effect $P(BL) = 22.4^d$. It is a little studied variable star. Hoffmeister (1936), based on observations from the Sonneberg Observatory, noted the star as a variable. In 2017, Mainz (2017) observed FI Sge over 5 nights. She studied the information from the literature in detail. Using her observational data, Mainz determined the FI Sge period to be P=0.50477d. This value is different from that given in the GCVS. Maintz studied the (O–C) values for the maxima of the light curves based on data from Richter (1961), Wils et al., (2006), Agerer and Hubscher (2002). She suggested that the period of variability changed after J.D. 2452000. She also noted that the phase curves constructed from NSVS and ASAS data differ in amplitude and phase. For NSVS data, the shift of the position of the maxima on the phase curve from the initial epoch was equal to 0.15 of the period of variability. Mainz did not discover the Blazhko effect. Skarka and Cagas (2017) also observed FI Sge in August, September and October 2017. Observations were made without a filter over 14 nights. They analyzed their data and determined the Blazhko effect period to be 22.4 days.

Thus, FI Sge is an RR Lyrae star that has the Blazhko effect. In addition to the Blazhko effect, the

star has a bicyclicity effect. The star also demonstrates the effect of shifting light curves along the phase curve. All these effects introduce changes in our final picture of its brightness fluctuations. Our task was to separate these changes and determine the contribution of each of them.

Blazhko modulation changes the shape of the light curve. Here, modulation of the amplitude of the light curve leads to the phase modulation. When light maximum increases, the period becomes longer. Accordingly, when light maximum decreases, the period becomes shorter. As a result, light maximum is slightly shifted in phase (0.1 cycle). Negative phase shifts always occur for fainter maxima, positive phase shifts for brighter maxima.

The next effect is the bi-cyclical effect. This is a conditional name, since there is no established name. The effect was described in 2010 by Smolek (2016). It consists in the fact that for some stars of the RR Lyrae type with the Blazhko effect, neighboring pulsation cycles differ significantly in amplitude. The modulation of the maxima also differs for these cycles. We consider these cycles to be distinct and construct a phase curve using a double period. This technique allows you to separate cycles with different types of pulsation activity on the phase curve. This method is described in more detail in Keir (2023).

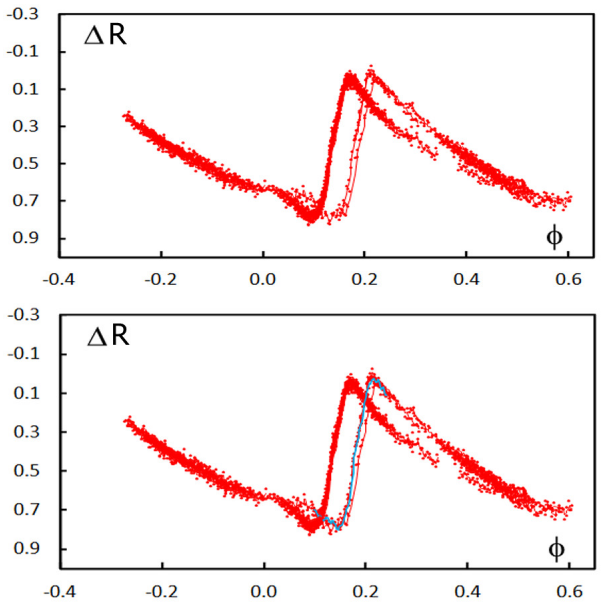

Figure 1: Observations FI Sge 2018 in the upper figure. The phase curve is plotted with a period of 0.50500*2 days. In the bottom figure, the light curve of October 10, 2018 (blue) is shifted to the right by one discrete shift (0.0430 phase value).

2. Observations

Our observations were carried out at the AZT-3 telescope in the Astronomical Observatory Odesa National University, located at the observational station N583 in Mayaki village. The AZT-3 telescope has a primary mirror diameter of 480 mm and a focal length of the Newton optical scheme F = 2024 mm, the exposure time was 90 sec. The images were registered with CCD Sony ICX429ALL (≈600x800 pixels) with the Peltier cooling, in the V, R photometric system. The registration complex was developed and installed by Udovichenko (2012).

The photometry of the original frames was made with Muniwin software (Motl, 2009). The comparison star was UCAC4-538-127214 ($J_{2000.0}$: RA : $20^h13^m14.876^s$ Dec : $+17°33'39.95''$, $V = 13.36^m$), and the control star was UCAC4-538-127074 ($J_{2000.0}$: RA : $20^h12^m59.405^s$, Dec : $+17°33'49.42''$, $V = 13.73^m$). We determined the Julian Date with the correction to the barycenter of the Solar and instrumental magnitudes for the variable star (V), comparison star (C), and control star (K) for each frame.

Fig. 1 shows observations in the R filter of the star FI Sge in 2018. They confirm the effect of shifting light curves along the phase curve to the initial epoch, discovered from observations in the V filter. The distance between the October maxima and the July maxima corresponds to one discrete shift (0.043 phases of the double period). This is confirmed in the bottom picture. The divergence of the maxima in phase in July is not a consequence of the Blazhko effect, since the higher maxima (July 12, 13) are located to the left of the weaker maximum (July 6). We consider only a small discrepancy in the light curves in each individual set of observations to be a manifestation of the Blazhko effect. This slight discrepancy is also proof that we have correctly determined the period of variability. We did not obtain maxima for the adjacent pulsation cycle in these observations. However, the descending part of the light curve on the left is flatter than in the cycle on the right. This means that the maximum of the left cycle will be fainter than the maximum of the right one. The difference in the amplitudes of the maxima of two neighboring cycles confirms the bicyclicity effect in this star. The amplitudes and moments of the maxima were determined by polynomials up to the seventh degree using the MCV program, which was created by Andronov and Baklanov(2004). Analysis of the amplitudes of the maxima in October 2018 shows that, as in the V filter, there is a statistically significant division of maxima on those whose numbers of cycles are multiples and those whose numbers of cycles are not a multiple of four. This means that within the Blazhko period there are at least two independent periods of oscillation.

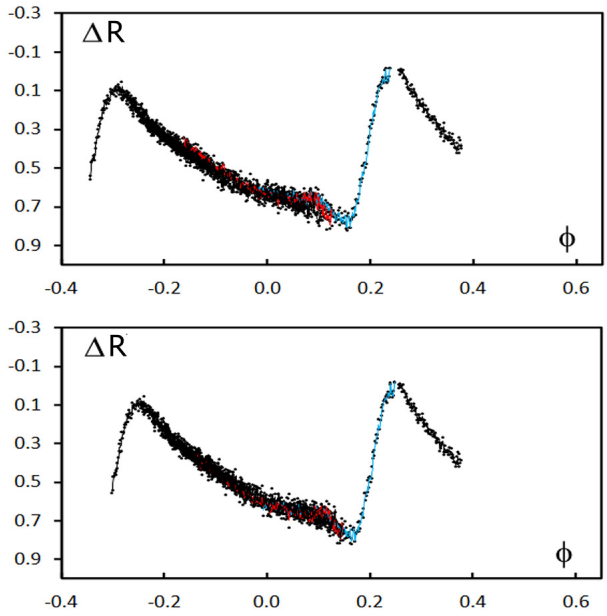

Figure 2: Observations of FI Sge 2021 (the upper figure). In the bottom figure, the light curve of 01 August (blue) is shifted to the right by 0.01075 phases. The light curves for August 14 and 15 (red) are shifted to the right by 1/2 discrete shift. All later light curves are shifted to the right by the amount of one discrete shift (0.0430 phase).

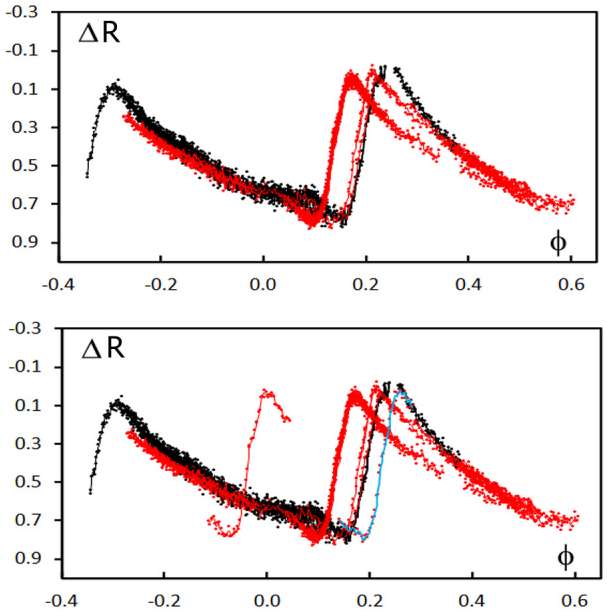

Figure 3: Observations of FI Sge 2018 (red) and 2021 (black) in the upper figure. The light curve for October 10, 2018 (blue) is shifted by two discrete shifts to the right (bottom figure).

There were fewer observations in 2021 than in 2018. We can see that in Figure 2 above. In the bottom graph of Fig. 2 we have combined all the light curves into one common phase curve. To do this, we shifted the light curve on August 1 to the right of the initial epoch by 0.01075 phase of the double period. This value is equal to the discrete shift (0.043 double period phase) divided by four. The light curves of August 14 and 15 are shifted to the right of the initial epoch by the same amount. All other light curves on August 26,28,30,31, September 2,3, October 29,30 and November 3 are shifted to the right from the initial epoch by one discrete shift (0.043 phases of the double period). In this way we combined them with earlier light curves. The figure shows that in this phase curve the period between maxima is exactly equal to the period of variability. We made fractional shifts from the discrete one for the first time, since there was no need for such shifts for V-filter observations, or so we thought. But, as we noted above, the light curve of July 6, 2018, falls out of the general picture of discrete shifts. However, if we shift it to the left toward the initial epoch by 0.01075 from the double period phase, it fits well with the light curves of July 12 and 13, 2018. Thus, in 2021 we observe discrete shifts of the light curves toward the initial epoch. In their meaning and direction, they are similar to the shift of the light curves in 2018.

3. Analysis of observations

The overall phase curve for all light curves is shown in Fig. 3 in the top graph. Here we see that the arrangement of the light curves of 2021 follows the light curves of 2018 with a slight shift in time. So the light curve of August 1, 2021 falls on the light curve of July 6, 2018. The bottom graph shows that the light curve of October 10, 2018, shifted by two discrete shifts to the right, complements the light curve of July 17, 2021, and the light curves of June 2018. To check, we shifted the light curve of October 9, 2018 to the left by four discrete shifts. As evident in Figure 3, the peak of light maximum coincides with zero phase..

For the data in the V filter, we were unable to estimate the period of change in the direction of displacements movements. A long break in observations from 2014 to 2017 prevented this. New observations in the R filter for 2021 help reconcile this uncertainty. The direction of displacement changes every year and a half. That is, every three years the direction of movement of the displacements is repeated. This agrees well with observations in both filters.

Next, we looked at whether there was a difference in the dynamics of the shifts of the light curves in the R

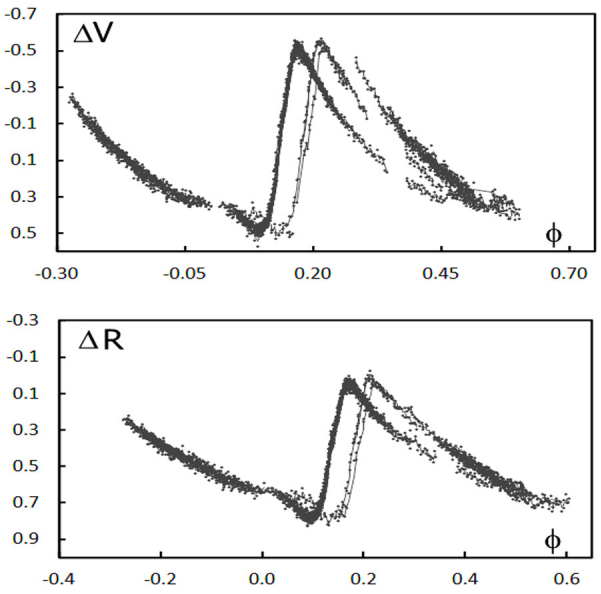

Figure 4: 2018 FI Sge observations in the V(upper) and R(bottom) filters.

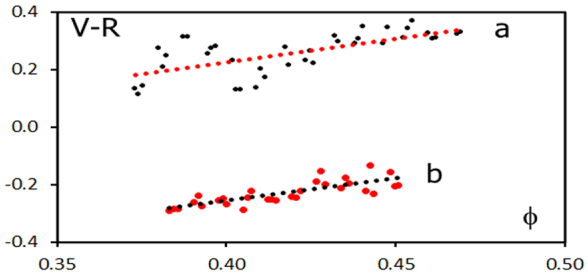

Figure 5: Value of the V–R color index on June 21, 2018 (a), and on June 23, 2018 (b).

filter and the V filter. In Fig. 4, the observations for 2018 in the V filter are shown at the top, and the observations in the R filter are below. As we can see, the shift of the light curves, which in the filter V occurred approximately on June 22, in the R filter it could occur no later than June 10. It was not possible to establish a more precise date. The lag of the shifts in the light curves in the V filter from the shifts in the R filter is at least 12 days. The given time interval is typical for changes associated with the Blazhko cycle. We can assume that the shifts of the light curves themselves along the phase curve are associated with the mechanism of the Blazhko effect.

We calculated the color index (V–R) for all data. It is believed to better reflect changes of the star's temperature. This figure varies greatly depending on what part of the light curve we are observing. The value (V–R) behaves in a mirror manner with respect to changes in the light curve. We show in Fig. 5 the value of (V–R) before the shift in the light curves on June 21, 2018 (top), and immediately after the shift for the date June 23, 2018 (bottom). As we can see from the figure, the index (V–R) has dropped significantly. We infer that the surfase temperature of the star increased during or immediately after the light curve shift.

4. Conclusions

Our observations of the star FI Sge in the R filter confirm the presence of a bicyclicity effect and an effect of shifting the moments of maxima along the phase curve in this star.

Observations in the R filter also confirm the presence of at least two periods of amplitude modulation within the Blazhko cycle, detected from observations in the V filter.

An analysis of the shifts in light curves for 2021 in the R filter leads to the conclusion that the value of the discrete shift for the star FI Sge needs to be changed from 0.0430 double period phase to a multiple of it 0.01075.

New observations from 2021 in the R filter suggest that the time of change in the direction of the light curves shifts is one and a half years, and the approximate period of these changes is three years.

A comparison of the light curves in the R filter and the V filter indicates that there is some delay in the time of the displacements in the V filter relative to the R filter. This delay is at least 12 days.

A change in the color index (V–R) indicates a likely increase in the temperature of the star, either at the moment the light curve shifts, or immediately after this shift.

References

Agerer F., Hubscher J.: 2002, *IBVS*, **5296**.
Andronov I.L., Baklanov A.V.: 2004, *AstSR*, **5**, 264.
Hoffmeister C.: 1936, *AN*, **259**, 37.
Keir L.E.: 2023, *OAP*, **36**, 59.
Maintz G.: 2017, *BAVSR*, **66**, 128.
Motl D.: 2009-21, *http://sourceforge.net/projects/c-munipack*.
Richter G.: 1961, *VeSon*, **4**, **434**.
Samus N.N., et al.: 2011, *GCVS database*, Version 2011Jan.
Skarka M., Cagas P.: 2017, *IBVS*, **6229**.
Smolec R.: 2016, *pas.conf*, **3**, 22.
Udovichenko S.: 2012, *OAP*, **25**, 32.
Wils P., Lloyd C., Bernhard K.: 2006, *MNRAS*, **368**, 1757.

https://doi.org/10.18524/1810-4215.2024.37.314146

THE PHOTOMETRIC BEHAVIOR OF A SYMBIOTIC STAR V919 SGR

L.S. Kudashkina[1], V.I. Marsakova[2], I.L. Andronov[1], L.L. Chinarova[1]

[1] Odesa National Maritime University, Odesa, Ukraine, *kuda2003@ukr.net*
[2] Odesa Richelieu Scientific Lyceum Odesa, Ukraine

ABSTRACT. We collected photometric observations of the symbiotic star V919 Sgr from the AAVSO and ASAS-SN databases, as well as UBVRI observations obtained at the Astronomical Institute of the Slovak Academy of Sciences. This symbiotic binary star belongs to the Z And type. Observers paid little attention to it until the latest outbursts that began in the 2000s The first observed outburst was described in 1991. In total, we found six outbursts of V919 Sgr. In particular, the star has recently shown significant activity, including a new active phase starting in 2022 and a re-brightening in 2023 that exceeded the previous year's outburst by about 0.4 magnitudes (in V passband).

To analyze the activity of V919 Sgr on short timescales, we used a "pattern scaling analysis" with a weighted "running parabola" (RP) approximation and additional "bi-square" weights. An optimal window half-width of 63 days minimized the rms statistical errors, and the B–V, V–R, and R–I color indices were determined. The B–V color index ranged from 0.53 at brightness maxima (10.15-10.76 in V) to 1.20 at magnitude 13.8. A periodogram analysis was also performed. However, due to the limited number of observations between outbursts, the period estimates are highly uncertain.

Keywords: stars; variable stars; symbiotic stars; photometry.

АНОТАЦІЯ. Ми зібрали дані спостереження симбіотичної зорі V919 Sgr з баз даних AAVSO і ASAS-SN, а також використали UBVRI спостереження, отримані в Астрономічному інституті Словацької академії наук. Ця симбіотична подвійна зоря належить до типу Z And. Спостерігачами приділяли їй мало уваги до спалахів, що почалися у 2000х. Перший спалах, що спостерігався, описаний в 1991 році. Загалом ми виявили сім спалахів V919 Sgr. Зокрема, нещодавно зоря продемонструвала значну активність, включаючи нову активну фазу, що почалася в 2022 році, і повторне поярчання в 2023 році, яке перевищило спалах попереднього року приблизно на 0,4 зоряної величини у фільтрі V.

Щоб проаналізувати активність V919 Sgr на коротких масштабах часу, ми використали шкалограмний аналіз зі зваженою апроксимацією «ковзаючими параболами» (RP) і додатковими «біквадратними» вагами. Оптимальна напівширина вікна в 63 дні мінімізувала середньоквадратичні статистичні похибки, також були визначені індекси кольору B–V, V–R і R–I. Індекс кольору B–V коливався від 0,53 при максимумах блиску (10,15–10,76 у B) до 1,20 при величині 13,8. Також був проведений періодограмний аналіз. Однак, через обмежену кількість спостережень між спалахами, оцінки періоду є дуже приблизними.

Ключові слова: зорі, змінні зорі, симбіотичні зорі; фотометрія.

1. Introduction

V919 Sgr (=EM* AS 337=VSX 28619) is a poorly understood symbiotic variable star of Z And type. Symbiotic variables of this type are close binary systems consisting of a hot star, a late-type star, and an expanding envelope excited by the radiation of the hot star. The total brightness shows uneven variations with an amplitude of usually up to 4 stellar magnitudes in the V band. This is a very heterogeneous group of objects.

The GCVS contains 46 Z And – type stars, with another 20 objects uncertainly classified as Z And (and V919 Sgr is among them) and three objects labeled as Z And+E, Z And+M, Z And+SR.

The classical representation of the symbiotic system model is considered to be the following structure: a giant star of spectral class M (less often G or K), with a radius of about 100 solar radii and a hot sub-dwarf or white dwarf (less usually a main sequence star) with radius <0.5 solar radii and temperature 10^5 K. The distances between the components are from 1 to 5 AU, the orbital periods are from 1 year to several years. Both components are surrounded by a common gas shell (or several shells) or disks. The red giant gives up its mat-

ter through stellar wind or pulsations. The gas shell can be both thin and very dense. Sometimes the system can look like a planetary nebula with two nuclei (Sokoloski, 2003).

Symbiotic variables are classified into several groups. The type of Z And is included in the group characterized by luminosity caused by a stable hydrogen layer of the white dwarf. The variability in brightness is caused by variations in the rate of fall of matter onto the hot component (Hoffmeister, 1984).

2. Symbiotic Star V919 Sgr Research

V919 Sgr is a relatively poorly studied symbiotic star despite being known since the seventies. The star has been observed in three active stages so far. The first documented outburst occurred in 1991 and was analyzed by Ivison et al. (1993). The second active phase commenced in 2007 (Munari et al., 2007) and witnessed several rebrightenings following the initial, most prominent outburst. According to the AAVSO light curve of V919 Sgr, the system returned to its quiescent brightness around 2015.

A new active stage began in 2022 (Munari et al., 2022), approximately 15 years after the onset of the previous one. Munari et al. classified the 2022 brightening as a 'cool'-type outburst based on spectroscopic data.

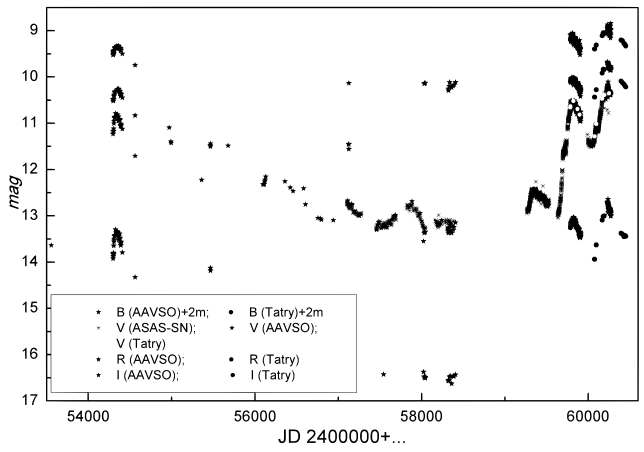

Figure 1: Light curve of V919 Sgr in 2006-2023.

Merc et al. (2023) report on the rebrightening of V919 Sgr observed in 2023. The ASAS-SN light curve well illustrates the system's brightness evolution. The peak brightness was reached in mid-October, and our BVRI photometric observations, available in the AAVSO database, show that the brightness is already decreasing. The B–V color of the system remained about the same during the maxima in 2022 and 2023, around 0.55 mag.

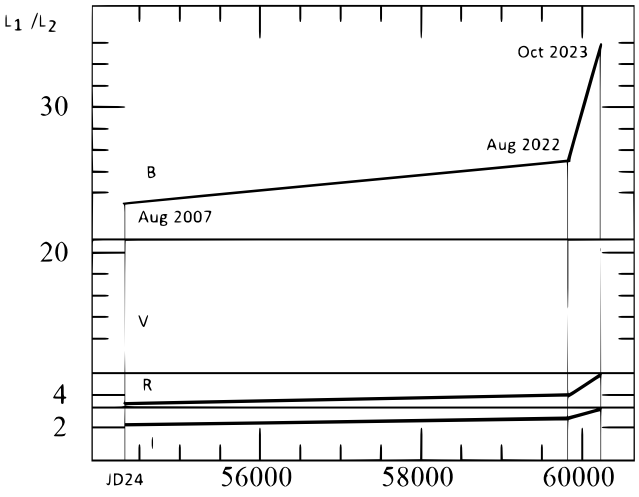

Figure 2: The luminosity of the system changed in comparison with the relatively quiet state in different bands. It can be seen that in the B-band during the last flare, the luminosity of the system increased by approximately 36 times.

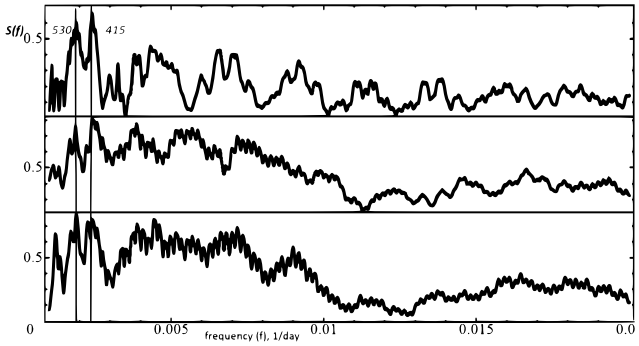

Figure 3: Periodograms for I-data calculated with the polynomial trends of orders $m = 0, 2$ and 3. The largest peaks are about 530 and 415 days.

We conduct photometric studies to analyze changes in the light curve and identify characteristic time intervals considering their evolutionary dynamics.

We used the observations of Astronomical Institute of Slovak Academy of Science (Tatry), ASAS-SN (V passband) and BVRI observations of AAVSO members. B-observations are shifted by 2^m for better visibility (Fig. 1).

The luminosity changes of the V919 Sgr in different passbands since the relatively quiet state (2007) and active state of 2022-2023 are schematically shown at Fig. 2.

The periodogram analysis was made using the completed mathematical model of a sinusoid with a polynomial trend of different order (Andronov, 1994, 2020), contrary to popular simplified methods

Table 1: Approximate times of outbursts.

data	JD	references
31.07–2.08.1991	2448470	Ivison et al., 1993
10.01.2005	2453380	Gromadzki et al., 2013
30.04.2006	2453856	Monard, 2007
12.08.2007	2454325	Munari et al., 2007
30.08.2022	2459822	Munari et al., 2022
19.10.2023	2460237	Merc et al., 2023

of preliminary detrending. Such a model was implemented in the software MCV (Multi-Column Viewer) by Andronov and Baklanov (2004). The software is available at http://uavso.org.ua/mcv/MCV.zip. The results of periodogram analysis for I-data is shown at Fig. 3.

Acknowledgements. We are thankful to S.Yu.Shugarov and colleagues from the Astronomical Institute of the Slovak Academy of Sciences as well as AAVSO members for their photometric observations. This work is in a frame of the "Inter-Longitude Astronomy" (Andronov et al., 2003) and "Ukrainian Virtual Observatory" (Vavilova et al., 2012) projects.

References

Andronov I.L.: 1994, *Odessa Astron. Publ.*, **7**, 49.
Andronov I.L.: 2020, in: *Knowledge Discovery in Big Data from Astronomy and Earth Observation,* Škoda, P., Adam, F., Eds.; (Elsevier: Amsterdam, The Netherlands), 191.
Andronov I.L., Baklanov A.V.: 2004, *Astron. School's Rep.*, **5**, 264.
Andronov I.L., et al: 2003, *AATr*, **22**, 793.
Gromadzki M. et al.: 2013, *AcA*, **63**, 405.
Hoffmeister C., Richter G., Wenzel W.: 1984, *Verändliche Sterne* (2nd edn.), (Springer, Berlin, Heidelberg), 335p.
Ivison R.J. et al.: 1993, *A&A*, **277**, 510.
Kochanek C.S. et al.: 2017, *PASP*, **129**, 980, 104502.
Kudashkina L.S., Breus V.V.: 2004, *The Astronomer*, **40**, 480, 321.
Monard B.: 2007, vsnet-alert, 9420.
Munari U. et al.: 2007, *CBET*, 999.
Munari U. et al.: 2022, *ATel*, 15528.
Merc J. et al.: 2023, *ATel*, 16326.
Sokoloski J.L.: 2003, *JAAVSO*, **31**, 89.
Vavilova I.B. et al.: 2012, *KPCB*, **28,** 85.

https://doi.org/10.18524/1810-4215.2024.37.313720

ACTIVE STAGE OF THE SYMBIOTIC STAR CH CYG IN 2015

Kh.M. Mikailov[1], A.B. Rustamova[2], I.A. Alekberov[2], B.N. Rustamov[1,2]

[1] Baku State University, Baku, Azerbaijan
[2] Shamakhy Astrophysical Observatory named after N. Tusi, Azerbaijan
mikailovkh@gmail.com

ABSTRACT. Symbiotic star CH Cyg is very different from other members of this group by the behavior of its photometric and spectral parameters. CH Cyg also belongs to a small subgroup of symbiotic stars in spectra where the high velocity absorption components have been observed – so called "Jet Absorption Structures" in the Hydrogen lines from the Balmer series. In this paper, the behavior of these jet absorption structures in Hα and Hβ lines in the spectrum of the symbiotic star CH Cyg during 18 nights from July to September of the year 2015 is described. Spectra has been obtained at the Cassegrain focus of the 2-meter telescope at Shamakhy Astrophysical Observatory with the help of echelle spectrograph with spectral resolution of R = 14 000. This paper also provides the profiles of the Hα and Hβ lines with absorption components on the blue wing. Based on the depth and the appearance, the absorption components have changed significantly and the short wavelength boundary reaches velocities of near 2500 km/s. The depth of absorption component on Hα is considerably less than the one at Hβ.

Keywords: symbiotic star – CH Cyg; echelle spectra; line profile; Jet Absorption Structures.

АНОТАЦІЯ. Симбіотична зоря CH Cyg значно відрізняється від інших членів цієї групи поведінкою фотометричних і спектральних параметрів. CH Cyg також належить до невеликої підгрупи симбіотичних зір, в спектрах яких спостерігаються компоненти, так звані Jet структури поглинання в лініях Гідрогену серії Бальмера. З історії фотометричного вивчення цієї зорі відомо, що починаючи з 1967 року було зафіксовано кілька моментів її фотометричної активності. Як правило, у цих активних фазах спостерігається блакитне зміщення високошвидкісних абсорбційних компонент в лініях Гідрогену серії Бальмера, а інколи, і в інших лініях. Починаючи приблизно з 2010 року яскравість зорі в U променях поступово збільшується і вже до кінця 2014 року досягає приблизно 7–8 зоряної величини. Одночасно із синхронним зростанням яскравості в V і U променях у 2014–2015 роках відбуваються помітні фотометричні і спектральні зміни. У цій роботі розглядається поведінка Jet структур поглинання в лініях Hα і Hβ з в спектрі CH Cyg протягом 18 ночей (приблизно 50 діб) з липня по вересень 2015 року. Спектри зорі програми були отримані на телескопі системи Кассегрен з діаметром головного дзеркала 2 м (Шамахинська астрофізична обсерваторія) за допомогою ешелле спектрографа з просторовою роздільною здатністю R = 14000. Фотометрично-активна фаза зорі у 2015 році не дуже сильно відрізняється від попередніх активних фаз, але така різноманітність Jet структур за формою і глибиною спостерігається тільки у 2015 році. Ми також наводимо профілі ліній Hα і Hβ з абсорбційними компонентами у блакитному крилі. Глибина і зовнішній вигляд компоненти поглинання суттєво змінилися і короткохвильова межа досягає швидкості близько 2500 км/с. Глибина складової поглинання в лінії Hα є значно меншою, ніж глибина лінії Hβ. Ми не знайшли залежності глибини короткохвильових границь променевої швидкості Jet структур поглинання від блиску зорі, а також від відношення інтенсивності блакитної і червоної емісійних компонент профілів вищевказаних ліній серії Бальмера.

Ключові слова: симбіотична зоря CH Cyg: ешелле спектри.

1. Introduction

Symbiotic stars – binary star system the spectrally resolved consisting of an interacting red giant and a white dwarf surrounded by a nebula. In this system, a strong flow of matter from the cold star to the hot star occurs through the stellar wind, leading to the formation of an accretion disk around the compact star.

CH Cyg star is a unique observational object, with characteristics of spectral and photometric variability that are very different from other symbiotic stars:

1. In 1984/85, the system showed a strong radio outburst, during which a double-sided jet with multi-

ple components was ejected (Taylor et al., 1986). This event enabled an accurate measurement of the jet expansion with an apparent proper motion of 1.1 arcsec per year. With a distance of 268 pc (HIPPARCOS) (Crocker et al., 2001), this leads to a jet velocity near 1500 km/s. The spectral energy distribution derived from the radio observations suggest a gas temperature of about 7000 K for the propagating jet gas (Taylor et al., 1986).

2. The photometric variability, such as flickering, occur of the CH Cyg symbiotic system. The source of these flickering's is believed to be the accretion disk. The disappearance of flickering's after flashes is explained by the disintegration of the disk.

3. The cold red giant in the CH Cyg symbiotic system pulsates with a period of 100 to 750 days, characteristic of o Cet type stars. This pulsation affects the accretion mode, resulting in more complex variations in the system.

4. Recently, many researchers have proposed that the 750-day periodic variation in the CH Cyg system may be due to the presence of a third star rather than pulsation. It is suggested that the 750-day period could correspond to the orbital period of this third star in an inner orbit of the symbiotic pair, which consists of the red giant and the white dwarf, with a longer orbital period of 5650 days.

5. One of the unique features of CH Cyg is its inclusion in the small group of symbiotic stars for which jet structures have been observed. "Jet Absorption Structures" have been detected in only 9 out of 220 stars cataloged as symbiotic stars. CH Cyg, along with MWC 560, serves as a natural laboratory for study the unique mechanism energy releaze due to the variety of shape, spectral parameters of the observed jets.

Most researchers agree that the CH Cyg symbiotic system consists of a pulsating red giant and a white dwarf. Matter is accreted from the red giant to the white dwarf, and the outflowing matter forms a disk around the star. This system is surrounded by a common shell. The observed spectral and photometric properties of this system are determined by the of the interaction of these three components and the physical accretion process.

This model, which has been sufficiently developed by many researchers over many years, and in many cases is in good agreement with observational results, is not accepted by a number of researchers. They suggest that there is a third star in this system. Although the triple star hypothesis is generally accepted by a number of researchers, there is no consensus on the role played by the third star in the physical processes taking place in this system. If a 3rd star is present, its spectrum should be visible (in some phase) as the red giant. Another interesting point is whether the 3rd star produced an eclipse, so far there have been no observations signs of such an eclipse.

Two main periods were found in the variation of photometric and spectral parameters of the CH Cyg star: a long period of 15.6 years (5400, 5600, 5800, 5900 days) and a short period around 750 days.

1. According to the first model, the approximately 15-year period represents the orbital period of the binary system, consisting of the red giant and the white dwarf, around their common center of mass. The short period of 750 days is attributed to the pulsation period of the red giant.

2. According to the second model, CH Cyg consists of three stars: the 15-year period represents the orbital period of the binary system, consisting of the red giant and the white dwarf, around their common center of mass. The short period of 750 days explained by the presence of a third star moving in the inner orbit.

2. Observations and data reduction

The spectral observations of symbiotic star CH Cyg have been performed at the Cassegrain focus of 2-m telescope of Shamakhy Astrophysical Observatory. Echelle-spectrometer with the CCD array (580×530 pixels) was employed. The wavelength range $\lambda\lambda$4700–6800 ÅÅ, spectral resolution R = 14 000, dispersion 10.5 Å/mm at Hα (Mikailov et al., 2005). We used 18 echelle spectra obtained for the period July–September 2015 (Table 1). Processing of echelle spectrograms were performed using software package DECH20T, developed at Special Astrophysical Observatory of RAS (Galazutdinov, 1992).

Data (day, month, year)	UT hrs, min	JD2450000+	Exposure time, s
18.07.2015	19 32	7222.31	1200
24.07.2015	17 06	7228.21	1200
26.07.2015	17 05	7230.21	1200
27.07.2015	17 28	7231.23	1200
29.07.2015	17 05	7233.21	600
30.07.2015	16 51	7234.20	600
30.07.2015	17 09	7235.22	600
01.08.2015	16 43	7236.20	600
04.08.2015	16 51	7239.20	900
07.08.2015	17 24	7242.23	1200
10.08.2015	16 49	7245.20	1100
12.08.2015	17 42	7247.24	1000
13.08.2015	16 54	7248.20	900
16.08.2015	17 43	7251.24	900
18.08.2015	17 55	7253.25	1200
19.08.2015	18 10	7254.26	1200
03.09.2015	17 06	7269.21	1200
04.09.2015	17 40	7270.21	1200

Table 1: Journal of spectroscopic observation.

Fig. 1 shows the historical light curve of the star CH Cyg in U and V magnitude for the period between the years 1967 and 2015, taken from (Skopal, 2015a). As

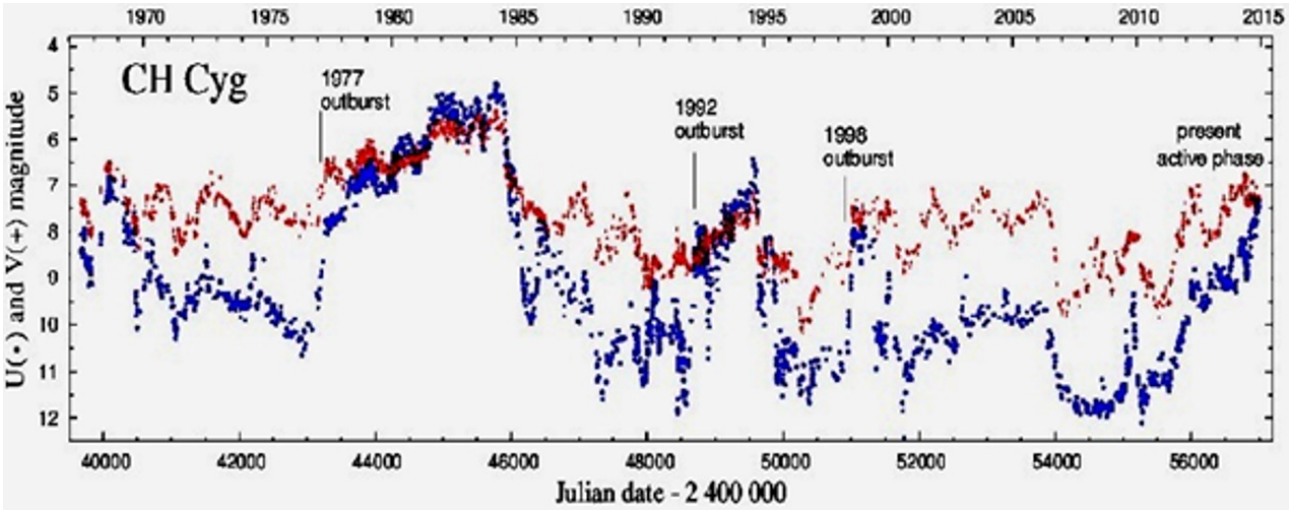

Figure 1: Historical light curve of the symbiotic star CH Cyg in U (dots, blue) and V (pluses, red), taken from (Skopal, 2015).

can be seen from the figure, several episodes of photometric activity of the star were recorded during this period (1984–1985; 1992–1995; 1998–2000; 2011–2015). As a rule, blue-shifted high-velocity absorption components are detected in these active phases in the lines of the Balmer series of hydrogen and sometimes in some other lines. Starting around 2010, the brightness of the star in U light gradually increases slowly and reaches a value of about 7^m–8^m (Skopal, 2015a) at the end of 2014. Along with the synchronous increase in U and V rays, remarkable photometric (Rspaev et al., 2014; Shugarov et al., 2015; 2008) and spectral (Rspaev et al., 2014; Skopal, 2015b,c,d) changes occurring in 2014–2015 leave no doubt that CH Cyg is entering into its next active phase.

Figure 2 shows the light curve in the visual region of the star CH Cyg for the period of our spectral observations – in July–September 2015 (AAVSO data for CH Cyg).

Vertical red lines indicate the time of spectral observations. As can be seen from the figure, in July–August the star's brightness increases slightly and at the beginning of September decreases again.

3. Results of observations

In 2015, during the spectral observations of the symbiotic star CH Cyg that has been conducted at the Shamakhy Astrophysical Observatory, unique "Jet Absorption Structures" have been discovered for the first time in the history of observations of this star. During the characteristic time of about 50 days, almost all types of Jet Absorption Structures established in symbiotic stars to date were observed.

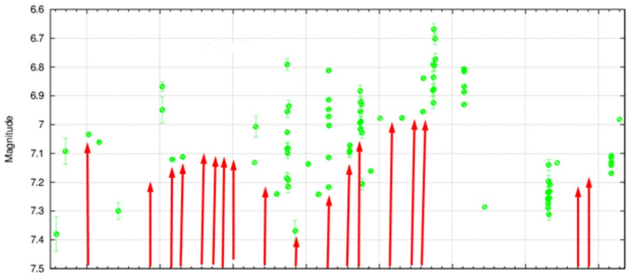

Figure 2: V light curve of the CH Cyg star in July–September 2015. Vertical red lines indicate the time of spectral observations

As can be seen from Fig. 1, the photometric active phase of the star CH Cyg in 2015 does not differ too much in appearance from previous active phases, but such a diversity in the shape and depth of jet structures absorptions was observed only in 2015.

The behavior of jet absorption structures in Hα and Hβ lines in the spectrum of the symbiotic star CH Cyg during 18 nights from July to September of the year 2015 is described. In Provides the profiles of the Hα and Hβ lines with absorption components on the blue wing. Based on the depth and the appearance, the absorption components have changed significantly and the short wavelength boundary reaches velocities of near –2500 km/s. The depth of absorption component on Hα is considerably less than the one at Hβ. Figure 3 shows the profiles of the Hα and Hβ lines in demonstrates temporal variations for the jet absorption structure of Hα and Hβ lines in the spectrum of the symbiotic star CH Cyg. Fig. 2 and Fig. 3 shows the type and wavelength boundaries of the "Jet Absorption

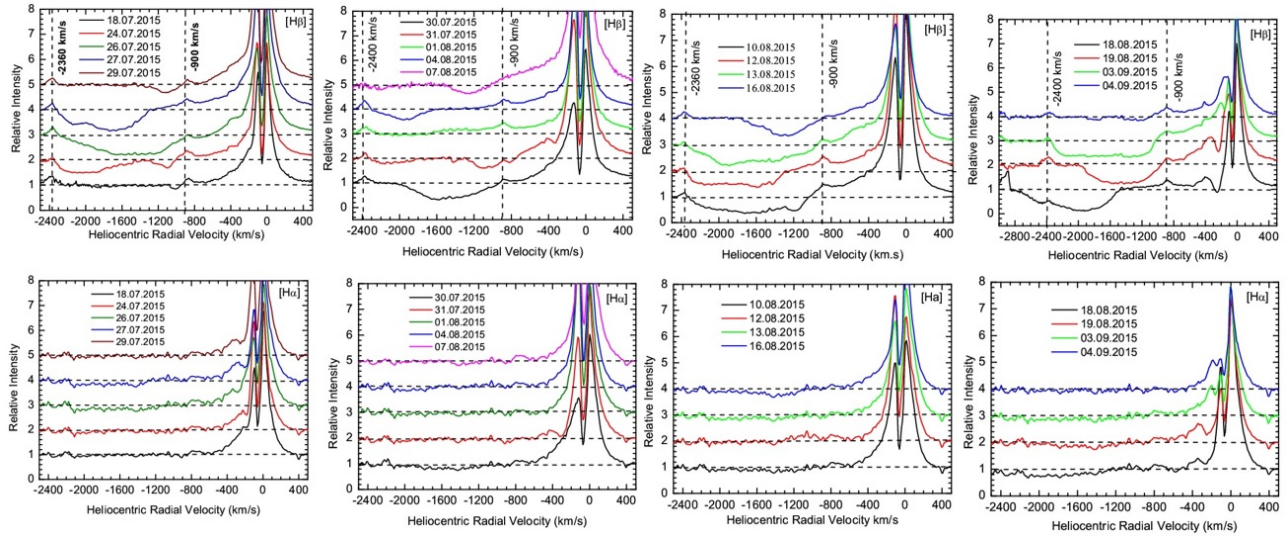

Figure 3: Temporal variations for the jet absorption structure of Hα and Hβ lines in the spectrum of the symbiotic star CH Cyg

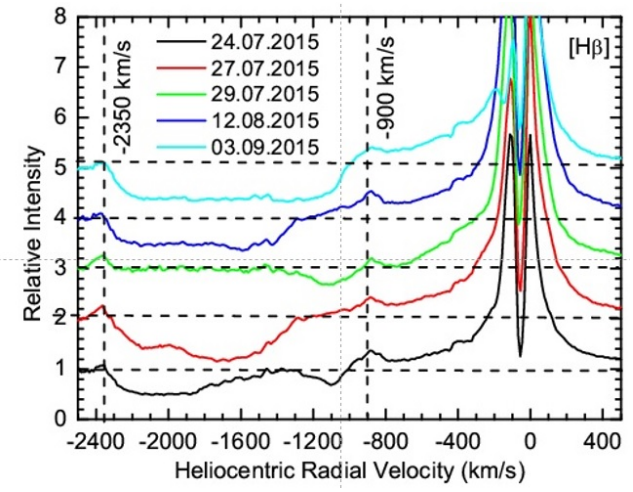

Figure 4: The selected profiles line Hβ, with the jet absorption in the spectrum of the symbiotic star CH Cyg

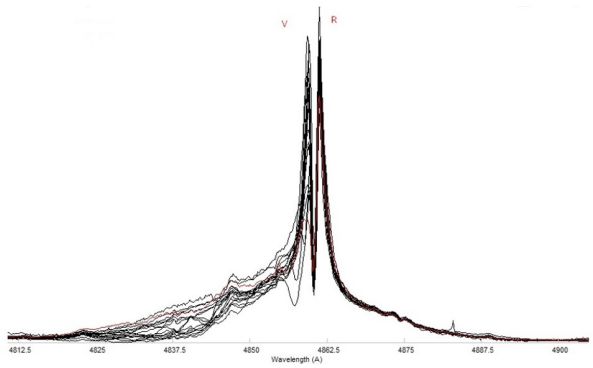

Figure 5: The profiles Hβ lines with jet absorption structure the superimposed one easer other, no normalized at the continuum.

Structures" do not depend on the brightness state of the star. Figure 4 shows selected characteristic profiles of line Hβ, with the jet absorption in the spectrum of the symbiotic star CH Cyg. Fig. 5 demonstrates that the Hβ line profiles with high-speed absorption components (Jet Absorption Structures) are not normalized to the continuum. According to this figure, the red emission component of the Hβ line practically does not react to the notable change occurring on the blue wing of the line. Fig. 6 displays the time dependence of the intensity ratios of the blue (V) and red (R) emission components of the Hα and Hβ lines. As inferred from this figure and Fig. 3, the shape of the "Jet Absorption Structures" does not depend on the V/R ratios either.

Our spectral observations only cover the Hα and Hβ lines from the hydrogen lines. Therefore, there is no information about other hydrogen lines.The given profiles of jet structures are a characteristic or averaged profile obtained on a given night of observations.

4. Conclusions

In symbiotic stars, the matter for accretion onto the compact object is supplied from the primary component which is the red giant. However, not every symbiotic star is a source of jets. It is still unclear what parameters this depends on. The velocity in the jets

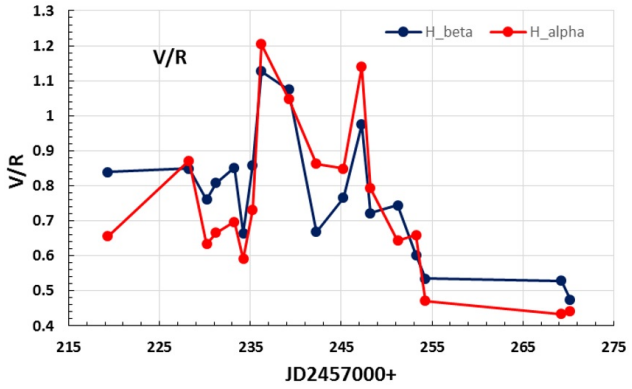

Figure 6: Variations of ratio V/R, for the intensities of blue and red emission components of Hα and Hβ lines in the spectrum of CH Cyg in July–September 2015.

of symbiotic stars reaches several thousand km/s. Apparently, these jets operate in a pulsed mode, and in the case of CH Cyg. The impulsive nature of the jet producing stars of symbiotic systems suggests that the critical mass for the formation of jets is required to get accumulated in the accretion disk around the white dwarf before the jets begin to form. In a binary system, this may occur due to a change in the flow in the stellar wind from the second component, and/or a change in the distance between the components during orbital motion at a significant eccentricity. Since the white dwarf may have a strong magnetic field, its role in the formation of collimated jets is not disregarded.

In spectroscopic observations of the symbiotic star CH Cyg conducted at the Shamakhi Astrophysical Observatory in July–September 2015, high-speed absorption components (Jet Absorption Structures) were discovered on the blue wing of the Hα and Hβ lines. The short-wavelength boundary of these absorptions reaches approximately –2500 km/s. Virtually all types of Jet Absorption Structures found in symbiotic stars to date were detected over the course of 18 nights (about 50 days).

References

Crocker M.M., Davis R.J., Eyres S.P.S. et al.: 2001, *MNRAS*, **326**, 781.

Galazutdinov G.A.: 1992, *Preprint SAO*, **92**.

Mikailov Kh.M., Khalilov V.M., Alekberov I.A.: 2005, *Tsirkular ShAO*, **109**, 21.

Rspaev F., Kondratyeva L., Aimuratov E.: 2014, *IBVS*, **6117**.

Shugarov et al.: 2008, *EASP*, **71–72**, 107.

Shugarov S., Sekeras A., Skopal A., Komissarova G.: 2015, *Physics of Evolved Stars (France)*, p. 67.

Skopal A.: 2015a, *ARAS Erupt. Stars Inform. Let.*, **13**, 25.

Skopal A.: 2015b, *ARAS Erupt. Stars Inform. Let.*, **14**, 56.

Skopal A.: 2015c, *ARAS Erupt. Stars Inform. Let.*, **16**.

Skopal A.: 2015d, *ARAS Erupt. Stars Inform. Let.*, **1**.

Taylor A.R., Seaquist E.R., Mattei J.A.: 1986, *Nature*, **319**, 38.

https://doi.org/10.18524/1810-4215.2024.37.312691

SPECIFIC FEATURES OF THE ENRICHMENT OF METAL-POOR STARS WITH NEUTRON-CAPTURE (R-PROCESS) ELEMENTS

T. Mishenina[1], T. Gorbaneva[1], A. Dmytrenko[2], M. Pignatari[3, 4, 5], F.-K. Thielemann[6,7]

[1] Astronomical Observatory, Odesa I. I. Mechnikov National University, Odesa 65014-UA, Ukraine, *tmishenina@ukr.net*

[2] Institute of Astronomy, V. N. Karazin Kharkiv National University; 4 Svobody Sq, Kharkiv, 61022, Ukraine

[3] Konkoly Observatory, HUN-REN, Konkoly-Thege Miklós út 15-17, Budapest, H-1121, Hungary

[4] MTA Centre of Excellence, Konkoly-Thege Miklós út 15-17, Budapest, H-1121, Hungary

[5] E. A. Milne Centre for Astrophysics, University of Hull, Hull HU6 7RX, UK

[6] Department of Physics, University of Basel, Klingelbergstrabe 82, CH-4056 Basel, Switzerland

[7] GSI Helmholtzzentrum für Schwerionenforschung, Planckstraße 1, Darmstadt, D-64291, Germany

ABSTRACT. In contrast to stars with near-solar metallicity (Galactic disk stars), metal-deficient stars show an abundance scatter of up to 3 dex in the enrichment with neutron-capture elements, in particular the r-process elements. The reasons of such a large variation in the in the r-process nucleosynthesis is currently matter of debate. Possible scenarios could be the presence of various r-process stellar and mechanisms in the early unevenly mixed Galaxy, as well as different stellar origin, either galactic or extragalactic, that reflect entering the Galaxy after the capture or coalescence of both individual stars and more complex stellar associations and star formations. In order to study differences in the enrichment with the r-process elements, we selected 20 metal-deficient stars, the spectra of which were collected in the UVES/VLT archive. We employed earlier determined atmospheric parameters to calculate the abundances of about 20 neutron-capture elements via the synthetic spectrum method, taking into account the hyperfine structure for a number of elements. We performed an analysis of the enrichment with the r-process elements grounded on multiple levels of enrichment intensity – namely, limited r-process, r-I and r-II – and the arrangement of stars by their belonging to different populations of the Galaxy, based on the stars' spatial velocity components.

Keywords: stars: abundances – stars: atmospheres – stars: stellar evolution.

АНОТАЦІЯ. На відміну від зір із близькосонячною металічністю (зорі диска Галактики), зорі з дефіцитом металів демонструють розкид вмістів до 3 dex у збагаченні елементами, що захоплюють нейтрони, зокрема елементами r-процесу. Причини такої великої варіації в нуклеосинтезі r-процесу наразі є предметом дискусій. Можливі сценарії полягають в наявності різноманітних зір і механізмів r-процесу в ранній нерівномірно змішаній Галактиці, а також різного походження зірок, галактичного чи позагалактичного, що відображає входження в Галактику після захоплення або злиття як окремих зірок, так і більш складних. зоряних асоціацій та зоряних утворень. Що б вивчити відмінності у збагаченні елементами r-процесу, було відібрано 20 зір з дефіцитом металів, спектри яких ми отримали з архіву UVES/VLT. Ми використовували раніше визначені параметри атмосфери для розрахунку поширеності близько 20 елементів, які утворені в процех захоплення нейтронів, за допомогою методу синтетичного спектра, враховуючи надтонку структуру ряду елементів. Ми провели аналіз збагачення елементами r-процесу на основі кількох рівнів інтенсивності збагачення, а саме обмеженого r-процесу, limited-r, та надлишкового збагачення r-I та r-II типів. Для зір категорії limited-r існує ймовірність збагачення елементами з атомним номером більше 70. Авторами запропоновано різні механізми та процеси збагачення у випадку зір, класифікованих як різні типи r-збагачення, це Наднові, колапсуючі в ядрі, швидко обертові магніто-гідродинамічні наднові, колапсари, та злипання нейтронних зір та чорних дір в різних варіантах. Показано, спираючись на компоненти просторової швидкості, що зорі досліджуваної вибірки належать до різних популяцій Галактики, як до товстого диска, так і до внутрішнього та акреційного гало.

Ключові слова: зорі: вміст – зорі: атмосфера – зорі: еволюція зір.

1. Introduction

The study of neutron capture elements in metal-deficient stars is important to understand the evolution of the early Galaxy, the Galaxy as whole, and to search for souses and mechanisms of their production.

Metal-poor stars in our Galaxy show marked enrichment in r-process elements, up to 3 dex (e.g. Roederer et al., 2014), compared to enrichment in the Galactic disk stars. The degree of enrichment in neutron capture elements was reviewed by Beers & Christlieb (2005), and the following classification was proposed dividing the stars into two main categories (Beers & Christlieb, 2005): the r-I stars have $0.3 \leq [Eu/Fe] \leq +1.0$, while r-II stars have $[Eu/Fe] > +1.0$; both require $[Ba/Eu] < 0$ to avoid contamination from the s-process. Currently, based on the work of Holmbeck et al. (2020); Cowan et al. (2021); Farouqi et al. (2022), we can talk about three different categories of r-process: (1) limited-r stars which have elements as heavy as Eu but no third r-process peak elements and essentially no elements with $Z > 70$. Its value for $[Eu/Fe] < 0.3$, but it could be reduced to $[Eu/Fe] < 0$ (Farouqi et al. 2022). Additional conditions for Sr and Ba are following: $[Sr/Ba] > 0.5$, $[Sr/Eu] > 0$. (2) r-I stars are clearly r-process enriched and show a close to solar r-process pattern with $0(0.3) < [Eu/Fe] < 1$ and $[Ba/Eu] < 0$, i.e. the Ba/Eu ratio being smaller than a solar-like s-process-dominated composition. (3) r-II stars are highly r-process enriched with $[Eu/Fe] > 1$ and follow a [Ba/Eu] constraint as in (2).

Sources (sites) of production of r-process elements are: a weak r-process, which is associated with supernovae, where the innermost ejecta close to the central neutron star were supposed to be neutron-rich (e.g. Wanajo, Janka & Kubono, 2011), a strong r-process, for which quite different scenarios are possible, such as neutron-star mergers (e.g. Freiburghaus, Rosswog & Thielemann, 1999), ejecta from binary neutron-star mergers (e.g. Eichler et al., 1989; Goriely et al., 2015; Thielemann et al., 2017; etc.), neutron star-black hole mergers (e.g. Lattimer & Schramm, 1974; Surman et al., 2008; etc.), certain rare classes of fast-rotating supernovae with powerful magnetic fields (e.g. Symbalisty, Schramm & Wilson, 1985; Nishimura et al., 2006; Winteler et al., 2012; etc.), as well as hypernovae or collapsars (e.g. Thielemann, Wehmeyer & Wu 2020; etc.), and perhaps to a lesser extent the innermost ejecta of regular core-collapse supernovae (CCSNe) (e.g. Woosley et al., 1994; Farouqi et al., 2010; Arcones & Thielemann, 2013; etc.).

The aim of this work is to determine uniformly and highly precisely the abundances of neutron-capture elements in a number of metal-deficient stars differing in the degree and pattern of the enrichment, as well as to analyse plausible causes of such differences.

2. Observations, spectrum processing, spatial velocity components

To study differences in the enrichment of r-process elements, we selected 20 metal-deficient stars, and we used spectra from the UVES/VLT archive, based on the data obtained from the ESO Science Archive Facility (DOI(s): https://doi.org/10.18727/archive/50): the resolution R = 41000-60000, the range of wavelengths λλ 3200-6500 ÅÅ, the signal-to-noise ratio S/N > 100. The spectral processing, including individual spectrum normalization to the local continuum, identification of spectral lines of different chemical elements, measurements of the line depth and equivalent width (EW), was performed for each star using the DECH30 software package developed by Galazutdinov (http://gazinur.com/DECH-software.html).

Spatial velocity components (U, V, W) with respect to the Local Standard of Rest (LSR) were computed based on the coordinates, proper motions and radial velocities from Gaia DR3 (Vallenari et al. 2023). We used the solar motion with respect to the LSR by Robin et al. (2022) from Gaia DR3: (U, V, W) sun =10.79±0.56, 11.06±0.94, 7.66±0.43 km·s^{-1}. The Toomre diagram for the stars under study is shown in Fig. 1.

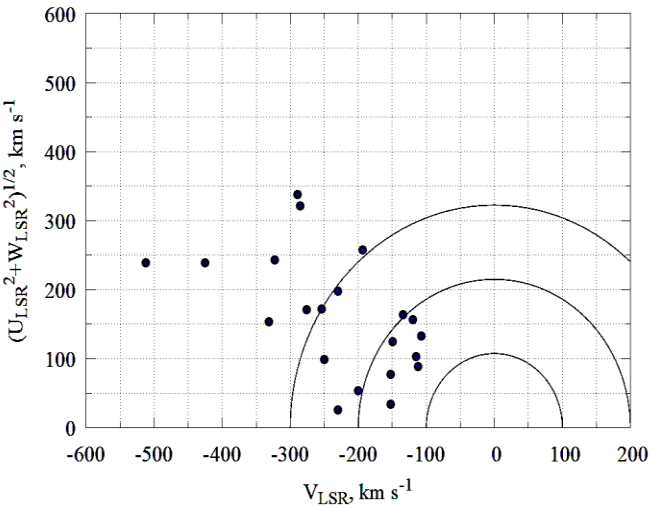

Figure 1: Toomre diagram for studied stars

3. Atmospheric parameters and abundance determinations

We used the atmospheric parameters determined earlier (Table 1).

To calculate the abundance of about 25 neutron capture elements (Sr, Y, Zr, Nb, Mo, Ru, Rh, Pd, Ba, La, Ce, Pr, Nd, Sm, Eu, Gd, Tb, Dy, Ho, Er, Tm, Yb, Hf, Os, Ir, Pb, Th) we used the LTE approach and the atmospheric models by Castelli & Kurucz (2004). The choice of model for each star was made by means of standard interpolation for Teff and log g. The abundances were employed the synthetic spectrum method by a new version of the STARSP software (Tsymbal, 1996) and new version of the VALD2018 line list (Kupka et al., 1999). Hyperfine structure for a number of elements (Ba, La, Eu) was take into account the, and solar isotope composition was used in the case of Ba. The spectrum synthesis fitting of the Ba and Eu lines to the observed profiles for star J01293113 is shown in Figs. 2, 3 with the values of [Ba/Fe] = 0.76 and [Eu/Fe] = 1.66.

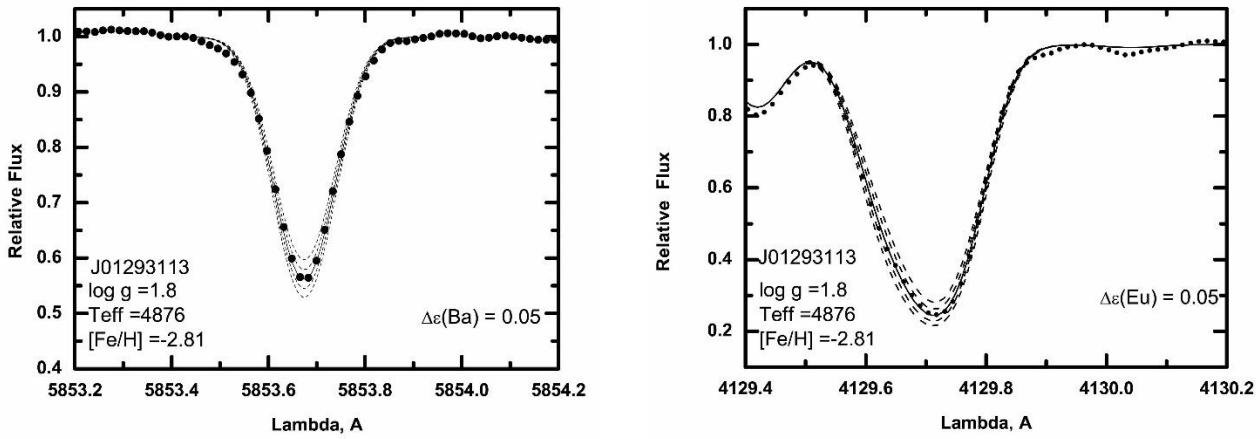

Figures 2, 3: Spectrum synthesis fitting of the Ba and Eu lines to the observed profiles.

Table 1: Lists the name of stars, the parameters (effective temperature T_{eff}, gravity logg, microturbulent velocity V_t, metallicity [Fe/H]) and the references of relevant papers.

Name	T_{eff}	log g	v_t	[Fe/H]	Ref
BD+17 4708	6000	4	0.7	-1.56	Mish03
BD+23 3130	5100	2.25	1	-2.62	Mish01
BD+23 3912	5750	3.7	1.3	-1.39	Mish00
BD+26 4251	5860	3.5	1.7	-1.42	Mish00
BD+29 2091	5850	4.2	1.6	-1.93	Mish03
BD-18 5550	4600	0.5	1.2	-3.01	Mish01
HD 002796	4900	1.6	1.5	-2.21	Mish01
HD 008724	4600	1.5	1.5	-1.65	Mish01
HD 019445	5830	4.00	1.10	-2.16	Mish17
HD 025329	4850	4.25	1.5	-1.73	Mish01
HD 026297	4300	0.5	1.7	-1.91	Mish01
HD 084937	6325	3.95	1.4	-2.24	Mish17
HD 108317	5250	2.4	1.7	-2.17	Mish01
HD 122563	4570	1.1	1.2	-2.42	Mish01
HD 216143	4455	1.05	1.90	-2.26	Mish17
HD 221170	4415	1.05	1.9	-2.26	Mish17
J20554594-3155159	4581	0.94	2.26	-2.67	Holm20
J03142084-1035112	4769	1.15	2.11	-3.75	Holm20
J12044314-2911051	4465	0.92	2.49	-2.35	Holm20
J01293113-1600454	4876	1.80	-2.81	-2.13	Hans18
J22021636-0536483	4668	0.93	-2.75	-2.57	Hans18

4. Results and discussions

4.1. Analysis of the behavior of the r-process elements in the studied stars

To consider the different various features of the r-process of enrichment of metal-deficient stars we compare the obtained Sr, Ba, Eu abundances for our studied stars to find (define) indicators (types) of the r-process or, in other words, to determine the degree of r-process enrichment based on the Sr, Ba, Eu abundance criteria.

As we noted in the introduction, three classes (types) of enrichment in r-capture elements are currently considered. The first criterion is the abundance of europium, often using [Eu/Fe], an element predominantly formed by the r-process. Among our stars, only one is of the r-II type, 11 stars are of the r-I type, and 8 stars are of the limited r type. Also for classification additional criteria are used for classes (types) r-I and r-II, this is the ratio of [Ba/Eu], this value confirmed the classification by [Eu/Fe]. And for stars of the limited-r type two additional criteria are introduced [Sr/Ba] and [Sr/Eu]. For two stars with very low europium abundance these criteria are met unconditionally, and for 6 stars, taking into account the errors of determinations for [Sr/Ba].

Let us consider the behavior of the element abundances depending on the Atomic Number for the groups (Fig. 4 upper. r-I and r-II stars, Figs. 5, 6 middle, bottom limited-r stars). For all groups we see different behavior of the r-process elements, increased for r-II, lower, but quite compact for r-I stars (spread about 0.5 dex), and with a large spread for limited-r stars (from -0.5 dex to -1.5 dex). Two figures for limited-r stars differ in the europium abundance, if in the first case (Fig. 5) these are small negative values of [Eu/Fe], then in the second (Fig. 6) these are stars with a fairly low value of [Eu/Fe], less than -0.6. As mentioned above, for limited-r stars there are essentially no elements with AN > 70, which is what we observe in the bottom (Fig. 6), and in the middle (Fig. 5) such elements are present. We believe that one reason for the presence of elements with AN > 70 may be a "shift" of the upper limit for r-I from 0 to -0.2 dex due to errors in the Eu abundance determination (~0.2 dex), and this may change the classification and transfer limited-r stars to the r-I category. However, this may also indicate that some limited-r stars have the elements with atomic numbers greater than 70, in other words, it may indicate contributions of two or more events to their enrichment.

At the moment, it is difficult to say whether this reflects the enrichment features of limited-r stars in general, or only in our particular set of stars.

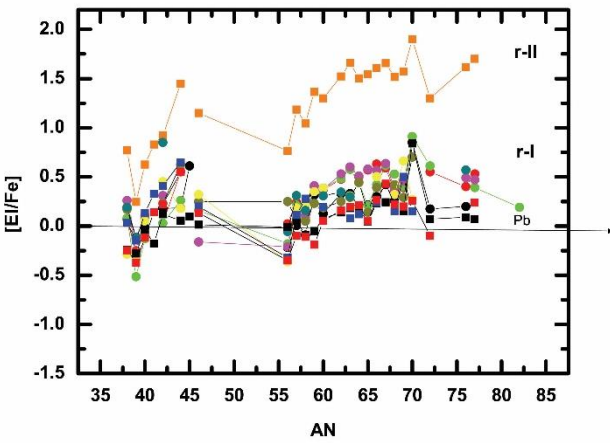

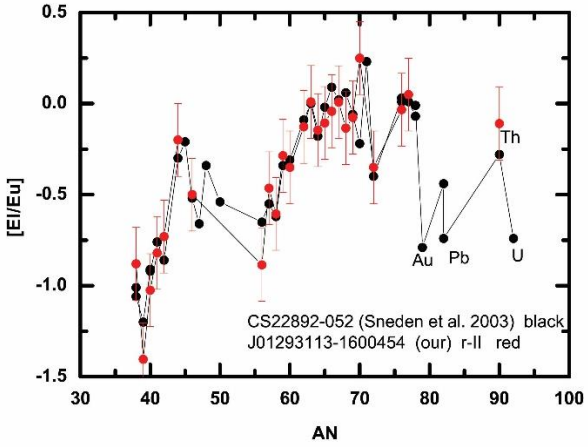

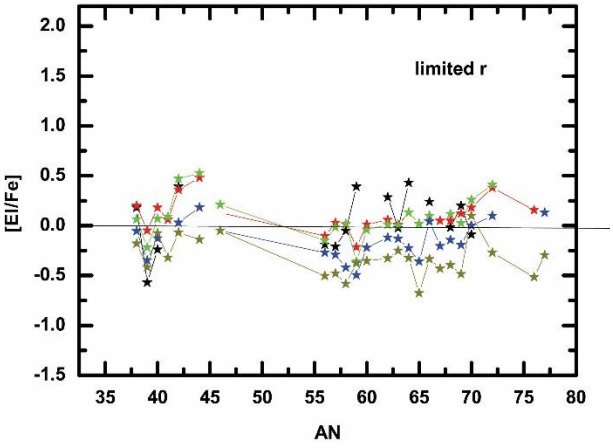

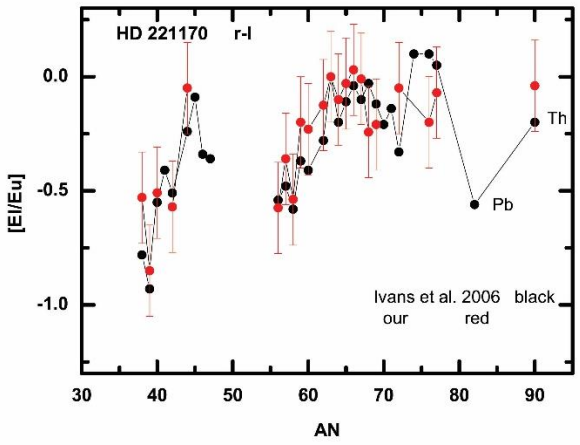

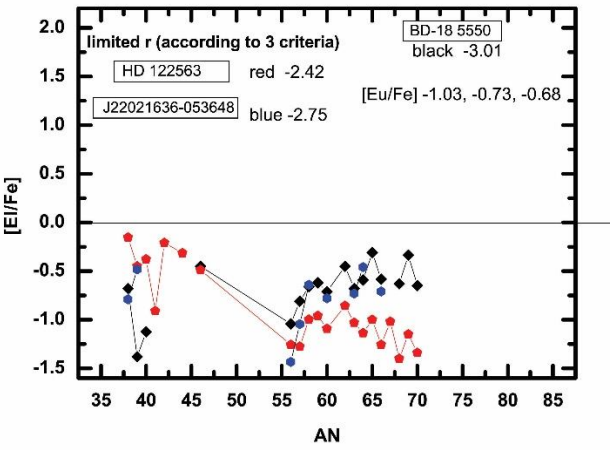

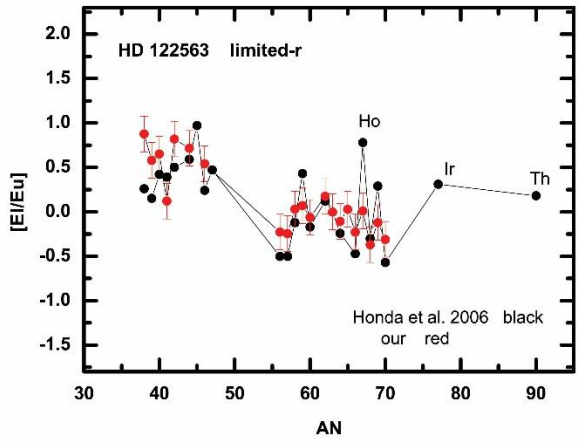

Figures 4, 5, 6: Distribution of the element abundances from the Atomic Number for these three groups (Fig. 4 upper. r-I and r-II stars, Figures 5, 6 middle, bottom limited-r stars).

Figures 7, 8, 9: Comparison our results for one typical star of each group with those of other authors.

We then compared our results for one typical star of each group with those of other authors, namely, J01293113-1600454 (r-II) with the classical r-process star CS22892-052 (Sneden et al., 2003) (Fig. 7), HD 221170 (r-I) with the work of Ivans et al. (2006) on this star (Fig. 8), and HD 122563 (limited-r) with the data of Honda et al., 2006 (Fig. 9), that show typical weak- r-process.

We see good agreement between the data (Fig. 7, r-II), confirming a noticeable enrichment in the r-process, as well as good agreement for HD 221170 (r-I), which is moderately enriched in the r -process (Fig. 8). As for HD 122563 (limited-r), this is a star with a noticeable europium deficiency, Honda et al. (2006) have found abundance of elements with AN > 70, the upper limit of iridium and thorium (Fig. 9). Is it caused by the errors in determination or there is a possibility of the enrichment in elements with AN > 70? Besides, it may also indicate that several (some) limited-r stars have the r-enrichment, i.e. two or more sources were involved in their enrichment. Note, there are also other possible interpretations, as e.g. Montes et al., 2007 (LEPP source).

4.2. Plausible sources of r-enrichment

In analysis of r-process nucleosynthesis and chemical evolution of Galaxy, two types of r-process sources with different delay times are considered, a quick source (e.g. CCSNe) and a delayed one (CBM – compact binary mergers, common name). As shown in a number of works (e.g., Wehmeyer, Pignatari & Thielemann, 2015; Farouqi et al., 2022; Mishenina et al., 2024; etc.) both a quick source (e.g. CCSN) and a delayed one (CBM) produce r-process material. We suggest that high values of the abundance of r-process elements in class (r-II) stars can be provided by CBM as the main astrophysical site of the r-process, as a result of the merger of neutron stars or black holes. A moderate enrichment of (r-I) also can be provided by CBM: it is still debated whether two types (r-I and r-II) are produced in different sites or result from variations within the same site (e.g. neutron star mergers) (Farouqi et al., 2022). Limited-r stars may be enriched predominantly from different types SNe (e.g. magneto-rotational SNe), but the presence of elements with AN > 70 substantiates the hypothesis of possible contributions from other sources with different delay times. Different mechanisms and sources of the r-process are responsible for the enrichment of stars of different r-types, but the exact yields of elements resulting from the r-processes in the indicated stars are still highly debatable, thus requiring additional research.

4.3. Kinematics

If we look at the space velocities and the Toomre diagram, using the criteria of Marsakov & Borkova (2006) to separate of different structures of the Galaxy, we can say that our stars belong to the thick disk, as well as to the proper and accreted halo (i.e. captured by the Galaxy). The velocity separating the thick disk and the halo is 180 km/s. We have about 8 such stars (3 r-I, 5 limited-r). Stars with residual velocities of 175–240 km/s belong to the proper halo of the Galaxy, 4 stars (3 r-I, 1 limited-r). Stars with velocities higher than 250 km/s belong to the outer accreted halo, taking into account retrograde velocities, there are 9 of them (1 r-II, 6 r-I, 2 limited-r). The star with the highest V velocity is BD+23 3130, limited-r, the second is J01293113-1600454 (r-II). Stars with different levels of r-process enrichment belong to different galactic populations.

5. Results and conclusions

1) The abundance of 25 r-process elements in 20 metal-poor stars was determined.

2) The r-enrichment type was determined for all stars and it was shown that, in general, the criteria under consideration are quite reliable.

3) For stars of the category, type limited-r, there is a probability of enrichment with elements with an atomic number greater than 70.

4) The authors suggest different mechanisms and processes of enrichment in the case of stars classified as different r-types.

5) The stars of the studied sample belong to different galactic structures, both to the thick disk of the Galaxy and to the inner and accreted halo.

Reference

Arcones A., Thielemann F-K.: 2013, *JPhG*, **40**, id.013201.

Castelli F., Kurucz R.: 2004, ArXiv *Astrophysics e-prints* astro-ph/0405087.

Farouqi K., Thielemann F.-K., Rosswog S., Kratz K.-L.: 2022, *A&A*, **663**, id.A70, 43pp.

Frebel A.: 2018, *ARNPS*, **68**, 237.

Hansen T., Holmbeck E., Beers T. et al.: 2018, *ApJ*, **858**, 92H.

Holmbeck et al.: 2018, *ApJ*, **859**, L24.

Holmbeck E., Hansen T., Beers T., et al.: 2020, *ApJS*, **249**, 30H.

Honda S., Aoki W., Ishimaru Y. et al.: 2006, *ApJ*, **643**, Issue 2, 1180.

Ivans et al.: 2006, *ApJ*, **645**, 613.

Korotin et al.: 2015, *A&A*, **581**, 70

Kupka et al.: 1999, *A&ASuppl.*, **138**, 119.

Lattimer J., Schramm D.: 1974, *ApJ*, **192**, 145.

Lippuner et al.: 2017, *MNRAS*, **472**, 904.

Marsakov V.A., Borkova T.V.: 2006, *Astron. Lett.*, **32**, Issue 8, 545.

Mishenina T.V., Korotin S.A., Klochkova V.G. et al.: 2000, *A&A*, **353**, 978M.

Mishenina T.V., Kovtyukh V.V.: 2001, *A&A*, **370**, 951.

Mishenina T.V., Kovtyukh V.V., Korotin S.A. et al.: 2003, *Astron. Rep.*, **47**, 422M.

Mishenina T., Pignatari M., Côté B. et al.: 2017, *MNRAS*, **469**, 4378M.

Mishenina T.V. et al.: 2024, *A&A*, **687**, id.A229, 24pp.

Nishimura et al.: 2017, *ApJ*., **836**, 21.

Roederer et al.: 2014, *AJ*, **147**, 136.

Rosswog et al.: 2014, *MNRAS*, **439**, 757.

Simmerer et al.: 2004, *ApJ*, **617**, 1091.

Sneden et al.: 2003, *ApJ*, 591, 936.

Spite et al.: 2006, *A&A*, **455**, 291

Spite et al.: 2018, *A&A*, **611**, 30.

Tsujimoto T., Nishimura N.: 2015, *ApJ*, **811**, 10.

Tsymbal V.: 1996, *ASP Conf. Ser.*, **108**, 198.

Gaia Collaboration, Vallenari et al.: *A&A*, **674**, A1

Winteler et al.: 2012, *ApJ*, **750**, 22.

Wehmeyer, Pignatari & Thielemann: 2015, *MNRAS*, **452**, Issue 2, p.1970-1981.

https://doi.org/10.18524/1810-4215.2024.37.313714

THIRD COMPONENT IN ALGOL TYPE ECLIPSING BINARY SYSTEMS

B.N. Rustamov[1,2], Kh.M. Mikailov[1], S.O. Mammadova[2], K.I. Alisheva[1], V.I. Aliyeva[2]

[1] Baku State University, Baku, Azerbaijan
[2] Shamakhy Astrophysical Observatory named after N. Tusi, Azerbaijan
bayram_rustam@yahoo.com

ABSTRACT. After the application of the echelle spectrograph in combinations with high sensitivity radiation receivers during the observations of short period Algol type binary star systems, in some cases there is a special feature observed in their spectrum which could indicate the presence of the potential third component. Currently the subclass of the star is distinguished among the Algol type stars in spectra of which similar features have been observed. The results of the spectral observations of two Algol type stars that belong to the subclass δ Lib and U Sge are also included. In both stars, there is an absorption detail that appears during the phases of the orbit (0.1 – 0.4) in red and (0.6 – 0.8) in blue wings of the Hα line. These phase intervals correspond to eclipse period of the secondary component. Preliminarily, we are suggesting that this observational fact could indicate the presence of the third component in the system and also provides alternative hypotheses that leads to similar physical conditions.

Keywords: individual: Algol, line profiles, radial velocity curve.

АНОТАЦІЯ. Після застосування ешелле-спектрографа в поєднанні з високочутливими приймачами випромінювання під час спостережень короткоперіодичних подвійних зоряних систем типу Алголя в деяких випадках в їх спектрах спостерігається особливість, яка може вказувати на наявність потенційного третього компонента. В даний час серед зір типу Алголь виділяється підклас зір, в спектрах яких спостерігаються подібні риси. Включені результати спектральних спостережень двох зір типу Алголь δ Lib і U Sge, які належать до цього підкласу.

Спектральні спостереження зорі U Sge проведено у фокусі Кассегрена 2-м телескопа Шамахинської астрофізичної обсерваторії ім. Н.Тусі на ShaFES з використанням ПЗЗ-матриці зі спектральною роздільною здатністю R = 28000, в області довжин хвиль $\lambda\lambda$ 3900–7500ÅÅ, у 2022–2023 роках. Криві радіальних швидкостей обох компонентів системи δ Lib та U Sge були побудовані на основі наших вимірювань радіальних швидкостей і запозичені з публікацій.

В спектрах обох зір є деталь поглинання, яка з'являється на фазах орбіти (0,1 – 0,4) у червоному та (0,6 – 0,8) у синьому крилах лінії Hα. Ці фазові інтервали відповідають періоду затемнення другого компонента. Попередньо ми припускаємо, що цей факт спостереження може вказувати на присутність третього компонента в системі, а також надає альтернативні гіпотези, які призводять до подібних ефектів, зокрема, лінію Hα видно на вторинному компоненті на початку та в кінці затемнення, або, можливо, що ефект Маклафліна–Россітера рідко спостерігається в подвійних системах типу Алголя. Усі три гіпотези є предметом обговорювання в міру отримання додаткових спостережень.

Ключові слова: індивідуальні: Алголь, профілі ліній, крива радіальних швидкостей.

1. Introduction

The Algol-type binaries are semidetached interacting binary systems in which the cool F–K III-IV secondary star has expanded to fill its Roche lobe and is transferring material through a gas stream onto the hot B–A V primary star (see Fig. 1).

As you know the prototype Algol type eclipsing binaries systems star β Per, is a triple system. Until recently, due to the weakness of the visible brightness of the third component, the influence of this component was not taken into account when modeling the light curve and radial velocities of the β Per system. Only in recent years, was it possible to build a satisfactory model of this star as a triple system using observations with many techniques and at many wavelengths.

The presense of the potential third component could be indefinied with special features observed in the spectrum of short period Algol type binary star systems af-

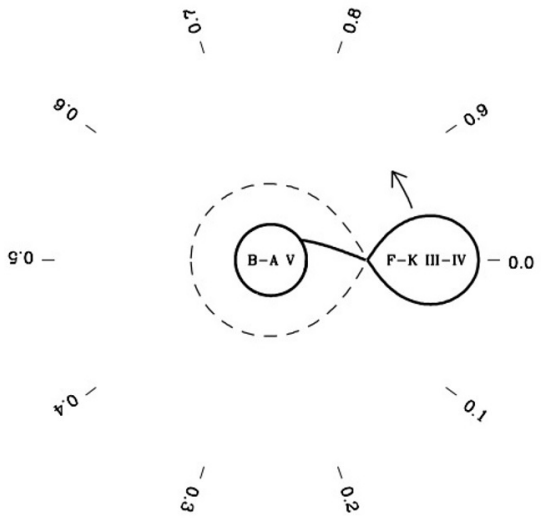

Figure 1: Scale model of an Algol-type binary system showing the predicted path of the gas stream, the range of spectral types, the spectral classes, and the lines of sight for different orbital phases

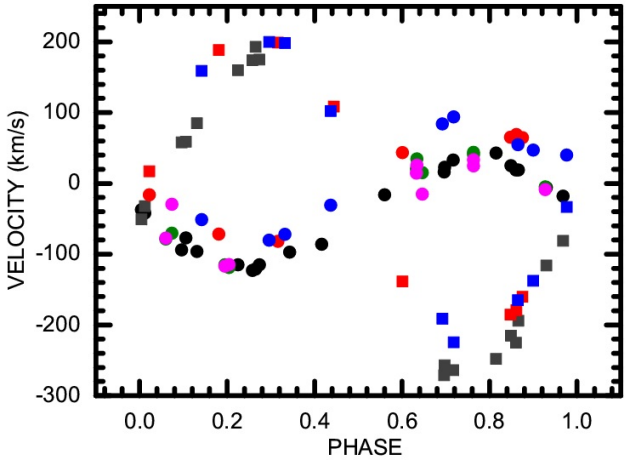

Figure 2: Primary and secondary components radial velocity curves of the δ Lib star Algol type binary system. **Primary component** full circles: black – Tomkin J., 1978 (date 1977); red – Baksh V., 2006 (Ondrejov, date: 1996, 1997 and 2003); blue – Baksh V., 2006 (Rozhen, date: 1996, 1997 and 2003); magenta – ShAO + Czech (Hα, this work); olive – ShAO + Czech (Hβ, this work); **Secondary component** full rectangles: black – Tomkin J., 1978 (date 1977); red – Baksh V., 2006 (Ondrejov, date:1996, 1997 and 2003); blue – Baksh V., 2006 (Rozhen, date: 1996, 1997 and 2003).

ter the application of the echelle spectrograph in combinations with high sensitivity radiation receivers during the observations. Currently the subclass of the star is distinguished among the Algol type stars in spectra of which similar features have been observed. (Tomkin, 1978; Tomkin, 1979 Tomkin, 1981; Tomkin, 1983; Tomkin, 1985; Tomkin, 1992; Francis,Tomkin, 1982).

At the Shamakhy Astrophysical Observatory named after N.Tusi is conducting a spectral study project of Algol-type stars from this subclass. Spectral observations will be carried out at the Cassegrain focus of 2-m telescopes of the Shamakhy Observatory over a period of time of the orbital period on a fiber-optic echelle spectrograph SHAFES, using a CCD matrix with a spectral resolution of R = 28000 and 56000 (Mikailov, 2020).

The following stars have been preliminary selected: δ Librae; U Sagittae; U Cephei; λ Tauri; EK Cephei; R Canis Majoris; V505 Sagittarii.

This paper presents preliminary results of spectral observations of two Algol-type stars belonging to this subclass: δ Lib and U Sge.

2. Observations and data processing

Spectral observations of the stars: δ Librae and U Sge were carried out at the Cassegrain focus of the 2-meter telescope of the Shamakhy Astrophysical Observatory named after N.Tusi, on the fiber echelle spectrograph ShaFES (Shamakhy Fiber Echelle Spectrograph) (Mikailov, 2020), using a CCD matrix, with a spectral resolution R = 28000, in the wavelength region $\lambda\lambda$ 3900–7500ÅÅ, in the years 2020-2023. Processing of echelle spectra was carried out according to the standard method using the new version of the DECH30 program developed by Galazutdinov (http://www.gazinur.com/ DECH software.html).

3. Results of observations

δ **Librae** (HR 5586, HD 132742, HIP 73473) is one of the nearest (≈90 pc) Algol systems a close, interacting binary made of A0V + K0IV stars with V ≈ 4.9 mag orbital period close to P = 2.327 days. The hotter and more massive star is A0 and it is on the main sequence; we will refer to it as star A. Its companion, which we call star B, is a cooler and less massive K0 subgiant filling its Roche lobe. Mass is being transferred from star B (the mass-donor) to star A (the mass-gainer).

Fig. 2 shows the radial velocity curve of the main and secondary components of the binary system δ Lib: Hα and Hβ are our measurements, others are borrowed from publications data. Phases computed with Koch's (Koch, 1962) ephemeris:

$$JD[Pr.Min.] = 2422852.3598 + 2.32735297E$$

U Sagittae (U Sge, HD181182): periods P=

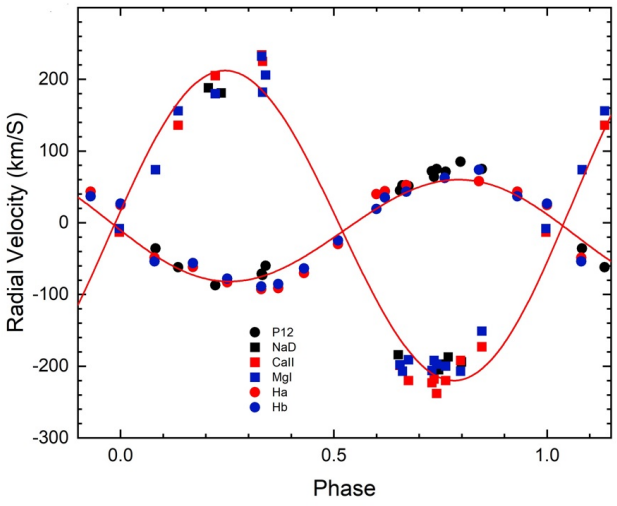

Figure 3: Velocity curves for the primary and secondary components of the U Sge Algol type binary system. **Primary component** full circles: black – P_{12} (Tomkin, 1978); red – Hα (ShAO); blue – Hβ (ShAO). **Secondary component** full rectangles: dark – DNaI; red – CaII; blue – MgI. (Tomkin, 1978)

3.381days, magnitude V=6.3 – 8.9, spectral types B7.5 (Pr.) – G4 III–IV (Sec.) or B8V (Pr.) – G2 III–IV (Sec.), orbital inclination 89^0, V_0 = –10 km/s, HJD min = 2440774.4856 (Olson, 1987).

Papameters: Primary component: M = 5.7 $M_\odot$, T = 12500 K, R= 4.20 $R_\odot$;

Secondary component: M = 1.9 $M_\odot$, T = 5500K, R= 5.50 $R_\odot$.

Fig. 3 shows the radial velocity curve of the primary and secondary component of the U Sge binary system: Hα and Hβ are our measurements, others are borrowed from publications data.

Orbital phases were calculated based on the ephemeris:

$$JD[Pr.Min.] = 2442207.8444 + 3.3806205E$$

borrowed from (Tomkin, 1979).

During the period of our spectral observations, both components of the KCaII resonance line are observed in the USge spectrum – interstellar (IS) and circumstellar (CS). Radial velocities (IS) of the KCaII component average (–23.6 km/s) in the phase range 0.1 – 0.5 and (–15.6 km/s) from 0.6-0.9. Fig. 4 shows the profiles of the KCaII line at close values of orbital phases on U Sge Algol type binary system. The radial velocities of the circumstellar (CS) and/or stellar components of the KCaII line correlate with the Hα line. Fig. 5 shows example the profiles Hα and KCaII lines in USge of Algol type binary star spectrum.

The fragments of Hα line region for 0.18, 0.19 and 0.62, 0.75 values of δ Lib binary system's orbital phases have been displayed on Fig. 6. As you see, the absorption element (depression) is being observed in the direction towards red of the Hα line at values 0.18 and 0.19 and towards violet at values 0.62 and 0.75.

As seen from the radial velocity curves provided at the Fig. 2 the lines of the secondary component of the system are not visible at the phase values 0.4 – 0.6 (Ondrejov and Roshen) or 0.35 – 0.7 (Tomkin). As observed, this phase interval corresponds to the period of the secondary component's eclipse (see Fig. 2).

Based on our measurements of the radial velocities of the lines Hα and Hβ and using published data, the radial velocity curves of both components of the U Sge system were constructed (Fig. 3).

In some phases of the orbital motion of the U Sge binary system, an absorption detail (depression) is observed on the red and blue wings of the line Hα.

Value of phases about 0.8 in the blue and about 0.3 the red wing of the absorption line Hα an additional absorption detail appears. As observed, phase interval [0.3 – 0.7] corresponds to the period of the secondary component's eclipse (see Fig. 6).

Fig. 6 shows for example fragments of Hα line region with additional absorption detail. Phase 0.05 corresponds to the eclipse of the primary component.

4. Conclusions

The radial velocity curves of both components of the δ Lib and U Sge systems were constructed based on our measurements of the radial velocities and are borrowed from publications data.

An absorption detail (depression) is observed on the red and blue wings of the Hα line in certain phases of the orbital motion of the binary systems δ Lib and U Sge. An additional absorption detail appears for δ Lib, at the orbital phases 0.18 and 0.19 in the red and at 0.62 and 0.75 in the blue wing of the absorption line, while for U Sge in value of phases about 0.3 in the red and about 0.8 the blue wing of the absorption line Hα. As inferred from Figs. 2 and 3, these phase intervals correspond to the eclipse period of the secondary component.

Thus, we are suggesting that this observational fact could indicate the presence of the third component in the system.

At the same time, we do not exclude alternative hypotheses that leads to similar physical conditions:

1. The Hα line are visible on the secondary component at the beginning and the end of eclipse.

2. The McLaughlin–Rossiter effect is rarely observed in Algol-type binaries systems.

All three hypothesis are the discussion topics of the Algol type binary system research. As more observation material is acquired, all three hypotheses will be widely researched and evaluated.

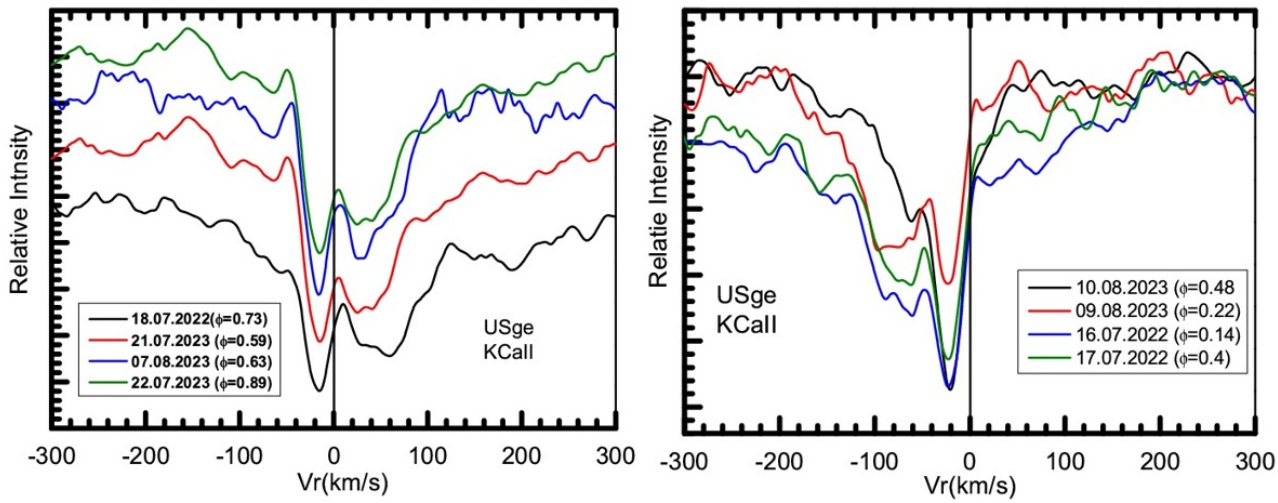

Figure 4: The profiles of the KCaII line at close values of orbital phases on U Sge of Algol type binary system

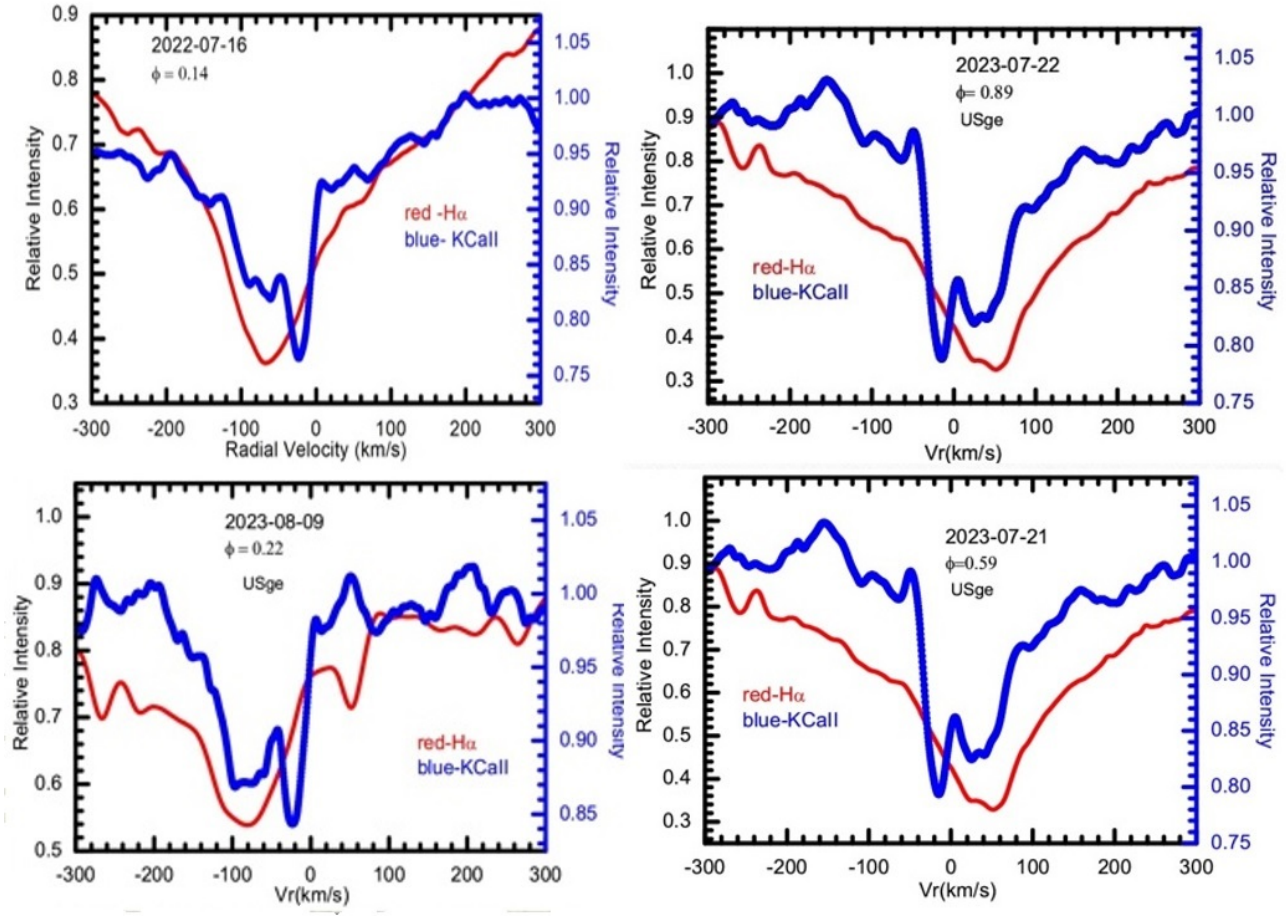

Figure 5: Example the profiles of the Hα and KCaII lines at close values of orbital phases on spectrum USge system

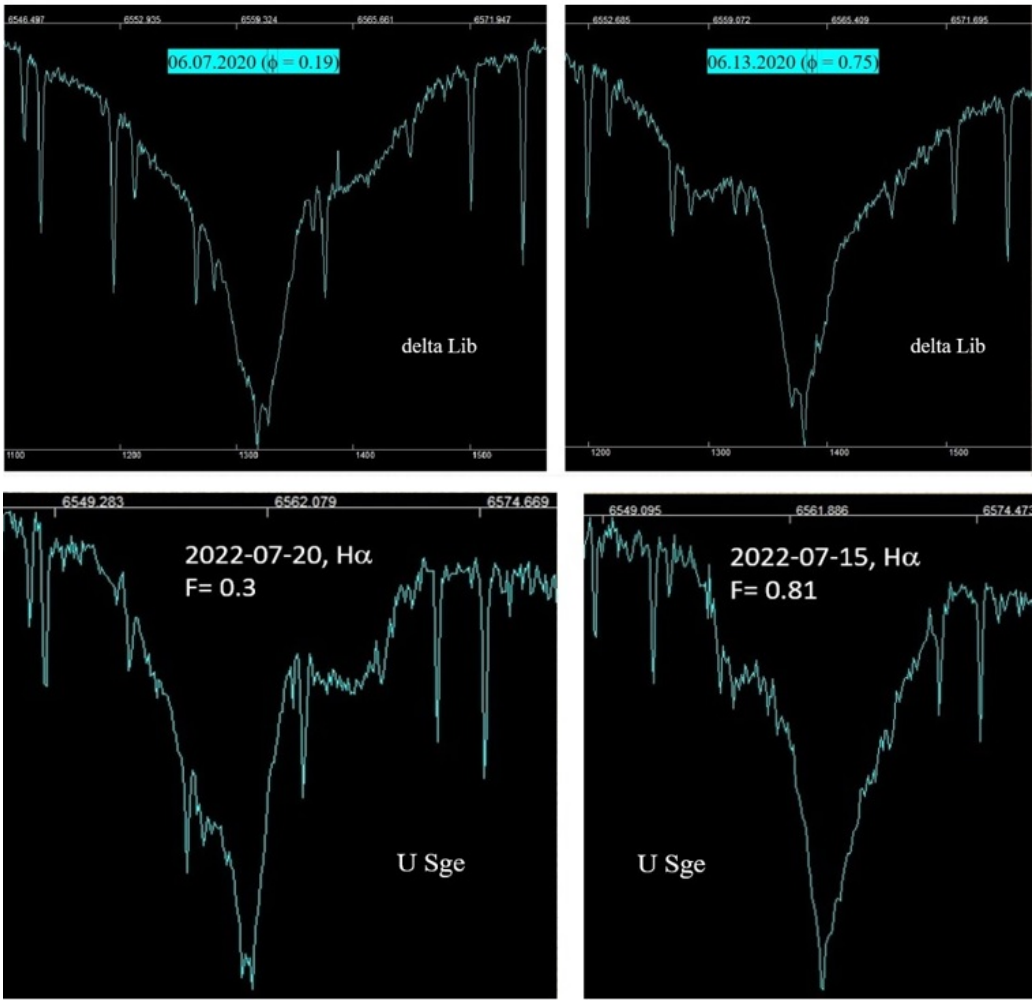

Figure 6: Examples from the fragments of Hα line region at the spectrum δ Lib and U Sge systems

References

Francis C., Fecal Jr., Tomkin J.: 1982, *ApJ*, **263**, 289-301.

Galazutdinov G.: 2007, http://www.gazinur.com/DECH software.html

Koch R.H.: 1962, *AJ.*, **67**, 130.

Mikailov Kh.M., Musaev F.A., Alekberov I.A., et al.: 2020, *KPCB*, **36**, 22.

Olson E.C., 1987, *PASP*, **97**, 731.

Tomkin J., 1978,*ApJ*, **221**, 608.

Tomkin J., 1979,*ApJ*, **231**, 409.

Tomkin J., 1981,*ApJ*, **244**, 546.

Tomkin J., 1983,*ApJ*, **271**, 717.

Tomkin J., 1985,*ApJ*, **297**, 250.

Tomkin J., 1992,*ApJ*, **387**, 631.

https://doi.org/10.18524/1810-4215.2024.37.314974

SPECTROSCOPIC STUDIES OF POLARIS: GETTING BACK TO NORMAL LIFE OF A CEPHEID?

I. A. Usenko,[1,2] A. S. Miroshnichenko,[3,4] S. Danford,[3] N. L. Vaidman,[4,5]
D. G. Turner,[6] D. J. Majaess,[7] S. V. Protsyuk[2]

[1] Astronomical Observatory, Odesa I. I. Mechnikov National University, Shevchenko Park, Odesa 65014, Ukraine *igus99@ukr.net*
[2] Mykolaiv Astronomical Observatory, Obsevatorna 1, Mykolaiv 54030, Ukraine, *procsys@gmail.com*
[3] Dept. of Physics and Astronomy, University of North Carolina at Greensboro, P.O. Box 261170, Greensboro, NC 27402, USA, *a_mirosh@uncg.edu; danford@uncg.edu*
[4] Fesenkov Astrophysical Institute, Observatory 23, Almaty, 50020, Kazakhstan
[5] Faculty of Physics and Technology, Al-Farabi Kazakh National University, Al-Farabi Ave. 71, Almaty, 050040, Kazakhstan, *nva1dmann@gmail.com*
[6] Dept. of Astronomy and Physics, Saint Mary's University 923 Robie Street, Halifax B3H3C3, Nova Scotia, Canada, *turner@ap.smu.ca*
[7] Mount Saint Vincent University,166 Bedford Hwy, Halifax NS B3M 2J6, Nova Scotia, Canada, *Daniel.Majaess@msvu.ca*

ABSTRACT. Based on 583 radial velocity (RV) measurements we obtained at the Three College Observatory (TCO, North Carolina, USA) in 2015–2024, (including 396 not previously analyzed from 2020–2024) as well as on 236 RV data from the German amateur R. Bücke (2011–2022), we calculated the pulsation period and amplitude of the Cepheid Polaris Aa system (α UMi). The analysis showed that the pulsation period was stable within a few minutes in 2020–2024. During this time, the pulsation amplitude was increasing and reached the 1960s level (4–6 km s^{-1}), when its sharp decline began. Since its new growth began after Polaris Ab, the system secondary component, passed a periastron, we concluded that the observed amplitude changes were due to its orbital motion. It is clear that Polaris Aa is returning to normal pulsating activity.

Key words: α UMi (Polaris Aa and Polaris Ab) system: radial velocities; Polaris Aa pulsation period and amplitude.

АНОТАЦІЯ. За десятирічний період спостережень системи Полярної (α UMi) в Обсерваторії трьох коледжів (Three College Observatory, Північна Кароліна, США) з 2015 по 2024 роки було отримано 583 оцінки радіальної швидкості (RV). Серед них маємо 396 нових, раніше не проаналізованих оцінок, отриманих у період 2020–2024 років. Цей набір RV, разом з додатковими 236 оцінками, що був отриманй німецьким аматором Р. Бюке у період 2011–2022 років, склав велику базу даних для розрахунку значень пульсаційного періоду та амплітуди радіальної швидкості цефеїди Полярної Aa. Як показав аналіз, період пульсації цефеїди виявився досить стабільним протягом кількох хвилин у 2020–2024 роках, але були деякі помітні зміни у 2015 та 2019 роках. Хоча з 2011 по 2019 рік амплітуда пульсації була нестабільною на рівні 3–4 км $с^{-1}$, але з 2020 року вона почала стабільно зростати і досягала вже 4–6 км $с^{-1}$. Такі значення амплітуди спостерігалися у 60-х роках минулого сторіччя, перед тим, як почалося її різке зниження. Оскільки це нове зростання почалося після того, як вторинний компонент системи Полярна Ab пройшов периастр орбіти, то ми дійшли до висновку, що ці спостережувані зміни амплітуди пульсації головного компонента були пов'язані з орбітальним рухом вторинного компонента. Цілком зрозуміло, що таким чином первинний компонент системи Полярна Aa повертається до нормальної цефеїдної пульсуючої активності, яка була майже 60 років потому.

Ключові слова: α UMi: Polaris Aa і Polaris Ab; радіальні швидкості; період пульсації Polaris Aa; амплітуда.

1. Introduction

In our previous paper (Usenko et al. 2020), we used 187 measurements of the Polaris radial velocity (RV), obtained between September 2015 and April 2020 at the TCO observatory, together with a number of observations from Anderson (2019), to study variations of the pulsation period and amplitude of the Cepheid Polaris Aa. In fact, all these 351 measurements turned out to be a unique set of data (excluding amateur observations) taken between 2011 and 2020. This time interval is interesting and important as it covers a fragment of the orbit of the Polaris Ab companion that contains passages through periastron and ascending node. Analysis of the RV data showed that the average pulsation period in 2015–2020 demonstrates a certain stability, and the amplitude of Polaris Aa pulsations demonstrates very strong changes showing an increase to HJD 2457350 followed by a decrease, which began even before the periastron passage. As can be seen in Fig. 7 from Usenko et al. (2020) and Fig. 7 from Torres (2023), the pulsation amplitude changes over these 9 years followed a sinusoidal curve, which gave a reason to make a forecast of the future decrease of the amplitude beyond 2020. These amplitude changes were explained by the influence of the orbital motion of the secondary component, Polaris Ab. Such amplitude changes suggested further careful observations of the Polaris system RVs.

However Torres (2023) added RV measurements from low-resolution spectra obtained by the German amateur Roland Bücke in 2011–2022. It is noticeable In Fig. 7 from his paper that the pulsation amplitude between Spring 2020 and Spring 2023 suddenly increased by ≈ 0.75 km s^{-1}, which is the opposite to our predictions. To test this important fact, we decided to use data from our observations carried out at TCO from July 2020 to April 2024. Additionally, our new RV measurements can be used for refining the orbit of Polaris Ab.

2. Observations and development of spectra

We use 396 spectra in the current data set: 74 were taken in July–December 2020, 106 in January–December 2021, 50 in January–May 2022, 24 in September–November 2022, 14 in January–May 2022, 87 in July–December 2023, and 41 in January–April 2024. All the observations were obtained with the 0.81 m telescope of the Three College Observatory (TCO) in North Carolina. This telescope is equipped with an échelle spectrograph manufactured by Shelyak Instruments [1]. The instrument operates in a spectral range from 3850 to 7900 Å with a spectral resolving power of $R \approx 12{,}000$ and no gaps the between 31 spectral orders. The average S/N ratio in the continuum was 150–200, while most spectral lines used in our analysis were taken from the range 4900–6800 Å. The data were reduced with the *échelle* package in IRAF. Additionally, we use 236 spectra provided to us by Roland Bücke, who used a 0.2 m and a 0.45 m telescopes and a self-built long-slit spectrograph ($R = 3,500$) in 2011–2022[2]. Some results of the latter program were published in Bücke (2021).

To measure the RVs, cross-correlation was used in the wavelength ranges of 5045–5388 Å of the TCO spectra and 6035–6425 Å of the Bücke spectra. Since the total number of derived RV (396 and 236) does not allow for their publication here, they will be published separately.

3. Pulsation, amplitudes and orbital period analysis

In our previous studies, the spectral line positions were measured using the DECH 30 software package[3] by matching original and mirrored profiles for over 100 lines. Typical RV measurement errors with this procedure were 1.0–1.8 km s^{-1}. In this study we used the IRAF package *rvsao* to calculate RVs from continuum-normalized several spectral orders connected together with removal the order parts, which have the lowest signal-to-noise ratios (edges). The relative RVs were calculated with cross-correlation with respect to the spectrum, which was taken chronologically first (2013/07/28 in the TCO data and 2011/02/21 in Bücke's data).

TCO spectra were taken in 10-20 individual 10–20 second-long exposures and summed up, while Bücke's spectra consisted of 4–6 individual 4–5 minute-long exposures. Typical RV measurement errors were 0.05–0.10 km s^{-1} for the TCO data and 0.4–0.5 km s^{-1} for Búcke's data.

The measurement results were then grouped into yearly (TCO) or 2/3–year (Bücke) data sets that are larger than in our previous studies. The data sets were analyzed using a *python* code that calculates best sinusoidal fits to the data as well as uncertainties of the fit parameters (semi-amplitude, period, mean RV, and zero-point of the pulsation phase). The fitting procedure was implemented using the Monte Carlo method on Markov chains which produces many subsamples of each fitting parameter and allows deriving their most probable value and statistical uncertainty (Foreman-Mackey et al. 2013). The fitting results are shown in Tables 1 and 2, while examples of the fits are shown in Figs. 1 and 2.

[1] http://www.shelyak.com

[2] https://www.astro.buecke.de

[3] http://gazinur.com/DECH-software.html

Table 1: Pulsational periods and amplitudes of Polaris Aa in 2015–2024. TCO data.

Year	HJD 2400000+	N	Rej	Period days	σ days	Ampl km s^{-1}	σ km s^{-1}
2015	57283–57376	20	1	3.9781	0.0014	3.42	0.08
2016	57623–57744	36	0	3.9659	0.0062	3.96	0.14
2017	57772–58109	37	3	3.9713	0.0023	3.70	0.06
2018	58120–58479	46	3	3.9711	0.0004	4.04	0.04
2019	58489–58837	28	2	3.9802	0.0036	3.84	0.20
2020	58907–59213	44	1	3.9713	0.0012	3.76	0.04
2021	59219–59575	124	3	3.9750	0.0005	4.34	0.16
2022	59583–59892	76	0	3.9721	0.0004	4.27	0.08
2023	59950–60310	97	0	3.9713	0.0005	5.02	0.04
2024	60314–60416	44	0	3.9715	0.0009	4.24	0.02

N – number of RV measurements, Rej – number of data points rejected from fitting, Period – pulsation period, Ampl – pulsation amplitude, σ – standard deviation of the corresponding parameter from the best-fit

Table 2: Pulsational periods and amplitudes of Polaris Aa in 2011–2022. Bücke data.

Year	HJD 2400000+	N	Rej	Period days	σ days	Ampl km s^{-1}	σ km s^{-1}
2011/02–2014/05	55624–56780	43	0	3.9734	0.0004	3.72	0.11
2014/08–2016/09	56895–57639	44	0	3.9722	0.0004	4.25	0.02
2016/09–2017/09	57657–58001	41	0	3.9720	0.0016	3.28	0.39
2017/10–2019/04	58033–58595	45	0	3.9717	0.0009	3.49	0.45
2019/07–2022/12	58688–59905	63	0	3.9730	0.0003	4.02	0.03

Column information is the same as in Table 1

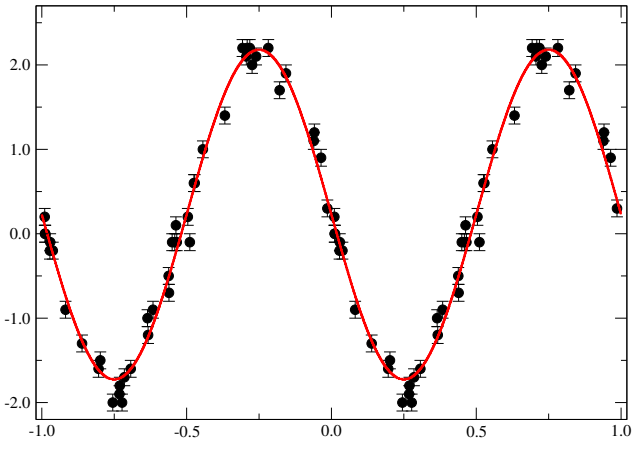

Figure 1: RVs measured from the 2024 TCO data and the best fitting sinusoidal approximation.

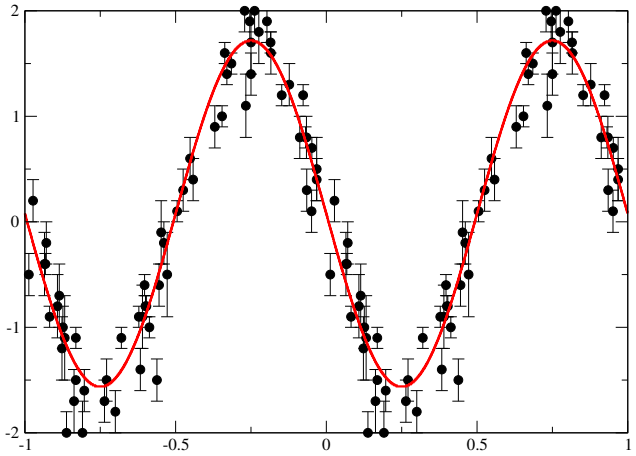

Figure 2: RVs measured from the 2019–2022 Búcke's data and the best fitting sinusoidal approximation.

The data sets analysis shows that the pulsation period of Polaris Aa was stable within 4.7 minutes (3.9733±0.0033 days), while the amplitude has been rising from ≈3.5 km s^{-1} to ≈3.5 km s^{-1} in 2011–2024. The average period is very close to that derived by Torres (2023), but a slight decrease predicted in this paper (see Fig. 6 there) is not obvious given the measurement uncertainties. The amplitude increase is consistent with the data shown in Fig. 9 from Torres (2023) and Fig. 4 from Bücke (2021). Our results are shown in Fig. 3.

Another result from our current study is the extension of the Polaris Aa/Ab binary orbit to the middle of 2024 (see Fig. 4). The relative TCO and Bücke's RVs were shifted to the heliocentric values

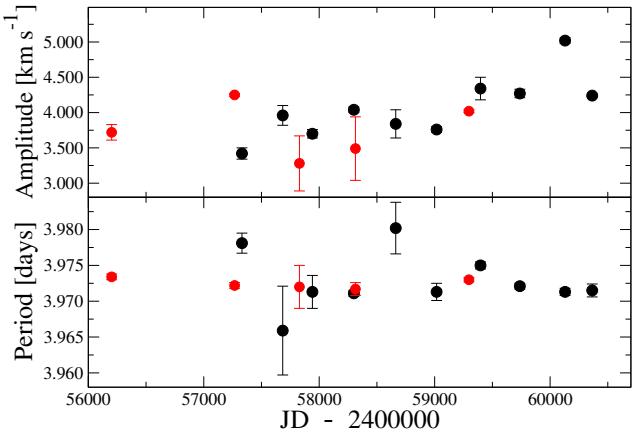

Figure 3: Variations of the pulsational amplitude (top panel) and period (bottom panel) of Polaris Aa. Symbols: black circles – TCO data, red circles – Bücke's data.

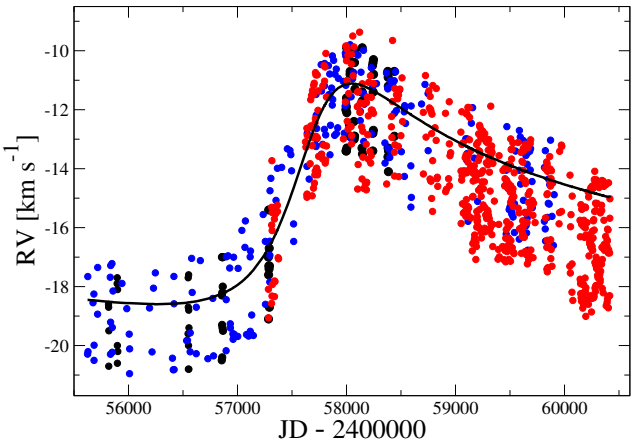

Figure 4: Updated orbit of the Polaros Aa/Ab binary system. Black circles represent data from Anderson (2019), blue circles show Bücke's data, and red circles show TCO data. Black solid line shows the orbital solution derived by Torres (2023), while the violet solid line shows the solution from Usenko et al. (2020).

from Anderson (2019) and compared to the orbital solution derived by Usenko et al. (2020) and Torres (2023). The comparison shows the RVs obtained after the last maximum achieved in 2017 decline faster than predicted. Since this orbital cycle is getting better and more accurately covered, it is important to continue monitoring the system to further improve the orbit and thus the system physical parameters.

5. Conclusions

The 583 RV observations obtained at TCO during the last ten years along with 164 RV data points published by Anderson (2019) and 236 ones obtained by Bücke (overall 983 measurements) covered a fragment of the Polaris Ab orbit, which contained passages through a periastron and an ascending node led us to the following conclusions.

1. The mean pulsational period during last four years has been stable within several minutes.

2. As mentioned earlier, the pulsation amplitude of Polaris Aa shows strong changes, which contain a growth before JD 2457350 with a subsequent decline. This decline has begun before the periastron passage, but the amplitude began increasing since 2021.

3. Our prediction (Usenko et al. 2020) that the pulsation amplitude would decrease after 2020 was wrong probably due to a different method of the data analysis. Apparently, after Polaris Ab passed the last periastron, the pulsation amplitude of the Polaris Aa Cepheid returns back to the pre-1960's level of 4 to 6 km s^{-1} (see Fig. 7 from Torres 2023).

4. Thus, we can assume that Polaris Aa is returning to the normal pulsating life of Cepheids. Therefore further Polaris Aa RV observations are essential during next coming years.

5. Orbital motion of Polaris Ab most likely influences the Polaris Aa pulsational amplitude.

References

Anderson R.I.: 2019, *A&A* **623**, A146.
Bücke, R.: 2021, *BAV Magazine Spectroscopy* **9**, 43.
Foreman-Mackey, D., Hogg, D. W., Lang, D., & Goodman, J.: 2013, *PASP* **125**, 306.
Torres, G.: 2023, *MNRAS* **526**, 2510.
Usenko I.A., Miroshnichenko A.S., Danford S., Kovtyukh V.V., Turner D.G.: 2020, *OAP* **33**, 65.

https://doi.org/10.18524/1810-4215.2024.37.314768

INVESTIGATION OF THE RADIOACTIVE PROMETHIUM LINES IN STELLAR SPECTRA

V. A. Yushchenko[1,2], V. F. Gopka[2], A. V. Yushchenko[3], Ya. V. Pavlenko[1], A. V. Shavrina[1], A. Demessinova[4], S. V. Vasilieva[2]

[1] Main Astronomical Observatory of the National Academy of Sciences of Ukraine, 27 Akademika Zabolotnoho St, Kyiv, 03143, Ukraine

[2] Odesa I. I. Mechnikov National University, the Scientific Research Institute "Astronomical Observatory", 1v Marazliivska St, Odesa, 65014, Ukraine; *vladimiryushchenko@gmail.com*

[3] Astrocamp Contents Research Institute, Goyang, 10329, Republic of Korea

[4] Al-Farabi Kazakh National University, Faculty of Physics and Technology, Almaty, 0500640, Republic of Kazakhstan

ABSTRACT. Eleven lines of promethium Pm II in the spectra of the magnetic peculiar A0 V star HD 25354 were analysed thoroughly in order to obtain information about how the short-lived element lines behave in spectra acquired on different observation dates. It has turned out that the intensity variations in time are typical for these lines with some of them being observed as emissive or absent at certain time intervals. The obtained list of Pm II lines in the spectra of the magnetic peculiar star HD 25354 has been employed to investigate promethium abundances in atmospheres of other stars, such as HR 465 (T_{eff} = 111,840 K), HIP 13962 (T_{eff} = 6,250 K) and BL 138 (T_{eff} = 3,939 K). The investigation interval has been limited to the spectral range of 4000–5800 Å and oscillator strengths within $-0.76 < \log gf < 0.4$.

Keywords: stars: abundances – promethium: atmospheres – stars: individual (HD25354, HR465, HIP13962, BL138).

АНОТАЦІЯ. Досліджується вміст радіоактивного прометію в атмосферах зір в діапазоні ефективних температур від 12800 до 4000 К, а саме: в атмосферах магнітно-пекулярних зір HD 25354 і HR 465, цефеїди HIP 13962, червоного гіганту BL 138, що належить кулястій карликовій галактиці Форнакс. Період піврозпаду найтривалішого ізотопу 17.7 років серед 24 нестабільних ізотопів прометію – цей факт привів до упередженого дослідження цього елементу в спектрах зір. З появою сил осциляторів для прометію, розрахованих Фіветом та ін. в 2007 році, з'явилась можливість дослідити кількісно цей елемент по відношенню до атомів водню в атмосферах зір. Першими оцінили Нієльсен та ін. (2020) вміст прометію в атмосфері магнітно-пекулярної зорі HR465, який виявився досить високим – трохи менше 5 dex. Дана робота є першою роботою, яка детальним чином досліджує лінії прометію в спектрах зір з використанням синтетичного спектру зір після детального дослідження параметрів їх атмосфер та хімічного складу стабільних елементів. Лінії прометію розглядались лиш ті, які не є блендованими іншими лініями. Для спостереження ліній прометію PmII в спектрах більш гарячих зір вміст прометію повинен бути більшим, ніж в спектрах холодних зір. Діапазон вмісту прометію від 6 dex до –0,5 dex при температурах атмосфер 12800 і 4000 К. Еквівалентні ширини не перевищують 20 міліангстрем в спектрах зір. Дана робота стимулює дослідження сил осциляторів в більш широкому діапазоні спектрів та більш низьких значень.

Ключові слова: зорі: кількість – прометій: атмосфера – зорі: індивідуальні (HD25354, HR465, HIP13962, BL138).

1. Introduction

Promethium is the only unstable element among lanthanides. The isotope ^{145}Pm is the longest-lived one with a half-live of only 17.7 years. Like other radioactive elements with short half-lives, promethium is not an element necessarily observed in stellar atmospheres. An active mechanism of replenishment of this element is a precondition for its observing in a spectrum, and it is most likely that such a production mechanism should not be the only one. Scenarios according to which promethium is likely to be produced in amounts sufficient for its spectral observability were considered in the study (Tjin et al., 1973), including scenarios of production of this element in the atmosphere of a binary star with a pulsar companion that emits high-energy particle fluxes to the target star. This scenario is corroborated by the case of the Cepheid HIP 13962, a former binary companion of a pulsar in the system that decayed just 3 million years ago, which is a too short period of time on the scale of the star's lifespan. Weak lines of the radioactive actinium with a short half-life can be observed in the star's spectra (Gopka et al., 2022). Identification of promethium lines in the spectra of HIP 13962 is an important substantiation of such a scenario.

According to the review of literature made in the study (Yushchenko et al., 2024), HD 25354 is an X-ray triple system made of three objects, including an additional 0.7 solar mass tertiary component separated by 2.246 AU with a period of orbit of 1.5–2 years about the centre of mass of the system that consists of the main component – HD 25354 – and a 1–2 solar mass invisible secondary component separated by 0.3 AU with an orbital period of 26 days. In this system of the main and secondary components a scenario of the radioactive enrichment of the HD 25354 atmosphere through the activity of the neutron star is not ruled out either. It bears reminding that the neutron star (pulsar) has a mass of about 1.4 solar masses and a diameter not greater than 30 km, which is in agreement with the observed characteristics of the invisible component.

This paper vividly demonstrates manifestation of the short-lived promethium lines in the spectra of HD 25354 obtained on two straight nights in 2006 as compared to the lines in the spectrum dated 1996 from the ELODIE archive (http://atlas.obs-hp.fr/elodie/). Each line with the maximum Pm contribution has been analysed, and the respective results are illustrated below. It allows us to avoid misunderstanding when using spectra obtained on other observation dates, for which the spectral pattern is different. Let us recall that the spectral lines intensity variations are typical for HD 25354, which was first reported by Babcock (1958). In order to compare promethium abundances in the atmospheres of cooler stars, we have considered the late-type red giant BL 138 with an effective temperature T_{eff} = 3,939 K that is located in the centre of the Fornax dwarf spheroidal galaxy, which is the most massive satellite galaxy of the Milky Way at twice the distance to the Magellanic Clouds.

2. Investigation of the radioactive promethium lines in the spectra of the atmospheres of HD 25354, HR 465 and BL 138

Promethium lines in the stellar spectra were identified based on the comparison of the synthetic spectrum with the observed one, having thoroughly examined parameters and chemical composition of the respective stellar atmospheres. Having employed the oscillator strengths for promethium lines determined in the study (Fivet et al., 2007), we identified promethium lines with the maximum contribution. The synthetic spectrum was calculated using the parameters found in our earlier study from the HD 25354 spectra covering the wavelength range of 4000–5800 Å: the effective temperature T_{eff} = 12,800 K; the surface gravity log g = 4.0; microturbulent velocity v_{mi} = 0.5 km s^{-1}, and chemical abundances as reported (Yushchenko et al., 2008) in the first approximation. We used the spectra obtained by Faik Adil oglu Musayev on two straight nights in 2006 – namely, on the nights of November 28 to November 29 and that one of November 29 to November 30 – with a 2-meter telescope at the Terskol Peak Observatory, as well as the ELODIE archive spectra acquired in 1996 at the Haute-Provence Observatory (OHP). Some lines in the spectra available exhibit profile and intensity variations even over two straight observation nights. However, the greatest variations can be observed in the spectrum obtained at OHP in 1996 that has narrow and sharp lines. Spectra acquired at the Terskol Peak Observatory in 2006 can be distinguished by their broad lines in which narrow emission lines of various intensities, sometimes strong ones, appear. The description of the spectral lines, given earlier in the study (Jaschek&Brandi, 1972) upon the analysis of two spectrogram plates obtained one month apart in 1957, has been completely borne out. We identified 11 absorption lines of promethium in the spectra of HD 25354 and determined the atmospheric promethium abundance. The magnetic peculiar star HR 465 (T_{eff} = 11,840 K; log g = 4.3; v_{mi} = 1.66 km s^{-1} as per (Fivet et al., 2007) and the red giant BL 138 (T_{eff} = 3,939 K; log g = 0.71; v_{mi} = 2.3 km s^{-1}, and the metallicity [Fe/H] = –1.01) were used to make a comparison of the respective promethium abundances with that one in the atmosphere of HD 25354 with T_{eff} = 12,800 K. We used the spectrum of BL 138 obtained by Letarte et al. (2010) with FLAMES multi-object instrument connected to GIRAFFE spectrograph with the high-resolution setups at the European Southern Observatory's (ESO) Very Large Telescope (VLT). The observation was performed with a spectral resolving power R = 30,000 in the wavelength ranges 5339–5608, 6119–6397 and 6308–6689 Å with a signal-to-noise ratio from 30 to 100 at different wavelengths.

Now let us consider fragments of the spectra of HD 25354 and BL 138 in the region of promethium lines. In this study, we used in-process fragments of spectra from the URAN software system (Yushchenko, 1998). The methods and techniques of investigation of promethium lines in the spectra of HIP 13962 are similar to those employed in the study of actinium lines (Gopka et al., 2022).

The results of the investigation of promethium lines in the respective spectra of HD 25354, HR 465, HIP 13962 and BL 138 are given in the Table. The first column presents the identified wavelengths of the Pm II lines. The second column shows the degree of ionization (61.01) of the lines that have been investigated. The third and fourth columns give oscillator strengths and energies of lower levels for each line. Equivalent widths for the observations from the ELODIE archive and those obtained at the Terskol Peak Observatory are listed in the fifth and sixth columns, respectively; likewise, promethium abundances determined from those observations are given in the seventh and eight columns, respectively. The ninth and tenth columns present the promethium abundance in the atmosphere of HD 25354 determined through the synthetic spectrum technique from the mean of either four or two observed spectra obtained at the Terskol Peak Observatory and the percentage of promethium at the corresponding line wavelength, respectively.

We obtained the following mean promethium abundances: log N(Pm) = 5.80 ± 0.15 and log N(Pm) = 5.91 ± 0.12 for the observations at OHP and Terskol Peak Observatory; and log N(Pm) = 5.84 ± 0.16 for the observations at the Terskol Peak Observatory using the synthetic spectrum technique. Further, the Table shows the results of our investigations of the promethium abundance in the Cepheid HIP 13962 log N(Pm) = –0.37 ± 0.15, and the mean Pm abundance in BL 138 log N(Pm) = –0.54 ± 0.12.

The results of our investigations of promethium in the atmosphere of HR 465 with the parameters from the observations at Bohyunsan Optical Astronomy Observatory

(BOAO) reported in (Fivet et al., 2007): T_{eff} = 11,840 K, log g = 4.3 and v_{mi} = 1.66 km s^{-1}, are presented lower in the Table. The mean promethium abundance is log N(Pm) = 5.05 ± 0.01.

Further, the Table shows the results of our investigations of the promethium abundance in the Cepheid HIP 13962 log N(Pm) = –0.37 ± 0.15, and the mean Pm abundance in BL 138 log N(Pm) = –0.54 ± 0.12.

3. Conclusions

This paper presents an analysis of the lines of the radioactive short-lived promethium Pm II whose longest-lived isotope ^{145}Pm has a half-life of only 17.7 years. We consider spectra of magnetic peculiar stars HD 25354 and HR 465, the Cepheid HIP 13962, a former binary companion of a pulsar in the system that decayed just 3 million years ago, and the late-type red giant BL 138 that along with BL 148 are located in the centre of the Fornax dwarf spheroidal galaxy, which is the most massive satellite galaxy of the Milky Way at twice the distance to the Magellanic Clouds.

As expected, promethium lines can be distinguished by the intensity variations in time. Promethium lines at a wavelength of 5561.73 Å are observed in the spectra within a broad spectral range with T_{eff} from 12,800 K to 4.000 K. Promethium abundances in hotter stars are higher than those in the atmospheres of late-type stars. If the promethium line identification is only performed based on the coincidence of the line wavelengths in the stellar spectra with the laboratory ones, then the number of such lines beyond the wavelength of 5800 Å would be considerably greater. When determining stellar abundances of promethium, Pm lines beyond the wavelength of 5800 Å are not observed in synthetic spectra, but they can be identified in actual spectra, which may indicate the necessity to correct the oscillator strengths used.

References

Babcock H.W.: 1958, *ApJ*, **128**, 228.
Fivet V., et al.: 2007, *MNRAS*, **380**, 771.
Gopka V.F., et al.: 2022, *KPCB*, **38**, 100.
Jaschek M., Brandi E.: 1972, *A&A*, **20**, 233.
Letarte B., et al.: 2010**,** *A&A*, **523**, A17.
Nielsen K.G., Carpenter G.V., Kober K.E., Wahlgren G.M.: 2020, *ApJ*, **899**, 166.
Tjin A Djie H.R.E., Takens R.J., van der Heuvel E.P.: 1973, *ApL*, **13**, 215.
Yushchenko A.V.: 1998, *vsr. conf.*, 201.
Yushchenko V.A., et al.: 2024, *Galax*, **12**, 57.
Yushchenko V.A., et al.: 2008**,** *OAP*, **21**, 153.

Analysis of the HD 25354 spectral lines at the Pm wavelength of 4137.95 Å

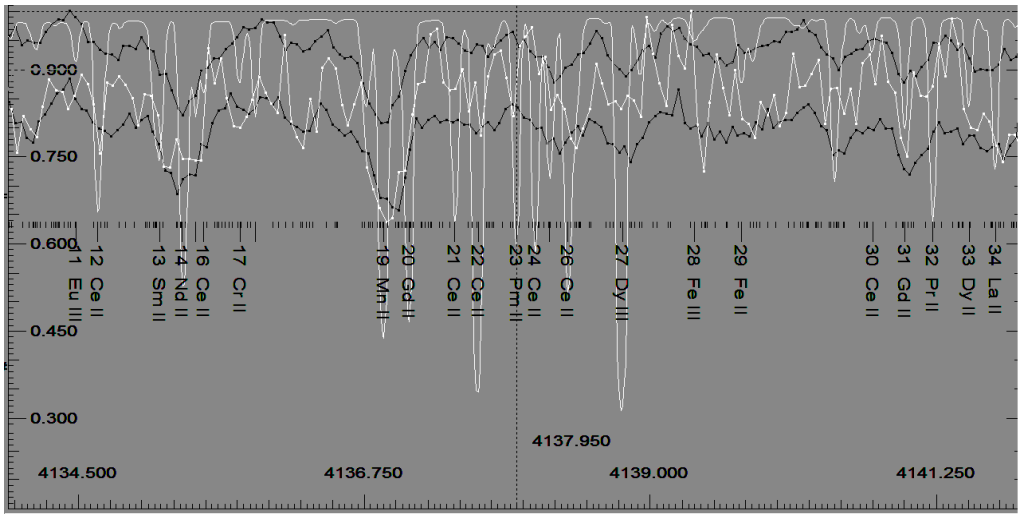

Figure 1: A fragment of the HD 25354 spectra obtained at the Terskol Peak Observatory, which are depicted in black colour. The upper spectrum was obtained on the second observation night – from November 29 to November 30, 2006 – while the lower one was acquired on the first night – from November 28 to November 29, 2006. The spectrum obtained at OHP is shown in white colour; in this spectrum, the promethium line is identified at a wavelength of 4137.95 Å, and the lines are sharp. The equivalent width is 16.2 mÅ, which corresponds to log N(Pm) = 5.69. In the spectra obtained at the Terskol Peak Observatory there is no Pm line at a wavelength of 4137.95 Å. As is seen, compared to the spectra obtained at the Terskol Peak Observatory, the spectrum from the ELODIE archive has stronger lines of other lanthanides, which are represented in the spectra by sharp lines (Ce II, Gd II, Dy II and La II).

For comparison, the promethium abundance in the atmosphere of HR 465 log N(Pm) = 5.0 at a wavelength of 4137.95 Å was determined from the spectra at the phase of stronger lanthanide lines with an equivalent width W = 12 mÅ and the following atmospheric parameters: T_{eff} = 11,840 K; log g = 4.3, and v_{mic} = 1.66 km s^{-1} (Fivet, 2007).

The line 4137.95 Å was used in the study by (Nielsen et al., 2020) to determine the promethium abundance, which yielded log N(Pm) < 4.2 and log N(Pm) < 4.9 at ϕ = 0.68 and 0.85 of the spectroscopic period, respectively, over the 21.5-year period.

Analysis of the HD 25354 spectral lines at the Pm wavelength of 4157.86 Å

Figure 2 represents the general appearance of the spectra in the region of the promethium line at 4157.86 Å. There are no absorption lines of promethium in the middle spectrum (obtained at OHP), the lines are sharp. Two lower spectra of HD 25354 were acquired on the first observation night – from November 28 to November 29, 2006 – at the Terskol Peak Observatory; they were recorded in the observation log as HD 25354-2181 and HD 25354-2182. Two upper spectra were obtained on the second observation night – from November 29 to November 30, 2006 – at the Terskol Peak Observatory; they were recorded in the observation log as HD 25253-2191 and HD 25354-2192.

The appearance of the spectra changed within the space of two straight nights: there is a strong emission line in the first observation at the Terskol Peak Observatory (HD 25354-2181), and then there is an emission line in the second observation on the first night as well, but it is weaker.

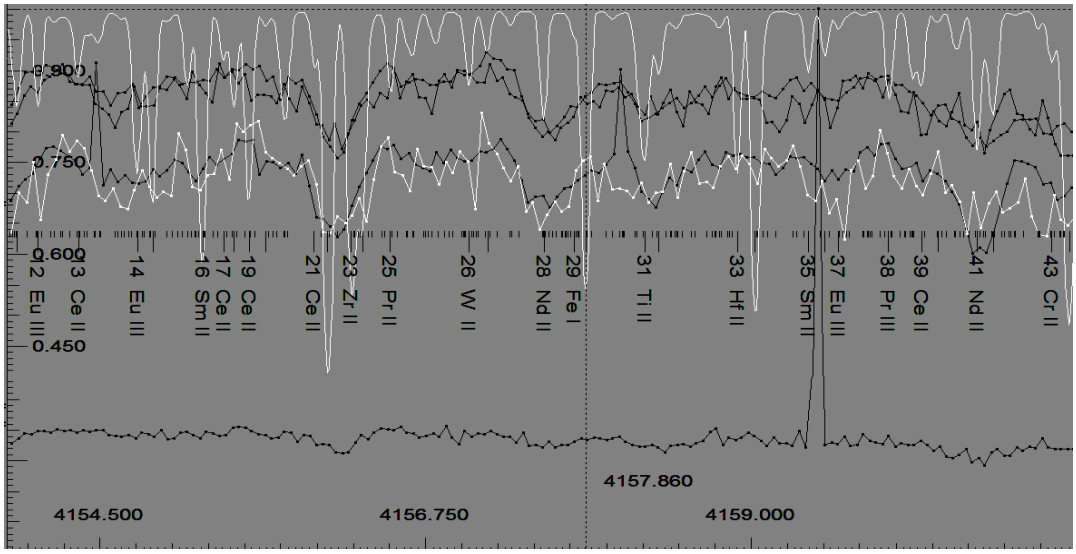

Figure 2a: An in-process fragment of spectra (from the URAN soft system (Yushchenko, 1998) taken when investigating the Pm line at 4157.86 Å in the spectra of HD 25354; it confirms the spectral line description given by (Jaschek & Brandi, 1972). In the spectrum obtained at OHP, plotted in white colour, the promethium line has not been identified. Th mean of the spectra obtained at the Terskol Peak Observatory was employed to determine the promethium abundance using a synthetic-spectrum technique.

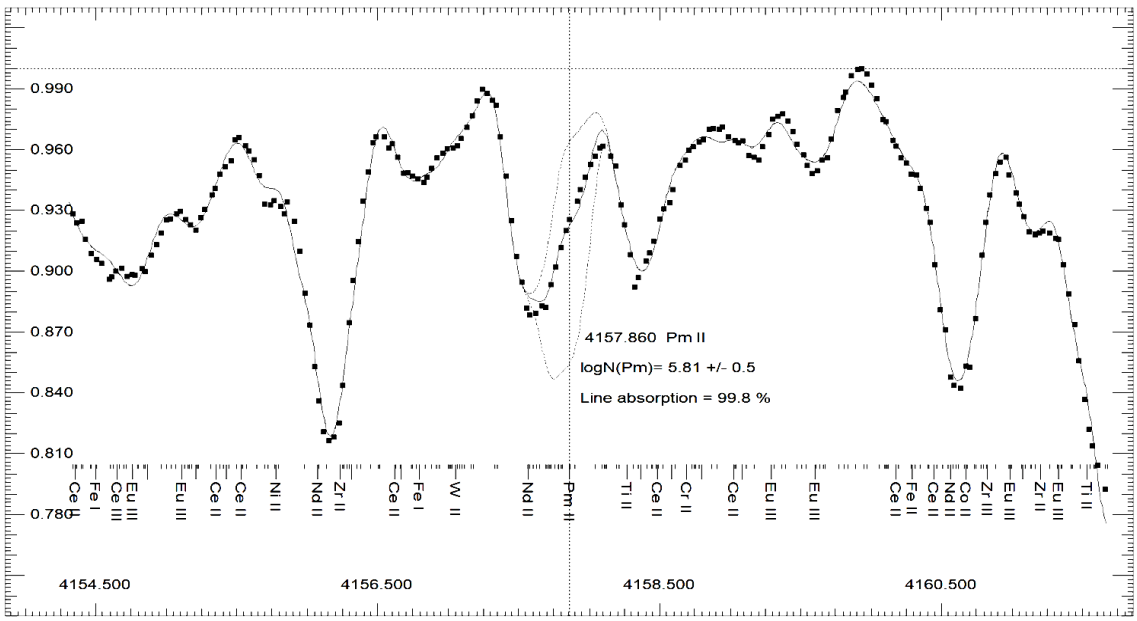

Figure 2b: The promethium abundance in the atmosphere of HD 25354 from the spectrum representing the mean of four observations at the Terskol Peak Observatory was determined through a synthetic-spectrum technique and equal to log N(Pm) = 5.81 ± 0.5. The percentage of promethium at a wavelength of 4157.86 Å is 99.8%, with the emission lines being excluded. The figure shows chemical elements for which the percentage is greater than 50%.

Analysis of the HD 25354 spectral lines at the Pm wavelength of 4186.03 Å

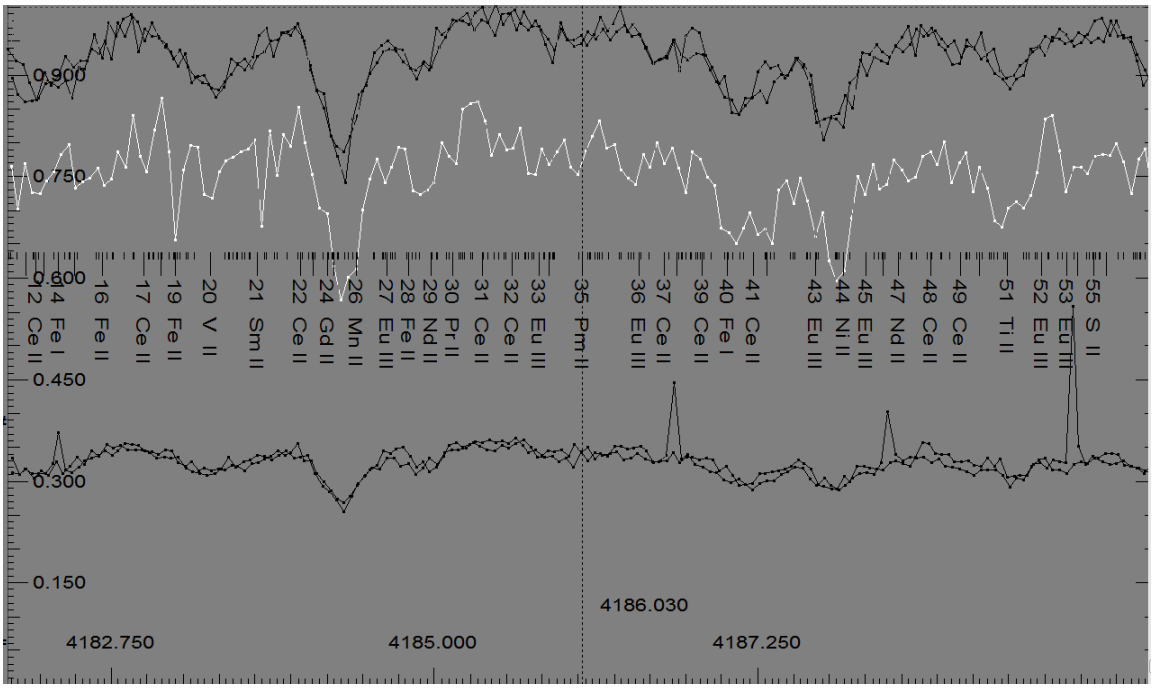

Figure 3a: The observed spectra in the region of the Pm II line at 4186.03 Å. The spectra are shifted relative to each other along the Y axis similar to Fig. 1. Narrow emission lines can be observed within the broad lines of the spectra obtained on the first observation night at the Terskol Peak Observatory. The Pm II line at 4186.03 Å in the spectrum dated 2005 has an equivalent width W = 17 mÅ, which corresponds to the Pm abundance log N(Pm) = 5.94 on the hydrogen scale log N(H) = 12. In the spectrum obtained on the second observation night at the Terskol Peak Observatory, recorded in the observation log as HD 25354-2192, which is best approximated by the Gaussian distribution, the promethium line has an equivalent width W = 16.4 mÅ, which corresponds to the Pm abundance log N(Pm) = 5.91.

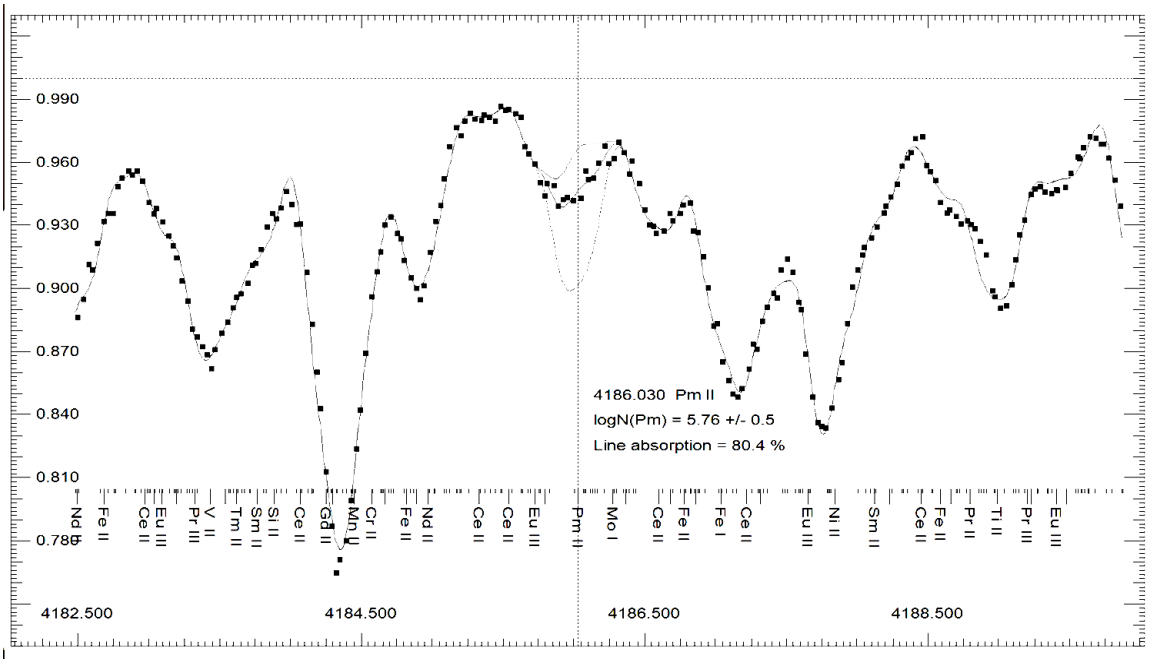

Figure 3b: Using the mean of four HD 25354 spectra obtained at the Terskol Peak Observatory, we determined the promethium abundance log *N*(Pm) = 5.76 from the Pm II line at 4186.03 Å with the promethium percentage of 80.4%.

Analysis of the HD 25354 spectral lines at the Pm wavelength of 4216.31 Å

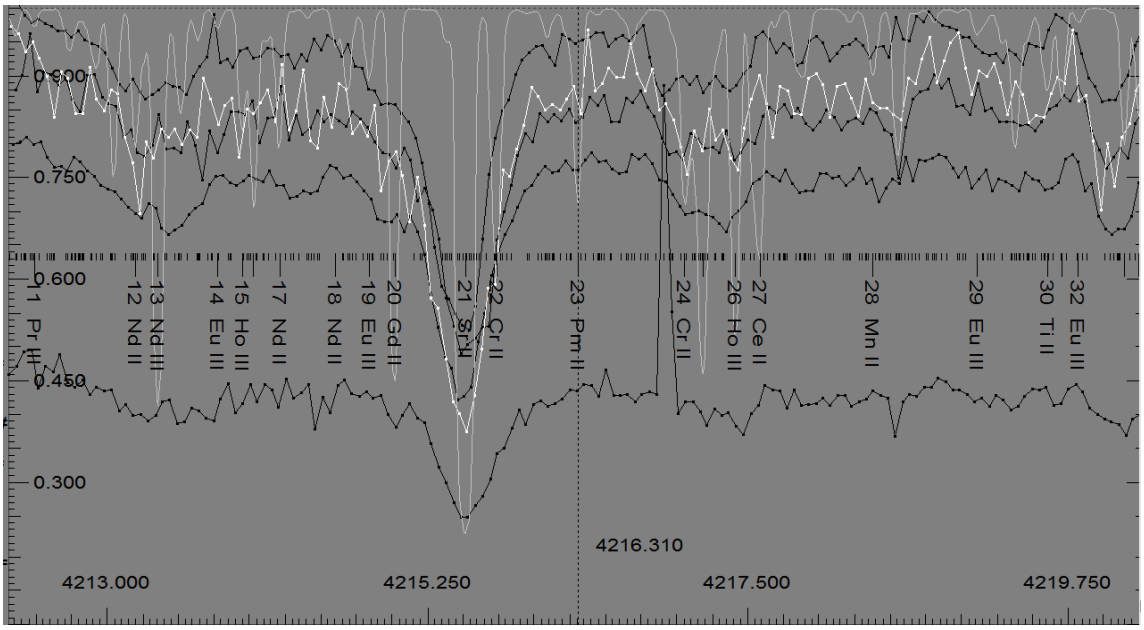

Figure 4: The spectrum obtained at OHP is depicted in white colour; it exhibits sharp and narrow lines. The equivalent width of the promethium line (λ 4216.31 Å) is 9.8 mÅ, which corresponds to the Pm abundance log N(Pm) = 5.60. From the spectrum obtained during the last observation at the Terskol Peak Observatory, recorded in the observation log as HD 25354-2192, the equivalent width W = 11.2 mÅ, which corresponds to log *N*(Pm) = 5.67.

For comparison, the promethium abundance in the atmosphere of HR 465 log N(Pm) = 5.08 at a wavelength of 4216.31 Å (W = 4 mÅ) was determined from the spectra at the phase of stronger lanthanide lines with an equivalent width W = 9 mÅ and the following atmospheric parameters: T_{eff} = 11,840 K; log *g* = 4.3, and v_{mic} = 1.66 km s^{-1} (Fivet, 2007).

Analysis of the HD 25354 spectral lines at the Pm wavelength of 4297.78 Å

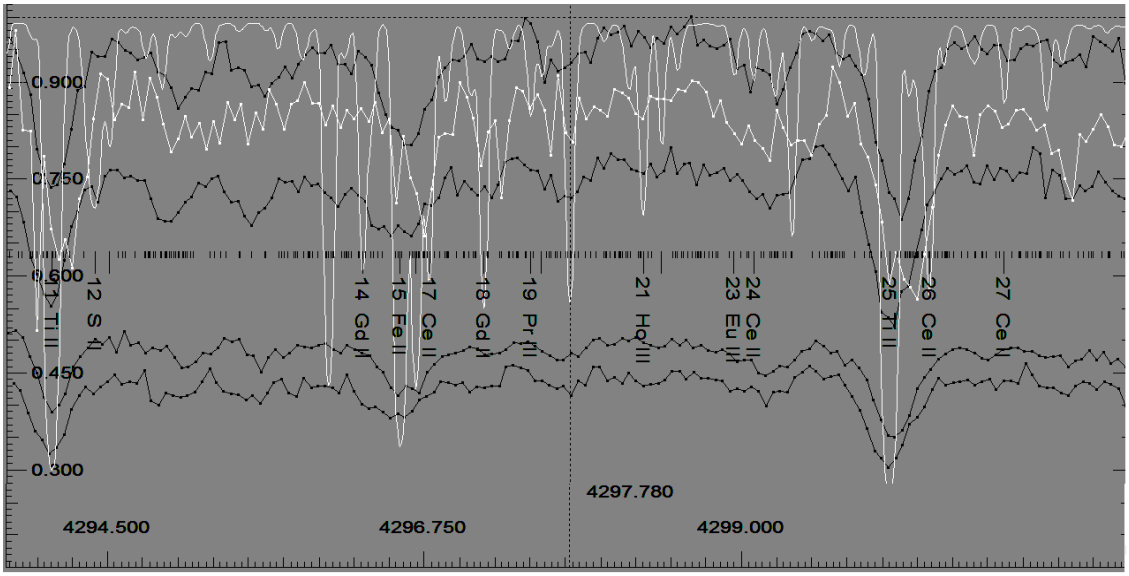

Figure 5a: Using the Pm II line at 4297.78 Å with an equivalent width of 11.7 mÅ, we determined the promethium abundance log *N*(Pm) = 5.523 on the scale of log N(H) = 12 (from the ELODIE archive spectrum). Stronger lanthanide lines (Pr III at 4297.50 Å; Ce II at 4297.575 Å, and Eu II at 4297.647 Å) can be observed in the blue wing of the Pm line in the spectra obtained at the Terskol Peak Observatory over two observation nights. The first observation at the Terskol Peak Observatory (recorded as HD 25354-2181, the middle spectrum) with the least blended line in the spectrum yields W = 20.5 mÅ, which corresponds to log *N*(Pm) = 5.91.

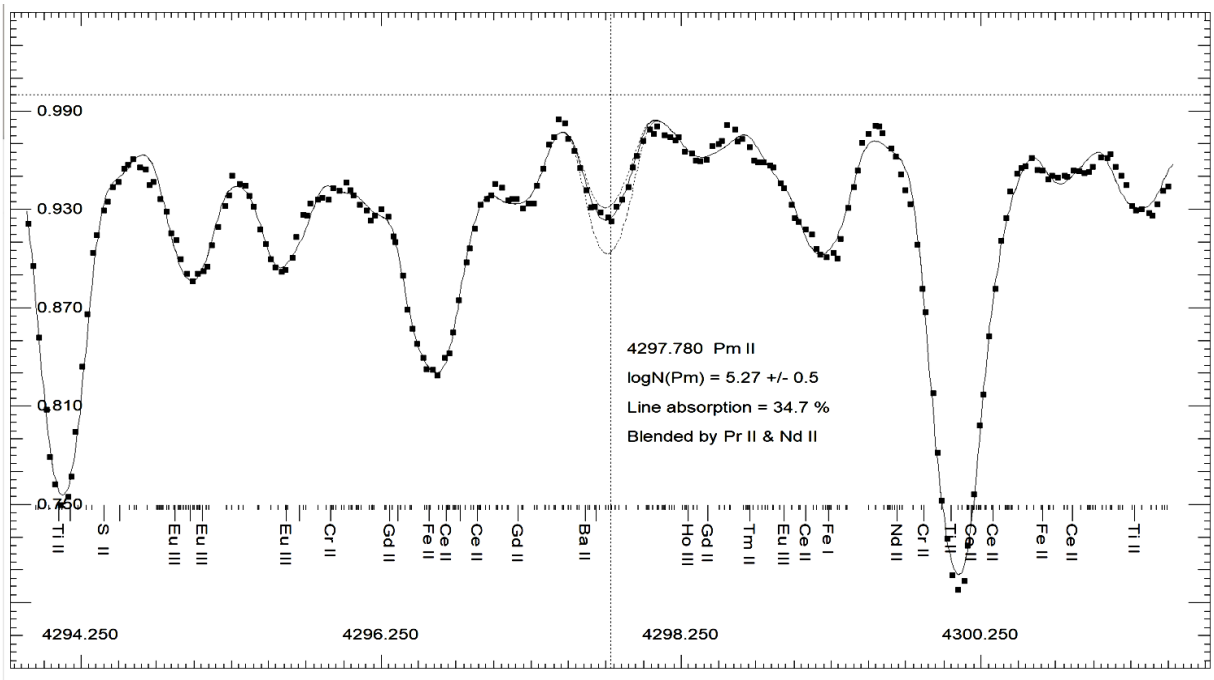

Figure 5b: Factoring in the blended lines of promethium results in an underestimated Pm abundance from the total spectrum.

Analysis of the HD 25354 spectral lines at the Pm wavelength of 4651.93 Å

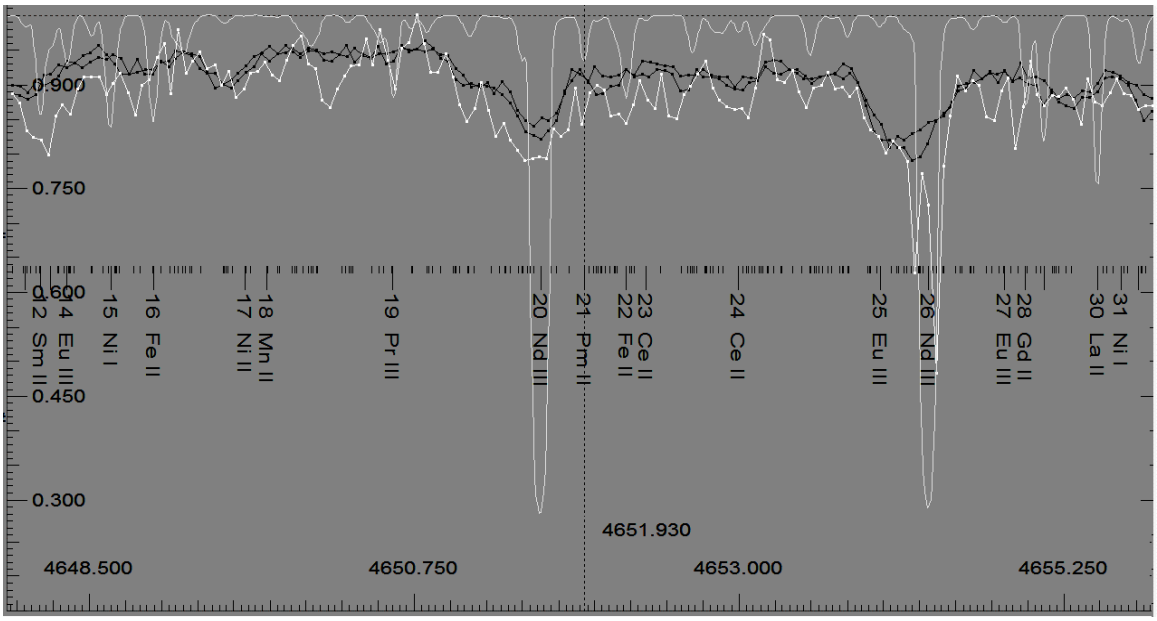

Figure 6: The Pm line at a wavelength λ 4297.78 Å in the spectrum obtained at OHP has an equivalent width of 5 mÅ (the spectrum is depicted as a white line). In the synthetic spectrum, shown in light grey colour, the profile of the Pm line is almost identical to the observed line profile in the spectrum acquired at OHP. The promethium abundance is log N(Pm) = 6.01.

Analysis of the HD 25354 and BL 138 spectral lines at the Pm wavelength of 5546.08 Å

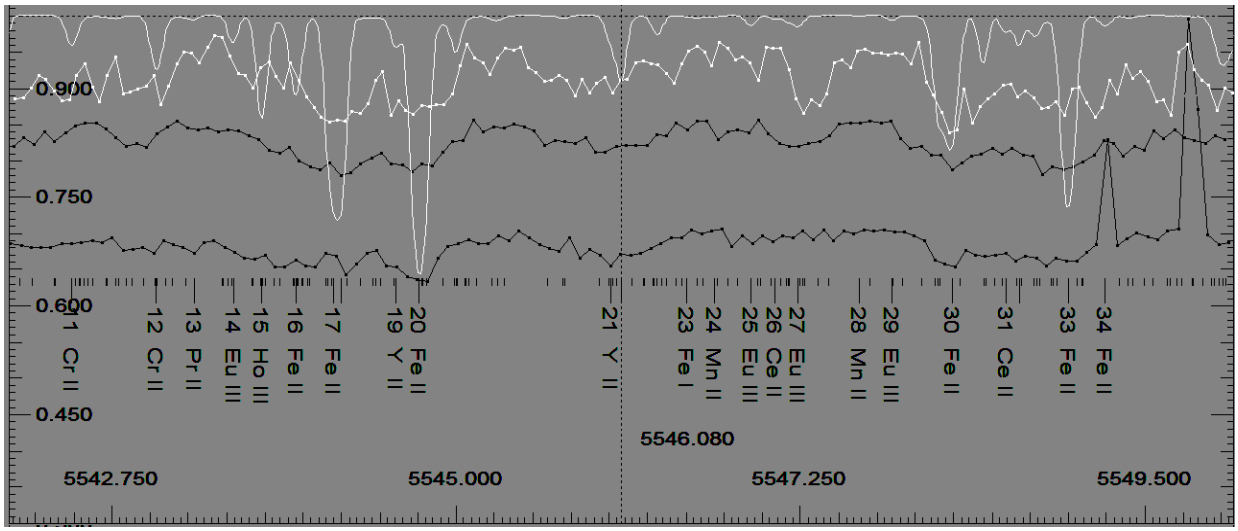

Figure 7a: The Pm abundance log *N*(Pm) = 5.80 was determined from the ELODIE archive spectrum using the Pm line at a wavelength λ 5546.08 Å with W = 4 mÅ. When using the spectrum obtained at the Terskol Peak Observatory without emission lines, the Pm abundance is log *N*(Pm) = 6.00 with W = 7.3 mÅ.

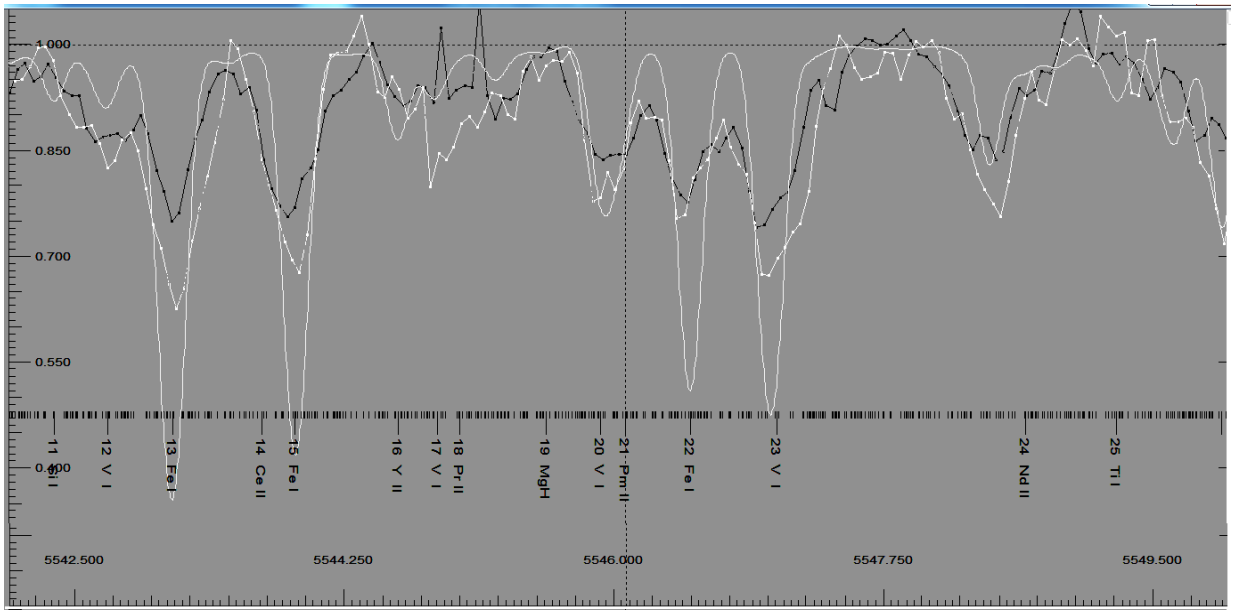

Figure 7b: In order to compare the Pm abundance in the atmospheres of late-type stars, we took the Pm line at a wavelength of 5546.08 Å from the spectrum of BL 138 located in the Fornax dwarf spheroidal galaxy; the selected line has an equivalent width W = 17.2 mÅ, which corresponds to the Pm abundance log *N*(Pm) = 0.76 (shown in black colour) on the hydrogen scale log *N*(H) = 12. The Pm line in the BL 18 spectrum is blended; this spectrum is depicted in white colour. We used the spectrum of BL 138 obtained by Letarte et al. (2010) with FLAMES multi-object instrument connected to GIRAFFE spectrograph with the high-resolution setups at the European Southern Observatory's (ESO) Very Large Telescope (VLT).

Analysis of the HD 25354 and BL 138 spectral lines at the Pm wavelength of 5561.73 Å

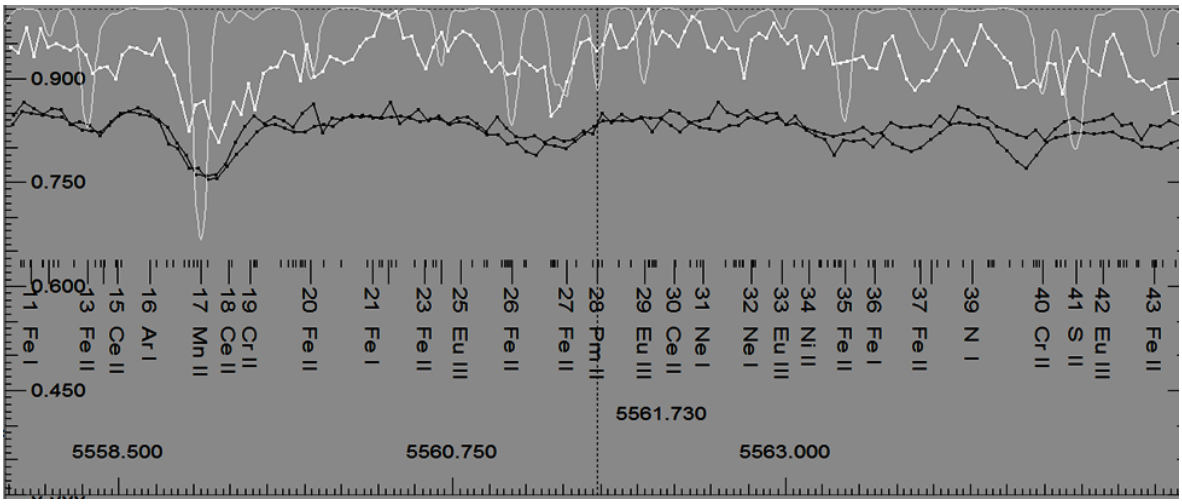

Figure 8a: A comparison between the spectra obtained at the Terskol Peak Observatory (the lower two spectra with broad lines) and at OHP (the upper spectrum with narrow and sharp lines). The Pm line at a wavelength of 5561.73 Å with an equivalent width W = 5 mÅ, which corresponds to the Pm abundance log N(Pm) = 5.65, has been identified in the spectrum obtained at OHP. The non-extended synthetic spectrum is plotted in light grey colour while the ELODIE archive spectrum is shown in white colour.

For comparison, according to a working hypothesis of Fivet et al. (2007) (Fivet, 2007), the promethium abundance in the atmosphere of HR 465 log N(Pm) = 5.08 at a wavelength of 5561.73 Å with an equivalent width W = 4 mÅ was determined from the spectra at the phase of stronger lanthanide lines with the following atmospheric parameters: T_{eff} = 11,840 K; log g = 4.3, and v_{mic} = 1.66 km s^{-1}. The effective temperature T_{eff} is lower than in HD 25354, so is the Pm abundance on the hydrogen scale log N(H) = 12.

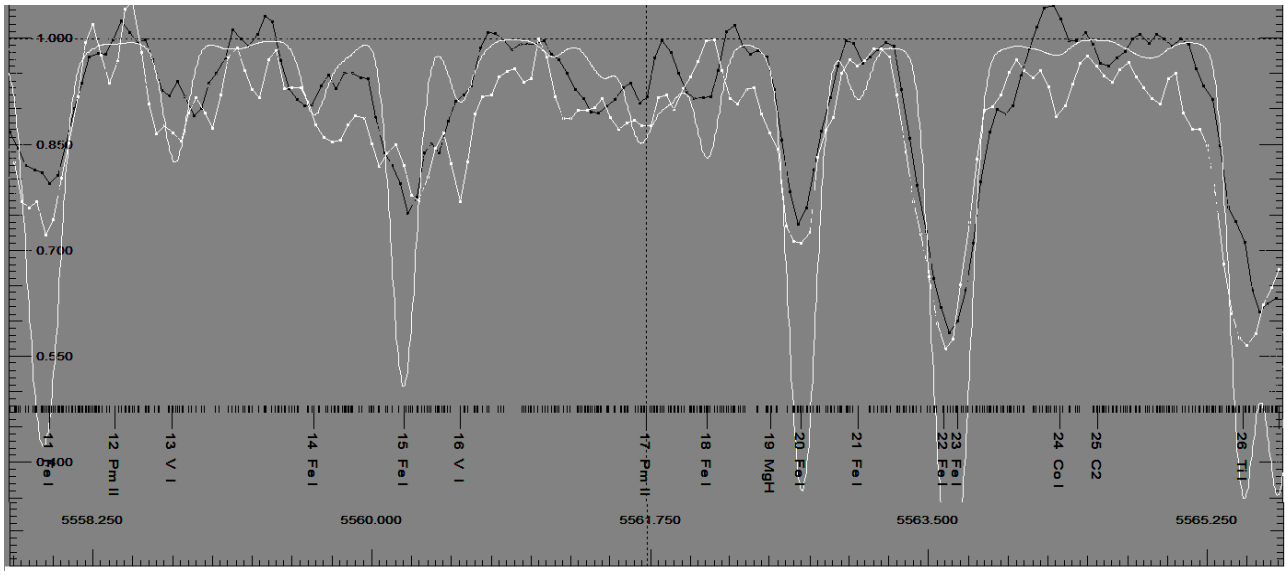

Figure 8b: The Pm line at a wavelength of 5561.73 Å with an equivalent width W = 11.9 Å, which corresponds to the Pm abundance log N(Pm) = –0.655 on the hydrogen scale log N(H) = 12, has been identified in the spectrum of BL 138 located in the centre of Fornax dwarf spheroidal galaxy (the line is shown in black colour). The blended Pm line in the BL 148 spectrum, depicted in white colour, is more intense as well. In the BL 148 spectrum, the Pm line at a wavelength of 5556.88 Å with an oscillator strength log gf = –0.036 and the energy of a lower level of 1.131 has an equivalent width W = 21.7 mÅ, which corresponds to the Pm abundance log N(Pm) = –0.16 on the hydrogen scale log N(H) = 12.

Analysis of the HD 25354 and BL 138 spectral lines at the Pm wavelength of 5576.02 Å

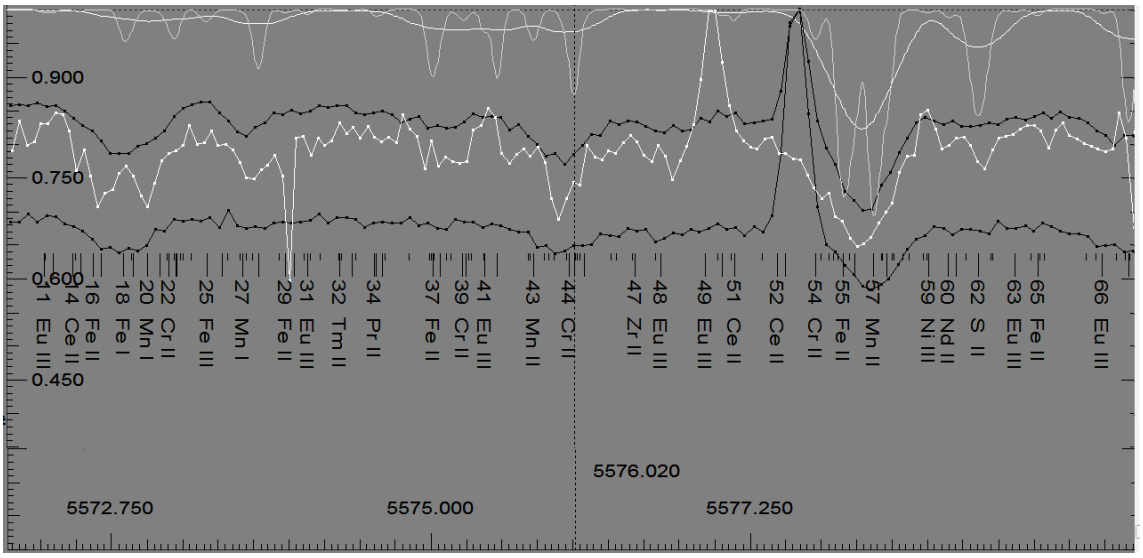

Figure 9a: The Pm line at a wavelength of 5576.02 Å with an equivalent width W = 10.5 Å, which corresponds to the Pm abundance log N(Pm) = 5.97 has been identified in the spectrum HD 25354-2181 (the lower spectrum depicted in black colour). In the ELODIE archive spectrum, shown in white colour, the Pm line at a wavelength of 5576.02 Å has an equivalent width W = 10.5 Å, which corresponds to the Pm abundance log N(Pm) = 6.05. All three spectra exhibit strong emission lines. The Pm line identified in the upper spectrum is blended with a relatively greater contribution of the chromium line.

Analysis of the BL 148 and BL 138 spectral lines at the Pm wavelength of 5576.02 Å

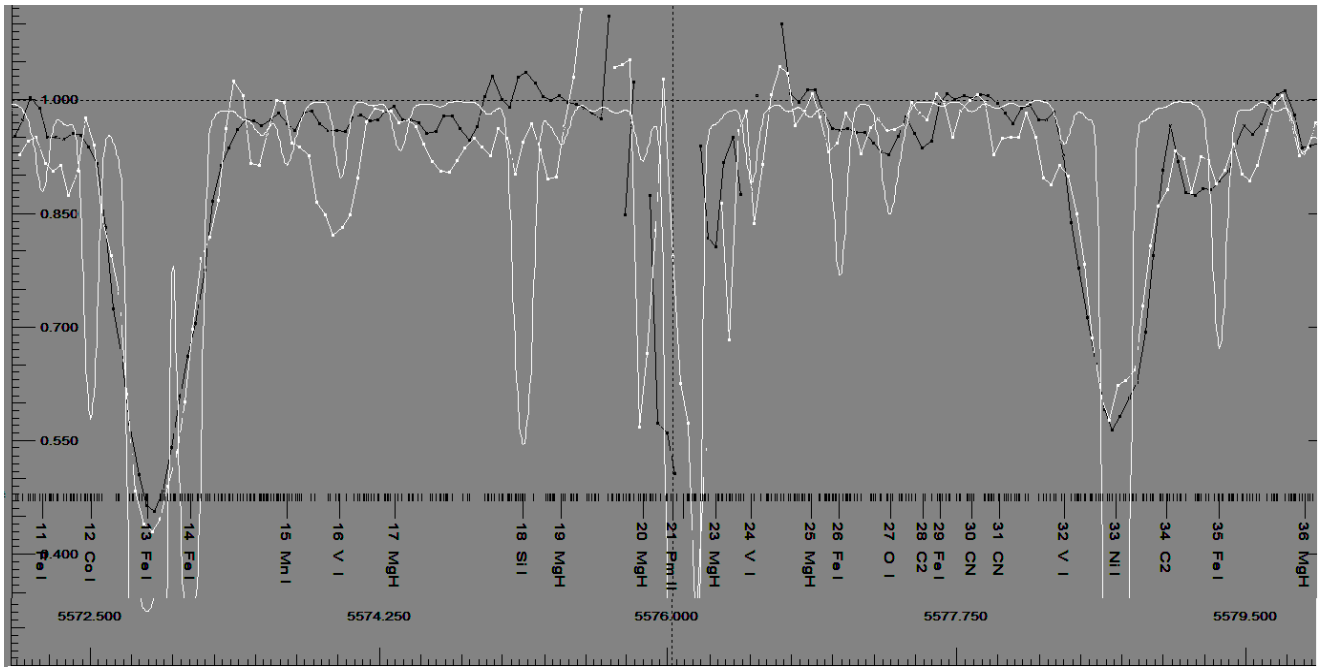

Figure 9b: The Pm line at a wavelength of 5576.02 Å in the spectra of BL 138 (shown in black colour) and BL 148 (depicted in white colour) exhibits a strong emission pattern.

Promethium emission lines in the spectra of HD 25354

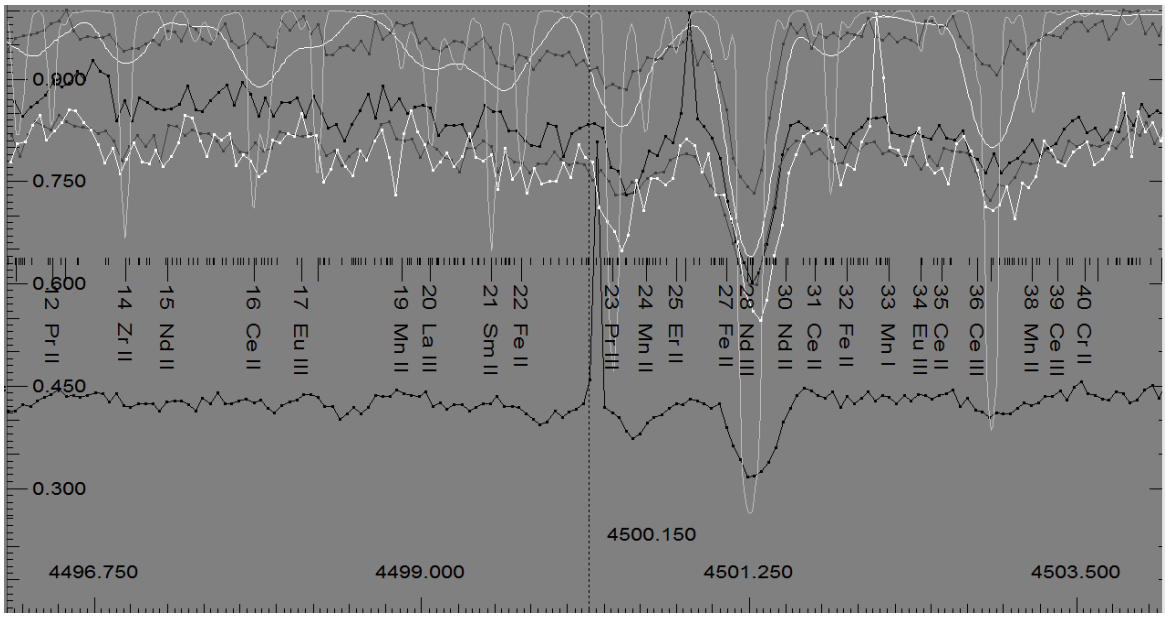

Figure 10: The line at a wavelength of λ 4500.15 Å has been identified as a blend of the Pm II at λ 4500.15 Å with the line Ni II at λ 4500.142 Å of a very weak intensity given the afore-specified stellar parameters. In the actual spectrum of HD 25354-2181, one can observe a strong emission line. The second spectrum HD 25354-2182 has a sharp emission line at λ 4500.85 Å as well. In the ELODIE archive spectrum (shown as a white line), an emission line can also be observed at λ 4502.22 Å. The synthetic spectrum lines are weak or practically absent at the wavelengths λ 4500.85 Å and λ 4502.2 Å. Observations performed on the second night at the Terskol Peak Observatory are depicted in dark grey colour; there are no emission lines in the respective spectra.

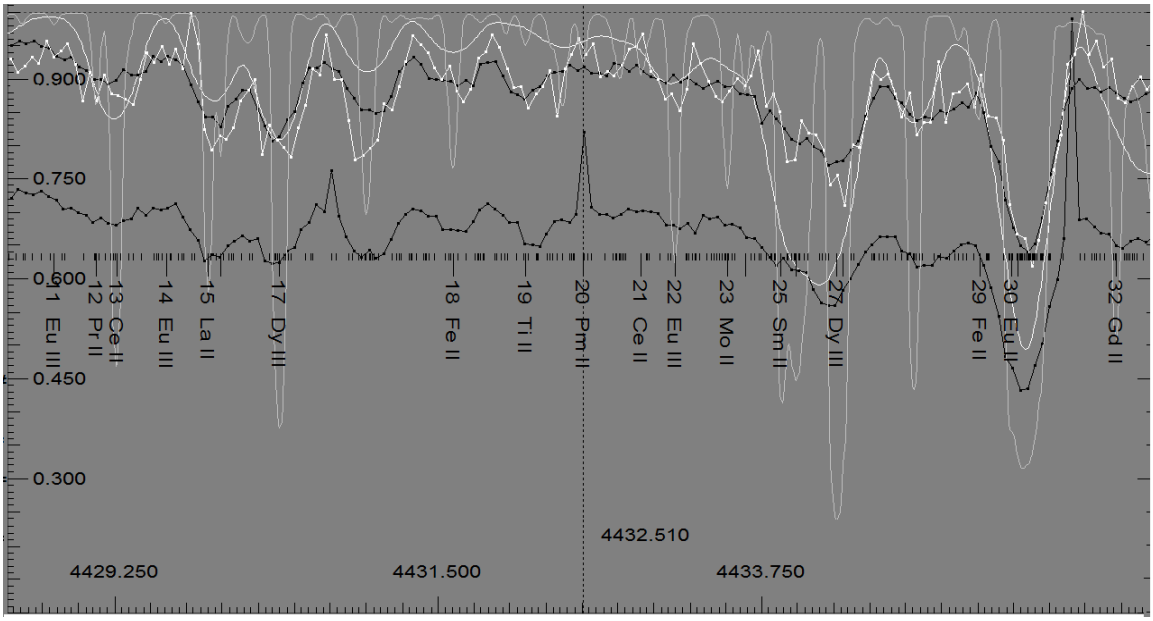

Figure 11: Either the absence of any line or wakening of the line intensity can be considered as a superposition of the absorption and emission lines.

Table: Investigation of the radioactive promethium lines in stellar spectra

HD 25354: T_{eff} = 12,800 K, log *g* = 4.15, v_{mic} = 0.23 km s^{-1}									
Wave	**Code**	**log *gf***	**E_{low}**	**The ELODIE archive spectra**		**The Terskol Peak Observatory spectra**		**Synthetic spectra from the mean of the Terskol Peak Observatory ones**	
				W(mÅ)	**log *N*(Pm)**	**W(mÅ)**	**log *N*(Pm)**	**log *N*(Pm)**	**% log *N*(Pm)**
4137.95	61.01	0.30	0.366	16.2	5.69	–	–	–	–
4157.86	61.01	0.36	0.246	–	–	–	–	5.81	99.8
4186.03	61.01	0.00	0.182	17.0	5.94	16.4	5.91	5.76	80.4
4216.31	61.01	–0.06	0.055	9.8	5.60	11.2	5.67	5.68	96.9
4297.78	61.01	0.08	0.000	11.7	5.52	20.0	5.91	5.27	34.0
4615.87	61.01	–0.76	0.199	3.4	5.87	4.0	5.94	–	–
4651.93	61.01	–0.67	0.331	5.0	6.01	–	–	–	–
5546.08	61.01	–0.26	0.760	4.0	5.80	7.3	6.00	–	–
5556.88	61.01	–0.03	1.131	0.48	5.83	–	–	–	–
5561.73	61.01	–0.04	0.873	5.0	5.74	–	–	–	–
5576.02	61.01	–0.17	0.661	9.0	5.97	10.5	6.05	6.10	68.1
					5.80 ± 0.15		5.91 ± 0.12		5.84 ± 0.16

HR 465: T_{eff} = 11,840 K, log *g* = 4.3, v_{mic} = 1.66 km s^{-1}					
Wave	**Code**	**log *gf***	**E_{low}**	**The Bohyunsan Optical Astronomy Observatory spectra**	
				W(mÅ)	**log *N*(Pm)**
4137.95	61.01	0.30	0.366	12.0	5.00
4216.31	61.01	–0.06	0.055	9.0	5.08
5561.73	61.01	–0.04	0.873	4.0	5.08
					5.80 ± 0.15

HIP 13962: T_{eff} = 6,250 K, log *g* = 1.2, v_{mic} = 12.0 km s^{-1}					
Wave	**Code**	**log *gf***	**E_{low}**	**The Bohyunsan Optical Astronomy Observatory spectra**	
				W(mÅ)	**log *N*(Pm)**
4137.95	61.01	0.30	0.366	12.4	–0.41
4157.86	61.01	0.36	0.246	14.5	–.045
4186.03	61.01	0.00	0.182	12.2	–0.30
4297.78	61.01	0.08	0.00	29.4	–0.16
4216.31	61.01	–0.06	0.055	6.9	–0.63
5561.73	61.01	–0.04	0.873	3.6	–0.25
					–0.37 ± 0.15

BL 138: T_{eff} = 3,939 K, log *g* = 0.71, v_{mic} = 2.3 km s^{-1}, [Fe/H] = –1.01					
Wave	**Code**	**log *gf***	**E_{low}**	**The Bohyunsan Optical Astronomy Observatory spectra**	
				W(mÅ)	**log *N*(Pm)**
5546.08	61.01	–0.26	0.760	17.2	–0.42
5561.73	61.01	–0.04	0.873	11.9	–0.65
5576.02	strong emission				
					–0.54 ± 0.12

SOLAR SYSTEM AND SPACE ENVIRONMENT

https://doi.org/10.18524/1810-4215.2024.37.315007

USING SYNTHETIC LIGHT CURVES OF ARTIFICIAL SATELLITE MODEL TO TEST THE PATTERNS METHOD FOR DETERMINING THE ROTATION AXIS ORIENTATION

N.I.Koshkin[1], L.S.Shakun[1], E.A.Korobeynikova[1], S.M.Melikyants[1], S.L.Strakhova[1], O.M.Kozhukhov[2]

[1] Astronomical Observatory of Odesa I. I. Mechnikov National University, 1v Marazliivska St, Odesa, Ukraine

[2] National Space Facilities Control and Test Center of the State Space Agency of Ukraine, Kyiv, Ukraine

ABSTRACT. In this paper we test a new method for determining the rotation axis direction in space for various resident space objects (RSOs). This method (Koshkin et al., 2024) is based on the structural analysis of the light curves of such RSOs and the search for similar fragments, called "photometric patterns", in observations obtained from one or several observatories simultaneously or over a short period of time. The method does not require prior knowledge of the RSO shape and does not impose strict requirements on the quality of observations, and this is its main advantage. First of all, this method is certainly applicable to rapidly rotating objects of complex shape with smooth surfaces. As a result, such RSOs are capable to reflect sunlight in a specular manner, when short-term brightness flares are present in the light curves forming a unique pattern. Identical patterns are observed when the angle between the phase angle bisector (PAB) and the rotation axis reaches the same values. However, the light curves of many RSOs have a significant diffuse component in addition to the specular flares. This diffuse component depends on both the phase angle value and the orientation of the phase angle plane relative to the RSO's plane of rotation. This paper is devoted to checking the assumption that the structure and shape of diffuse-specular patterns will remain similar to themselves within certain limits of variation of the value of these two angles at moments of equality of the PABs' latitude. The analysis is based on simulation using synthetic light curves of the RSO model, observed from several points on the Earth's surface.

Keywords: space object, model, light curve, photometric pattern, rotation axis.

АНОТАЦІЯ. Знання кінематичних властивостей, таких як кутова швидкість обертання та просторове положення осі обертання, великих відпрацьованих супутників і корпусів ракет, необхідна для прогнозування їхньої орієнтації в кожний момент часу. Ця інформація має вирішальне значення як, наприклад, для успіху місій активного видалення з орбіти цих об'єктів, так і для підвищення точності прогнозування їх орбітального руху на низьких навколоземних орбітах. Визначення стану обертання штучних космічних об'єктів (КО) здійснюється різними засобами, проте історично це робилося за допомогою оптичних наземних датчиків (фотометрів) шляхом отримання кривих блиску, їх обробки та аналізу. У цій роботі ми тестуємо новий метод для визначення напрямку осі обертання у просторі резидентних космічних об'єктів. Цей метод заснований на структурному аналізі кривих блиску таких об'єктів та пошуку схожих фрагментів ("фотометричних патернів"), у спостереженнях, які отримані з однієї або кількох обсерваторій одночасно або протягом короткого періоду часу. Основна перевага даного методу полягає в тому, що його використання не вимагає знання форми КО і не висуває жорстких вимог до якості спостережень. Перш за все, цей метод безумовно застосовується до складних за формою об'єктів, що швидко обертаються, мають у складі гладкі поверхні і, внаслідок цього, здатні відбивати сонячне світло дзеркально, в результаті чого в кривих блиску присутні короткочасні спалахи блиску утворюють унікальний патерн. Однакові патерни спостерігаються тоді, коли кут між бісектрисою фазового кута і віссю обертання досягає тих самих значень. Однак, крім дзеркальної складової, криві блиску багатьох КО мають значну дифузну складову, яка залежить як від величини фазового кута, так і від орієнтації площини фазового кута щодо площини обертання. Дана робота присвячена перевірці того припущення, що структура і форма дифузно-дзеркальних патернів залишатиметься подібною в деяких межах варіації величини цих двох кутів у моменти коли широти бісектрис бувають однаковими. Аналіз зроблено на основі синтетичних кривих блиску моделі КО, спостереження якої імітуються з декількох пунктів на поверхні Землі.

Ключові слова: космічний об'єкт, модель, крива блиску, фотометричний патерн, вісь обертання.

1. Introduction

Knowledge of kinematic properties, such as angular velocity of rotation and spatial position of the rotation axis, for large defunct satellites and upper stages of launch vehicles is necessary to predict their orientation at any given

time. This information is of crucial importance, for example, for the success of active debris removing (ADR) missions for these objects, as well as for improving the accuracy of predicting the orbital motion of space objects at LEO. The rotation state of artificial space objects (SOs) is determined by various means, but historically it has been done using optical ground-based sensors (photometers) by obtaining light curves, processing and analyzing them. The period of proper rotation of a SO around its center of mass can be fairly easily estimated by measuring the period of brightness variations. However, determining the SO's rotation axis direction in space is much more difficult if the shape of this SO is often insufficiently known. Most studies on this topic offer specific methods for determining the SO's rotation axis orientation, that are suitable only for a certain type of objects.

The attempt to solve the general problem of the so-called "inversion" of the light curve, as well as attempts to separate the contribution of the SO shape and the orientation of its rotation axis to the external view of light curves, have not been successful even for fairly simple non-convex bodies. Nevertheless, one of the real ways to perform the inversion of light curves (or determination the SO's shape and rotation axis orientation) is, first of all, the ability to estimate the current direction of the rotation axis in space. Therefore, the development of new approaches to determining the rotation axis orientation, in particular, based on photometry, remains actual.

In this paper, we use and test a new method for estimating the SO rotation axis direction in space. This method is based on the structural analysis of SO light curves and the search for similar fragments, which we call "photometric patterns", in observations obtained from one or several observatories (or observation points, OPs) simultaneously or over a short period of time (Koshkin et al., 2024). The main advantage of this method is that its use does not require knowledge of the SO shape. In addition, this method does not require a very high frequency of brightness measurements and high accuracy of the timing of photometric observations, i.e., in fact, it does not put forward strict requirements for the quality of observations. Nevertheless, it also has its constraints. First of all, this method is certainly applicable to objects with complex shapes that have smooth surfaces and, as a result, are capable of reflecting sunlight in a specular manner. In the structure of the light curves of such SOs, one can expect the presence of short-term brightness flares. If several such "specular" flares were observed in the light curve during one rotation of the SO, they can form a unique photometric pattern (in the sense of unique intervals between the specular flares). A similar pattern can also be observed in another light curve, for example, obtained at another observatory or during another passage of the given SO. In this case, it can be stated that the same patterns are observed when the angle between the PAB and the rotation axis reaches equal values in both cases (Fig. 1). However, in addition to the specular component, the light curves often have a significant diffuse component depends both on the phase angle value and on the orientation of the phase angle plane (light scattering plane) relative to the rotation plane (θ angle in Fig. 1). We assume that within certain limits of variation of these two geometric factors, the structure and shape of diffuse-specular patterns will remain similar to themselves, provided that the latitudes βi of these PABs are equal at the moments of observation of these patterns. This paper is devoted to check this assumption based on input data in the form of simulated synthetic light curves of the SO model observed from several sites on the Earth's surface.

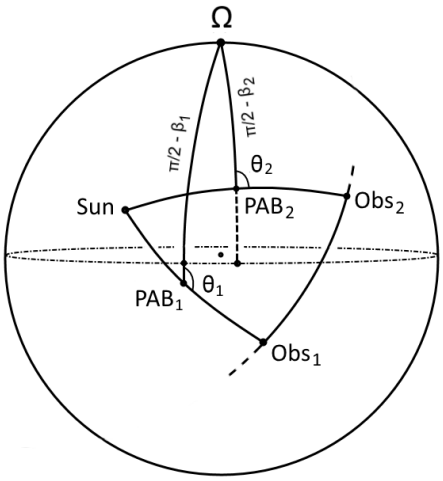

Figure 1: Satellite-centric position of the main vectors that determine the conditions of its illumination and visibility. Arc "Sun-Obs$_i$" determines the current phase angle. Arc "Ω-PAB$_i$" is equal ($\pi/2 - \beta_i$), where β_i – PAB latitude relative to the pole of the rotation axis Ω. Angle θ_i determines the current position of the light scattering plane relative to the SO's rotation plane.

2. Simulation technique

In the method of photometric patterns (Koshkin et al., 2024), to find the RSO rotation axis orientation, it is necessary to obtain photometric observations from one or several OPs in a quantity sufficient to identify several types of patterns on the light curves (each pattern needs to be detected at least twice) over a sufficiently short time interval (the desired RSO rotation axis orientation can be considered fixed during this interval).

In order to be sure to detect the same photometric pattern on different light curves of a given SO, it is necessary that the mutual configurations of the three vectors mentioned above (the rotation axis and the satellite-centric directions to the Sun and to the observer) were identical. On the other hand, to determine the rotation axis direction, we need the directions of the PAB vectors in the inertial space for the same photometric pattern have to be maximally different. This contradiction can be overcome if the photometric pattern can be reproduced with different configurations of the said vectors. It is always true for "specular" patterns and, as we will show below, it is also possible for "diffuse-specular" patterns.

In practice, we currently do not have a sufficient number of observations of any RSO obtained in the required geometry, and it limits the possibility of making reliable estimates of the direction of the RSO rotation axis in the inertial coordinate system. However, it is possible to use synthetic light curves of the RSO model obtained using animation and visualization programs for three-dimensional scenes such as Blender (Kudak et al., 2024), 3D-Max (https://

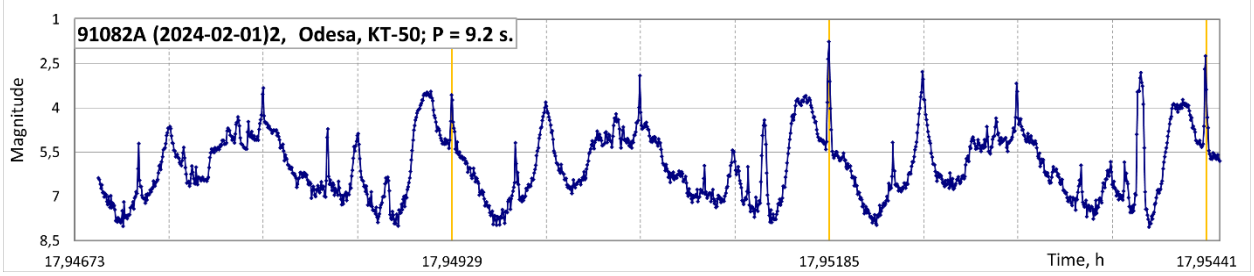

Figure 2: A fragment of the light curve of the spacecraft 91082A (DMSP 5D-2 F11), obtained on February 1, 2024 in Odessa on the KT-50 telescope in tracking mode. The rotation period of the spacecraft is 9.2 seconds (it is marked with vertical lines on the light curve).

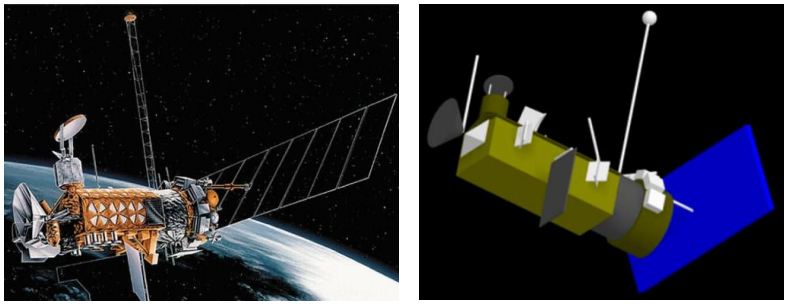

Figure 3: The spacecraft DMSP 5D3 and model used to calculate the synthetic light curves

Table 1: Optical characteristics of the spacecraft model's individual parts specified in 3D-Max

Nomenclature	Color (RGB)	Diffuse Color	Specular Level	Glossiness
Main body of model	80, 80, 0	80, 80, 0	15	90
Small boxes, Small panels, Rods	150, 150, 150	150, 150, 150	990	100
Cylinder, cone, screen, disk	50, 50, 50	50, 50, 50	100	100
Solar Panel	0, 0, 170	0, 0, 170	10	60

help.autodesk.com/view/3DSMAX/2023/ENU/), etc. We have accumulated experience using the 3D-Max package (Koshkin et al., 2018; 2019), which allows us to generate a fairly adequate geometric shape of the RSO model using the Max-script language, to set the required coefficients of diffuse and specular reflection of light for each elementary surface, as well as its color.

It is also important that in any simulator it is possible to set the correct ratio of the distances between the light source, the model and the radiation receiver in relation to the model dimensions. Since the observer always sees the RSO as a point source of light illuminated by the Sun's rays, all rays reflected towards the observer in a narrow solid angle (almost parallel to each other), for example, from all areas of a large flat surface of solar panels, should simultaneously hit the receiver. Otherwise, if the distance to the model is comparable to its dimensions, such a panel will be "visible" to the receiver in parts, i.e. "scanning" will be observed and a light flare, for example, from two strictly parallel solar panels located on both sides of the satellite body will look like a double one, which is not observed for real RSOs in orbit.

We used the 3D-Max package and a model whose shape is approximately similar to a DMSP-type spacecraft (https://space.skyrocket.de/doc_sdat/dmsp-5d2.htm) for our task. There are many observations of objects of this series in our photometric database (Koshkin et al., 2017; 2021), and it can be noted that many of them often demonstrate periodicity of light changes, have a complex structure of light curves and the presence of a significant number of specular flares. As an example, Fig. 2 shows a fragment of the light curve of the spacecraft with COSPAR ID 91082A (DMSP 5D-2 F11). Fig. 3 shows an images of the spacecraft and model used to obtain synthetic light curves. Table 1 contains the optical parameters that we used to specify the optical properties of light reflection for different surfaces of this model.

It was assumed the model rotates stably around a fixed axis, rigidly connected to the body, which is perpendicular to the base and longitudinal axis of the satellite. In this case, we have a flat rotation of the model around one axis, which also maintains its orientation in inertial space over relatively short time intervals.

3. Results of light curves simulation for different observation points

Simulations of the synthetic light curves of the model were made for several OPs located in different places in the northern and southern hemispheres (see Table 2).

To calculate the visibility conditions of the model from different locations, a real near-Earth orbit similar to the orbit of the 22154B spacecraft (i = 98.75, e = 0014, n = 14.17) and typical conditions of object observability were used. To model the light curves, the date of 02.12.2024 was selected, when visibility was realized from all seven selected OPs. We considered only those passages of SO when the trajectories of the PAB vectors fall into a common region (see Fig. 4a)) and, accordingly, the PAB latitudes can have a common range of change. For this purpose, in subsequent calculations of the light curves, the pole of the model rotation axis, was taken in the direction determined by the equatorial coordinates ($\alpha\,\Omega = 260°$, $\delta\,\Omega = +23°$). The graphs of the change in the PAB latitude over time in the coordinate system associated with this rotation axis for all selected passages are shown in Fig. 4b). We can see that the ranges of latitude change PAB overlap well in groups separately for northern and southern observation points. For the selected pole of rotation, these groups also partially overlap each other in the latitude range of about +24° ÷ +38°.

Let us now consider the obtained synthetic light curves of this model for the given observation conditions. The rotation period of the model was 18 sec and up to 30 complete rotations were observed in different passes. Therefore, it is possible to present all the light curves in their entirety only on a very compressed scale. We will present here only 5-6 fragments of each light curve, which most fully reflect the change in their shape over time. Figures 5a) and 5b) show sequential fragments of the light curves for three northern and four southern OPs.

Table 2: Observation points locations used for simulation of the synthetic light curves

Site Name	Abbreviated Name	Geographical latitude, deg	Geographical longitude, deg
Odesa	Ods	46.5	30.7
Novosilki	Nov	50.6	30.6
Lviv	Lvi	49.9	24.0
New Zealand	NZel	–44.0	170.5
Northern Australia	NAus	–17.6	123.8
South Africa	SAfr	–32.4	20.7
Argentina	Arg	–45.6	–69.1

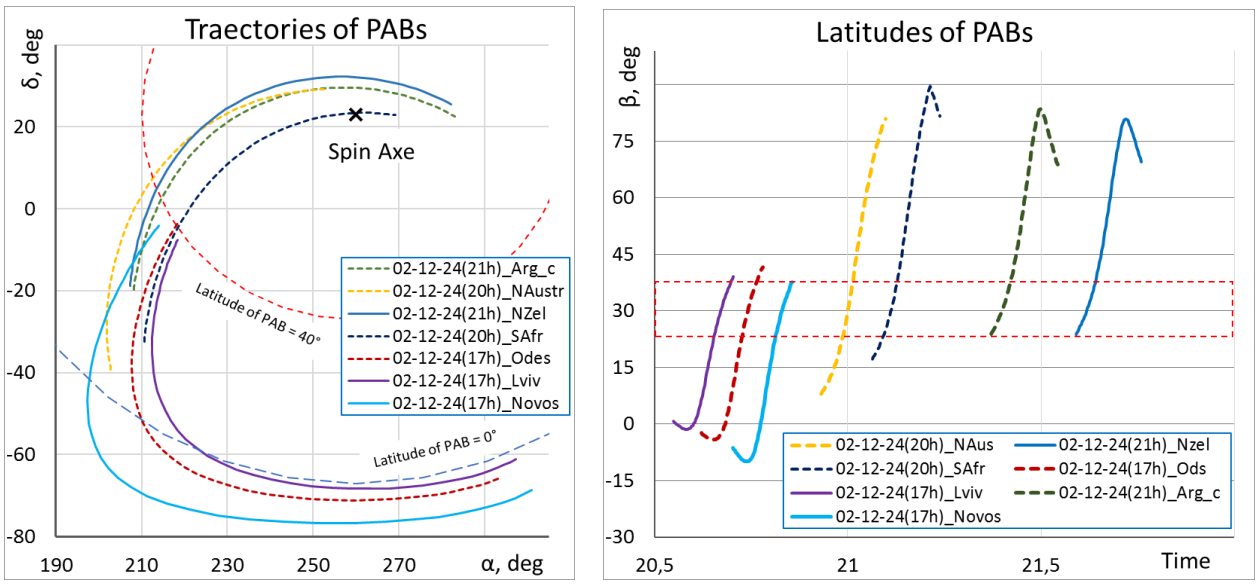

Figure 4: a) – Trajectories of PAB vectors in seven passes of the SO model over different OPs, for which synthetic light curves were calculated. The cross indicates the selected pole of the model's rotation axis, for which two latitude circles are shown. b) – Graphs of the change in latitude of PAB over time for these passages with the selected position of the pole of the rotation axis (graphs are arbitrarily shifted along the time axis).

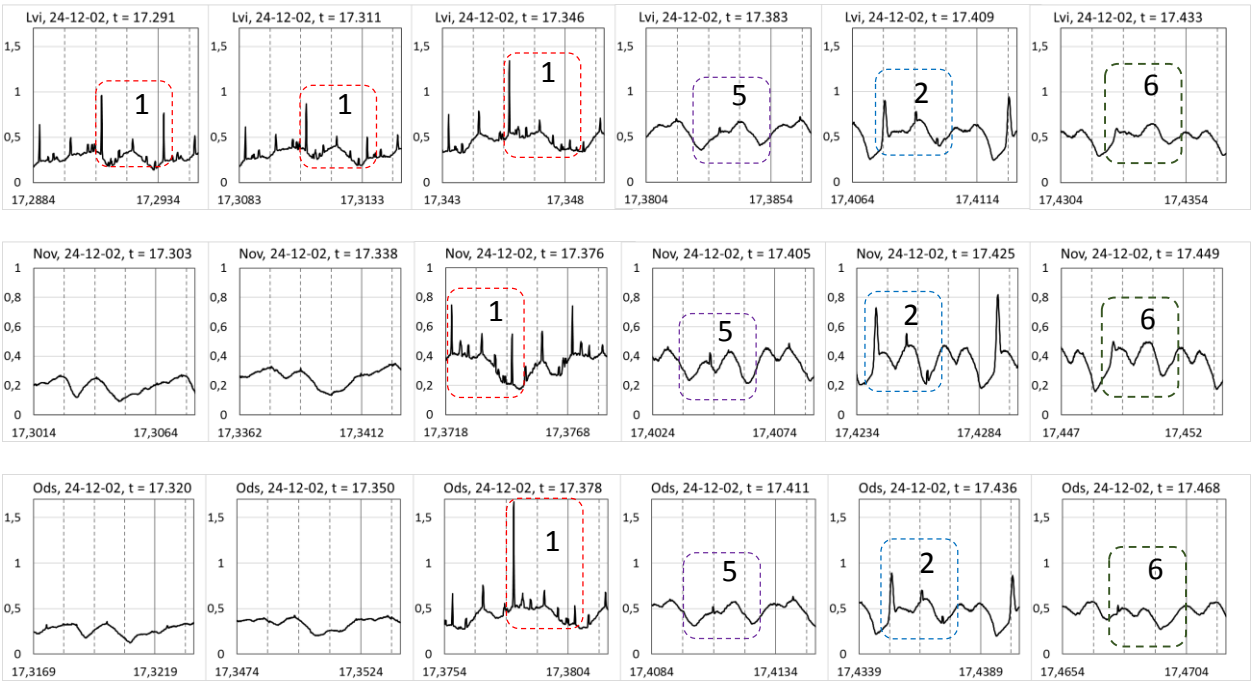

Figure 5a): Fragments of simulated light curves for northern OPs

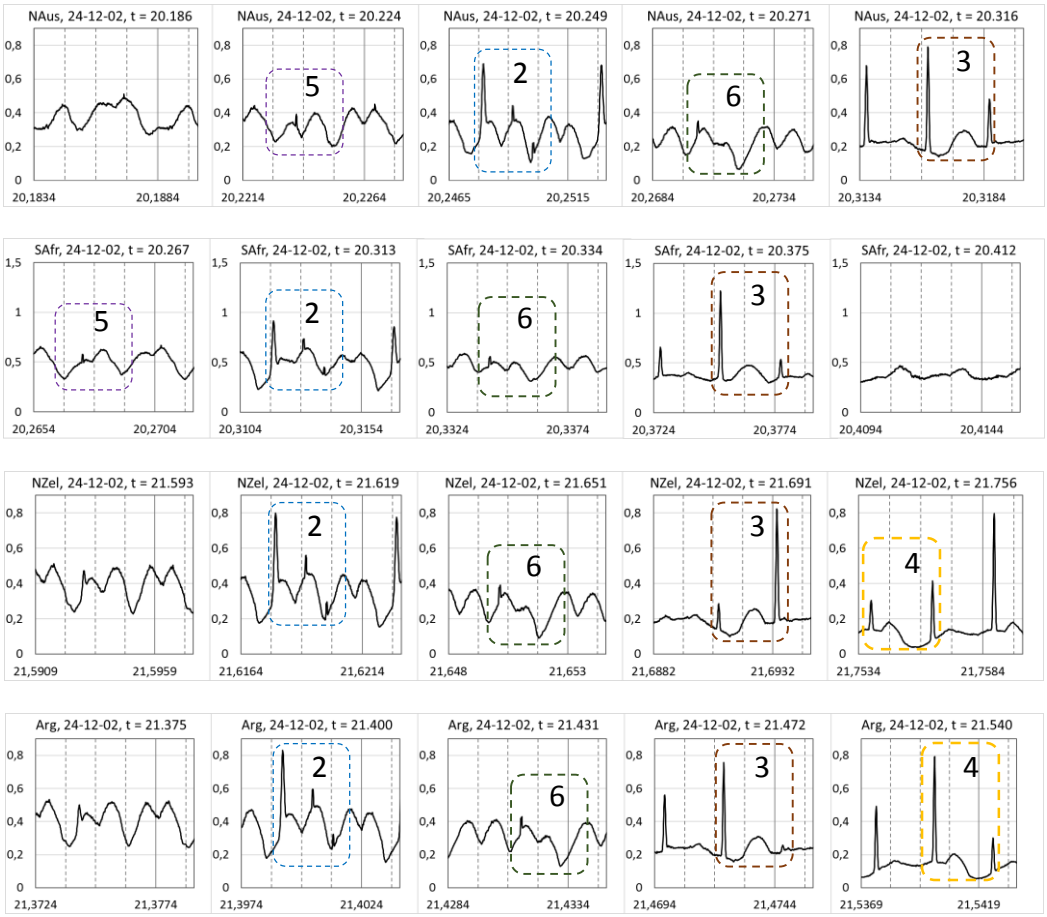

Figure 5b): Fragments of simulated light curves for southern OPs

Table 3: List of photometric patterns identified in different synthetic light curves and coordinates of the corresponding PAB vectors

No.	Date	Observ. Point	UT, h	RA of PAB	Decl. of PAB	Type of pattern	Phase angle	θ	Longitude of PAB	Latitude of PAB
1	02.12.2024	NAus	12.224	202.23	–21.67	5	86.9	44.6	214.50	18.00
2	02.12.2024	NAus	12.249	205.93	–5.75	2	89.7	56.4	202.00	29.80
3	02.12.2024	NAus	12.270	212.92	7.96	6	93.1	64.9	190.30	43.00
4	02.12.2024	NAus	12.316	238.91	26.95	3	100.0	70.4	163.90	70.50
5	03.12.2024	Arg	2.400	209.71	–11.47	2	78.3	56.2	209.00	30.50
6	03.12.2024	Arg	2.431	215.38	3.89	6	84.1	67.7	197.50	42.50
7	03.12.2024	Arg	2.472	237.50	25.44	3	97.7	73.5	168.00	69.50
8	03.12.2024	Arg	2.540	282.09	23.09	4	110.7	56.4	4.63	69.69
9	02.12.2024	NZel	10.619	208.66	–10.03	2	81.4	56.3	207.00	30.00
10	02.12.2024	NZel	10.650	213.39	4.52	6	88.1	65.5	194.50	41.60
11	02.12.2024	NZel	10.691	236.38	28.01	3	103.2	66.8	161.00	68.50
12	02.12.2024	NZel	10.759	282.28	25.49	4	114.6	50.9	12.00	69.80
13	02.12.2024	SAfr	19.267	210.71	–31.75	5	71.0	36.7	227.40	17.70
14	02.12.2024	SAfr	19.313	213.98	–15.42	2	67.9	56.3	216.50	30.50
15	02.12.2024	SAfr	19.334	218.41	–4.75	6	69.0	69.2	209.00	40.90
16	02.12.2024	SAfr	19.375	239.47	17.76	3	81.9	94.8	191.50	70.08
17	02.12.2024	Ods	15.378	214.83	–58.91	1	88.4	7.7	248.00	0.04
18	02.12.2024	Ods	15.411	208.44	–29.93	5	74.4	38.5	224.60	17.50
19	02.12.2024	Ods	15.437	212.56	–15.15	2	70.4	55.4	214.80	30.00
20	02.12.2024	Ods	15.468	217.31	–5.30	6	70.0	67.5	208.60	39.80
21	02.12.2024	Nov	15.377	197.52	–44.06	1	95.1	25.0	230.20	2.00
22	02.12.2024	Nov	15.405	203.56	–21.75	5	84.1	45.0	214.95	19.15
23	02.12.2024	Nov	15.425	208.32	–12.52	2	79.9	54.5	209.60	28.20
24	02.12.2024	Nov	15.449	213.14	–5.26	6	77.2	62.9	205.80	36.00
25	02.12.2024	Lviv	15.291	296.12	–61.76	1	102.0	28.0	286.20	0.50
26	02.12.2024	Lviv	15.311	281.93	–66.52	1	98.2	21.6	278.56	–1.04
27	02.12.2024	Lviv	15.346	232.18	–63.68	1	86.3	2.2	258.06	0.62
28	02.12.2024	Lviv	15.383	212.41	–33.33	5	68.3	34.8	229.64	17.70
29	02.12.2024	Lviv	15.409	214.44	–18.81	2	65.1	53.0	219.43	28.95
30	02.12.2024	Lviv	15.433	217.23	–10.29	6	65.4	64.0	213.76	36.51

4. Similar patterns selection

Structural analysis of the obtained light curves for seven OPs allows us to notice their sections similar to each other. The sections of the light curves in Fig. 5a) and 5b) bounded by dotted rectangles can be assigned to several different groups of patterns. The numbers of the group that include a given section are indicated in the corresponding rectangles. First of all, it is worth to select the sections containing series of short specular brightness flares, paying attention to the intervals between them. These relative intervals should be invariant with respect to changing observation conditions, including differences in the phase angle and orientation of the scattering plane (see Fig. 1 and Table 3). However, the amplitude of these flares can differ significantly due to possible differences in the degree of obscuration for the reflecting elements of the structure by other parts of the SO. Thus, we identified six different photometric patterns. At the same time, two of them (types 1 and 2) can be considered more reliable since they contain at least 3 specular flares. The third and fourth patterns contain two flares each, following after half a period, but considering the shape of the adjacent section of the light curves caused by diffuse scattering of light, these patterns can also be confidently considered similar to each other. Finally, the 5th and 6th patterns should be classified as mixed diffuse-specular, since they include only one mirror flare in their structure, and are therefore less reliable. Nevertheless, their shape and structure allow them to be unambiguously combined into two different groups.

Table 3 contains a list of patterns that we used to solve the problem of determining the orientation of the rotation pole using the method described above. For the average moment of each pattern given in the table, the equatorial coordinates of the PAB vectors corresponding to this moment are indicated. The values of the phase angle and the angle θ are also given there, as well as the spherical coordinates of the PAB in the coordinate system fixed with the rotation axis.

The equatorial coordinates of the PAB vectors corresponding to the moments of registration of a particular pattern are shown in Fig. 6a). We see that the points – traces of the PAB vectors form groups which ideally should have the form of arcs of small circles whose common center is the pole of the model's rotation axis (the pole specified in the calculations is indicated by a cross). Fig. 6b) shows the values of the spherical coordinates of the same PAB vectors in a coordinate system in which the z-axis coincides with the a priori specified axis of rotation. Here, the points corresponding to different patterns are located at different latitudes corresponding to the location of light-reflecting flat smooth faces and other surfaces forming this pattern on the surface of the spacecraft model. The numbers in the ovals in Fig. 6 indicate the identifiers of the patterns according to Table 3. The indicated points are located at the corresponding latitude with some scatter. The greatest spread is in the PAB latitude values related to the sixth, that is, mixed diffuse-specular type of pattern. As was said above, this scatter is caused by the non-synchronism of the change in the latitude of the PAB and the rotation of the SO during observations. It is the value of this scatter that determines error in estimating the coordinates of the rotation axis pole.

5. Results of calculating the direction of the rotation axis

Based only on the average moments of registration of the selected patterns and the corresponding equatorial coordinates of the PAB vectors in different passes of the simulated satellite (Table 3), we obtained a solution for the unknown coordinates of the rotation pole using the method described in (Koshkin et al., 2024). In this case, by changing the set of input data, it was possible to evaluate how this affects the resulting solution.

Using all 30 patterns from Table 3, the following solution for the pole was obtained: RA_pole = 262.04° and Decl_pole = 19.24°. For other combinations of input data, the solutions for the pole, residuals, and total deviation from true pole are given in Table 4.

As we expected, the best result (in terms of residuals with the true values of the rotation axis pole coordinates) was obtained using all four specular photometric patterns containing at least two specular brightness flares – the deviation from the given true pole is about 2.6 degrees. Also, a quite acceptable solution was obtained for all 30 selected patterns, the deviation was about 4.3 degrees. Using only the first type of pattern (five equatorial directions of the PAB vectors, most widely distributed in space) led to a solution that was accurate in the RA coordinate, but had an error of about 9 degrees in declination. The least accurate solution was obtained when only diffuse-specular patterns with one specular flare were used, the deviation was about 19 degrees. Apparently, this is due to increased errors in determining the average moments of these patterns and the corresponding PAB vectors due to the influence of differences in the observation geometry at different OPs.

Table 4: Coordinates of the model rotation pole obtained depending on the set of photometric patterns used

Patterns used	RA_pole, deg	Decl_pole, deg	(O-C)_RA, deg	(O-C)_Decl, deg	Deviation, deg
All patterns	262.0	19.2	2.0	–3.8	4.3
1-st patterns only	260.2	13.9	0.2	–9.1	9.1
1-4 patterns	262.4	24.1	2.4	1.1	2.6
5-6 patterns	249.0	7.2	–11.0	–15.8	19.2

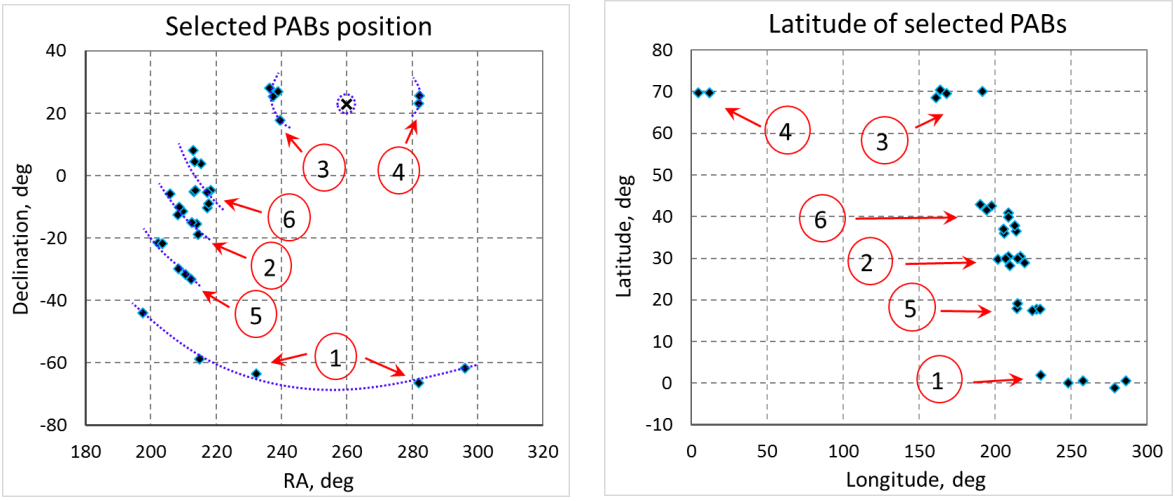

Figure 6: a) – Equatorial coordinates of the PAB vectors corresponding to the moments of pattern registration. The cross indicates the a priori given pole of the model's rotation axis. b) – Latitude and longitude of PAB vectors at the moments of observation of selected patterns. The numbers indicate the identifiers of the corresponding patterns.

Consider the diagram shown in Fig. 7, which relates two geometric parameters that influence the shape of the diffuse component of the light curves – the phase angle and the θ angle. Groups of similar patterns identified in different passages are also marked there.

We see that for the 5th diffuse-specular pattern in different passages the range of values of the angle θ was 10 degrees, and the range of values of the phase angle was 18.6 degrees. Despite this, the scatter of individual positions of the corresponding PAB vectors in Fig. 6a) and 6b) did not exceed 0.5 degrees, which means that the patterns were correctly identified on five different light curves. At the same time, for the patterns of the 6th type, the spread of positions of the PAB vectors in Fig. 6 is quite large, which is apparently due to the wide range of realized values of the phase angle: they are almost 28° (the values of the angle θ are limited to a range of only 6.3°). For the specular types of patterns, the values of the phase angle and the angle θ do not affect the presence of the flare on the light curves and, accordingly, the shape of the pattern. It is illustrated by a fairly wide range of realized values of these parameters, for example, for the 1st and 3rd patterns.

It is worth paying attention to the preserved sequence of the corresponding pattern appearance on the light curves in different passages. It is of course determined by the shape of the model body and the same direction of change in the PAB latitude in the overlapping ranges.

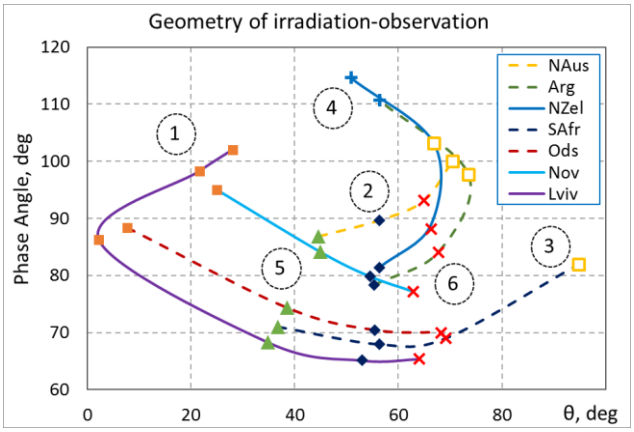

Figure 7: Geometrical conditions of illumination and visibility of the spacecraft model, realized in the described simulation experiment, in the form of trajectories in the parameter space "phase angle – angle θ" for the moments of appearance of patterns identified in different passes. Different types of patterns are depicted by different symbols, and their type (according to Table 3) is indicated by numbers in an oval.

6. Conclusions

The new method proposed in (Koshkin et al., 2024) for estimating the direction in space of the rotation axis of a complex-shaped SO rotating fairly quickly relative to the duration of passage over observation point requires verification on sets of photometric data of different types. In this paper, synthetic light curves of the SO model are used as input data for estimating the coordinates of the pole of the rotation axis. The light curves of the used model have a complex structure and contain, in addition to the diffuse component, also a significant number of short-term "specular" brightness flares. Over a time interval of about 14 hours, a set of seven simulated light curves was obtained for seven OPs located both in the northern hemisphere (within Ukraine) and in the southern hemisphere (widely distributed in longitude).

For all calculations of these synthetic light curves, it was assumed that the model rotates about one axis, fixed both in the body and unchanging in space. 30 short sections (less than the duration of one SO revolution) are identified on the light curves, and based on their similarity they are classified into six groups. For the average moments of their appearance on the light curves, the coordinates of the PAB were calculated and they were used to determine the direction (pole) of the model rotation axis. Comparison of the estimates of the rotation axis pole position obtained using different sets of photometric patterns with a given pole value used to calculate the light curves shows different values of the residuals for different sets of input data. The best result was obtained for photometric patterns containing at least two specular flares (types 1-4, 18 patterns in total) with a deviation from the true pole position of 2.6 degrees. The largest deviation from the true pole (about 19 degrees) was obtained for diffuse-specular patterns of types 5 and 6 (4 and 8 patterns, respectively).

Thus, this numerical experiment shows that diffuse-specular patterns similar in structure are successfully detected, which allows them to be used to determine the pole of rapidly rotating RSOs.

It should be emphasized once again that the change in the pattern of the light curves is determined by the ratio of the SO rotation speed and the rate of change of the PAB latitude in a given passage. The latter parameter is exactly the variable that determines which elements of the structure at a given moment reflect light specularly in the direction of the observer. However, the rotation of the object around its axis is an independent process and at the moments when the same values of the PAB latitude are reached, the same phases of the object rotation are not necessarily observed. This is the main fundamental reason for the errors in choosing the optimal moments of time and the corresponding PAB vectors, and, ultimately, in determining the orientation of the SO rotation axis by this method. Nevertheless, the considered method of photometric patterns can find wide application for various objects in orbit if there is a sufficient number of light curves for such an analysis, obtained in the tracking mode by a distributed network of observatories over a short period of time.

References

https://help.autodesk.com/view/3DSMAX/2023/ENU/
https://space.skyrocket.de/doc_sdat/dmsp-5d2.htm
Koshkin N.I., et al.: 2017, *OAP*, **30**, 226; 10.18524/1810-4215.2017.30.117655.
Koshkin N. (ed.), et al.: 2021, ATLAS of light curves of space objects Odessa I.I. Mechnikov national univ., Ukraine research inst. "Astronomical observatory", Dep. of space research. – Odesa, 2021. – Part 6 (2019 – 2020). – 200 p.; 10.18524/Atl_v.6(2019-2020).2021
Koshkin, N.I., Melikyants S., et al.: 2019, *OAP*, **32**, 158; 10.18524/1810-4215.2019.32.183899.
Koshkin N., Shakun L., et al.: 2018, *OAP*, **31**, 179; 10.18524/1810-4215.2018.31.147807.
Koshkin N., Shakun L., et al.: 2024, *AdSpR*, **74**, 11, 5725; 10.1016/j.asr.2024.08.038.
Kudak V., et al.: 2024, *ArtSat*, **59**, Iss. 2, 42; 10.2478/arsa-2024-0003.

https://doi.org/10.18524/1810-4215.2024.37.313465

DETERMINATION OF THE ROTATION PERIOD OF ASTEROIDS FROM A SHORT SERIES OF BRIGHTNESS OBSERVATIONS UNEVENLY SPREAD OVER A LONG TIME INTERVAL

D.Svincicka, I.Eglītis

Institute of Astronomy, University of Latvia,
3 Jelgavas St, Riga, LV-1004, Latvia,
darja.svincicka@gmail.com, ilgmars.eglitis@lu.lv

ABSTRACT. The main belt asteroids, situated between two planets (Jupiter and Mars), are subject to a significant influence from these planets (Mars-crossers by Mars), as well as from other planets. This is particularly concerning in the case of asteroids with small asteroid-Earth minimum orbit intersection distances (MOIDs), as these have the potential to pose a significant hazard to Earth. In this study, we present light curves for 15 main belt and Mars-crossing asteroids with small asteroid-Earth MOIDs, which are smaller than 1.1 AU. These asteroids are particularly likely to become Earth-crossing or near-Earth asteroids. In order to obtain brightness measurements, photometry was performed using CCD images captured by the Baldones Schmit telescope (1.2-metre mirror, equipped with two STX-16803 CCDs). The light curves were obtained by comparing the brightness of the asteroids with the Sun-like colour index of five to six stars, processed with MaxIm DL. The remaining brightness measurements are derived from the Minor Planet Center (MPC) database, based on data from 18 observatories and the Transiting Exoplanet Survey Satellite (TESS). The brightness measurements are only complementary to the asteroid position measurements. Therefore, these brightness measurements are typically not very precise and are separated by different time intervals that may be quite extensive. In order to find the asteroid rotation period, it is sometimes necessary to employ data correction as well as programs that are able to identify the period in unevenly scattered data. Our analysis employed the Lomb–Scargle method, which identified period values for 14 of the asteroids. The method can be used to obtain results for the simple rotations of asteroids, provided that the asteroids are observed in phases within the range of 7 and 40 degrees, that their shape is nearly an elongated ellipsoid, and that their rotation axes are almost perpendicular to their heliocentric orbital planes.

Keywords: photometry, asteroids, Lomb–Scargle method, rotation period.

АНОТАЦІЯ. Астероїди головного поясу, розташовані між двома планетами (Юпітером і Марсом), схильні до значного впливу з боку цих планет (марс-кросери по Марсу), а також з боку інших планет. Це особливо викликає занепокоєння у випадку астероїдів з малими MOID (мінімальними відстанями перетину орбіт астероїдів і Землі), оскільки вони потенційно можуть становити значну небезпеку для Землі. У цій роботі ми представляємо криві блиску для 15 астероїдів головного поясу та астероїдів, що перетинають Марс, з малими MOID астероїд-Земля, меншими за 1,1 а.о. Ці астероїди з великою ймовірністю стануть астероїдами, що перетинають Землю або навколоземні. Для отримання вимірювань яскравості було проведено фотометрію з використанням CCD-зображень, отриманих телескопом Baldones Schmit telescope (1,2 м дзеркало, оснащене двома ПЗЗ-матрицями STX-16803). Криві блиску були отримані шляхом порівняння яскравості астероїдів із сонцеподібним колір-індексом п'яти-шести зір, обробленим за допомогою MaxIm DL. Решта вимірювань яскравості отримані з бази даних Центру малих планет (MPC) на основі даних 18 обсерваторій та супутника Transiting Exoplanet Survey Satellite (TESS). Вимірювання яскравості лише доповнюють вимірювання положення астероїда. Тому ці вимірювання яскравості, як правило, не дуже точні та розділені різними часовими інтервалами, які можуть бути досить великими. Для того, щоб знайти період обертання астероїда, іноді необхідно використовувати корекцію даних, а також програми, які здатні ідентифікувати період у нерівномірно розкиданих даних. У нашому аналізі використовувався метод Ломба–Скаргла, який визначив значення періоду для 14 астероїдів. Цей метод може бути використаний для отримання результатів для простих обертань астероїдів за умови, що астероїди спостерігаються з фазами в діапазоні від 7 до 40 градусів, що їхня форма – майже витягнутий еліпсоїд, і що їхні осі обертання майже перпендикулярні до їхніх геліоцентричних орбітальних площин.

Ключові слова: фотометрія, астероїди, метод Ломба–Скаргла, період обертання.

1. Introduction

The influence of planets on asteroids can result in significant alterations to their orbits. These influences include gravitational perturbations (Nesvorný et al., 2002; Morbidelli et al., 2002) and orbital resonances (Nesvorný

et al., 2002). The Yarkovsky (and YORP) effect (Bottke, 2006) can assist in this process, exerting a particularly strong influence on asteroids with a diameter of less than 40 km. It is of great importance to study those asteroids with small asteroid-Earth MOIDs, since they are particularly unstable and the most likely to evolve into Earth crossers and near-Earth asteroids (NEAs) over time.

We present a method for analysing asteroids using brightness measurements, that are available alongside positional measurements. The principal objective of these observations is to obtain position measurements. These observations are typically conducted on several occasions throughout the night, over the course of several nights, with an inter-measurement interval of approximately 5–30 minutes. It should be noted that observations are frequently separated by a considerable interval of time, even spanning years and may be lacking sufficient precision due to external factors such as weather conditions or overexposure.

Subsequently, the data are corrected so that the resulting light curves are dependent solely on the rotation period (Zeigler & Hanshaw, 2016). Moreover, when constructing phase-magnitude diagrams, any brightness values that deviate by more than three standard deviations per night are removed, as they are likely to be the result of an error.

A period search was conducted using the Lomb Scargle program from the astropy package in Python (Astropy Collaboration, 2024), which was incorporated into the Python script written at the Institute of Astronomy. The Lomb Scragle method was selected due to its capacity to analyse unevenly sampled data and to perform an analytical analysis of white noise, thereby highlighting only those spikes that are significant. It is possible that erroneous strikes may be observed as a result of factors such as observation periodicity, alliance frequencies, or other effects (VanderPlas, 2018). In order to ascertain the correct period, a Gaussian shape spike exceeding a significant power of 0.2 was sought.

The final period was calculated using the results from all observatories, weighted according to the number of observations, peak power, and deviation from the linear phase-magnitude diagram relationship.

2. Results

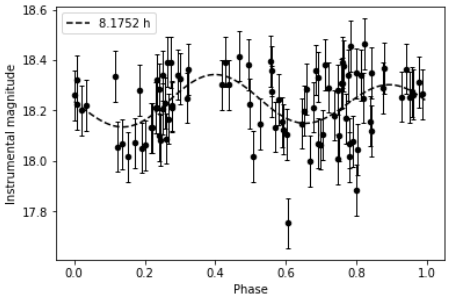

Figure 1: The light curve of asteroid 1205, observed at observatory W68 in the O-band.

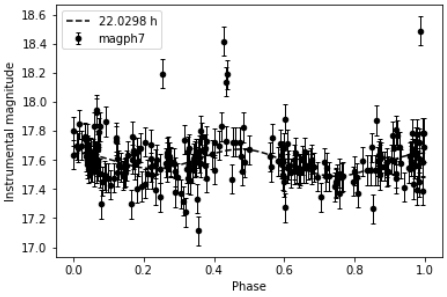

Figure 2: The light curve of asteroid 1779, observed at observatory T05 in the O-band. P_w= 22.071 ± 0.072 h

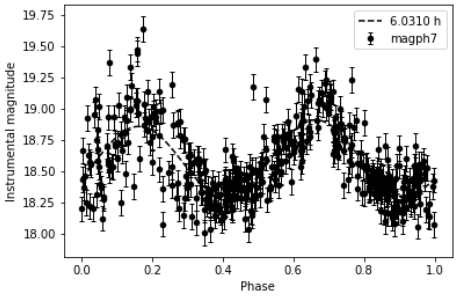

Figure 3: The light curve of asteroid 1818, observed at observatory T08 in the O-band. P_w= 6.031 ± 0.001 h

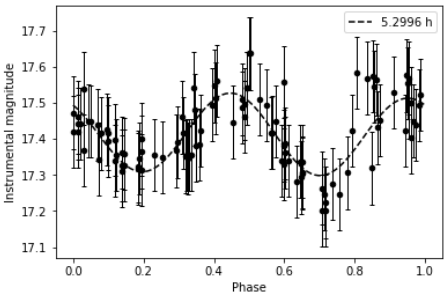

Figure 4: The light curve of asteroid 1951, observed at observatory I41 in the R-band. P_w=5.306 ± 0.007 h

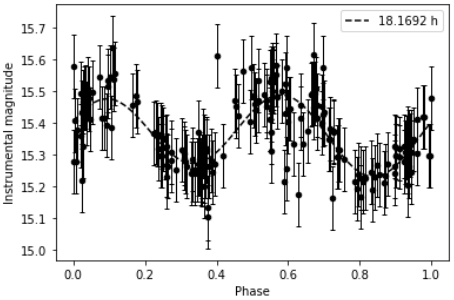

Figure 5: The light curve of asteroid 1963, observed at observatory M22 in the O-band. P_w= 18.181 ± 0.012 h

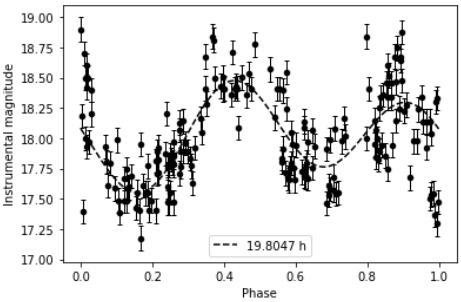

Figure 6: The light curve of asteroid 2128, observed at observatory T05 without the use of a filter. P_w= 19.777 ± 0.097 h

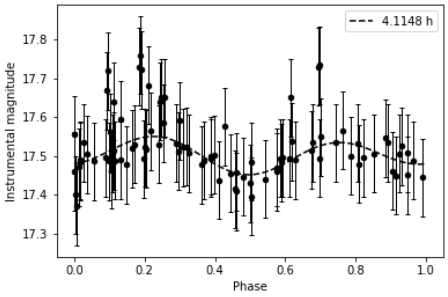

Figure 7: The light curve of asteroid 2134, observed at observatory I41 in the R-band. P_w= 4.113 ± 0.003 h

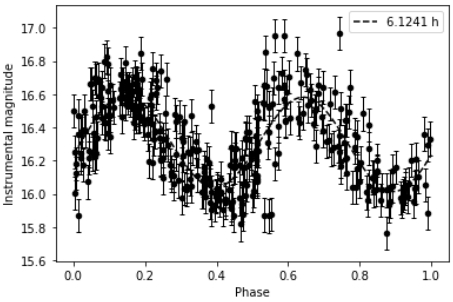

Figure 8: The light curve of asteroid 2150, observed at observatory T05 in the O-band. P_w=6.125 ± 0.005 h

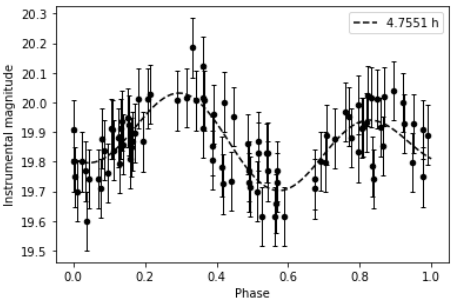

Figure 9: The light curve of asteroid 2174, observed at observatory G96 in the G-band. P_w= 4.785 ± 0.006 h

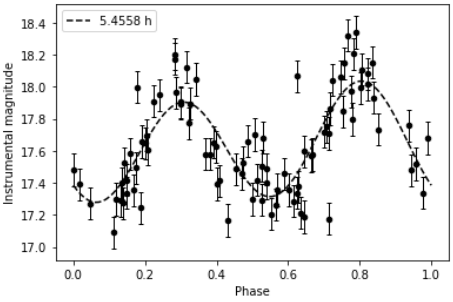

Figure 10: The light curve of asteroid 2318, observed at observatory W68 in the O-band. P_w= 5.458 ± 0.002 h

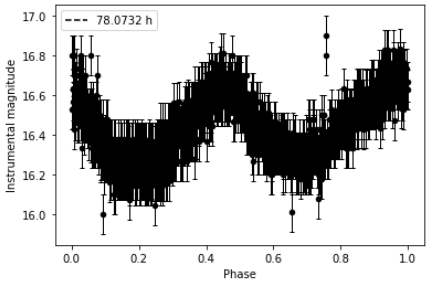

Figure 11: The light curve of asteroid 2497, observed at observatory TESS in the G-band. P_w= 77.760 ± 0.065 h

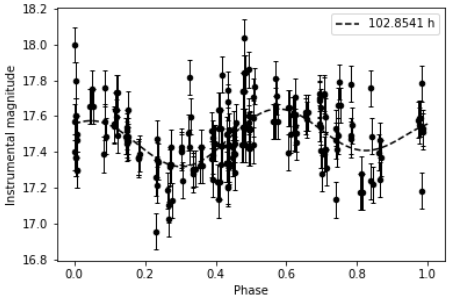

Figure 12: The light curve of asteroid 2503, observed at observatory T05 in the O-band. P_w= 102.984 ± 0.101 h

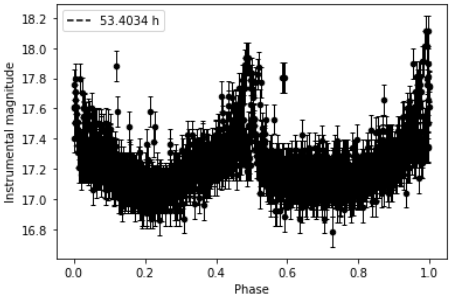

Figure 13: The light curve of asteroid 2538, observed at observatory TESS in the G-band. P_w= 53.401 ± 0.033 h

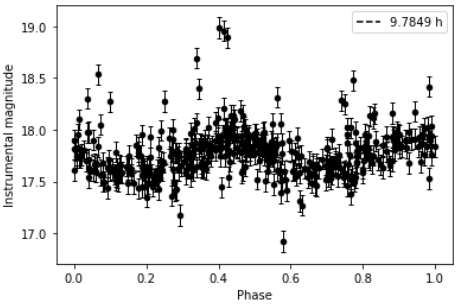

Figure 14: The light curve of asteroid 2539, observed at observatory T08 in the O-band. P_w= 9.789 ± 0.008 h

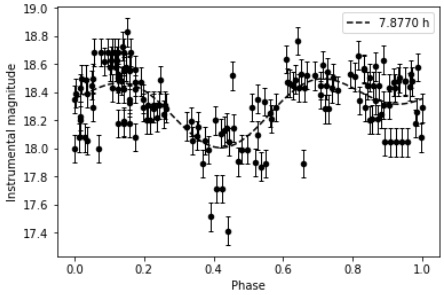

Figure 15: The light curve of asteroid 2583, observed at observatory 703 in the G-band. P_w= 7.790 ± 0.001 h

3. Conclusion

We employed a combination of CCD photometry and MPC brightness data to obtain brightness measurements, which were subsequently corrected and used to derive light curves for 15 asteroids. Subsequently, the Lomb–Scargle method was employed, resulting in the determination of a period for fourteen asteroids. However, insufficient data was available for asteroid 1205 to yield a reliable result. Our findings were compared with those of other authors. The periods were known for five of the

asteroids, four of which were in agreement, but the period of one 2174 asteroid was inconsistent with our value. This may be due to limitations in our methodology. The rotational periods of asteroids can be determined using this approach, provided they exhibit simple rotation, are observed during phases within 7 to 40 degrees, are elongated ellipsoids, and have nearly perpendicular rotation axes to their heliocentric plane.

References

Astropy Collaboration: 2024, Lomb–Scargle Periodograms, [online] Available at: (https://docs.astropy.org/en/stable/timeseries/lombscargle.html) [Accessed 14 Oct. 2024].

Bottke W.F., Vokrouhlický D., Rubincam D.P., Brož M.: 2006, *AREPS*, **34**, 157.

Minor Planet Center: MPC Archive Database, [online] Available at: (https://minorplanetcenter.net/iau/ECS/MPCArchive/MPCArchive_TBL.html) [Accessed 14 Oct. 2024].

Morbidelli A., Bottke W.F., Froeschlé C., Michel P.: 2002, in Asteroids III /eds. Bottke W.F. et al., (Univ. Arizona Press, Tucson), 409.

Nesvorný D., Bottke W.F., Dones L., Levison H.F.: 2002, in Asteroids III /eds. Bottke W.F. et al., (Univ. Arizona Press, Tucson), 379.

VanderPlas J.T.: 2018, *ApJS*, **236**, 1, art, id 16.

Zeigler K., Hanshaw B.: 2016, *MPBu*, **43**, 199.

https://doi.org/10.18524/1810-4215.2024.37.313921

ASTROMETRY OF NASA LUCY MISSION TARGETS (617) PATROCLUS, (3548) EURYBATES, AND (21900) ORUS AT OPPOSITION 2021

V. Troianskyi [1,2,3], H. Okhotko [3,4], V. Kashuba [3], S. Udovichenko [3], L. Keir [3,4], Ya. Romanyuk [5], V. Savanevych [6], S. Khlamov [7], A. Briukhovetskyi [8], V. Zhukov [5], I. Lishchynskyi [2], O. Poplavskyi [2], T. Trunova [7]

[1] Astronomical Research Station of Vasyl Stefanyk Precarpathian National University, 57 Shevchenko St, Ivano-Frankivsk, 76018, Ukraine, *volodymyr.troianskyi@pnu.edu.ua*

[2] Department of Physics and Methods of Teaching, Faculty of Physics and Technology, Vasyl Stefanyk Precarpathian National University, 57 Shevchenko St, Ivano-Frankivsk, 76025, Ukraine

[3] Astronomical Observatory of Odesa I. I. Mechnikov National University, 1v Marazliivska St, Odesa, 65014, Ukraine, *v.troianskyi@onu.edu.ua*

[4] Department of Physics and Astronomy, FMPIT, Odesa I. I. Mechnikov National University, 42 Pastera St, Odesa, 65082, Ukraine

[5] Main Astronomical Observatory of the National Academy of Sciences of Ukraine, 27 Akademika Zabolotnoho St, Kyiv, 03143, Ukraine

[6] Department of Systems Engineering of Kharkiv National University of Radio Electronics, 14 Nauki Ave, Kharkiv, 61166, Ukraine

[7] Department of Media Systems and Technologies of Kharkiv National University of Radio Electronics, 14 Nauki Ave, Kharkiv, 61166, Ukraine

[8] Western Radio Technical Surveillance Center, State Space Agency of Ukraine, Kosmonavtiv St, Mukachevo, 89600, Ukraine

ABSTRACT. In this paper we present the result of the combined use of the OMT-800, AZT-3, KIT telescopes, and the Lemur software of the CoLiTec project. The paper considers in detail several of the astrometric observations of Jupiter Trojan asteroids: (617) Patroclus, (3548) Eurybates, and (21900) Orus from a long list of small bodies of the Solar System.

Keywords: minor planets, asteroids, observations.

АНОТАЦІЯ. Місія Lucy складається з п'яти прольотів повз троянські астероїди Юпітера, з метою дослідження відмінностей у поверхневих та внутрішніх властивостях цієї популяції. Під час п'яти прольотів ми зможемо спостерігати вісім троянських астероїдів.

У статті детально розглянуто астрометричні спостереження троянських астероїдів Юпітера: (617) Patroclus, (3548) Eurybates і (21900) Orus з метою підтвердження положення (орбіти) астероїдів.

Астрометричні спостереження проводилися протягом 11 ночей на двох обсерваторіях: обсерваторії Одеса–Маяки та Київській кометній станції. У роботі представлено результати спільного використання телескопів OMT-800, AZT-3, KIT та сучасного програмного забезпечення Lemur проекту Collection Light Technology (CoLiTec). Стандартні астрономічні спостереження та обробку зображень виконано за допомогою CoLiTec.

Астероїд (617) Patroclus спостерігався в ніч з 16 на 17 квітня 2021 року в обсерваторії Одеса-Маяки. В результаті спостережень отримано 15 позицій астероїда. Астероїд (3548) Eurybates спостерігався сім ночей (312 позицій) у 2021 році телескопами OMT-800 та AZT-3. Додаткові спостереження цього астероїда проводилися в ніч з 26 на 27 грудня 2021 року на Київській кометній станції. Зібрані дані дають нам можливість визначити 58 положень астероїда за цю ніч. Астероїд (21900) Orus спостерігався в ніч з 17 на 18 жовтня 2021 року телескопом AZT-3 (24 позиції) та в ніч з 27 на 28 жовтня 2021 року телескопом OMT-800 (4 позиції).

У статті представлено астрономічні зображення астероїдів (617) Patroclus, (3548) Eurybates і (21900) Orus у програмі перегляду зображень LookSky програмного

комплексу Lemur. В результаті до бази даних MPC додано усі астрометричні спостереження даних астероїдів.

Ключові слова: малі планети, астероїди, спостереження.

1. Introduction

The Lucy mission (Levison & Lucy Science Team, 2016) consists of five flybys of Trojan asteroids to investigate the differences in surface and internal properties across the population of Trojan asteroids. From these five encounters we will be able to observe eight Trojan asteroids: (3548) Eurybates and its small satellite Queta, (15094) Polymele and its satellite Shaun, (11351) Leucus, (21900) Orus, (617) Patroclus, and Meneotius.

We make astrometric observations of selected targets ((617) Patroclus, (3548) Eurybates, (21900) Orus) to confirm the position (orbit) of asteroids.

2. Observations

Astrometric observations were carried out for 11 nights at the two observatories, namely the Odesa–Mayaky Observatory [code: 583], and the Kyiv Comet Station [code: 585].

2.1. Odesa–Mayaky Observatory

Observations were also made on the OMT-800 and AZT-3 telescopes (Astronomical Observatory of Odesa I. I. Mechnikov National University), which is installed at the Mayaky observation station:

- The OMT-800 telescope (Andrievsky et al., 2013; Troianskyi et al., 2014) has 0.8-m main hyperbolic mirror and effective focus ratio f = 1/2.7. As an imaging detector, the FLI ML09000 camera together with a four-lens field corrector, is installed at the primary focus providing a field of view of 58.6'×58.6' and has an image scale of 1.15 arcsec/pixel. All series of images were obtained in the sensitivity band of the sensor without the use of photometric filters;
- Reflector AZT-3 (Udovichenko, 2012) is a serial telescope of the Leningrad Optical Mechanical Association. A UAI CCD detector is installed on the telescope, which was created by the engineers of the Odesa Observatory. As a result, a field of view of 11.4'×8.58' and an image scale of 0.864 arcsec/pixel. All series of images were obtained with the use of *R* filter.

2.2. Kyiv Comet Station

Observations in Kyiv were made with the KIT telescope of the Main Astronomical Observatory of NASU, which is installed at the Kyiv comet station. The KIT (0.356-m, *f*/11; Romanyuk et al., 2012; Romanyuk & Vidmachenko, 2015), a serial telescope with Celestron 14-inch optical tube installed with the White Swan-240 mount made in Ukraine by Sergii Verbytskyi. As an imaging detector the SBIG ST-8XME camera provides a field of view of 12.3'×8.2' and an image scale of 1.44 arcsec/pixel. All series of images were obtained with the use of *BVRI* filters.

3. Results

We did the standard astronomical observations and image processing using the modern Lemur software of the Collection Light Technology (CoLiTec) project (https://colitec.space) (Khlamov et al., 2024).

The Lemur software (Khlamov et al., 2023) is designed to perform a sequence of the following main steps: preprocessing (astronomical information collection -> worst data rejection -> useful data extraction -> data mining (Khlamov et al., 2022) -> classification -> background alignment -> brightness equalization), image processing (segmentation -> typical form analysis -> recognition patterns applying -> detection of the object's image -> astrometry -> photometry -> objects identification -> tracks detection) (Savanevych et al., 2023), knowledge discovery (Solar System objects or artificial satellites to be discovered, tracks parameters for the investigation, light curves of the variable stars, scientific reports in the international formats) (Khlamov & Savanevych, 2020).

For the astronomical reduction of the raw data, we used bias subtracting, dark subtracting and flat-fielding. For details see Oszkiewicz et al. (2019; 2020; 2021; 2023), Savanevych et al. (2022), and Troianskyi et al. (2023a,b).

In Table 1 presents the accuracy of our observations. Where: Signal-to-Noise Ratio (SNR) - the most important quantity for astronomical observations, the ratio of the signal from an astronomical source to the noise, represented in ADU (Analogue-to-Digital Unit); Full Width at Half Maximum (FWHM in units of pixel) - is a measure of the width of an intensity distribution at the point where the intensity is at its highest; Astrometric observation residuals (normalized value of the root mean squared absolute error; RMS) are the difference between an observed and a calculated position (this is known as an O–C residual).

Table 1: Observation accuracy

Asteroid	**SNR [ADU]**	**FWHM [pix]**	**RMS Residuals by RA [arcsec]**	**RMS Residuals by DE [arcsec]**
(617) Patroclus	350.2	5.20	0.500	0.404
(3548) Eurybates	101.2	2.60	0.565	0.211
(21900) Orus	274.8	3.35	0.489	0.156

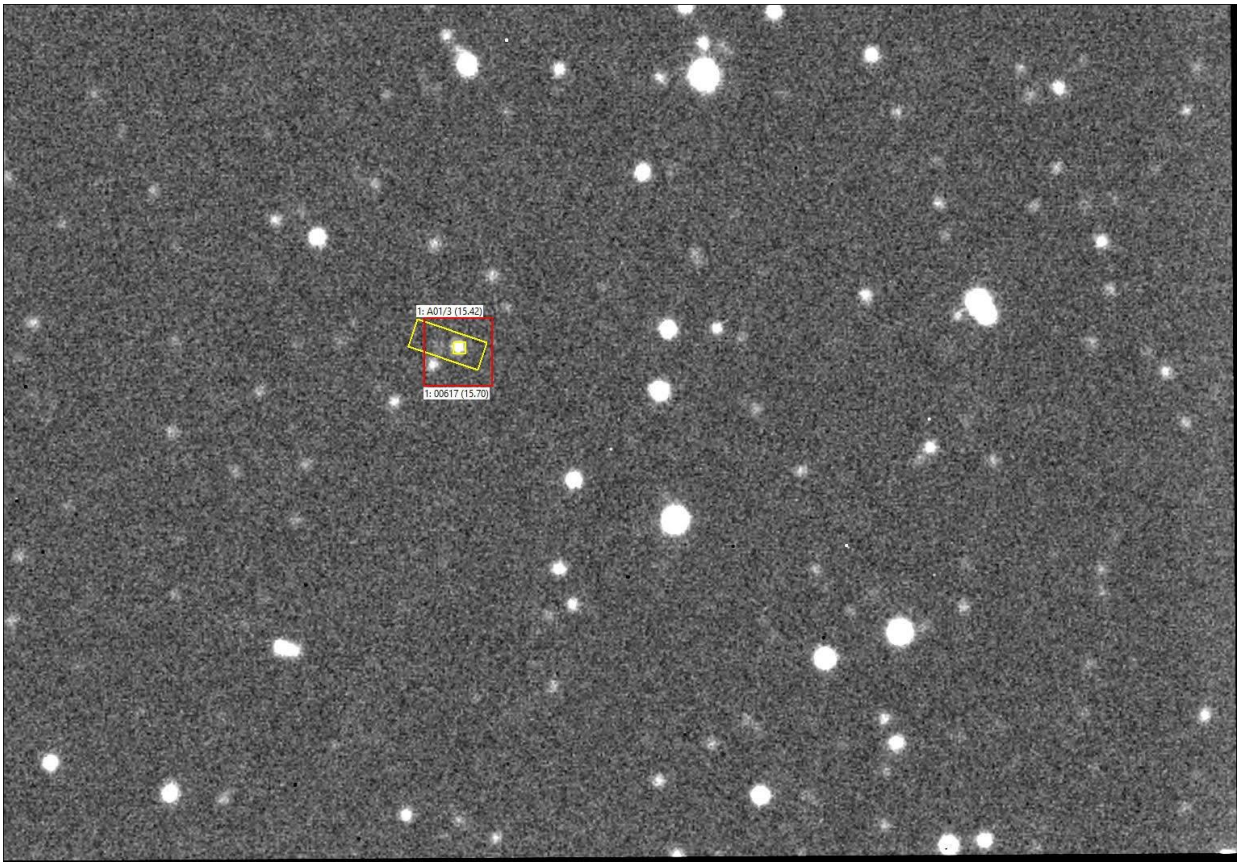

Figure 1: The observed asteroid (617) Patroclus by the AZT-3 telescope

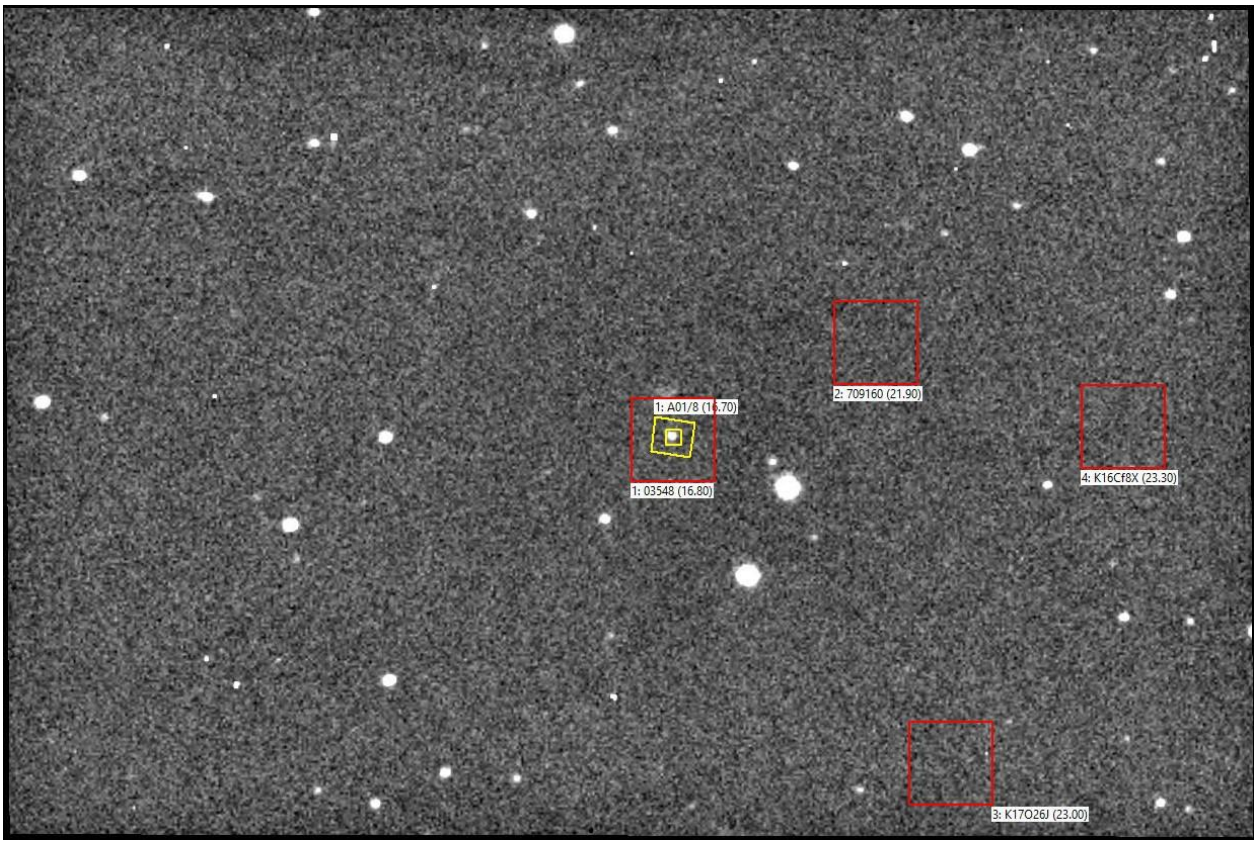

Figure 2: The observed asteroid (3548) Eurybates by the KIT telescope

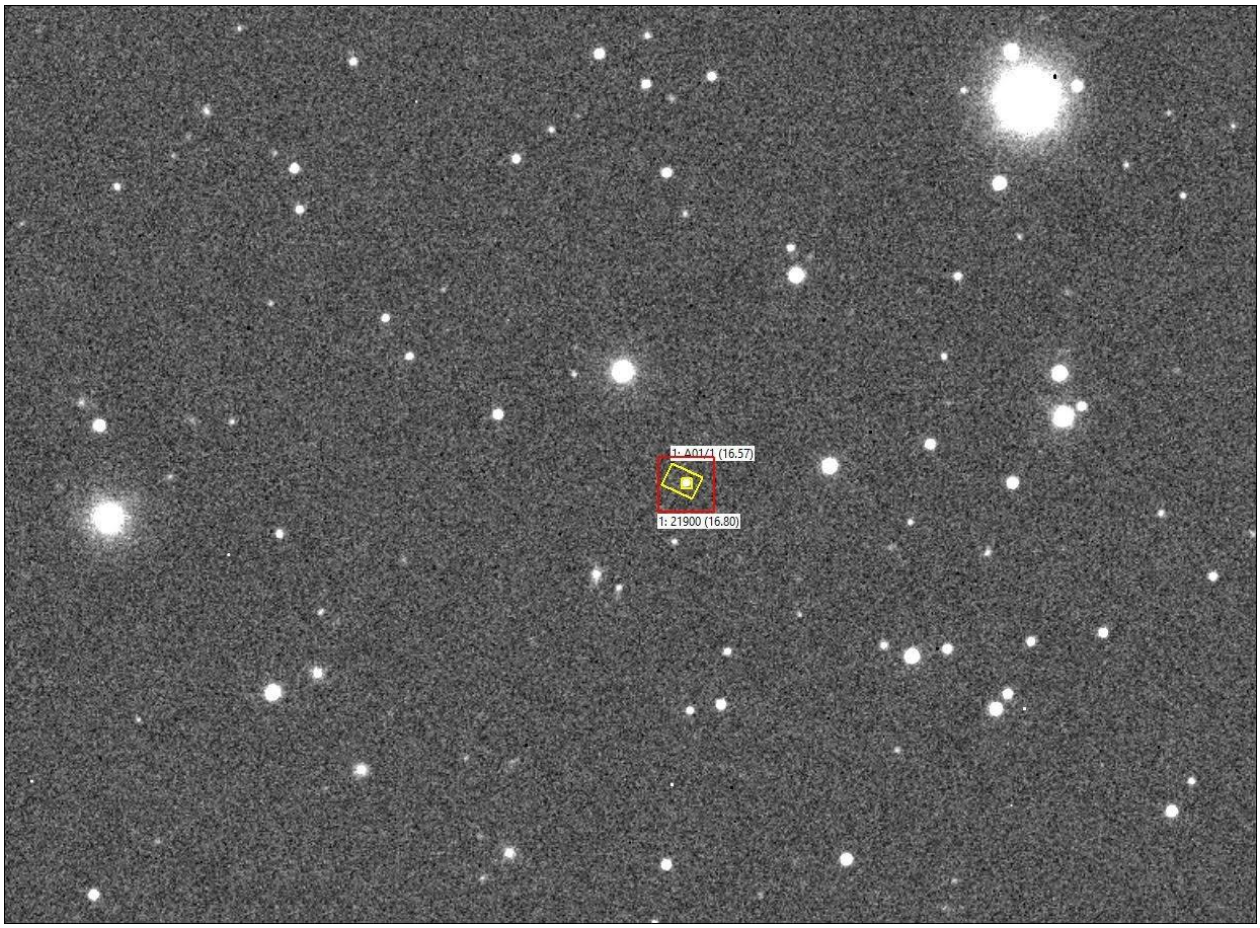

Figure 3: The observed asteroid (21900) Orus by the OMT-800 telescope

3.1. Asteroid (617) Patroclus

Jupiter Trojan asteroid (617) Patroclus was observed during 16th/17th of April 2021 night on Odesa–Mayaky Observatory. As a result, observations of 15 positions, which were obtained on the AZT-3 telescope, were added to the MPC database (https://www.minorplanetcenter.net; MPS 2117685).

An astronomical image of the detected asteroid (617) Patroclus in the LookSky image viewer tool of the Lemur software package is presented in Fig. 1.

3.2. Asteroid (3548) Eurybates

Jupiter Trojan asteroid (3548) Eurybates was observed seven nights (312 positions) in 2021 by the OMT-800 and AZT-3 telescopes at Odesa-Mayaky Observatory. All points added to the MPC database.

Additional observations of this asteroid were done during 26th/27th of December 2021 night on Kyiv comet station. Collected data give us a possibility to determine 58 positions of the asteroid for this night.

An astronomical image of the detected asteroid (3548) Eurybates in the LookSky image viewer tool of the Lemur software package is presented in Fig. 2. All these observations were published in Minor Planet Supplement (see details in MPS 1497901, MPS 1497902, MPS 1518978, MPS 2118348, MPS 2118349, MPS 2118350).

3.3. Asteroid (21900) Orus

Jupiter Trojan asteroid (21900) Orus was observed during 17th / 18th of October 2021 night by the AZT-3 telescope (24 positions) and during 27th/28th of October 2021 night by the OMT-800 telescope (4 positions).

An astronomical image of the detected asteroid (21900) Orus in the LookSky image viewer tool of the Lemur software package is presented in Fig. 3. All points added to the MPC database (MPS 1499517, MPS 2132569).

4. Conclusion

The combined use of the OMT-800, AZT-3, KIT telescopes, and the CoLiTec/Lemur software showed good results for the astrometry of the small bodies in the Solar System.

Astrometric observations are very important for accurate calculations of ephemeris of studied objects and for further research (numerical integration of orbits) of small bodies of the Solar System (Troianskyi & Bazyey, 2018; Troianskyi et al., 2022; Troianskyi et al., 2023a).

Acknowledgements. VT was supported by the National Scholarship Programme of the Slovak Republic – academic year 2023/2024.

References

Andrievsky S.M., et al.: 2014, *OAP*, **26**, 6-25.

Khlamov S. & Savanevych V.: 2020, Knowledge Discovery in Big Data from Astronomy and Earth Observation, 1st Edition. Edited by Petr Skoda and Fathalrahman Adam. (Elsevier), 331

Khlamov S., et al.: 2022, *CEUR Workshop Proceedings*, **3171**, 1043-1055.

Khlamov S., et al.: 2023, *Proceedings of the 6th IEEE UkrMiCo*, 5-8.

Khlamov S., et al.: 2024, Measurements and Instrumentation for Machine Vision, Chapter 12: (CRC Press, Taylor & Francis Group), 269.

Levison H.F., Lucy Science Team: 2016, *47th Annual Lunar and Planetary Science Conference*, **1903**, 2061.

Oszkiewicz D., et al.: 2019, *A&A*, **632**, A170.

Oszkiewicz D., et al.: 2020, *A&A*, **643**, A117.

Oszkiewicz D., et al.: 2021, *Icarus*, **357**, id.114158.

Oszkiewicz D., et al.: 2023, *Icarus*, **397**, id.115520.

Romanyuk Ya.O., et al.: 2012, *ASInC*, **7**, 297.

Romanyuk Ya.O., Vidmachenko A.P.: 2015, *AstSR*, **11(2)**, 157-162.

Savanevych V.E., et al.: 2022, *A&C*, **40**, 100605.

Savanevych V.E., et al.: 2023, *Math*, **11 (10)**, 2246.

Troianskyi V.V., et al.: 2014, *OAP*, **27**, 154-155.

Troianskyi V.V., Bazyey O.A.: 2018, *CoSka*, **48**, 356-380.

Troianskyi V., Kankiewicz P., Oszkiewicz D.: 2022, *16th Europlanet Science Congress 2022, Spain*, id.EPSC2022-888.

Troianskyi V., Kankiewicz P., Oszkiewicz D.: 2023, *A&A*, **672**, A97.

Troianskyi V., et al.: 2023a, *CoSka CoSka* **53(2)**,

Troianskyi V., et al.: 2023b, *2023 IEEE 18th International Conference on Computer Science and Information Technologies (CSIT)*, 1.

Udovichenko S.N.: 2012, *OAP*, **25**.

RADIO ASTRONOMY

https://doi.org/10.18524/1810-4215.2024.37.313757

EVOLUTION OF THE JET EMISSION OF RADIO SOURCES WITH THE STEEP LOW-FREQUENCY SPECTRA

A.P. Miroshnichenko

Institute of Radio Astronomy of the NAS of Ukraine,
Kharkiv, Ukraine, *a.p.miroshnichenko@gmail.com*

ABSTRACT. We suppose the relation of source emission at the decameter and infrared bands as the estimate of the jet structure contribution relatively the central region of the source. This relation is examined for the sample of galaxies and quasars with steep low-frequency spectra from the UTR-2 catalogue. We have derived the relations of corresponding flux densities (at the frequency 25 MHz and at the frequency $1.38 \cdot 10^{14}$ Hz (near-infrared band)) and their connection with source's redshifts, characteristic ages, jet propagation velocities. At the same value of the jet emission relation (at the separate value of this relation) the very close values of the characteristic age and the jet propagation velocity are derived for the examined galaxies and quasars with the same steep-spectrum type. So, the evolution of the galaxies and quasars with the steep linear radio spectrum (type S) may be similar. Analogously, one is similar for galaxies and quasars with the steep break radio spectrum (type C+). The considered relations have positive correlation for the corresponding redshifts, the jet propagation velocity. The radio sources with the steep linear spectrum display the smaller characteristic age ($\sim 10^7$ years) than ones with the steep break spectrum ($\sim 10^8$ years). And the obtained mean values of the jet propagation velocity for the examined galaxies and quasars with the steep linear spectrum ($\sim 10^9$ cm/s) are more by one order than these for the examined galaxies and quasars with the steep break spectrum ($\sim 10^8$ cm/s). The derived results may evidence for the cyclic activity of the steep-spectrum radio sources.

Keywords: steep-spectrum radio sources, jets, galaxies, quasars, characteristic age of radio sources.

АНОТАЦІЯ. Ми припускаємо, що відношення випромінювання джерела в декаметровому та інфрачервоному діапазонах є оцінкою внеску джетової структури відносно центральної області джерела. Це відношення досліджується для вибірки галактик і квазарів з крутими низькочастотними спектрами з каталогу УТР-2. Ми отримали відношення відповідних густин потоків (на частоті 25 МГц та в близькому інфрачервоному діапазоні $1{,}38 \cdot 10^{14}$ Гц) та їх зв'язок з червоним зміщенням джерел, їхнім характерним віком, швидкістю поширення джетів. При однаковій величині відношення для випромінювання джетів (при виділеному значенні цього відношення) отримано дуже близькі величини характерного віку і швидкості поширення джетів для досліджуваних галактик і квазарів з однаковим типом крутих спектрів. Отже, еволюція галактик і квазарів з крутим лінійним радіоспектром (тип S) може бути подібною. Аналогічно, подібна еволюція у галактик і квазарів з крутим радіоспектром зі зламом (тип C^+). Розглянуті відношення мають позитивну кореляцію для відповідних червоних зміщень, швидкості поширення джетів. Радіоджерела з крутим лінійним спектром виявляють менший характерний вік ($\sim 10^7$ років), ніж радіоджерела з крутим спектром зі зламом ($\sim 10^8$ років). А отримані середні величини швидкості поширення джетів для досліджуваних галактик і квазарів з крутим лінійним спектром ($\sim 10^9$ см/с) більші на порядок, ніж відповідні величини для досліджуваних галактик і квазарів з крутим спектром зі зламом ($\sim 10^8$ см/с). Одержані результати можуть свідчити про циклічну активність радіоджерел з крутим спектром.

Ключові слова: радіоджерела з крутим спектром, джети, галактики, квазари, характерний вік радіоджерел.

1. Introduction

As we know, the theoretical and observed data prove the central active nuclei with the supermassive black hole as the source of energy for galaxies and quasars. Studies of these objects at the different frequency ranges display that their central region (accretion disk, dust torus) is more prominent at the high frequencies (Imanishi et al., 2018). At that time, the powerful outflows from accretion disk (jets with cocoons) are more intensive at the low frequencies, corresponding to the decameter wavelength band (Miroshnichenko, 2023). To continue study the steep-spectrum sources from the UTR-2 catalogue (Braude et al., 1978, 1979, 1981, 2003) (particularly, at the frequency 25 MHz) we analyze their properties in connection with central region of a source. We suppose the relation of source emission at the decameter and infrared bands as the estimate of the jet structure contribution relatively the central region of the source.

2. Jet emission relation for the sources

From the UTR-2 catalogue we have compiled four samples (G_S, Q_S, G_{C+}, Q_{C+}) of the steep-spectrum galaxies and quasars: 78 galaxies with steep linear spectrum (radio

spectrum type S), 55 quasars with steep linear spectrum (radio spectrum type S), 54 galaxies with steep break spectrum (radio spectrum type C+), 36 quasars with steep break spectrum (radio spectrum type C+) (Miroshnichenko, 2023). We have used the NED data base for the necessary data. So, for samples G_S, Q_S, G_{C+}, Q_{C+} the relation of emission for examined sources at the decameter and infrared bands was determined as the relation $lg(S_{25}/S_{IR})$ (where S_{25} is the flux density of source at 25 MHz , S_{IR} is the flux density of the source at $1.38 \cdot 10^{14}$ Hz - NIR band). One can see the distribution of the obtained jet emission relations at the Fig. 1.

The mean values of the derived jet relations and the corresponding redshifts are:

G_S $< lg(S_{25}/S_{IR}) > = 4.58\ (\pm 0.17)$ (n = 29)

$< z > = 0.694\ (\pm 0.103)$;

Q_S $< lg(S_{25}/S_{IR}) > = 4.70(\pm 0.14)$ (n = 15)

$< z > = 1.123(\pm 0.100)$;

G_{C+} $< lg(S_{25}/S_{IR}) > = 3.67(\pm 0.19)$ (n = 24)

$< z > = 0.298(\pm 0.070)$;

Q_{C+} $< lg(S_{25}/S_{IR}) > = 4.30(\pm 0.11)$ (n = 14)

$< z > = 0.950\ (\pm 0.092)$.

Also we have determined the characteristic ages (Jamrozy et al., 2005) of examined steep-spectrum galaxies and quasars (as the time of synchrotron decay of relativistic electrons):

$$t_{syn} = 50.3 \frac{B^{1/2}}{B^2 + B_{CMB}^2} [\nu_b (1+z)]^{-1/2} ,$$

B – is the magnetic field strength of source in 10^{-5} Gauss, $B_{CMB} = 0.32(1+z)^2$ – is the equivalent magnetic field strength corresponding to intensity of microwave background, in 10^{-5} Gauss, ν_b - is the critical frequency of the synchrotron spectrum (in GHz). The value B we obtained earlier, $B \approx 10^{-5}$ Gauss (Miroshnichenko, 2012). The important characteristic of the jet structure of the source is the jet propagation velocity and it was calculated by us for the considered radio sources (Miroshnichenko, 2019; 2021).

So, the obtained mean values of the characteristic age and the jet propagation velocity for the examined steep-spectrum sources are:

G_S $< t_{syn} > = 5.22(\pm 0.36) \cdot 10^7$ (years)

Q_S $< t_{syn} > = 5.80(\pm 0.34) \cdot 10^7$ (years)

G_{C+} $< t_{syn} > = 4.74(\pm 0.41) \cdot 10^8$ (years)

Q_{C+} $< t_{syn} > = 2.02(\pm 0.25) \cdot 10^8$ (years)

G_S $< v_j > = 2.97(\pm 0.67) \cdot 10^9$ (cm/s)

Q_S $< v_j > = 3.12(\pm 0.31) \cdot 10^9$ (cm/s)

G_{C+} $< v_j > = 5.49(\pm 0.39) \cdot 10^8$ (cm/s)

Q_{C+} $< v_j > = 1.65(\pm 0.46) \cdot 10^9$ (cm/s).

Let us consider the evolution of the jet emission contribution relatively the redshift (cosmological epoch), relati-

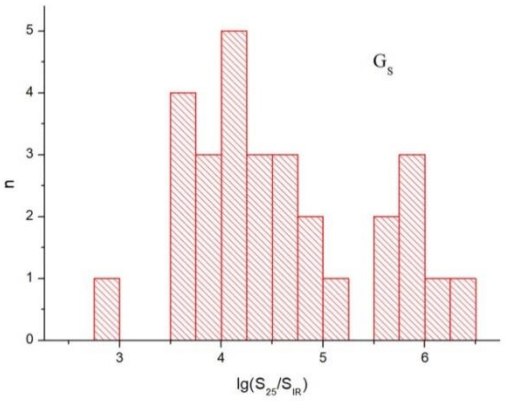

a)

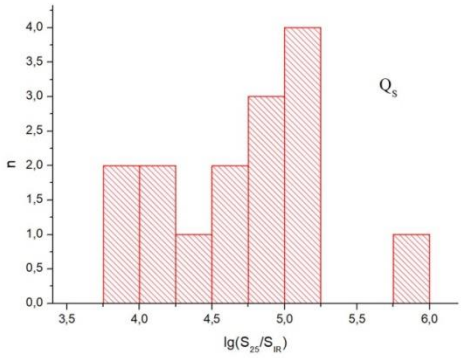

b)

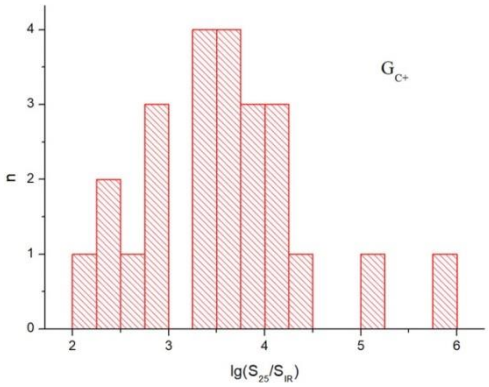

c)

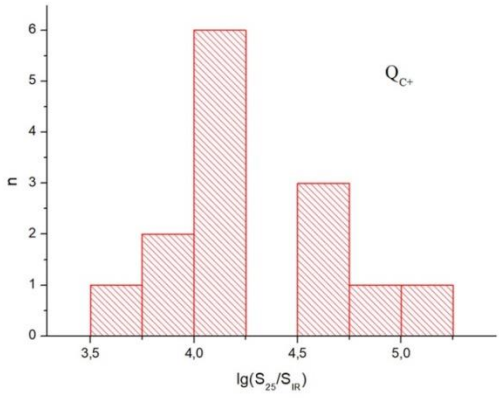

d)

Figure 1: Distribution of relation $lg(S_{25}/S_{IR})$ for examined galaxies and quasars

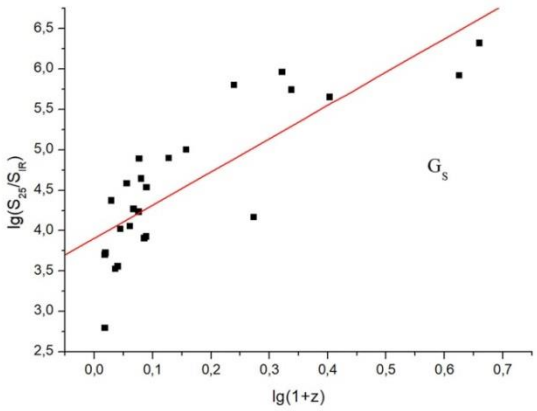

a)

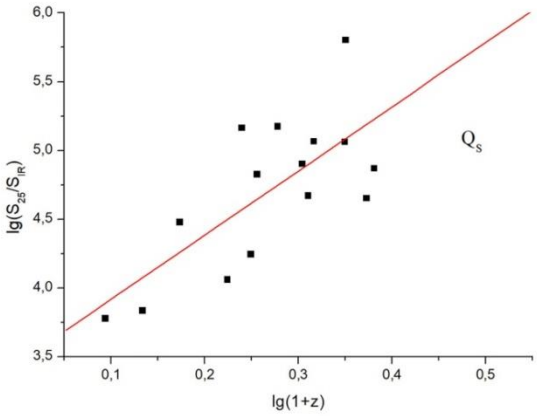

b)

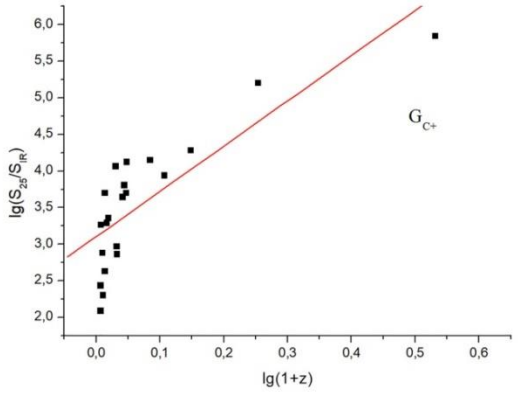

c)

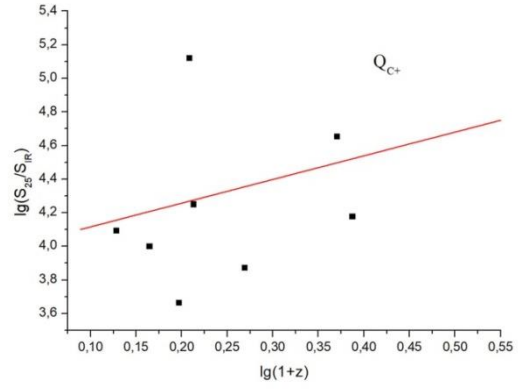

d)

Figure 2: Relation of jet contribution vs redshift

vely the jet propagation velocity. We obtain the positive correlation for the jet emission contribution and the redshift (Fig. 2), and the same for the jet propagation velocity (Fig. 3).

It is interesting to study properties of the steep-spectrum sources at the same interval of relation $lg(S_{25}/S_{IR})$. We separate the interval $lg(S_{25}/S_{IR})$ = 3,5÷3,9 and obtain such parameters for the examined galaxies and quasars, corresponding to the separate value of the jet emission relation:

G_S (n = 5)

$< lg(S_{25}/S_{IR}) > = 3.73(\pm 0.16)$

$< t_{syn} > = 5.07(\pm 2.69)\cdot 10^7$ (year)

$< v_j > = 6.63(\pm 2.30)\cdot 10^8$ (cm/s) ;

G_{C+} (n = 5)

$< lg(S_{25}/S_{IR}) > = 3.76(\pm 0.11)$

$< t_{syn} > = 5.08(\pm 2.10)\cdot 10^8$ (year)

$< v_j > = 8.21(\pm 7.32)\cdot 10^7$ (cm/s) ;

Q_S (n = 2)

$< lg(S_{25}/S_{IR}) > = 3.81(\pm 0.03)$

$< t_{syn} > = 5.94(\pm 1.23)\cdot 10^7$ (year)

$< v_j > = 1.03(\pm 0.23)\cdot 10^9$ (cm/s) ;

Q_{C+} (n = 3)

$< lg(S_{25}/S_{IR}) > = 3.78(\pm 0.09)$

$< t_{syn} > = 2.57(\pm 0.58)\cdot 10^8$ (year)

$< v_j > = 4.83(\pm 1.246\cdot 10^8$ (cm/s) .

3. Conclusion

1. The jet emission contribution relatively the central region of the radio source with steep low-frequency spectrum displays positive correlation for the corresponding redshift, for the jet propagation velocity.

2. At the same value of the jet emission contribution, the examined galaxies and quasars with the same type of radio spectrum have mutually closed values for the source's characteristic age and the jet propagation velocity. This may testify on the similar evolution for galaxies and quasars with steep low-frequency spectrum.

3. It is important, that the characteristic age of sources with the steep break spectrum (type C+) exceeds by one order the characteristic age of sources with steep linear spectrum (type S). This may be as manifestation of the cyclic activity of the examined galaxies and quasars.

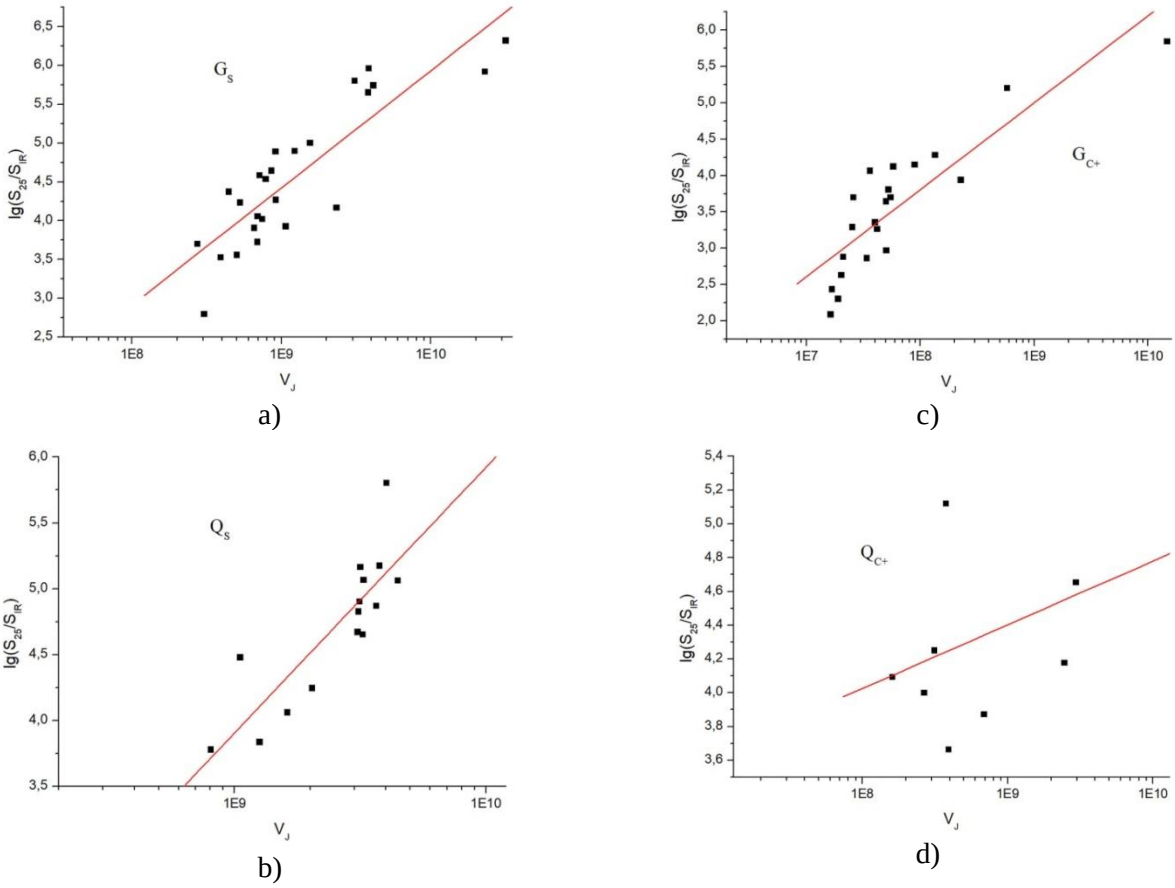

Figure 3: Relation of jet contribution vs jet propagation velocity

Acknowledgements. This research has made use of NASA's Astrophysics Data System Bibliographic Services.

References

Braude S., et al.: 1978, *Ap&SS*, **54**, 37.
Braude S., et al.: 1979, *Ap&SS*, **64**, 73.
Braude S., et al.: 1981a, *Ap&SS*, **74**, 409.
Braude S., et al.: 1981b, *Ap&SS*, **76**, 279.
Braude S., et al.: 2003, *KPCB*, **19**, 291.
Imanishi M., et al.: 2018, *ApJL*, **853**, L25.
Jamrozy M., et al.: 2005, *A&A.* **433**, 467.
Miroshnichenko A.: 2012, *RPRA*, **3**, 215.
Miroshnichenko A.: 2013, *OAP*, **26/2**, 197.
Miroshnichenko A.: 2019, *Ap&SS*, **364**, A92.
Miroshnichenko A.: 2021, *RPRA*, **26**, 165.
Miroshnichenko A.: 2023, *OAP*, **36**, 127.

https://doi.org/10.18524/1810-4215.2024.37.313649

S-BURSTS OF JOVIAN DECAMETRIC RADIO EMISSION STORMS UNDER THE INFLUENCE OF LOW AND HIGH FREQUENCY MHD DISTURBANCES IN STREAMER-LIKE SOURCES

N.O.Tsvyk

Institute of Radio Astronomy of the NAS of Ukraine, Kharkiv, Ukraine,
natalitsv69@gmail.com

ABSTRACT. There are analyzed a model for the DAM-bursts radiation by maser-cyclotron generation mechanism in the streamer-like sources that have been activated on ionization processes and MHD waves of high and low frequencies in Jupiter magnetosphere. It was accounted that the ion-atom collision processes in the magnetosphere of low-ionized plasma change the velocities and decay times of MHD waves at ultralow frequencies, because of the high and low frequency MHD disturbances have different properties and do different functions in Jupiter magnetosphere. Thus, it is shown that the typical periodicities of high frequency (HF) in S-burst-storm pattern, of about 0.5 kHz and higher 1 Hz, may be associated with HF Alfven waves, which activate the processes of DAM burst radiations. On the other hand, the typical low-frequency (LF) periodicities of S-storm radiation, of about 5 and 20 min time-scales, may be associated with LF Alfven waves, which activate the processes of plasma ionization and its stratification into streamers.

There was studied the propagation process of HF and LF MHD waves in Jupiter magnetosphere, when plasma flux is streaming inside the Io-Jupiter tube. Then, the process of maser generation of DAM bursts in presence of HF MHD-waves is investigated. We show that HF-Alfven waves perturb the electron plasma density and its velocity distribution, which give us the conditions to emit the DAM radiation effectively.

Finally, we discussed the particular properties of HF Alfven and MS wave modes in the plasma streamers, and how they form the DAM bursts, and next one, it was shown how to fit the observational data to the plasma processes that may be to work in this source model.

Keywords: DAM radio emission, bursts, MHD waves, magnetosphere inhomogeneity, Jupiter.

АНОТАЦІЯ. Проаналізовано модель випромінювання S-сплесків, в якій сплески генеруються циклотронним мазером в розшарованих на стримери джерелах, що активуються завдяки процесам іонізації та МГД хвилям високих і низьких частот в магнітосфері Юпітера.

В дослідженнях враховано, що процеси зіткнення іонів з атомами газу у магнітосфері з низько іонізованої плазми змінюють швидкості та час загасання МГД хвиль на наднизьких частотах, оскільки високо та низько частотні МГД збурення плазми мають різні властивості і виконують різні функції в магнітосфері Юпітера. Показано, що типові періодичності S-сплесків високої частоти (ВЧ), приблизно 0,5 кГц і 1 Гц, можуть бути пов'язані з ВЧ хвилями Альфвена, які активують мазерну генерацію сплесків декаметрового випромінювання. З іншого боку, типові низькочастотні (НЧ) періодичності випромінювання S-бурі, з часовою шкалою близько 5 і 20 хв, можуть бути пов'язані з НЧ хвилями Альфвена, які активують процеси іонізації плазми та її розшарування на стримери.

Досліджено процес поширення ВЧ і НЧ МГД хвиль в магнітосфері Юпітера в середині потокової трубки Іо–Юпітер, розшарованої на стримери, в яких збуджуються одночасно по декілька мод хвиль Альфвена. Та досліджено процес мазеріної генерації сплесків декаметрового випромінювання в присутності ВЧ МГД-хвиль. Показано, що ВЧ хвилі Альфвена збурюють щільність електронної плазми та розподіл швидкостей, що утворює умови задля ефективної генерації декаметрового випромінювання.

Нарешті, обговорено особливі властивості мод ВЧ і НЧ хвиль Альфвена, що існують в плазмових стримерах, та як вони формують S-сплески декаметрового випромінювання, і показано відповідності даним спостережень. Також, обговорено інші альтернативні процеси, які можуть працювати в досліджуваній моделі джерела. Зокрема, зазначено, що надтонкі ВЧ альвенівські моди можуть збуджуватися під час іонізаційного вибуху при відбитті НЧ хвиль Альфвена від верхніх шарів іоносфери Юпітера. Саме ці ВЧ альвенівські збурення керують розподілом електронної плазми в стримерах, та формують промінь декаметрового випромінювання, що повертається та спостерігається як S-сплески. Також, обговорено особливості випромінювання при утворенні пучків електронів на осі стримера, які можуть стати чинником мазерної активації S-сплесків променями із плазмових хвиль, збуджуваними на частоті біля електронного циклотронного резонансу.

Ключові слова: декаметрове радіовипромінювання, сплески, МГД хвилі, неоднорідність магнітосфери, Юпітер.

1. Introduction

Jupiter DAM radio emission is observed in the storms of duration at 1–2 hr with quasi-periodic bursts of various forms and types. The finest Jupiter bursts are S-type that has a fast-drifting structure of dynamical spectrum with duration of 2–10ms at frequency fixed and quasi-periodic separation of 5–30 ms or slower quasi-periods of 1 sec and 5–20 min. There are many DAM observations of Jupiter's radio emission since 1955, for example, the dynamical spectra of S-storms were observed by the UTR2 telescope (in Ukraine, see: Ryabov & Gerasimova, 1990; Ryabov et al., 2014) and by the Florida Radio Observatory (see FRO catalog: Flagg et al., 1991). So, in this work we take into account the typical periodicities of S-bursts that can be associated with such frequencies of MHD oscillations: $\omega_{A1..5} = 2\pi/\tau_{A1..5}$, where $\tau_{A1} \approx 0.05$ s, $\tau_{A2} \approx 0.2$ s, $\tau_{A3} \approx 1$ s, $\tau_{A4} \approx 300$ s, $\tau_{A5} \approx 20$ min.

These S-bursts are emitted by limb-sources on Jupiter's surface: Io-A,B (at S-pole Jupiter) and C (at N-pole). The Io-A,C sources are mainly associated with Jupiter's longitude meridian $\lambda_{III} \approx 180^o$, and the Io-C: $\lambda_{III} \approx 60^o$ (see: Ryabov & Gerasymova, 1990; Leblanc et al., 1993). All the bursts to be observed are mainly polarized as extraordinary X-type electromagnetic waves, and they radiate in a direction nearly perpendicular to the magnetic field lines that located at the sources in Jupiter's southern or northern hemisphere. In dynamical spectra we see the fast drifts of S-bursts, and they are superposed with the slow-drifting lanes. Typical burst drifts in the FRO catalog are $df/dt \sim -f$, about –20 MHz/s, which corresponds to a source moving from the surface of Jupiter at about $0.1c$ at an altitude of $0.1\ R_j$ (where c is the speed of light). The drift of lanes is about 20 to 200 kHz/s. They can be interpreted as the effect of Jupiter's rotation or diffraction effects in the propagation of DAM radiation (see: Ryabov & Gerasymova, 1990). And the other way, some lanes may be associated with the source modulation by low velocity waves. In this work we analyze a model in which bursts of DAM emission are triggered by MHD waves in Jupiter's lower magnetosphere, where streamer-like inhomogeneity arises due to ionization. We assume that some lanes may be forming due to wave modulation effects, and we will study haw the S-burst generation mechanism work. This approach continues the model that was studied in the works of Boev et al. (1991, 1993) and Tsvyk (2019, 2023).

The other way, we assume now that the DAM radiation emits a burst under MHD waves in Jupiter's lower magnetosphere, in the Cyclotron Maser generation mechanism mainly. So, Hess et al. (2007) there was proposed a good and popular model for the generation of fast-drifting S-bursts in current sheets of Alfvén waves. These Alfvén waves occur during the Io–Jupiter interaction, and the electron distribution of the loss cone appears from the magnetically mirrored the electron population, leading to cyclotron maser instability (CMI, see Wu, 1985; Melrose, 1986) for X-mode bursts of EM DAM radiation. In this work we improve that model to analyze the streamer inhomogeneity of weakly ionized plasma in Jupiter's lower magnetosphere, which can be associated with ultralow-frequency Alfvén modes with a period of several minutes.

The properties of high- and low-frequency MHD waves, as well as their propagation in the Jupiter magnetosphere with gaseous matter, are studied. We take the ionization processes that allow us to form the streamer and consider how low- and high-frequency MHD waves (Alfvén and magnetosonic) are transported in the conditions of this plasma, and how CMI occurs in sheets of electron density fluctuations associated with streamer oscillations.

2. Active source model

We will analyze the source model in which S- bursts of DAM radiation are caused by MHD waves in the presence of streamer-like inhomogeneities formed in the lower magnetosphere as a result of ionization processes and MHD disturbances. This happened in Io-A,B sources that start to emit when Io tube moves over the zones of Jupiter with max-B_0 at z_j=0: $\lambda_{III} \approx 180^o$ with magnetic field is $B_{0z} \approx 14$ G, and Io-C: $\lambda_{III} \approx 60^o$ with $B_{0z} \approx 10$ G.

The effects of the Io-Jupiter interaction excite the strong Alfven-wing with the current pulses in the flux tubes as standing waves as they bounce off Jupiter's ionosphere (see, for example, Ryabov & Gerasymova, 1990). The current direction changes with periods τ_A>300 s, and this gives us a long-term modulation of Jupiter's DAM emission by Alfvén wings, which to shear the Jupiter's magnetosphere into large-scale tubes, and to start the ionization process in the lower magnetosphere in the presence of gas and flows with Io-volcanic dust.

So, the low-frequency Alfven waves, $\omega < \omega_{A4} \approx (300\text{s})^{-1}$, support a streamer formation in wave-reflected processes, and the electric E-field is activated due to the wave-current passes through the Jupiter ionosphere with v_{fx} -velocity, $E \rightarrow [\boldsymbol{v}_{fx} c^{-1} \times \boldsymbol{B}_{0z}]$ (see: Smirnov, 1995; Boev, et al. 2001; Boev, 2005). This streamer is directed nearly along to the magnetic field line or with some slope to it. The e-particle velocity distribution is anisotropic because of the flux-mirror effects, ionized plasma diffusion in the streamer; and when the MHD-oscillations maintain the cone-like electron distribution at streamer surface or accelerate an e-beam in the streamer core (see: Tsvyk, 2023).

The MHD waves properties and its velocities in weakly-ionizes plasma are varied by frequency, due to the MHD equations for low-frequency waves, $(\omega\tau_{ia})<1$, should be considered in approximation of multi-components plasma of gas mattering (see: Smirnov, 1995; Akhiezer, et al. 1974; Braginski, 1963). Therefore, as soon as the low-frequency Alfvén waves interact with the gas (of density N_a) and they velocity c_A is greatly reduce, from c_{Ai} to c_{Ag}, and these waves start the process of plasma ionization with the streamers' formation (with ion density n_i):

$$c_A \rightarrow c_{Ai} \cong B_{0z} / \sqrt{4\pi\, n_i m_p}, \omega > \tau_{ia}^{-1},$$
$$c_A \rightarrow c_{Ag} \cong B_{0z} / \sqrt{4\pi\, N_a m_p}, \omega > \tau_{ia}^{-1},$$

where $\tau_{ia} \cong 1/(v_{Ti}\, N_a a_\lambda^{\,2})$, v_{Ti} is kinetic ion velocity and $a_\lambda \approx 10^{-8}$ cm is a size of H-atom.

At frequency of $\omega < \omega_{Ag}=2\pi/\tau_{ia}$ the Alfven velocity decrease in a factor $>(n_e/N_a)^{1/2}$ because of energy dumping, running the ionization plasma processes and streamer cre-

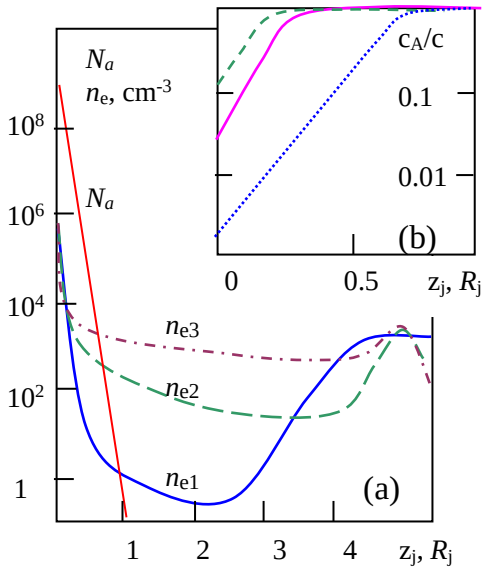

Figure 1: Plate (a) is the models for plasma n_e and gas N_a density variation at Jupiter magnetosphere altitudes z_j (in Jupiter radius units). A curve (1) is model of Su et al. (2006), (2) – Sentman, et al. (1975) and (3) – Witsers, Vogt (2017). Plate (b) is the Alfven velocity for HF ($\omega > \omega_{Ag}$), and for LF ($\omega < \omega_{Ag}$) streamer-modes variation from z_j-altitudes.

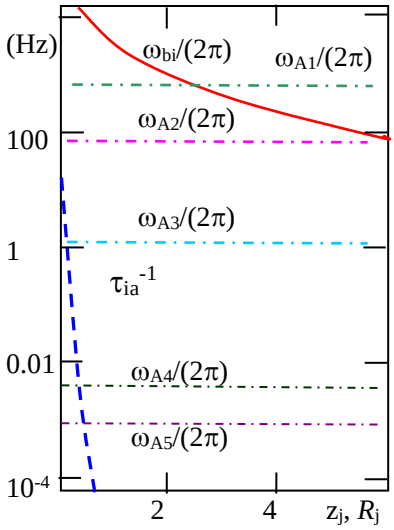

Figure 2: The ion cyclotron frequency ω_{bi} and the plasma-gas collision frequency $1/\tau_{ia}$ are varied from z_j, in compare to the typical frequencies of Alfven waves in the S-burst storm, $\omega_{A1..5}$.

ation with width of $a_x \sim 1/k_{min}$. The Alfven wave energy concentrated inside the streamer $r_x < a_x$, and in this area the value of Alfven velocity is some slower then ones in external free space. And it needs to account the relativistic effect in Alfven waves transport in matter of a low-plasma density (at high magnetosphere altitudes).

3. Variation of MHD waves properties from magnetosphere altitudes

Now we consider the main properties of MHD waves in the streamer-stratified plasma when the magnetosphere altitude is varied. We take the wave deviation of the plasma parameters as a function of $\propto \exp(ik_z z + im_k\theta - i\omega t)$. These MHD waves in streamer plasma were studied, for example, in the works of Bembitov et al. (2014), Kadomtsev (1963), Tsvyk (2023). They showed that MHD waves split into modes, their properties change depending on the streamer radius direction, and the change in their properties depending on the magnetosphere altitudes will be investigated below. So, we will watch now how the speed of the Alfvén wave changes in Jupiter's magnetosphere, and consider how the magnetosphere affects the Alfvén waves at frequencies $\omega_{A1..5}$, that are corresponded to the typical quasi-periodicities of the S-spectra.

Thus, we use the models for plasma density variation in Jupiter magnetosphere, which are presented in Fig. 1. We can see on curve (1) the plasma density is much lower in the model of Su et al. (2006), and on (2,3) are slightly higher density in models of Sentman, et al. (1975) and Witsers, Vogt (2017). The fact that those models have a higher plasma density may indicate the ionization processes occurring. So, the neutral matter is present at low altitudes of Jupiter magnetosphere only (z_j<0.5 R_j); and at these altitudes we observe the occurrence of S-bursts.

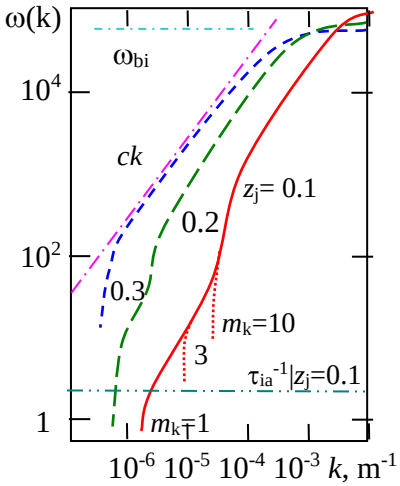

Figure 3: The typical dispersion curves $\omega_A(k)$ for Alfven modes at z_j is fixed. Here we take the streamer width a_x =200 km and $n_{e\,St}$ =20 $n_{e\,ext}$ in the model of plasma density variation by Su et al. (2006).

The Fig. 2 shows the typical frequencies of Alfvén waves, which correspond to the quasi-periods in the S-storm $\omega_{A1..5}$ in comparison with the frequency of collisions of plasma and gas, $\omega_{Ag}=2\pi/\tau_{ia}$. And we find that $\omega_{A1..3}>\omega_{Ag}$ are mostly HF modes, and $\omega_{A4,5}<\omega_{Ag}$ are LF modes in the lower magnetosphere of Jupiter. The plate of Fig. 1,b shows us the change of the Alfven velocity from z_j-altitudes for these waves, and Fig. 3 shows us the typical dispersion curves for Alfven modes at $z_j \approx 0.1 R_j$. Here we

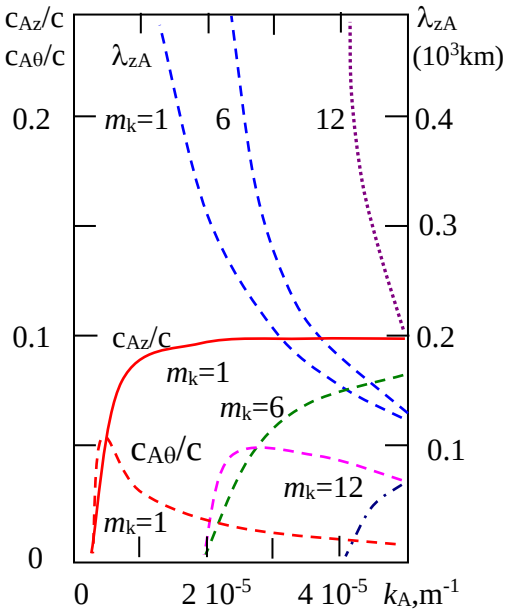

Figure 4: The velocity $c_{Az,\theta}$ of wave phase profile in z_j and θ direction from wave number k_A for m_k= 1,6,12 Alfven modes. And the wave length λ_{zA} is varied from k_A for those modes. Here is we take the streamer width of a_x=300 km at z_j=0.1 R_j altitude.

take the typical streamer width $a_x \approx$200 km and $n_{e\,St} \approx 10\, n_{e\,ext}$ in the model Su et al. (2006).

So, the last figure shows us that Alfvén waves can be damped strongly at low frequencies, $\omega \approx \omega_{Ag} = 2\pi\, \tau_{ia}^{-1}$, and streamer waves exist at $k > k_{min} \approx a_x^{-1}$. The dispersion curves for Alfven wave m_k-modes in the streamer are:

$$\omega(k) \cong (c_A^{-2}(k^2 - m_k^{\,2}/a_x^{\,2})^{-1} + \omega_{bi}^{-2})^{-2},$$

where ω_{bi} is the cyclotron ion frequency here.

The type of MHD modes that can exist in a streamer varies depending on the radius zones of the streamer, and their properties also to vary. Thus, in the streamer core there are modes of the Alfven-wave of LF (of m_k=0,1) and the electron beam is accelerated (v_b~0.1 c). Whereas in the zone $r_x \le a_x$ there are high-frequency Alfven modes (of m_k>1 mainly) and the n_e-density fluctuation exists in current sheets. Lastly, in the zone $r_x \ge a_x$, there are exist high-frequency modes of fast magneto sonic waves (m_k = 0,1,2…) with fluctuations of ions and electron density.

4. The MHD wave modes of low frequencies

The Alfven wave modes of m_k=0 may have at low frequencies strong dumping in the streamer surface. They velocity is reduce strongly at that $k \to k_{min} \approx a_x^{-1}$ in a factor of $(n_e/N_a)^{1/2}$. That wave oscillations are: $v_{er} \approx j_r/e\, n_e$; $v_{e\theta} \approx v_{i\theta}$; {$E_r$, B_θ}, and E-field strongly pumps at the streamer surface which can start the ionization process when the wave energy is high.

The Alfvén wave modes m_k = 1 can arise at about $k \to 1/a_x$ as Helical-kink modes (see Kadomtsev, 1963), and thus the waves interaction in streamer surface can convert the wave energy from mode #0 to mode m_k=1, with $k_z << 1/a_x$. This mode #1 can exist at the frequency ω_{A2} or ω_{A3}, as a mode with a wave-phase profile moves slowly in z-direction, $c_{Az} \sim c_A\,(k_z/k)^2 = c_A(1 - m_k^2(a_x k)^{-2})$, and the energy of MHD wave is transported at a speed c_A along the B_{0z} axis (during of τ_{A4} period from Io to Jupiter); and they gives us a good condition for the acceleration of the electron beam ($v_b \sim c_A \approx 0.1\, c$) due to the E_z wave-fluctuation in the streamer core.

The wave modes $m_k > 1$ exist at $r_x \approx a_x$ aria, where this wave fluctuation get a maximum value, and $k_\theta \approx m_k/a_x$. All wave modes with $m_k \ge 1$ have a phase rotation speed of $c_{A\theta} = c_A m_k (a_x k)^{-1}(1 - m_k^2 (a_x k)^{-1})^{1/2}$ which will move bunch of electron density maximum around a streamer axis. There are represented in Fig. 4 the dispersion curves of that Alfven wave modes in form of wave velocities c_{Az}, $c_{A\theta}$ that are varied from k when wave-phase is fixed, and $\lambda_z(k) \approx 2\pi/k_z$. These wave modes $m_k > 1$ may have dumping at low frequency $k \to k_{min} \approx m_k a_x^{-1}$ in the streamer surface, and they c_A-velocity are reduce strongly here. We have: $\lambda_z(k_{min}) \to \infty$, and a pattern of wave-phase moves slowly with fast rotation, and then goes to stop state, c_{Az}, $c_{A\theta} \to 0$. Therefore, the most likely we have LF Alfven waves' excitation (at $\omega_{A2..4}$) as the low-number modes (m_k = 1), alternatively to high frequency Alfven wave (ω_{A1}) is excited at high m_k. The other way, at high ω_A-frequency and for high k, those wave modes move along the streamer with the same velocity of $c_{Az} \sim c_A$, away from Jupiter and with slow rotation.

5. The MHD wave modes of high frequencies

The HF Alfven waves may consider for $m_k \ge 1$ modes at frequency $\omega \sim \omega_{A1,2} >> c_A/a_x$, and they wave pattern can move at velocity of c_A or some slower. Thus, the finest Alfven fluctuation of $\omega_{A1} \approx 10^3 s^{-1}$ corresponds to the S-burst time-width, while the burst length on frequency and time corresponds to the low Alfven modes, $\omega_{A2,3}$, which overlap each other.

The finest HF-Alfven-wave modes may originate to burn as an ionization fluctuation pulse at low magnetosphere altitudes. This pulse lasts about $\tau_{e\_ioniz} < 10^{-3}$ s, when low-frequency strong Alfven wave energy reached to Jupiter ionosphere and interacted with gas (e.g., see: Smirnov, 1995; Akhiezer, 1974; Boev et al., 2001, Boev, 2005). The HF Alfven waves at $\omega_{A1..3}$ with $k_z >> m_k/a_x$ do not interact with gas matter and here $c_{Az} \approx c_A$. Only in low z_j-altitudes of magnetosphere this condition may be changed (see Fig. 3). The other way, at frequencies of $\omega_A \to \omega_{bi}$, MHD waves (Alfven and FMS) are dumping at the ion cyclotron resonance, and Alfven waves here are transformed to kinetic modes (see Akhiezer et al., 1974; Su et al., 2006). But in Jupiter's lower magnetosphere, where we observe the S-burst sources, we have $\omega_{A1,2} < \omega_{bi}$, and only at high $z_j > 2R_j$ altitudes this ω_{bi} resonance is reached.

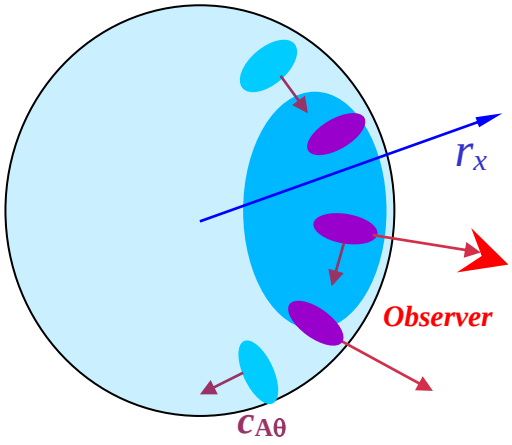

Figure 5: The sketch of the streamer for z_j is fixed, when the maximum of electron density zone is adjusted by superposition of two Alfven wave modes, m_k = (1;10), and it is rotated in θ-direction with $c_{A\theta}$ velocity, corresponding to the mode of large number (m_k = 10). This gives us the CMI radiation ray rotate direction, and get to the observer.

Thus, if we represent the pattern when a phase of Alfven wave is fixed, and correspond to the density n_e= max, this give us the wave-profile moves with c_{Az}-velocity in z_j-direction, and rotate with velocity of $c_{A\theta}$ in θ-direction, alternatively to the Alfven wave energy transports with c_A-velocity along the magnetic field lines. So, for two or more wave discrete modes may excite at the same moment (see Fig. 5). In this case, the highest ω_{A1}-frequency mode is responsible to S-burst 'width' on its time-duration. And, when this wave mode is superposed with the other m_k-modes, we have the all duration of S-burst by time and frequency that correspond to the slow and low-frequency MHD modes.

Here is represented in Fig. 5 the sketch of wave phase profile for m_k=(1;10) Alfven modes when z_j is fixed in the streamer, that is correspond to the maximum electron density zone which is adjusted by superposition of the wave phases, and it is rotated in θ- direction with $c_{A\theta}$ velocity of high frequency mode of larger number (m_k=10). In this toy model we have two Alfven modes that are exited in the streamer: the altitude $z_j \approx 0.1\ R_j$, streamer width ~300km, the wave frequencies are ω_{A1} (m_1=10 mode) and ω_{A2} (m_2=1 mode); wave numbers are $k_1 \approx 10^{-4}$m^{-1} ($\lambda_{1z} \approx$60 km), $k_2 \approx 10^{-5}$m^{-1} ($\lambda_{2z} \approx$ 600km); the velocities are $c_{A1z} \approx 0.1c$, $c_{A2z} \approx 0.05c$; and the rotate oscillation times are $\tau_{A1} \approx 6$ ms, $\tau_{A2} \approx 60$ ms. We see here as the electron density bunches are rotate and move in limited zones that correspond to low-number Alfven modes. But the bunch width and they drift-speed are obtained by ω_{A1}-mode, and this way the S-bursts may radiate.

6. DAM S-burst radiation in MHD-activated magnetosphere with streamers

An unstable electron velocity distribution relatively to the cyclotron-maser instability has a form of loss-cone distribution (see: Wu, 1985; Melrose, 1986). The Maser cyclotron resonance will be got for the extraordinary (XEM) wave mode in velocity-resonance, when the velocities of the wave and the electron particle (v_z, v_x) coincide, and it has a form:

$$\omega + \frac{m_x \omega_{be}}{\Gamma(v)} - k_z v_z = 0\ .$$

Here $\Gamma(v) = \left(1 - \frac{v^2}{c^2}\right)^{-1/2}$, $v = \sqrt{v_x^2 + v_z^2}$, m_x= -1, and the XEM-wave disperse curve $\omega_x(k)$ may be use a form by Ginzburg (1970) or the other approximation, that depends on the k-wave number and the electron cyclotron and a plasma frequencies, ω_{be} and ω_{pe}: $u\omega_{be}^{-2} = v\omega_{pe}^{-2} = \omega_x^{-2}$, $\omega_x^{-2} \cdot (kc)^2 \cong 1 - v(1-u)^{-1}$. The Maser cyclotron instability gives us the XEM-wave generation with an increment, which depends on the gradient on particle velocities distribution in velocities space, and θ-distribution of electrons and waves parameters to the magnetic field line.

CMI-resonance condition for XEM wave and electron velocities may be illustrated in the resonance cycles on (v_x, v_z) plates when θ and $k_z = k\cos\theta$ are fixed. Here cyclotron Maser instability arise when $df/dv > 0$ on the resonance cycle integrated. This condition realized when $kc/\omega_{be} \leq 1$ and $\theta \approx 0.4\pi$ for XEM waves, and then XEM-ray may refract within the source and $\theta \rightarrow \pi/2$. By analyze, the radiation diagram for XEM-waves may estimate as $d\omega_x/d\theta < 0$.

If we consider the fluctuation of the electron density under the influence of Alfvén waves of HF and LF modes, which have an anisotropic velocity distribution, then we will see that the fluctuations of the wave electric field control this electron anisotropy. The extraordinary EM Maser waves can be emitted inside the e-density bunches, so it gives us the rays that directed nearly to streamer perpendicular and straight into "free space". When the source-ray is turned toward the line of sight, we see these S-bursts.

When the phase profile of HF Alfven waves has a fast speed along magnetic field line, this gives us the fast drift in the S-burst frequency. In addition, the HF FMS-waves may exist at the streamer surface, and they may focus the burst ray. A picture of the burst pattern for A- and B-storms may be some different because of a streamer slope to magnetic field lines, and that way we see the multi-burst train pattern in the B-storm and the pattern with long single or long-separated S-bursts in the A-storm.

We will discuss now an additional condition for XEM burst generation. If the e-beam is accelerated within the streamer, it may be the source of plasma longitude (L) waves of $\omega \sim \omega_u \approx \omega_{be}$ by Cherenkov generation mechanism (see Boev et al., 1991). That L-ray may be to transform latter to extraordinary EM wave-ray near the streamer surface, or to supervise the XEM-wave generation at $r_x \approx a_x$ streamer areas on CMI.

The Cherenkov condition is: $\omega_l - k_z v_z = 0$,

$$\omega_l(k) \cong ((\omega_{03}^2 + c^2k^2)^{-1} + \omega_u^2)^{-1/2} - v_{Te}k.$$

The L-waves have anomaly dispersion, so they phase velocity be directed inside the streamer when the wave energy velocity directed away. The transformation L→XEM mechanism may be connected with streamer surface pro-

cesses, and may be supported by FMS-wave the collision wave effect, or the linear transformation. The other way, the linear transformation may be got with induction of CMI process of S-burst generation in the streamer plasma surface with anisotropy e-distribution. And this leads to form of the bright S-burst pattern.

7. Conclusion

The LF-Alfven waves (ω_A<0.003 s^{-1}) arise due to the Io rotation and they lead to the streamer formation in λ_{III} ≈60° and 180° zones of Jupiter's lower magnetosphere with streamer width of $a_x \approx$ 20–500 km. This come to the DAM bursts generation within the streamer at the current sheets and electron density bunches on wave lengths of $\lambda_z \approx$ 10 to 5000 km.

The HF-Alfven waves (ω_A > 1 s^{-1} up to $\omega_A \approx$ 5000 s^{-1}) cause the fast-drifting electron bunches that give us the observed S-bursts. These fast S-pulses can occur when there is a burst of ionization arise due to a high-energy low-frequency (ω_A < 1 s^{-1}) Alfvén wave interacts with and reflects off Jupiter's ionosphere.

The DAM radiation may generated by Cyclotron Maser instability from bunches with cone-type electrons kinetic distribution, producing under the Alfven plasma oscillations within the streamers. In alternatively, the Cherenkov instability inside the streamer from the sub-relativistic electron beam (speed of ~0.1 c) may generate plasma waves near ω_{be}-frequency that will be transformed to XEM waves at a streamer surface, or they can be caused by the maser generation of XEM waves within the MHD-electron-bunches near the streamer surface.

Finally, we concludes that our model of Jupiter magnetosphere with streamers and Alfven waves may explain the observed S-bursts trains due to the Alfven-wave disturbance of m_k modes. And this model is some better then model of Hess-Zarka (2007) to explain the observed S-burst drifts and there sub-periodicity trains.

References

Akhiezer A.I., et al.: 1974, Plasma electrodynamics (Nauka, Gl. red. phys.-mat. literature, edds. Akhiezer A.I., Moscow), 719, (*in Russian*)

Bembitov D.B., et al.: 2014, *AnGeo*, **32**, 1189.

Boev A.G., Luk'yanov M.Yu.: 1991, *SvA*, **68**, 853.

Boev A.G., Luk'yanov M.Yu., Tsvyk N.: 1993, *KPCB*, **9**, 37.

Boev A.G., Udal'tsova N.M., Yantsevich A.A.: 2001, *RPRA*, **6**, 252.

Boev A.G.: 2005, *RPRA*, **10**, 367

Bragynskyi S.I.: 1963, The questions of plasma theory (Gos. izdatel'stvo literatury po nauke i tekhnike, edds. Leontovich M.A., Moscow). **1**, 183 (*in Russian*)/

Flag R.S., et al.: 1991, A Catalog of High Resolution Jovian Decametric Radio Noise Burst Spectra (University of Florida, Gainesville), **1**, 199.

Ginzburg V.L.: 1970, The propagation of electromagnetic waves in plasmas (Pergamon Press), 480.

Hess S., Mottez F., Zarka P.: 2007, *JGRA.*, **112** , A11212.

Kadomtsev B.B.: 1963, The questions of plasma theory (Gos. izdatel'stvo literatury po nauke i tekhnike, edds. Leontovich M.A., Moscow), **2**, 132, (*in Russian*).

Leblanc Y., Bagenal F., Dalk J.A.: 1993, *A&A*, **276,** 603.

Melrose, D.B.: 1986, *JGRA*, **91**, A7, 7970.

Ryabov B.P., Gerasymova N.N.: 1990, Decameter sporadic radioemission of Jupiter (Naukova dumka, Kyev), 240 (*in Russian*)

Ryabov V.B., et al.: 2014, *A&A*, **568**, A53.

Sentman D.D., Allen J.A., Goerts C.K.: 1975, *GeoRL*, **2**, 465.

Smirnov B.M.: 1995, The physics of the low ionized gas (Nauka, Glav. red. phys.-mat. literature, Moscow), 424 (*in Russian*)

Su, Y. J., et al. 2006. *JGRA*, **111**, A021094.

Tsvyk N.O.: 2019, *OAP*, **32**, 105.

Tsvyk N.O.: 2023, *OAP*, **36**, 145.

Witsers P., Vogt M.F.: 2017, *ApJ*. **836**, 114

Wu C.S.: 1985, *SSRv*, **41**, 215.

https://doi.org/10.18524/1810-4215.2024.37.313643

ANGULAR BRIGHTNESS DISTRIBUTION OF QUASAR 3C268.4 AT DECAMETER WAVELENGTHS

R.V. Vashchishin[1], V.O. Shepelev[2], O.O. Litvinenko[3], A.B. Lozinsky[4]

[1] Gravimetric Observatory of the Institute of Geophysics of the NAS of Ukraine Poltava, Ukraine, *vrv.uran2@gmail.com*

[2] Institute of Radio Astronomy of the NAS of Ukraine, Kharkiv, Ukraine

[3] URAN-4 Observatory of the Institute of Radio Astronomy of the NAS of Ukraine, Odesa, Ukraine

[4] Karpenko Physico-Mechanical Institute of the NAS of Ukraine, Lviv, Ukraine

ABSTRACT. Using the URAN VLBI network, we studied an angular structure of the 3C268.4 quasar at the decameter wavelengths. It is shown, that the brightness distribution of the source in the decameter range differs significantly from the decimeter image of the quasar. At low frequencies, the source model consists of two extended components and a compact feature, whose sizes and positions coincide with the parameters of lobes and one of the hot spots of 3C268.4 observed in the decimeter range. The radio emission of the second hot spot at decameter wavelengths is quite weak and does not significantly affect interferometer response. The probable spectra of the quasar components and their changes in the range from decameter to decimeter wavelengths are determined in the study as well. It is noted that, in contrast to the high-frequency image, where compact hot spots predominate in the 3C268.4 radiation, at decameter wavelengths about 65% of the source flux density is provided by more extended lobes. We have also shown that the change in the slope of the full spectrum of the quasar at 230 MHz is caused by synchrotron losses in its lobes.

Keywords: decameter range, brightness distribution, decameter model.

АНОТАЦІЯ. За допомогою РНДБ мережі УРАН, було досліджено кутову структуру квазара 3C268.4 на декаметрових довжинах хвиль. Показано, що розподіл яскравості джерела в декаметровому діапазоні суттєво відрізняється від дециметрового зображення квазара. На низьких частотах модель джерела складається з двох протяжних компонентів і одного компактного елемента, розміри і положення яких збігаються з параметрами пелюсток і однієї з гарячих плям 3C268.4, що спостерігаються в дециметровому діапазоні. Радіовипромінювання другої гарячої плями на декаметрових довжинах хвиль досить слабке і не впливає істотно на відгук інтерферометра. У дослідженні також визначаються ймовірні спектри компонентів квазара та їх зміни в діапазоні від декаметрових до дециметрових довжин хвиль. Відзначається, що на відміну від високочастотного зображення, де в випромінюванні 3C268.4 переважають компактні гарячі плями, на декаметрових хвилях близько 65% густини потоку джерела забезпечується більш протяжними пелюстками. Ми також показали, що зміна нахилу повного спектру квазара на частоті 230 МГц викликана синхротронними втратами в його пелюстках.

Ключові слова: декаметровий діапазон; розподіл яскравості; декаметрова модель

1. Introduction

Studies of extragalactic radio sources associated with active galactic nuclei have shown that most such sources have a structure in the decameter range noticeably different from their images observed at shorter wavelengths. To investigate this difference, we observe radio galaxies and quasars with the URAN interferometers at the lowest frequencies.

The radio source 3C268.4 optically associated with a quasar at a redshift of 1.4 has an FRII-type structure at decimeter wavelengths (Reid et al., 1995). It consists of a weak core and two radio lobes with hot spots at their ends spaced 10" apart. The southwestern hot spot provides about 68% of the total source flux density while the northern-eastern one does only 10%. Their angular sizes are about 1". The rest of the radiation comes from the more extended lobes of the source. The lowest frequency where the 3C268.4 structure was earlier studied with MERLIN was 408 MHz (Lonsdale & Morrison, 1983). The total source spectrum is bent near the frequency 230 MHz (Herbig & Readhead, 1991) showing a possibility of structure modifications at lower frequencies. The source power and angular dimensions of its components are suitable for its observation with the URAN interferometers (Megn et al., 1997) in the decameter range and the study of this quasar was never conducted before at such low frequencies.

2. Observations and data reduction

Observations of 3C268.4 were carried out using the URAN interferometer network at 20 and 25 MHz simultaneously. Signals were recorded in separate 10-minute

scans at hour angles of +/-150 minutes relative to the culmination moment. Interferometer pairs were formed by multiplying the recorded signals of the north-south antenna of the UTR-2 radio telescope with the signals of each URAN antenna.

It is known that the visibilities obtained at different baselines carry information about the brightness distribution of the object under study. With good filling of the UV plane, the source brightness distribution can be reconstructed by the inverse Fourier transform of the set of their complex values. However, we do not use this approach with URAN due to the limited number of baselines and insufficient filling of the UV plane. Besides that visibility phases at decameter wavelengths are severely distorted by the influence of the propagation medium which makes it impossible to apply direct mapping methods. Therefore, to reconstruct radio images of sources in the decameter wavelength, we use the method of fitting the brightness distribution models only by the visibility modules.

The method is described in (Megn et al., 2001) and consists in representing the real brightness distribution at the map of the source by a model consisting of a certain number of elliptical components with Gaussian brightness distribution. Then changing the parameters of this initial model and calculating its interferometric response we use the least squares method to minimize the differences between calculation and experimental data collected with the URAN interferometers. The result of the fitting procedure is a model distribution of brightness at decameter wavelengths consistent with the URAN observational data.

We used the map obtained with the VLA at 1.69 GHz (the NVAS can be browsed through http://www.vla.nrao.edu/astro/nvas/) to determine the initial model for fitting the low-frequency model of 3C268.4. The parameters of the initial model are given in Table 1.

Table 1: The model of brightness distribution of 3C268.4 fitted to a 1.69 GHz map

	α,"	δ,"	S/S_0,%	θ,"	a/b	ψ,°
HS_{NE}	3.5	3.2	10	0.9	1	0
L_{NE}	3.5	3.2	6	1.9	1.2	90
Core	0	0	1	0.9	1	0
HS_{SW}	–2.1	–3.7	68	1.1	1.7	128
L_{SW}	–2.1	–3.6	15	2.1	1.4	128

Notes:
HS – hot spot; *L* – lobe;
α, δ – coordinates of the components center;
θ – size at a half power level;
a/b – ellipticity;
ψ – position angle of the component;
S/S_0 – percentage of total flux.

As an example, measured with the URAN-2 and URAN-3 interferometers the experimental dependences of the visibility modules on hour angle are shown in Fig. 1 and Fig. 2 by symbols *3*. Line *1* marks the response of the initial high-frequency model at these baselines, and shows what visibilities measured at decameter band would be if the image of the radio source did not change with frequency decreasing. A noticeable distinction between this

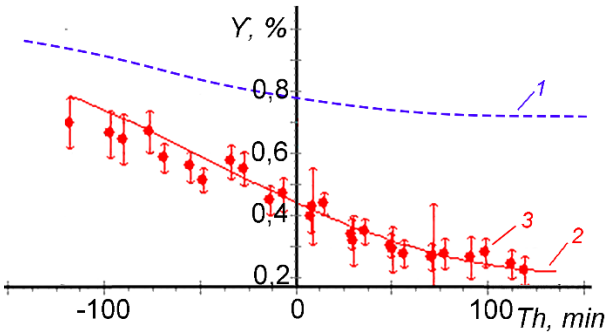

Figure 1: Visibility module of the decameter model for the URAN-2 interferometer: *1* – high frequency model; *2* – fitted decameter model; *3* – experimental data

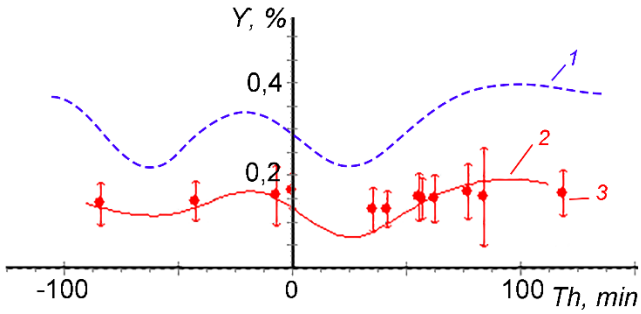

Figure 2: Visibility module of the decameter model for the URAN-3 interferometer at 25 MHz: *1* – high-frequency model; *2* – fitted decameter model; *3* – experimental data

curve from experimental data means changes in the source structure. A low-frequency model was then fitted based on experimental data obtained with all interferometers of the URAN network at frequencies of 20 and 25 MHz. The calculated responses of the fitted model at 25 MHz for URAN-2 and URAN-3 are shown in Fig. 1 and Fig. 2 by line *2*.

The parameters of the decameter model at frequencies of 20 and 25 MHz are given in Table 2.

Table 2. The decameter model at frequencies at 20 and 25 MHz

	α,"	δ,"	S/S_0,%	θ''_{25}	θ''_{20}	a/b	ψ,°
HS_{NE}	3.5	3.2	9	1.1	1.3	1	0
L_{NE}	3.5	3.2	32	2.8	3.1	1	0
HS_{SW}	–2.1	–3.7	26	1.1	1.2	1.7	128
Lsw	–2.1	–3.6	33	4.1	4.3	1.4	128

3. The results

By comparing the two tables, it is easy to see what is causing the discrepancies observed. At high frequencies, the main contribution to the total flux density is made by compact details – hot spots. Their fraction in the total flux of the quasar is about 78%, while at low frequencies the total source radiation is predominantly formed by extended details – lobes. Their contribution to the source total flux in the decameter range is about 65%. Fig. 3 and Fig. 4 show the high-frequency and decameter models on a loga-

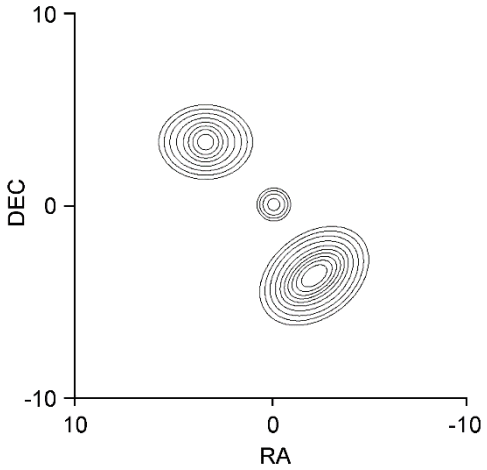

Figure 3: Model fitted to 1.69 GHz map

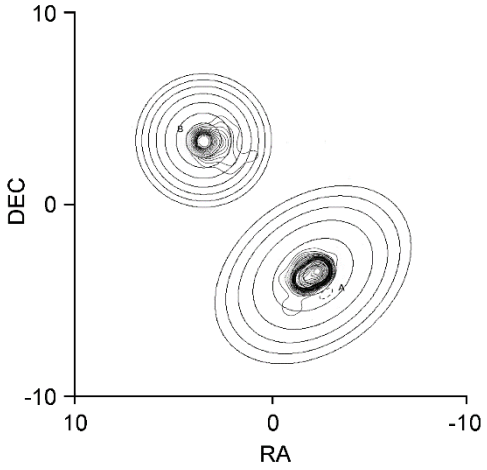

Figure 4: Decameter model overlaid on a 408 MHz map

rithmic scale of brightness. The latter model is shown against the background of a 408 MHz map with an angular resolution of 0.9" (Lonsdale & Morrison, 1983).

Fig. 5 shows the total spectrum of the quasar – *1* and probable spectra of its components: *2* and *4* – spectra of the southwestern and northeastern hot spots, *3* and *5* – southwestern and northeastern lobes. The spectral index of each spectrum is shown in the same color above it.

Linear approximation of the total spectrum was performed by the least squares method separately for the sections from 20 to 230 MHz and above 230 MHz according to the data of (Kellermann & Paulini-Toth, 1969; Viner & Erickson, 1975; Laing & Peacock, 1980; Roger et al., 1986). Spectra of hot spots – according to our data, obtained at frequencies of 20 and 25 MHz and data at 1.69 and 4.8 GHz.

As can be seen from the figure, a bend is observed in the total spectrum at a frequency of about 230 MHz. This bend is related to the behavior of the lobe spectra, typical for synchrotron losses. The lobe spectra in this figure were obtained by subtracting the hot spot spectra from the total spectrum, taking into account the ratio of lobe fluxes at 20, 25 MHz, and 1.69 GHz.

Knowing the magnetic field strength in the lobe (Liu et al., 1992) and the inflection point of the spectrum, using formula (1) from (Liu et al., 1992), we can calculate the synchrotron age of the quasar, i.e. the time that has passed

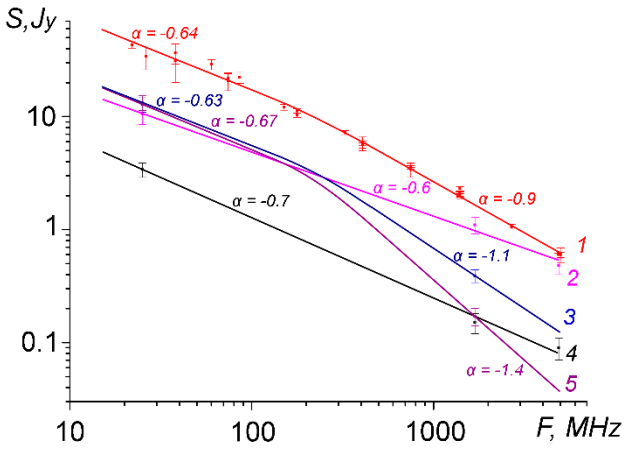

Figure 5: The total spectrum of 3C268.4 and the probable spectra of its components: *1* – total spectra; *2* – southwestern hot spot; *3* – southwestern lobe; *4* – northeastern hot spot; *5* – northeastern lobe

since the last acceleration of electrons. According to our data, the age of the quasar is about 8.4 million years.

It should be noted here, that the ratio of the fluxes of the source components, calculated by us at a frequency of 408 MHz, agrees well with the data of (Lonsdale & Morrison, 1983).

4. Conclusion

For the first time, an investigation of the angular structure of the quasar 3C268.4 was carried out in the decameter range. The most optimal model of the angular brightness distribution at frequencies of 20 and 25 MHz was obtained. It was found that:

1. The sizes of the source components increased compared to high-frequency ones due to interstellar scattering (in hot spots) and synchrotron losses (in lobes).

2. The main contribution to the total source flux at low frequencies is made by the lobes – 65% and the southern hot spot – 26%, which significantly differs from the high frequencies where nearly 78% of the total flux is provided by hot spots. The radio emission of the northern hot spot at decameter wavelengths is quite weak and does not significantly affect interferometer response.

3. It has been established that the bending of spectra at a frequency of about 230 MHz is caused by synchrotron losses. The approximate age of the source was found to be about 8.4 million years.

References

Herbig T., Readhead A.C.S.: 1992, *ApJS*, **81**, 83.
Kellermann K. I., Paulini-Toth I. I. K.: 1969, *ApJ*, **157**, 1.
Laing R.A., Peacock J.A.: 1980, *MNRAS*, **190**, 903.
Liu R., Pooley G., Riley J.M.: 1992, *MNRAS*, **257**, 545.
Lonsdale C.J., Morison I.: 1983, *MNRAS*, **203**, 833.
Megn A.V., Braude S.Ya., Rashkovsky S.L., et al.: 1997, *AJ*, **2**, 4, 385.
Megn A.V., Rashkovsky S.L., Shepelev V.A.: 2001, *RPRA*, **6**, 1, 9.
Reid A., Shone D.L., Akujor C.E. et al.: 1995, *A&AS*, **110**, 213.
Roger R.S., Costain C.H., Stewart D.I.: 1986, *A&AS*, **65**, 485.
Viner M.R., Erickson W.C.: 1975, *AJ*, **80**, 11, 931.

SUN, SOLAR ACTIVITY, SOLAR-TERRESTRIAL RELATIONS AND ASTROBIOLOGY

https://doi.org/10.18524/1810-4215.2024.37.312685

THE EXISTENCE OF SIMPLEST BIOLOGICAL STRUCTURES IN THE FIELD OF HARD RADIATIONS

Doikov D.M.[1,2], Doikova E.M.[3], Jerdev M.[4]

[1] Dept. of Physics, Medical laboratory of the North Medical Center, Poria, Israel

[2] Dept. of Mathematics, Physics and Astronomy, Odesa National Maritime University, Ukraine *dmitro.doikov@gmail.com*

[3] Dept. of Radiology, of the North Medical Center, Poria, Israel, *doikovaekaterin@gmail.com*

[4] Dept. of Radiology, of the North Medical Center, Poria, Israel, *jerdev.michael@gmail.com*

ABSTRACT. The paper deals with the application of biophysics in astrobiology and space medicine. The interaction between cells, bacteria, and hard radiation in near-Earth space is calculated. We studied role of photons on the destruction of elementary biological structures. Depending of the spectra and intensity of X-rays and soft γ-radiation we declared, that calculations of photon energy deposition has been practical interest from the point of view of space flight safety and the survival of various forms in space. It was found how radiation energy transfer processes in cells and bacteria, changes their spectrum. This is leads to changing the cross sections of interaction between quanta and biological structures, i.e., membranes and organelles of cells and bacteria. We considered only structure of this interaction, percentage contribution in total extinction of the photon component of solar radiation in the standard biological structure named “Soft Tissue”. The main standards of biological tissues and anatomical structures were used for calculations and their interpretation. Different biological objects are stored in specialized standards. In particular, in the National Institute of Standards and Technology (NIST). Radiation field in determine survivability of some types of microorganisms from ionizing radiation is significantly increased by drying and freezing. Drying and freezing significantly increases the radiation survival of microorganisms when used separately, and the combination of excision and freezing significantly increases radiation survival. Within the framework of Astrobiology, the study of the conditions proposed for consideration helps to understand the possibility of transporting multi-atomic structures (sugars, amino acids, etc.), primary bacteria in comets and some types of meteorites. It is noted that these cosmic bodies provide sufficient shielding from external exposure to cosmic rays during such transportation.

Keywords: astrobiology, energy deposition in bacteria, radiology and space medicine, cell damage.

АНОТАЦІЯ. У роботі розглянуто застосування радіаційної біології в астробіології та космічній медицині. Зроблено розрахунки взаємодії між клітинами, бактеріями та жорстким випромінюванням у навколоземному просторі. Нами отримано, що вплив фотонів на руйнування елементарних біологічних структур залежить від інтенсивності та довжини хвилі рентгенівського та м’якого γ-випромінювання. Згідно результатам розрахунків виникає практичний інтерес з точки зору безпеки космічних польотів і виживання різних примітивних біологічних форм у космосі. Отримано, що у процесі переносу радіаційної енергії в клітинках та бактеріях її спектр змінюється, що доводить до змін перерізів взаємодії квантів з біологічними структурами. Це стосується мембран та органел клітинок та бактерій. Ми розглядали лише структуру взаємодії між фотонним компонентом сонячного випромінювання та біологічною структурою яка моделювалася вигляді параметру «М’яка тканина». Для розрахунків та їх інтерпретація були використані головні стандарти біологічних тканин та анатомічних структур. Різни біологічні об'єкті зберігаються в спеціалізованих стандартах. Зокрема в Національному інституті стандартів і технологій США (NIST). Головні пункти, які розглянуто у роботі підтверджують раніше отримані експериментальні висновки. Тобто – що живучість деяких типів мікроорганізмів від іонізуючого випромінювання значно підвищується при висушуванні та заморожуванні. Одночасне висушування та заморожування значно збільшує радіаційну виживаність мікроорганізмів при окремому застосуванні. В межах Астробіології вивчення запропонованих для розгляду умов допомагає зрозуміти можливість транспорту багатоатомних структур (сахари, амінокислоти та інші), первинних бактерій у кометах та деяких типах метеоритів. Зазначено, що ці космічні тіла забезпечують достатнє екранування від зовнішнього опромінення космічними променями під час такого транспортування.

Ключові слова: астробіологія, депонування енергії в бактеріях, радіологія та космічна медицина, пошкодження клітин.

Highlights:

1. Ionizing radiation survivability of some type micro-organisms is greatly increased by desiccation and freezing.
2. Desiccation and freezing greatly increased radiation survival of microorganisms when applied separately,

and when combined, desiccation and freezing increased radiation survival even more so.

1. Introduction

As a first approximation, we consider the interaction of cosmic rays (therefore CRs) with soft tissues, referred to as "Soft-Tissue" in the NIST standard. The CR consists is energetic particles and quanta. It was considered only the radiation component. The pattern of exposure to ionizing radiation depends on the shape of the radiation component of solar flares. A significant fraction of soft X-ray radiation mainly falls in the energy intervals 0.2 – 10 keV In motion of X-ray quanta in "Soft-Tissue" we observe photo absorption, Compton and Rayleigh scattering. In the spectral interval between 0.2 keV and 10 keV the energy transfer of X-rays is determined by strong photo absorption. Here the striking power of the radiation is maximal. In the interval 10 keV – 60 keV, in the given figures one can trace also the geometrical effect. Namely, the dependence of the calculations results of the spectrum coming out of the absorber on the effective sizes of cells or tissues. An increase in the percentage of scattered radiation as the size of biological systems increases is observed. The sizes of cells and bacteria are limited to 150 nm, This results are presented in Fig. 1.

2. X-ray energy transport in Astrobiology

By the mid of1970-s, a number of papers by (Hoyle & Wickramasinghe, 1983; Wallis et al., 1992; Dayal et al., 2019; Stancheva et al., 2002) with therein reference had raised the question of surface reactions for the synthesis of complex molecules on ultracold particles within gas-dust conglomerates. Typical reaction times of macromolecule synthesis τ_{reac} are much shorter than the lifetime of gas-dust nebulae τ_{cloud}. In 1970s, radio astronomy began the pursuit of recording complex molecules down to sugars, amino acids, etc. At the same time, even small doses of hard radiations cause the appearance of surface charge of dust particles, which further reduces the values of the τ_{reac} On the other hand, the survival of macromolecules strongly depends on the spectrum of cosmic rays crossing these conglomerates. The question about the cross sections of cosmic ray interactions with macromolecules is reduced to their interactions with the atoms composing the molecule. The high-energy part of the CR distribution mainly penetrates into gas-dust nebulae. And the interaction of these particles gives very small cross sections in the interaction with atomic electron shells of the considered molecules and do not significantly affect the formation of macromolecules. Moreover, when solving such a class of problems and the energy ratio, we can consider these molecules with their constituent electrons as quiescent. To solve the above problem, it is necessary to calculate the total energy losses for dust particles and molecular atoms separately.

3. Direct and Non-Direct, Internal

3.1. Direct interaction

Numerical calculations of macromolecule survival in the field of hard radiation are gained prominence and relevance after the publication of the articles (Kyriakou et al., 2022), and (Imserti et al., 2018). In this source the open code version is now in widespread use Giant4-DNA 11.2. The simplified version of these codes is G. Weber X-Ray calculator (see link). The various model studies of protozoan bacteria in media with standard dimension 150 nm presented in Fig. 1. A main component of deposit energy's is E_{dep} for photon field includes only photo absorption. From Fig. 1 we may get the upper limit of the energy absorbed by the proto-bacterium has $E_{dep} = 0.12\ eV$. The presented in Fig. 1. results define only direct interaction of quanta with bacterial and cellular structures. It is important to note that E_{dep} energy is sufficient to excite the fluorescence of a certain type of bacteria exposed directly to the X-ray radiation presented in Fig. 1.

3.2. Non-Direct interaction

If bacteria live in water or liquid biological substrate to the direct effects of X-ray and γ-ray radiation is added the mechanism of radiolysis in these liquids. The general scheme of the hard-radiation interaction processes was consistent with the solutions adopted in open code Giant4-DNA 11.2. Taking into account characteristic times, we divide the chain of processes into stages: ionization → radiolysis + free radicals → reactions between free radicals and bacterial membranes and organelles. The given scheme was necessary for comparative characterization of prediction of bacteria existence in biological environment and without it. This algorithm begin from estimation of energy deposition in "Soft-Tissue".

3.3. Internal interaction

Internal interaction refers to the process of penetration of radioactive isotopes from the environment surrounding a bacterium or cell. These may be the free radicals described in the previous section but containing a radioactive isotope. These events are depends from the nuclear transformations inducing their appearance. This issue has not attracted the attention of researchers because of its low probability relative to other events. There is a non-zero probability that a radioactive isotope is present in a transport molecule that participates in metabolic processes.

3.4. Radiology and space medicine

The new opportunities now study the effects of radioactive isotopes penetrating across cell membranes and decaying inside cells and bacteria. The advent of PET CT led to the use of the decaying isotope $^{18}_{9}F$, which is part of the transport radiopharmaceuticals molecule (hereinafter RFP)-Fluorodeoxyglucose (hereinafter FDG), a biological analog of glucose. Its full name is 2-fluoro-2-deoxy-D-glucose. When $^{18}_{9}F$ atom is introduced into the preparation, the names are supplemented with its mention,

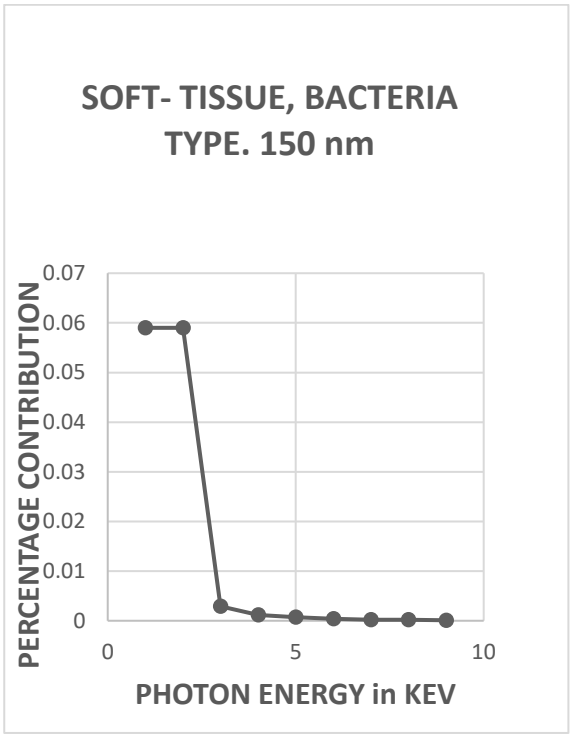

Figure 1: Attenuation in 150 nm bacteria wth size 150 mm

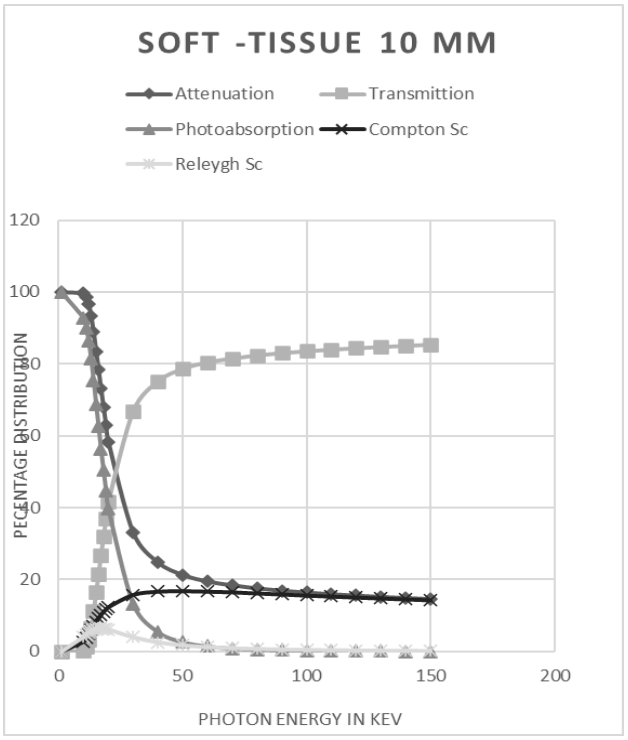

Figure 2: Extinction in Soft Tissue. Layer size is 10 mm

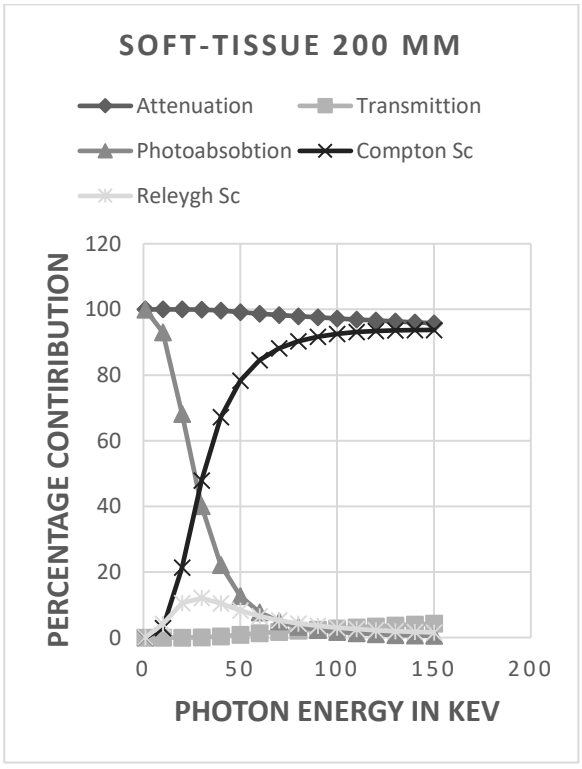

Figure 3: Ibid for Soft-Tissue size 200 mm

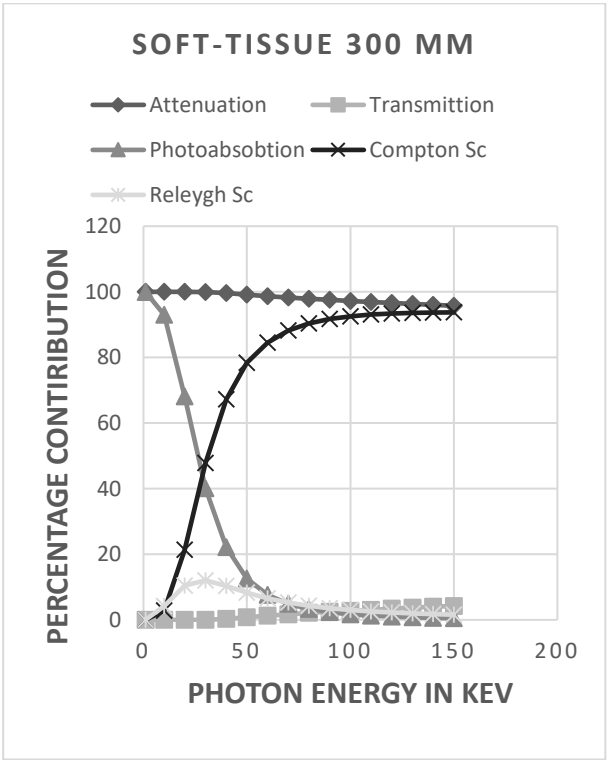

Figure 4: Ibid for Soft-Tissue size 300 mm

e.g. $^{18}_{9}F$ -FDG. For the model experiment the medium conventionally called "living environment" (hereinafter referred to as LE) is chosen. The LE experiences the direct effect of positrons and gamma-quanta formed by decay in the RFP. The calculations of the various model studies of protozoan bacteria in media filled with radiopharmaceuticals (hereinafter RFP)-Fluorodeoxyglucose (hereinafter FDG). In this case a biological analog of glucose, were carried out. Its full name is 2-fluoro-2-deoxy-D-glucose. When $^{18}_{9}F$ atom is introduced into the preparation, the names are supplemented with its mention, e.g. $^{18}_{9}F$-FDG. For the model experiment the medium conventionally called "living environment"

(hereinafter referred to as LE) is chosen. The LE experiences the direct effect of positrons and gamma-quanta formed by decay in the RFP. Bacteria or cell are placed inside the LE. Having the results of measurements of hard radiation fluxes on the PET CT, we set the field of gamma rays and diffusely moving particles – decay products in the form of positrons and recoil nuclei. As a result, we have two reactions channels: ${}^{18}_{9}F \rightarrow {}^{18}_{8}O + e^{+}$ and $e^{+} + e^{-} \rightarrow 2\gamma$.

The second case is applied to space conditions. Here the field of hard radiations interacts directly with the microorganism. The participation of RFP – Glucose Fluorine in the processes of metabolism and synthesis was considered in the form of different variants of their placement in space. The effects of the decay products of the isotope ${}^{18}_{9}F$ in RFP on protozoan organisms and cells are considered in the following cases:

– Free radicals during radiolysis arise in the bio-solution around the bacterium and enter the intracellular space (Kyriakou et al., 2022), and (Imserti et al., 2018).

– Decaying within the bacterium.

– Direct interaction of the cell membrane, organelle and macromolecule with radioactive decay products.

The role of the RFP decay product ${}^{18}_{8}O$ inside the bacterium or cell as a result of ionization and direct destruction of components of the internal structure of the bacterium or cell is important because he mean free path is drastically shorter. In consequences of this presence of ${}^{18}_{8}O$ as a decay product of ${}^{18}_{9}F \rightarrow {}^{18}_{8}O + e^{+}$ and involved in the damage of complex organic molecules were specificities.

4. Discussion

The calculation of the survival rate of already formed complex molecules and possible simplest life forms is the basis of the present work The free path lengths of positrons $L_{e^{+}}$ and ${}^{18}_{8}O$ atoms as $L_{{}^{18}_{8}O}$ are noticeably longer than the specified size of a bacterium or cell. Therefore, the localization of the decay point of the radioactive isotope in or outside the cell or bacterium is irrelevant. In this case it is necessary to solve the problem for the case of direct interactions taking into account chemical reactions of radiolysis.

In present time development of space technology requires new approaches to the study of biological aspects of prolonged stay of equipment and people in aggressive environment. In order to model the properties of biological systems, the program Geant4-DNA was extended and applied to solve new biomedical problems in the program Giant4-DNA 11.2 In some cases, Weber codes have been used for the sake of simplicity. The proposed codes are integrated into the NIST international databases, on proteins and their interaction cross-section with ionizing radiation.

The preliminary results allow us to construct inferred spectra of radiation passing through biological tissues. In present work, nanometer-sized volatiles and bacteria in the X-ray radiation field form specific induced emission in the form of classical fluorescence. The considered macroscopic biological structures almost completely transform the directed X-ray radiation into scattered Compton radiation. On the other hand, the obtained laboratory and model data are readily transferable to Astrobiology tasks (Lifshits et al., 2005), and (Horne et al., 2022). In particular, using Fig. 1, we can conclude that in dense gas-dust clouds cosmic rays do not destroy complex molecules and damage the simplest bacteria.

5. Conclusion

The calculations of X-ray and soft gamma radiation transfer through soft tissues, cells and bacteria in space and radiology have been carried out. Consideration has been given to all detailed processes of energy absorption and scattering between quanta in biological tissues are taken into account. The yield spectra of X-ray and γ-ray emission from Soft-Tissue tissues at different geometric sizes were determined. Percentage contribution of each mechanism to the formation of the spectral response of tissues is highlighted. Based on these data, conclusions are made regarding the role of photo absorption and incoherent Compton scattering in the formation of absorbed dose. The calculations showed that at soft tissue sizes larger than 10 mm these two processes compete. The absorbed dose at quantum energies up to 10 keV is formed exclusively due to photo absorption by atoms of biological medium. If the size of soft tissues exceeds 100 mm, we get an exclusive contribution of Compton scattering of X-ray and gamma-quanta on free and weakly bound electrons of atoms and molecules. In other words, initially directed ionizing radiation becomes completely scattered. Moreover, as it moves through soft tissues, the long-wave part of the X-ray spectrum is significantly amplified, reaching 10 keV and being completely absorbed by the substance.

Acknowledgements. The authors are grateful to the administration of Tsafon Medical Center for material assistance. D.D. thanks Prof. Avi Peretz for creating the conditions for this work and Dr. Natalia Volinski for constructive discussion of our work.

Contribution. The authors acknowledge the same contribution to the writing of the article and have no claims against each other.

Reference

Dayal N.C., Wickramasinghe·C. A. Tout·J.C., et al.: 2019, *A&ApSS*, **364**, 205.

Hoyle F., Wickramasinghe N.C.: 1983, *Nature*, **305**, Iss. 5930, 161; DOI: 10.1038/305161a0.

Horne W.H., Volpe R.P., Korza G. et al.: 2022, *Astrobiology*, **22**, Iss. 11, Nov., 1271-1375. https://doi.org/10.1089/ast.2022.0065.

Imserti S., Kyriakou M.A., Bernal M. et al.: 2018, *Medical Physics*, **45**, 772.

Kyriakou I., Sakata D., Tran H. N., Perrot Y., Shin W.-G., Lampe N., et al.: 2022, *Cancers*, **14**, 35.

Lifshits M.A., Chernetskii V.A., Mitrofanov I.G. et al.: 2005, *Astron. J.* (rus.), **82**, 11, 1025–1041.

Stantcheva T., Shematovich V.I., Herbst E.: 2002, *A&A*, **391**, 1069–1080.

Wallis M.K., Wickramasinghe N.C. and Hoyle F.: 1992, *Adv. in Space Res*., **12**, 282–285.

Weber G. https://web-docs.gsi.de/~stoe_exp/web_programs/x_ray_absorption/index.php

https://doi.org/10.18524/1810-4215.2024.37.312667

DIAGNOSTICS OF SOLAR PROTON EVENTS AND CORONAL SHOCK WAVES BY THE PARAMETERS OF SOLAR RADIO BURSTS OF TYPE II AND IV

E.A.Isaeva

Institute of Radio Astronomy of the NAS of Ukraine, *isaevaode@gmail.com*

ABSTRACT. This paper presents the results of a study of the relationship between solar cosmic rays (SCR) and coronal shock waves (CSW) with the parameters of solar microwave continuum radio bursts of type IV (μ–bursts), as well as with the parameters of type II radio bursts. A total of 349 solar proton events (SPE) were analyzed for the period from 03–02–1986 to 12–02–2018. For the analysis, we used original records of solar radio emission at 8 fixed frequencies in the range of 245–15400 MHz based on data from the Radio Solar Telescope Network (RSTN), original records of dynamic spectra from the SRS (Solar Radio Spectrograph) in the range of 25–180 MHz, tabular data for the velocity of coronal shock waves, as well as original records of the SCR proton flux intensity with proton energies E_p in the range of >1–100 MeV based on data from the GOES series devices.

It has been previously shown that for most proton events there is a strong relationship between the SCR proton flux and the parameters of type IV continuum microwave bursts, which indicates a dominant role of the SCR acceleration process in the flare region. However, as a result of recent detailed studies of the fine structure of type II radio bursts, a strong relationship was found between the intensity of the mid–relativistic SCR proton flux and certain parameters of type II radio bursts in the 25–180 MHz range. The presence of a strong relationship between the SCR proton flux and the parameters of type II radio bursts indicates an important role of SCR proton acceleration at the fronts of coronal shock waves. A fairly strong relationship was also found between the velocity of coronal shock waves and the parameters of type IV microwave bursts, which definitely indicates that coronal shock waves are associated with solar flares.

Keywords: proton events, proton flux intensity, type II radio bursts, coronal shock waves.

АНОТАЦІЯ. У цій роботі представлені результати дослідження зв'язку сонячних космічних променів (СКП) та корональних ударних хвиль (КУХ) з параметрами мікрохвильових континуальних радіосплесків IV типу, а також з параметрами радіосплесків II типу. Загалом було проаналізовано 349 сонячних протонних подій (СПП) за період із 03–02–1986 по 12–02–2018 роки. Для аналізу використовувалися оригінальні записи радіовипромінювання Сонця на 8 фіксованих частотах в діапазоні 245–15400 МГц за даними RSTN (Radio Solar Telescope Network), оригінальні записи динамічних спектрів з SRS (Solar Radio Spectrograph) в діапазоні 25–180 МГц, табличні дані корональних ударних хвиль, а також оригінальні записи інтенсивності потоку протонів СКП з енергією протонів у діапазоні >1–100 МеВ за даними апаратів серії GOES.

Раніше вже було показано, що для більшості протонних подій існує сильний зв'язок потоку протонів СКП з параметрами мікрохвильових континуальних сплесків IV типу, що вказує на домінуючу роль процесу прискорення СКП у спалахової області. Однак в результаті останніх детальних досліджень тонкої структури радіосплесків II типу також було виявлено сильний зв'язок між інтенсивністю потоку середньорелятивістських протонів СКП і певними параметрами радіосплесків II типу в діапазоні 25–180 МГц. Наявність сильного зв'язку потоку протонів СКП з параметрами радіосплесків II типу вказує на важливу роль прискорення протонів СКП на фронтах ударних корональних хвиль. Також було виявлено досить сильний зв'язок між швидкістю корональних ударних хвиль і параметрами мікрохвильових сплесків IV типу, що безумовно вказує на те, що корональні ударні хвилі пов'язані з сонячними спалахами.

Ключові слова: протонні події, інтенсивність потоку протонів, радіосплески II типу, корональні ударні хвилі.

1. Introduction

In this paper, we present the results of a comparative analysis of the relationship between SCRs and coronal shock waves (CSWs) with the parameters of type IV continuum radio bursts in the 245–15400 MHz range and with the parameters of type II radio bursts in the 25–180 MHz range. Previously, some issues regarding the relationship between the SCR proton flux and the parameters of type II radio bursts were considered in (Tsap & Isaeva, 2011; 2012; 2013). As a result of studying the relationship between the frequency drift velocity of meter-decameter type II bursts and the SCR proton flux intensity I_p of different energies, two families of proton events were discovered, which, according to Tsap (Isaeva & Tsap, 2011), suggests the generation of shock waves both in the region of flare energy release and by a moving coronal mass ejection (CME). The works (Isaeva & Tsap, 2011; 2012; 2013) present the results of the study of the efficiency of SCR acceleration by coronal and interplanetary shock waves, and also provide arguments in favor of the model of a two-stage process of proton acceleration (Wild et. al., 1963; Tsap & Isaeva, 2012). A comparative analysis

showed that the acceleration of protons by coronal shock waves is more efficient than by interplanetary shock waves, and that the main acceleration of protons occurs in the flare region and additionally at the fronts of shock waves (Tsap & Isaeva, 2012).

2. The relationship between the intensity of the proton flux of the SCR I_p and the parameters of type IV microwave bursts

Previously, the relationship between the ntensity of the proton flux of solar cosmic rays I_p and various parameters of solar microwave bursts
of type IV (μ-bursts) was studied based on a large sample of proton events. The studied sample contained 143 proton events accompanied by solar continuous bursts of type IV for the period from 06–02–1986 to 14–10–2014.

Proton events were selected according to generally accepted criteria of protonity. It is known that for events with a *U*- or *W*-shaped type
of frequency radio spectrum of solar radio bursts with maxima in the meter and centimeter wavelength ranges and with a minimum in the decimeter range, the best correlation between the parameters of μ-bursts and the intensity of the flux of subrelativistic electrons and protons of solar cosmic rays is observed.

Previously, in the works (Isaeva, 2018; 2020), the relationship between the integral flux $\int F_f dt$ of type IV radio bursts at a given frequency f and the flux of SCR protons I_p with an energy of > 30 MeV was already investigated. It was shown that the maximum relationship between I_p and $\int F_f dt$ is observed for microwave bursts (μ-bursts) and for subrelativistic protons.

In this work, the relationship between the proton flux intensity I_p and three microwave burst parameters, namely the maximum value F_m , the rise time t_{rise} and the duration of type IV μ-bursts t at a frequency of 8800 MHz, was investigated simultaneously. Figures 1 a) and b) show the scattering diagrams between the proton flux and the μ-burst parameters F_m, and t, and Figure 1c) shows the scattering diagram between the calculated $I_{p,c}$ (1) and the observed values of the SCR proton flux I_p. A comparative analysis showed

$$\log_{10} I_{p,c} = 1.209 \cdot \log_{10} F_m + 0.725 \cdot \log_{10} t_\mu + 1.110 \cdot \log_{10} t_{rise} - 4.087 \quad (1)$$

that the correlation coefficient r between the observed I_p and calculated values of the proton flux $I_{p,c}$ (1) is slightly higher ($r \approx 0.83$) than with the integral flux of μ-bursts $\int F_\mu dt$ at a frequency of 8800 MHz (Isaeva, 2018, 2020), where the correlation coefficient r between I_p and $\int F_f dt \approx 0.80$.

The presence of a strong connection between the SCR proton flux and the parameters of microwave radio bursts definitely indicates the acceleration of SCR protons in the flare region. However, there are many indications that shock waves also play an important role in the acceleration of solar cosmic rays (Gopalswamy et al., 2002; Cliver et al., 2004). In this regard, detailed studies of the fine structure parameters of type II radio bursts and their connection with SCRs were carried out.

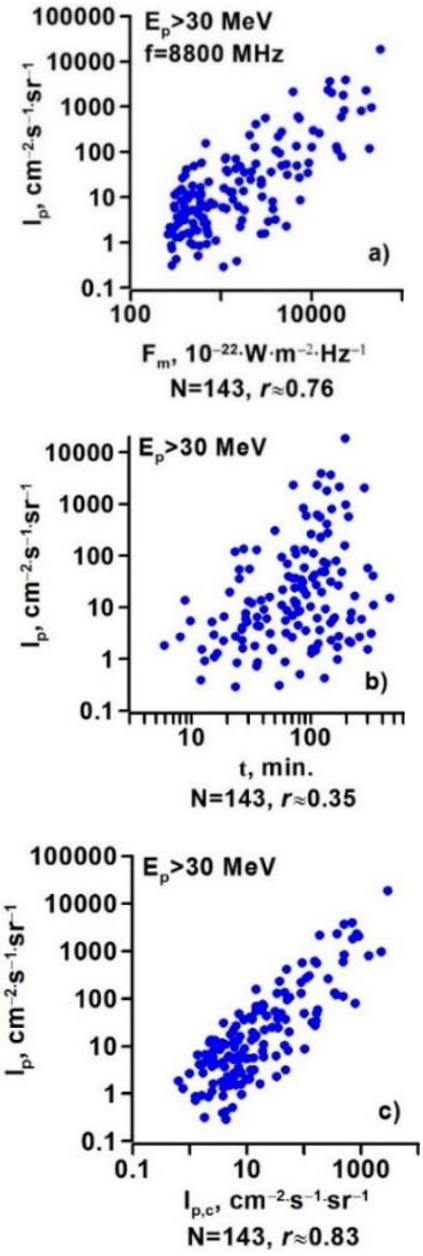

Figure 1: a). and b). Relationship of the proton flux of solar cosmic rays I_p with the parameters of μ-bursts F_m and t; c). scattering diagram between the calculated $I_{p,c}$ (1) and observed values of the intensity of the proton flux of solar cosmic rays I_p.

3. The relationship between the intensity of the proton flux I_p of the SCR and the parameters of type II radio bursts

The relationship between the proton flux intensity of the solar cosmic rays I_p and various parameters of type II radio bursts has been previously studied. As a result of these studies, a strong relationship was found between the proton flux intensity I_p and the parameters $f_{min,1}$ and V_{II} (Isaeva, 2019; 2020). In the present work, multiple correlation and regression analysis was used to study the rela-

tionship between the proton flux I_p simultaneously with three parameters $f_{min,1}$, V_{II} and λ (2),

$$\log_{10} I_{p,c} = -4.608 \cdot \log_{10} f_{min,1} + 1.707 \cdot \log_{10} V_{II} + 0.596 \cdot \log_{10} \lambda + 11.882 \quad (2)$$

$$b_{min} = \frac{f_{min,2} - f_{min,1}}{f_{min,1}} \quad (3)$$

$$V_{II} = \frac{f_2 - f_1}{t_i - t_0} \quad (4)$$

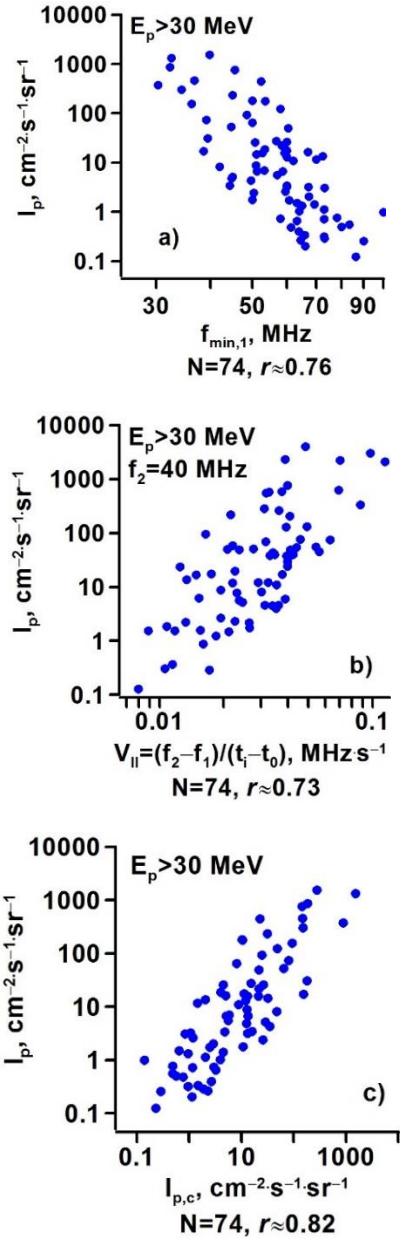

Figure 2: a). The relationship between the proton flux intensity I_p and the frequency $f_{min,1;}$ b). The relationship between the proton flux intensity I_p and the parameter of type II radio bursts V_{II}; c). Scattering diagram between the observed I_p and calculated values of the proton flux intensity $I_{p,c}$ (2) with proton energy $E_p > 30$ MeV.

where $f_{min,1}$ is the frequency at the first harmonic at the time t_{min} of the minimum relative distance b_{min} (3) (Isaeva, 2019; 2020) between the harmonics of type II bursts, and V_{II} (4) (Isaeva, 2018; 2020) is a parameter that to some extent characterizes the shift of the shock front over time t_i, where f_1 and f_2 are the frequency of the type II burst at the 1-st and 2-nd harmonics, and λ is the heliolongitude attenuation coefficient of the solar cosmic ray proton flux I_p (Ochelkov, 1986).

Figures 2 a) and b) show the relationship of the SCR proton flux intensity I_p with the parameters $f_{min,1}$ and V_{II}, respectively. Figure 2a) shows that the relationship of I_p with $f_{min,1}$ and V_{II} is slightly worse than for the full sample in (Isaeva, 2020). This is due to the fact that in this case only those events were selected for which the parameters $f_{min,1}$ and V_{II} could be determined simultaneously with sufficient accuracy. Therefore, the results differ somewhat from the results presented in (Isaeva, 2020). But despite this, the relationship of I_p with three parameters $f_{min,1}$, V_{II} and λ is much higher (see Figure 2c) than with each parameter separately. Figure 2c) shows the scattering diagram between the calculated $I_{p,c}$ (2) and the observed values of the proton flux I_p .

As can be seen in Figure 2c), the correlation coefficient r has significantly increased from 0.73-0.76 to 0.82. The increase in the connection of I_p with two parameters $f_{min,1}$ and V_{II} also indicates that the parameters $f_{min,1}$ and V_{II} are closely related to each other.

4. The relationship between the intensity of the proton flux of SCR I_p and the integral flux of μ-bursts $\int F_\mu dt$ and with the parameter of type II radio bursts V_{II}

The discovered high correlation of the intensity of the proton flux of SCR I_p with the parameters of μ-bursts, as well as with the parameters of type
II radio bursts, does not allow us to unambiguously answer the question of where and how the acceleration of SCR protons occurs.

In this connection, the connection between the intensity of the SCR proton flux I_p and three parameters (5) was investigated simultaneously, namely, with the integral flux of μ-bursts $\int F_\mu dt$ at a frequency f=8800 MHz, with the parameter V_{II} (4), which to some extent characterizes the displacement of the shock wave front over time t_i,

$$\lg I_{p,c} = 0.461 \cdot \lg \int f_\mu \, dt + 2.493 \cdot \lg V_{II} + 0.835 \cdot \lg \lambda + 3.216 \quad (5)$$

and with the coefficient of heliolongitudinal attenuation of the SCR proton flux λ (Ochelkov, 1986).

For this purpose, only those proton events were selected that were simultaneously accompanied by type IV microwave bursts at a frequency of 8800 MHz and type II radio bursts in the range of 25–180 MHz. Original records of solar radio emission were used for the analysis. The parameters $\int F_\mu dt$ and V_{II} were not chosen by chance, since it was previously shown that there is a strong connection between I_p and $\int F_\mu dt$ and V_{II} (Isaeva, 2018; 2020), where the correlation coefficient r between I_p and the parameters $\int F_\mu dt$ and $V_{II} \approx 0.80$. Figure 3a) shows the scattering diagram between

the integral flux of μ-bursts $\int F_\mu dt$ at a frequency of 8800 MHz and the intensity of the SCR proton flux I_p, and Fig. 3b) between the parameter V_{II} and I_p . In Fig. 3a) it is evident that for proton events for which a strong correlation between the proton flux I_p and the parameter of type II V_{II} radio bursts is observed (Fig. 3b), the correlation between I_p and the integral flux of μ-bursts $\int F_\mu dt$ turned out to be significantly worse ($r \approx 0.65$) compared to what was previously established based on a large sample of proton events (N = 147) (Isaeva, 2018; 2020), where the correlation coefficient r between $\int F_\mu dt$ and $I_p \approx 0.80$.

Thus, based on the obtained results, it can be concluded that for the overwhelming majority of proton events (and there were 147 of them), the main acceleration of SCR protons occurred in the flare region in current sheets, and for other proton events that were accompanied by meter-decameter type II bursts, the main acceleration of SCR protons occurred at the fronts of coronal shock waves. And therefore, for such events, a lower correlation is observed between the integral flux of microwave bursts $\int F_\mu dt$ and the flux of SCR protons I_p, where the correlation coefficient between $\int F_\mu dt$ and I_p does not exceed 0.65. But despite the fact that the connection of I_p with $\int F_\mu dt$ for such events is low, nevertheless, if we consider the connection of I_p simultaneously with three parameters $\int F_\mu dt$, V_{II} and the coefficient of heliolongitudinal attenuation of the proton flux of solar cosmic rays (5) (Ochelkov, 1986), then a significant increase in the connection between I_p and the studied parameters is observed, where the correlation coefficient r increases to ≈ 0.86 (Fig. 3c).

Figure 3c) shows the scatter diagram between the calculated $I_{p,c}$ values of the SCR proton flux intensity (5) and the observed I_p values. The significant increase in the correlation of $I_{p,c}$ with the parameters $\int F_\mu dt$ and V_{II} in model (5) indicates that the parameters $\int F_\mu dt$ and V_{II} are related, which in turn confirms the relationship between coronal shock waves and solar flares.

5. Relationship between coronal shock waves and parameters of type IV microwave radio bursts

It is known that shock waves can be generated by both solar flares and coronal mass ejections. It is believed that meter-wave type II bursts are associated with shock waves generated in flares (Wagner et al., 1983; Vrsnak et al., 1995), and bursts in the decameter-hectometer range are associated with the propagation of interplanetary shock waves generated by CMEs (Gopalswamy et al., 1998; Classen et al., 2002). The most reliable indicator of shock waves in the solar corona are slowly drifting type II bursts. It is believed that the plasma mechanism of radio emission is responsible for their generation (Cairns et al., 2003).

Further detailed studies showed that there is a certain connection between the parameters of microwave bursts IV and the parameters of bursts II type in the range of 25-180 MHz. The original records of dynamic spectra of radio emission of the Sun in the range of 25-180 MHz were used for the analysis.

$$\lg f_{i,j} = a_j \cdot \sqrt{t_i} + b_j \qquad (6)$$

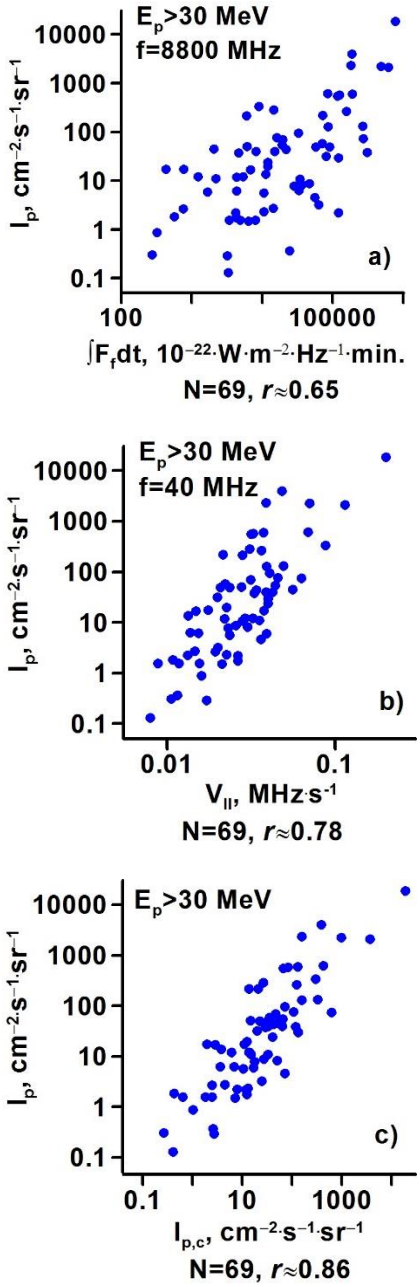

Figure 3: a). The relationship of the proton flux of solar cosmic rays I_p with the integral flux of μ-bursts. b). The relationship of I_p with the parameter of radio bursts of type II bursts. c). Scattering diagram between the calculated $I_{p,c}$ (5) and the observed values of the intensity of the proton flux of solar cosmic rays I_p.

Comparative analysis showed that there is a fairly strong relationship between the parameter a_j in the regression model (6) (Isaeva & Tsap, 2017) characterizing the decrease in the frequency drift rate of type II radio bursts in the range of 25–180 MHz and the rise time of t_{rise} μ-bursts at a frequency of 8800 MHz. The correlation coefficient r between t_{rise} and a_j is ≈ 0.68 (see Fig. 4a). Due to the fact that μ-bursts differ significantly in duration, the rise time of t_{rise} is expressed as a percentage of the duration of μ-bursts. In this case, the burst duration for each event was equal to 100%.

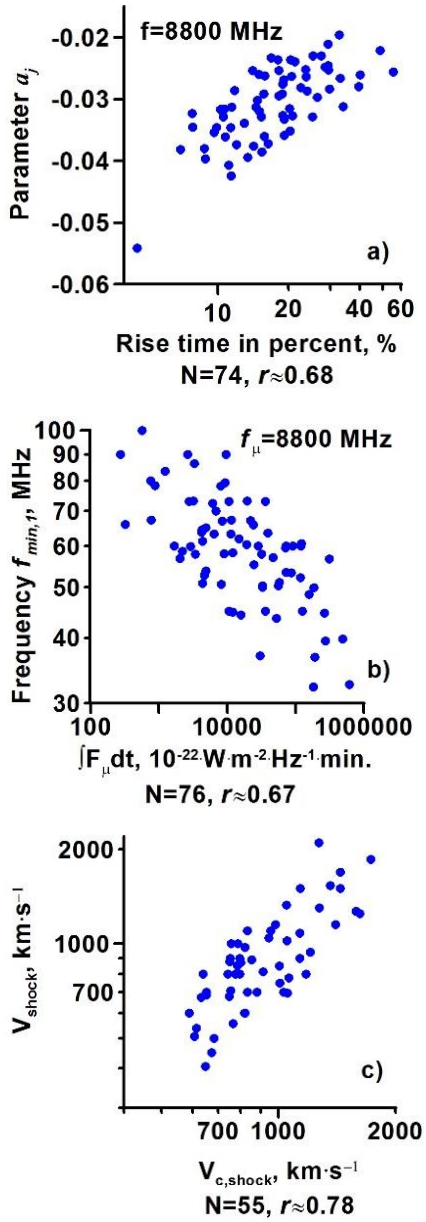

Figure 4: a). The relationship between the parameter a_j and the rise time t_μ of type IV microwave bursts at 8800 MHz; b). The relationship between the frequency $f_{min,1}$ and the integral flux $\int F_\mu dt$ of type IV microwave bursts at 8800 MHz; c). The scattering diagram between the calculated $V_{c,shock}$ (7) and the observed values of shock wave velocity V_{shock}

A fairly strong connection was also found between the integral flux of μ-bursts $\int F_\mu dt$ at a frequency of 8800 MHz and the value of the frequency $f_{1,min}$ at the 1-st harmonic at the moment of the minimum relative distance between the harmonics of type II bursts (3), where the correlation coefficient r between the studied parameters is ≈ 0.67 (see Fig. 4 b)).

$$\log_{10} V_{c,shock} = 0.197 \cdot \log_{10} F_m + 0.242 \cdot \log_{10} t_\mu - 0.243 \cdot \log_{10} t_{rise} + 2.111 \quad (7)$$

In the present work, the relationship between the coronal shock wave velocity V_{Shock} (tabular data) and various parameters of type IV radio bursts was also investigated. A comparative analysis showed that there is a strong relationship between the coronal shock wave velocity $V_{c,shock}$ and the parameters of microwave bursts (7) (see Fig. 4c), where F_m is the maximum value, t_μ is the duration and t_{rise} is the rise time of the μ-burst at a frequency of 8800 MHz, where the correlation coefficient r between the calculated $V_{c,shock}$ (7) and the observed values of shock waves V_{shock} is ≈ 0.78. In Fig. 4c), the number of events is significantly smaller (N=55) than in Fig. 4 a) and b). This is due to the fact that not all type II bursts have original records or estimated values for the coronal shock wave velocity V_{shock}.

The presence of a fairly strong connection between the parameters of type IV continuous microwave bursts and the parameters of type II meter-decameter bursts, as well as with the velocity of shock waves, definitely indicates that coronal shock waves are associated with flares, which is quite consistent with the results of other authors (Wagner et al., 1983; Vrsnak et al., 1995).

6. Conclusion

As a result of detailed studies, it was shown that for the overwhelming majority of proton events, the main acceleration of SCR protons occurs in the flare region and for such events, a strong relationship is observed between the proton flux and the parameters of type IV continuum microwave bursts. For the remaining part of the proton events, which were accompanied by type IV and type II radio bursts in the range of 25–180 MHz, the main or additional acceleration of SCR protons occurs at the fronts of coronal shock waves and for such events, a strong relationship is observed between the SCR proton flux and the parameters of type II radio bursts. It was also shown that for proton events, which were simultaneously accompanied by type IV and type II radio bursts, a sufficiently strong relationship is observed between the velocity of coronal shock waves and the parameters of type IV microwave bursts, which definitely indicates that coronal shock waves are generated by solar flares.

References

Cairns I., Knock S., Robinson P., Kuncic Z.: 2003, *SSRv*, **107,** 27.
Classen H. et al.: 2002, *A&A*, **384,** 1098.
Cliver E., Kahler S., Reams D.: 2004, *ApJ.*, **605**, 902.
Gopalswamy N. et. al.: 1998, *JGR*, **103**, 307.
Gopalswamy N., Yashiro S., Michalek G. et al.: 2002, *ApJ.*, **572**, 103.
Isaeva E., Tsap Yu.: 2011, *BCrAO*, **107**, 78.
Isaeva E., Tsap Yu.: 2017, *OAP*, **30**, 222.
Isaeva E.: 2018, *OAP*, **31**, 132.
Isaeva E.: 2019, *OAP*, **32**, 122.
Isaeva E.: 2020, *OAP*, **33**, 79.
Ochelkov Lu. P.: 1986, *Ge&Ae*, **26**, 1007.
Reames D.: 1999, *SSRv.*, 1999, **90**, 413.
Tsap Yu., Isaeva E.: 2012, *BCrAO*, **108**, № 1,52.
Tsap Yu., Isaeva E.: 2012, *Ge&Ae*, **52**, № 7, 921.
Tsap Yu., Isaeva E.: 2013, *CosRe*, **51**. № 2. 108.
Tsap Yu., Isaeva E., Kopylova Yu.: 2020, *AstL*, **46**, № 2, 144.
Vrsnak B. et al.: 1995, *SoPh*, **158,** 331.
Wagner W. et al.: 1983, *A&A*, **120**, 136.
Wild J., Smerd S., Weiss A.: 1963, *AnRevA&A*, **1**, 291.

https://doi.org/10.18524/1810-4215.2024.37.313214

EVOLUTION AND FLARE ACTIVITY OF CARRINGTON-CLASS SOLAR ACTIVE REGION NOAA 13664 AND ITS IMPACT ON THE EARTH

N.M. Kondrashova, M.M. Pasechnik, S.M. Osipov, M.I. Pishkalo

Main Astronomical Observatory of the NAS of Ukraine,
Kyiv, Ukraine

kondr@mao.kiev.ua; rita@mao.kiev.ua; osipov@mao.kiev.ua; pish@mao.kiev.ua

ABSTRACT. We have analyzed the temporal and spatial evolution and the flare activity of the active region (AR) NOAA 13664 and its impact on the Earth. The large group of sunspots that formed it definitely belonged to the Carrington class. The region appeared in the southern hemisphere of the solar disk on 2024 May 1. The number of sunspots was growing rapidly and its area increased from 40 to 2400 millionths of the solar hemisphere. The AR had a complex multipolar configuration of the magnetic field beginning on May 7. On May 8, solar flares of intensity X1.0, M8.7 and M9.9 took place in it, which caused coronal mass ejections (CMEs). These CMEs reached the Earth on May 10, causing strong and extreme geomagnetic storms with bright and very long-lasting auroras. The event was classified as a G5 geomagnetic storm, making it the most intense storm since 2003. On May 9-11, flares of intensity X2.3, X1.5, X4, and X5.8 occurred, each of which caused a CME. The radiation from the X5.8 flare caused a deep shortwave radio blackout over the Pacific Ocean. On May 14, an X8.7-class flare occurred on the western limb of the Sun, the most powerful in solar cycle 25 at that time. The CME that formed caused a short-wave radio blackout over America.

On May 9 during observations at the Ernest Gurtovenko solar horizontal telescope of the Main Astronomical Observatory of the National Academy of Sciences of Ukraine the X2.3 flare spectrograms in its main phase were obtained.

The active region 13664 passed beyond the solar disk and returned on May 29. It has been renumbered as NOAA 13697. On May 31 and June 1 AR produced three X-flares: X1.1, X1.4, and X1.0. Each of them formed CMEs, which reduced the power of shortwave transmissions at all frequencies below 30 MHz. Radiation from M9.8-class flare on June 8 ionized the upper part of the Earth's atmosphere, causing a deep shortwave radio blackout in the western Pacific Ocean.

On June 24 AR13664 returned again. This was its 3rd trip across the solar disk. It was renamed as NOAA 13723. Although the sunspot region was already fragmented to a fraction of its former size, its magnetic component continued to produce powerful solar flares. On June 23, M9.3-class flare occurred in AR, CME from which caused a moderate shortwave radio blackout in Western Europe and Africa.

In total, AR13664 produced 198 C-class, 87 M-class, and 17 X-class flares during its three passes across the Sun's disk.

By studying in detail the evolution of this hyperactive region NOAA 13664 and its impact on Earth, we are improving our ability to predict solar activity and warn of the extreme space weather events it causes.

Keywords: active regions, sunspots, solar flares, coronal mass ejections, geomagnetic storms.

АНОТАЦІЯ. Ми проаналізували часову та просторову еволюцію та спалахову активність активної області (АО) NOAA 13664 та її вплив на Землю. Велика група сонячних плям, яка її утворила, безумовно належала до класу Керрінгтона. Область з'явилася в південній півкулі сонячного диска 1 травня 2024 р. Кількість сонячних плям швидко зростала, їх площа збільшилася від 40 до 2400 мільйонних частин сонячної півкулі. Починаючи з 7 травня АО мала складну мультиполярну конфігурацію магнітного поля. 8 травня в ній відбулися сонячні спалахи інтенсивністю X1.0, M8.7 і M9.9, які викликали корональні викиди маси (КВМ). Ці КВМ досягли Землі 10 травня, спричинивши сильні та екстремальні геомагнітні бурі з яскравими та дуже тривалими полярними сяйвами. Ця подія була класифікована як геомагнітна буря G5, що робить її найсильнішою бурею з 2003 року. 9-11 травня відбулися спалахи інтенсивністю X2.3, X1.5, X4 та X5.8, кожен з яких викликав КВМ. Випромінювання від спалаху X5.8 спричинило глибоке короткохвильове радіозатемнення над Тихим океаном. 14 травня на західному лімбі Сонця відбувся спалах класу X8.7, на той момент найпотужніший у 25-му сонячному циклі. КВМ, яке утворилося, спричинило короткохвильове радіо-затемнення над Америкою.

9 травня під час спостережень на сонячному горизонтальному телескопі імені Ернеста Гуртовенка Головної астрономічної обсерваторії НАН України отримано спектрограми спалаху X2.3 у його головній фазі.

Активна область 13664 вийшла за межі сонячного диска і повернулася 29 травня. Вона була перенумерована як NOAA 13697. 31 травня та 1

червня AR створила три X-спалахи: X1.1, X1.4 і X1.0. Кожен з них утворив КВМ, які зменшили потужність короткохвильових передач на всіх частотах нижче 30 МГц. Радіація від спалаху класу M9.8 8 червня іонізувала верхню частину земної атмосфери, спричинивши глибоке короткохвильове радіозатемнення в західній частині Тихого океану.

24 червня AR13664 знову повернулася. Це була її третя подорож по сонячному диску. Її перенумерували на NOAA 13723. Хоча АО вже була фрагментована до частки свого колишнього розміру, її магнітний компонент продовжував створювати потужні сонячні спалахи. 23 червня в АО стався спалах M9.3, КВМ від якого спричинив помірне короткохвильове радіовимкнення в Західній Європі та Африці.

Загалом AR13664 під час своїх трьох проходів по диску Сонця створила 198 спалахів класу C, 87 спалахів класу M і 17 спалахів класу X.

Детально вивчаючи еволюцію цієї гіперактивної області NOAA 13664 та її вплив на Землю, ми вдосконалюємо нашу здатність прогнозування сонячної активності та попереджати про екстремальні явища космічної погоди, які вона викликає.

Ключові слова: активні області, сонячні плями, сонячні спалахи, викиди корональної маси, геомагнітні бурі.

1. Introduction

The Carrington Event in early September 1859, a solar flare with an associated geomagnetic storm, is considered one of the most extreme space weather events in observed history and the first direct evidence of a connection between the Sun and Earth's environment. The Carrington flare has become a benchmark as the earliest and brightest solar flare ever recorded. The flare's power estimate from ≈X80 to ≈X14 on the GOES X-ray scale, obtained by scientists using different methods, is given in the paper (Hayakawa et al., 2023). On September 1, british astronomers R. Carrington and R. Hodgson independently observed this flare (Carrington, 1859; Hodgson, 1859), which caused a large coronal mass ejection (CME). It reached Earth after 18 hours. On September 1-2, the largest geomagnetic storm in history began, which caused the failure of telegraph systems throughout Europe and North America. The magnetometers went off the scale. The aurora borealis has been seen all over the world, even by people in Cuba, Jamaica and Hawaii who have never seen anything like it before. The Carrington event became a benchmark of space weather impact on our planet. The Carrington event is certainly one of the most extreme space weather events, but it is not unique. Research indicates that Carrington-class storms occur every 40 to 60 years. The NOAA 13664 active region studied in this paper was one of the largest and most active solar regions observed in the current 25th solar cycle. It rivaled the Carrington sunspot group in size. AR produced many powerful flares that caused strong magnetic storms on the Earth (Hayakawa et al., 2024; Romano et al., 2024). In present paper we analyze the evolution and flare activity of this active region and its impact on Earth. Studying the properties of such regions can be useful for improving methods for predicting solar activity and extreme space weather events.

2. Observational data

The magnetograms, continuum images and EUV-images were provided by the Solar Dynamics Observatory (SDO) the Helioseismic and Magnetic Imager (HMI) and the Atmospheric Imaging Assembly (AIA). The X-ray data were obtained at Geostationary Operational Environmental Satellite (GOES). Data on the solar flares are taken from the site https://www.lmsal.com/solarsoft/latest_events_archive.html and data on SMEs and their impact on Earth from the site https://www.swpc.noaa.gov. NOAA's Space Weather Prediction Center (SWPC) is a division of the National Weather Service. The spectrograms for X2.3-class flare were recorded on 2024 May 9 with the Ernest Gurtovenko solar horizontal telescope at the Main Astronomical Observatory in Kyiv. The Hα line profiles were obtained.

3. Active region NOAA 13664

We analyzed the temporal and spatial evolution and flare activity of the active region 13664 and its impact on Earth. The region appeared in the southern hemisphere of the solar disk on May 1, 2024 of the current 25th cycle of solar activity. This AR attracted attention because its structure was rapidly changing (Fig. 1). Figure 2 shows how the spots number and its area changed during the first passage of the region across the Sun's disk. It can be seen that the maximum number of spots (N=81) in AR was observed on May 10, and the area occupied by them reached a maximum (S=2400 millionths of the solar hemisphere) on May 11. In a few days the active region not only increased significantly in size (up to ≈ 20 Mm), but its magnetic structure also became significantly more complex. Figure 3 shows AR magnetograms obtained by SDO/HMI on May 3 and 7. Starting from May 7, AR had a complex (βγδ) multipolar configuration of the magnetic field. It contained powerful and entangled magnetic fields, which allowed it to produce a series of moderate and strong solar flares that began on May 8. On May 8, solar flares of intensity X1.0, M8.7, X1.02 and M9.9 took place in AR, which caused powerful coronal mass ejections (CMEs) towards the Earth. When the CME reaches Earth, it can cause powerful effects on its magnetosphere, causing various space weather effects. Among the possible effects are aurora borealis, magnetic storms, malfunctions of electrical equipment, deterioration of radio wave propagation conditions. The three CMEs that formed on May 8 reached Earth on May 10, causing the strongest and most extreme geomagnetic storms in nearly 20 years. The event was classified as a G5 geomagnetic storm, making it the most intense storm since 2003. In 2003, the most powerful flare on record took place, estimated at about X18+. It created long-lasting radiation storms. The geomagnetic storm of May 10–11, 2024 was so strong (on

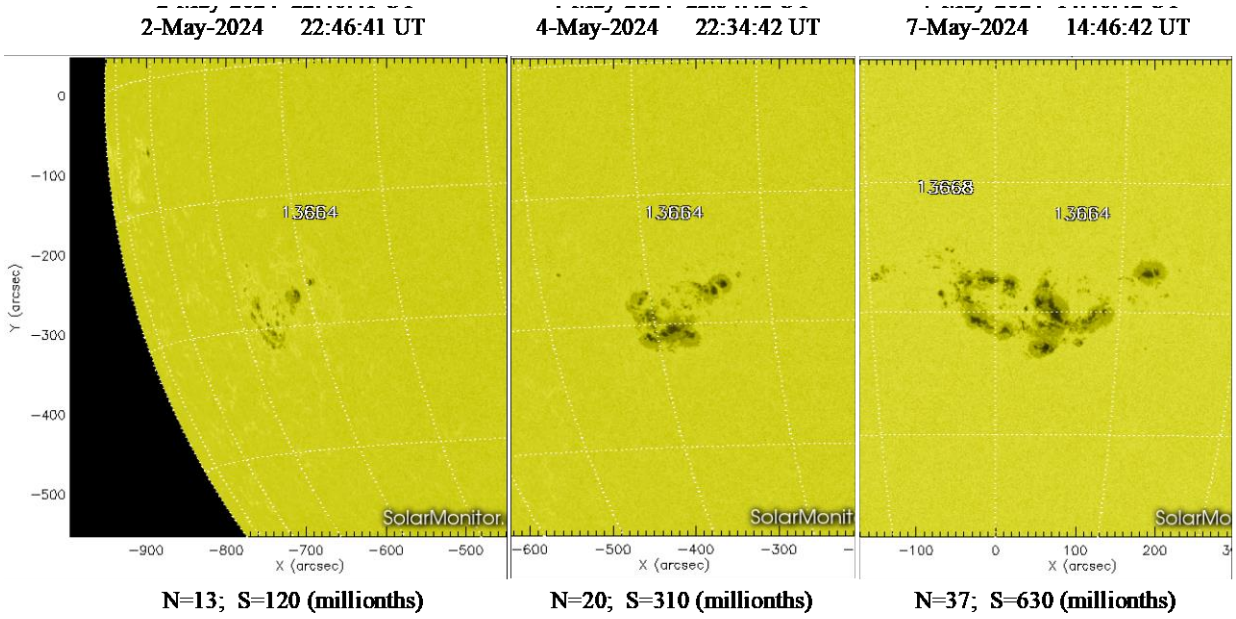

Figure 1: Change in the structure of the active region NOAA 13664.

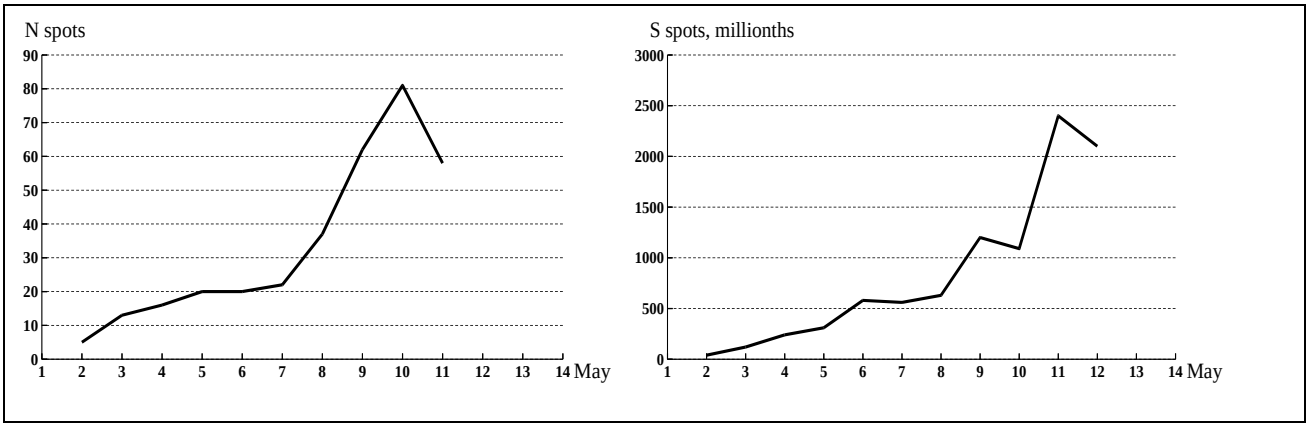

Figure 2: Change in the number of sunspots (N) and the area occupied by them (S, millionths) during the first passage of AR13664 across the Sun's disk.

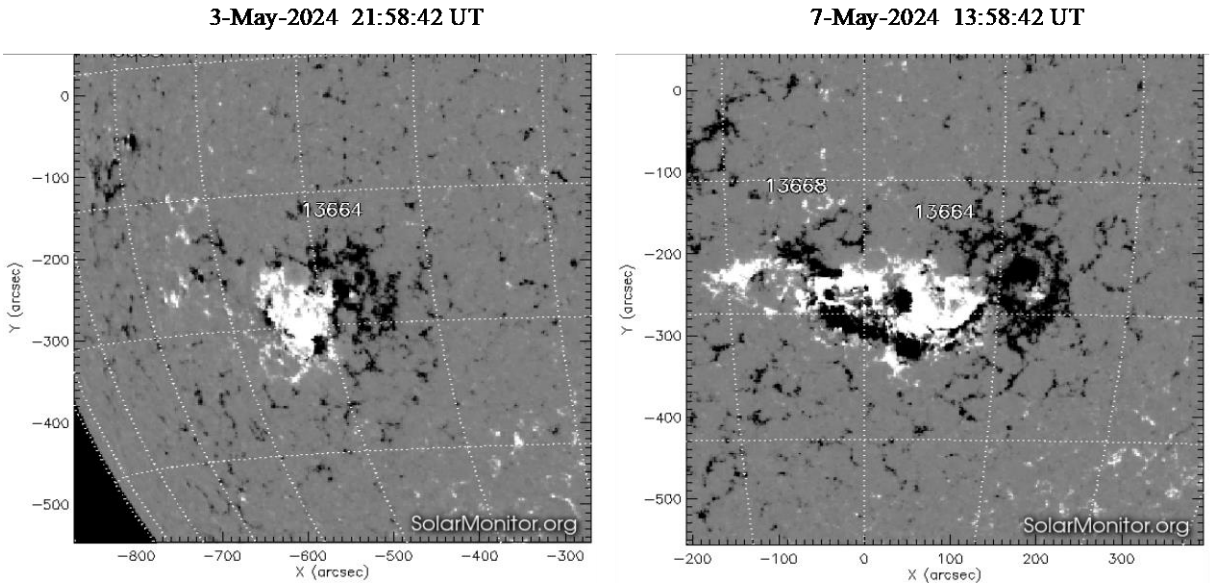

Figure 3: AR13664 magnetograms obtained with the SDO/HMI instrument on May 3 and 7, 2024. The positive and negative polarities are indicated by white and black colours, respectively.

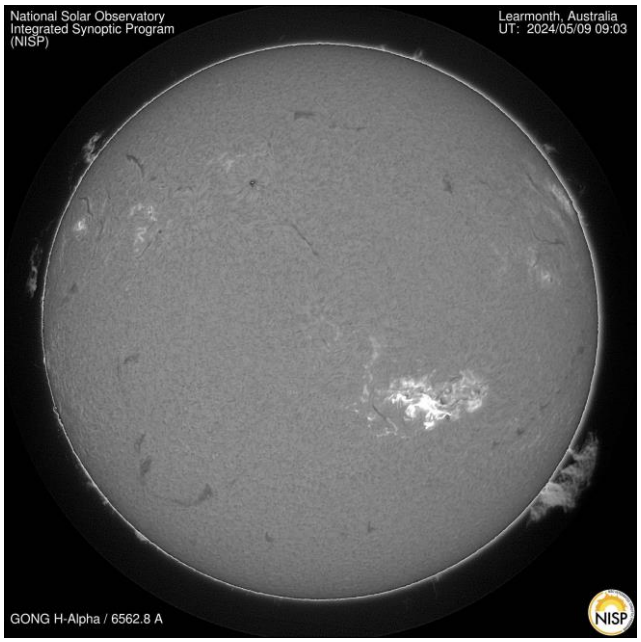

Figure 4: AR13664 May 9, 2024, flare X2.3.

May 11, the Kp index reached 9) that the US National Oceanic and Atmospheric Administration (NOAA), which predicts solar storms and their impact on our planet, issued for the first time in almost two decades storm warning After receiving the warning, NASA put at least one of its satellites, ICESat-2, into safe mode. Geomagnetic storm caused auroras across Europe, Asia, Mexico, and all 50 US states, even in Hawaii. Many people around the world saw the aurora borealis for the first time in their lives, for example, such as the residents of Puerto Rico at 18.1° north latitude. The Northern Lights were also observed in many regions of Ukraine at this time. Usually, such a phenomenon can be observed at a distance of 20–35° from the Earth's magnetic poles, and Ukraine is located at a latitude of 52°–44°, which makes the northern lights a rare phenomenon here.

On May 9, there were flares of intensity X2.3 (Fig. 4) and X1.1, each of which caused a CME. Spectrograms during the main phase of the X2.3 flare were recorded on May 9 at the Ernest Gurtovenko solar horizontal telescope of the Main Astronomical Observatory in Kyiv by observers S.M.Osipov and M.I.Pishkalo. The observation interval was 09:14:44 – 09:33:28 UT. The Hα line profiles show a strong emission during the flare main phase. Figure 5 shows examples Hα-spectra and Hα line profiles obtained for this flare.

Heading toward the western edge of the Sun, AR continued to produce powerful M- and X-class flares. On May 10 an X4.0 flare occurred in this AR. May 11, NASA's Solar Dynamics Observatory recorded a bright X5.8 flare. The radiation from this flare caused a deep shortwave radio blackout over the Pacific Ocean. Loss of signal at frequencies below 30 MHz was observed within an hour after the peak of the flare. A solar-proton storm of intensity S1 also occurred in the region. May 12 AR produced flare of intensity X1. There was a geomagnetic storm that began on May 10, but it was minor (G1). On the May 13, AR which was approaching the western limb of the Sun, i.e. was already leaving the zone of influence on the Earth, created a series of M-class flares that ejected CMEs into space. May 14 AR produced flares of intensity X1.2, X1.7, X8.7. Since the AR was beyond the edge of the solar disk, the strongest flare of the current solar cycle, the X8.7, was partially eclipsed and probably even stronger than it appeared (Fig. 6). The extreme ultraviolet radiation from the flare ionized the upper part of the Earth's atmosphere, resulting in signal loss at all frequencies below 30 Mhz. May 15 AR produced flare of intensity X3.5.

Figure 7 shows how many flares of different classes occurred in the AO during its first passage across the Sun's disk from May 1 to 15. In total, AR3664 produced 48 C-class, 55 M-class and 12 X-class flares in the first half of May. AR turned out to be one of the most powerful among all observed on the Sun in recent years.

4. Active region NOAA 13697

Active region 13664 went beyond the edge of the solar disk and returned on May 29 and was renumbered as NOAA 13697. AR was collapsing: the number of sunspots (maximum N=42) and the area occupied by them (maximum S=420 millionths of the solar hemisphere) were decreasing. But during its exit, the AR had an unstable magnetic field of the βγδ Hale class, which contained the energy for powerful flares (Fig. 8). On May 27, it created a X2.9 class flare at the eastern edge of the solar disk. After it came into view, it also produced X1.4 class flare on May 29. From May 31 to June 1, it produced three X-flares: X1.1, X1.4 and X1.0. Each caused a radio blackout on the Earth day side, with almost all longitudes affected by one or more flares. Although AR13697 was losing power, it produced another very strong M9.8 solar flare on June 8, ejecting a large CME into space. Radiation from the flare ionized Earth's upper atmosphere, causing a deep shortwave radio blackout in the western Pacific Ocean. The flare also caused a radiation storm category S2. On June 10, just beyond the sun's western limb, an X1.6 flare occurred in the AR, which was partially obscured by the Sun edge. As a result, it was not very geoeffective. In total, AR13697 produced 127 C-class, 30 M-class, and 6 X-class flares during its second pass across the Sun's disk from May 27 to June 10.

5. Active region NOAA 13723

Hyperactive AR13664 returned on June 24 again. This was its rare 3rd trip across the solar disk. It was renamed as NOAA 13723. It became much smaller compared to the previous ones, the maximum N=12 and their area S=210 millionths of the solar hemisphere were observed on June 26. Although the sunspot region was already fragmented to a fraction of its former size, its magnetic component continued to produce powerful solar flares (Fig. 8). On June 23, M9.3-class flare occurred in AR. It caused moderate

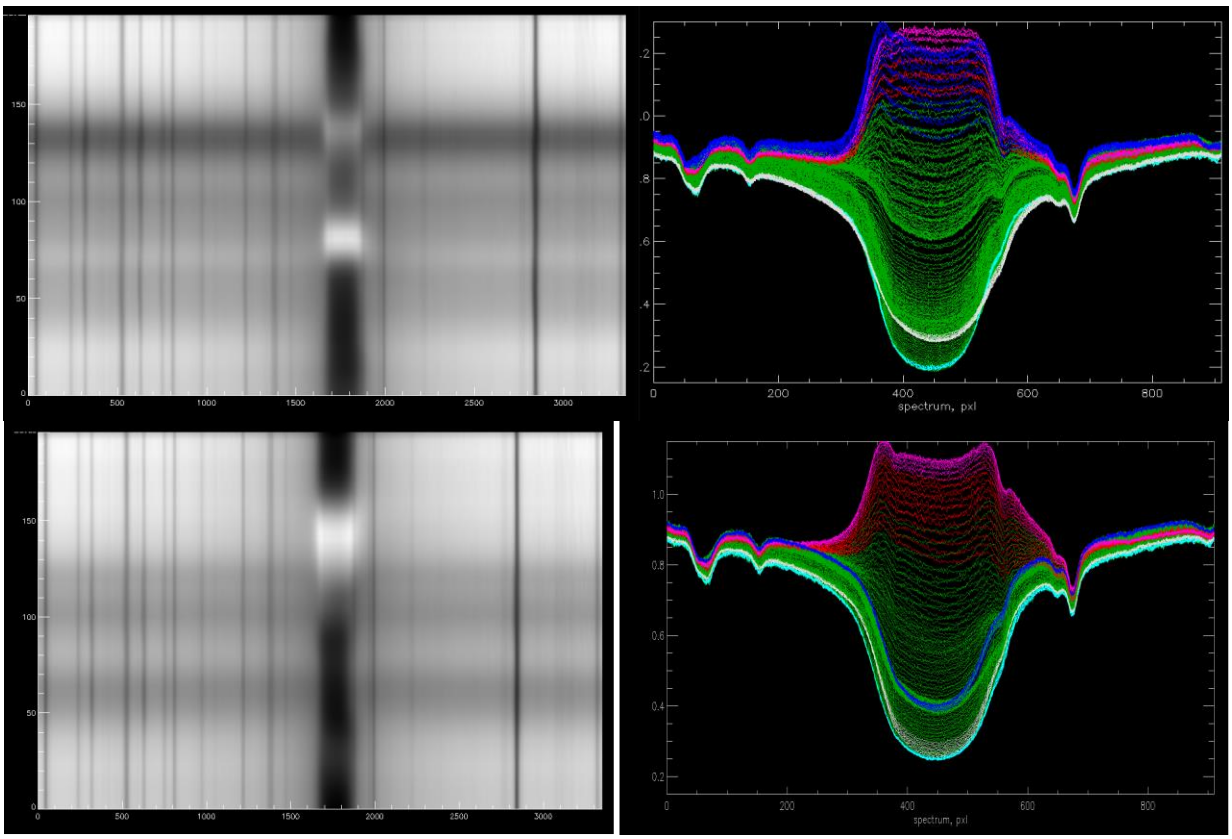

Figure 5: Examples of obtained Hα-spectra and Hα-line profiles for a flare X2.3-class

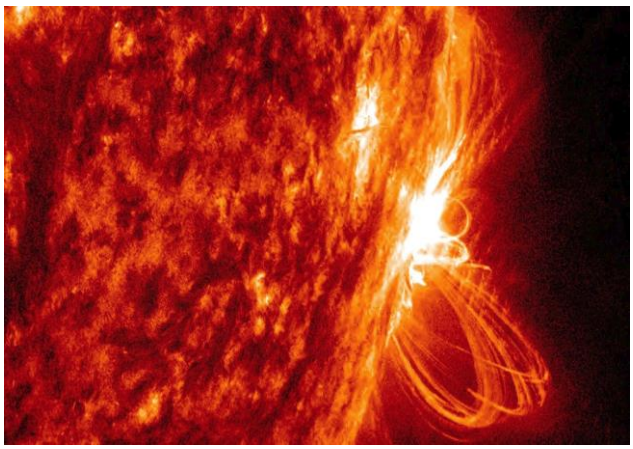

Figure 6: AR13664, flare X8.7.

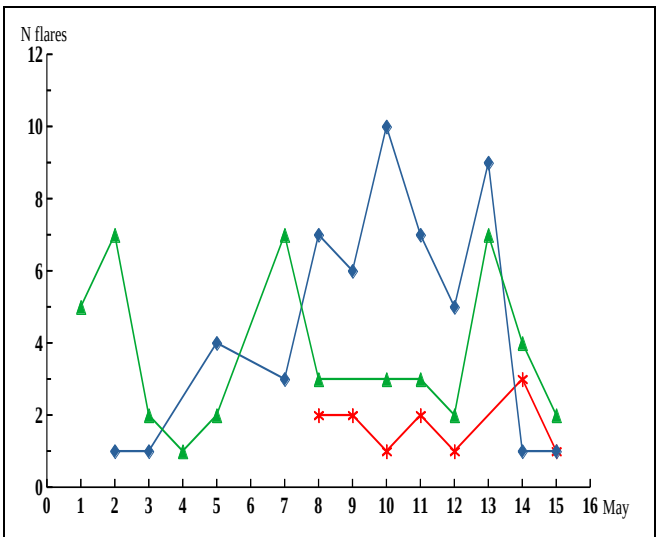

Figure 7: The number of various class flares produced in the AR13664 during its first passage across the Sun's disk. Blue curve – number of C-class flares, green curve – M-class and red curve – X-class

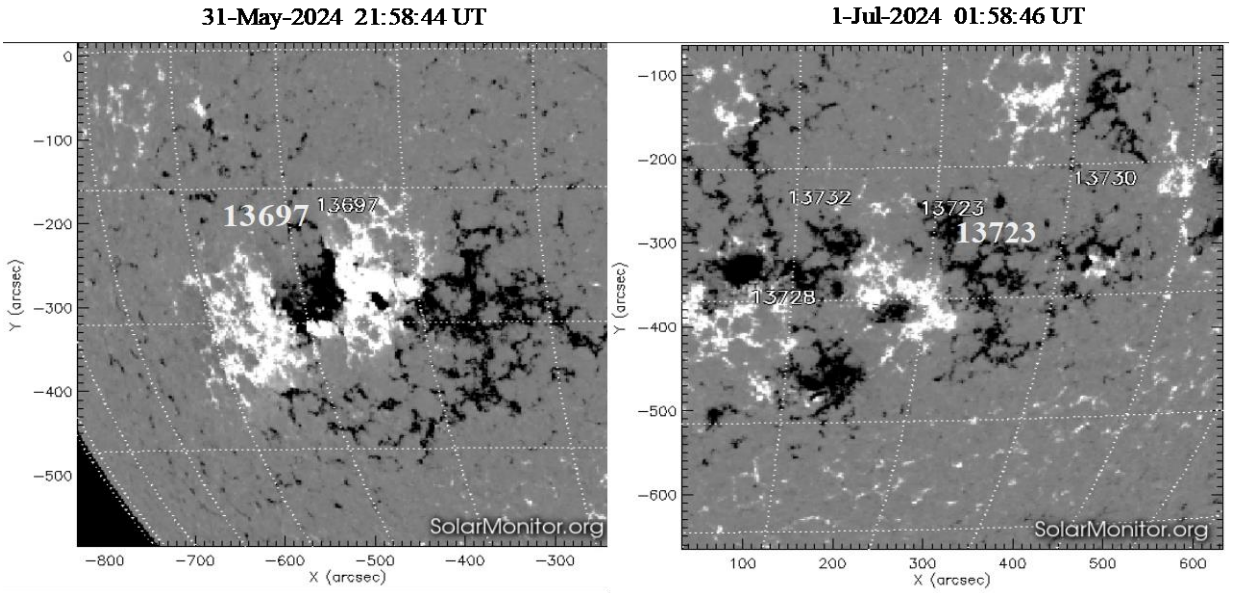

Figure 8: AR13697 and AR13723 magnetograms obtained with the SDO/HMI instrument on May 31 and July 1, 2024, respectively. The positive and negative polarities are indicated by white and black colours, respectively.

shortwave radio outages in Western Europe and Africa. Starting from June 29, AO had β Hale class magnetic field configuration. In total, AR13723 produced 23 C-class and 1 M-class flares during its third pass across the Sun's disk from June 24 to July 6.

6. Conclusion

The AR13664/AR13697/AR13723 belonged to the Carrington class. It was not only one of the largest sunspot groups rivaled Carrington's sunspot of 1859, it turned out to be one of the most powerful among all those observed on the Sun in the current 25th solar cycle. It was the source of the strongest flares M- and X- class, that triggered largest CMEs and associated geomagnetic storms which were very geoeffective and created bright auroras at much lower latitudes than usual, both in the northern and southern hemispheres. The geomagnetic storm of May 10–11, 2024 was the strongest and most extreme in nearly 20 years and classified as a G5.

By studying in detail the evolution of this hyperactive region NOAA 13664 and its impact on Earth, we are improving our ability to predict solar activity and warn of the extreme space weather events it causes, such as powerful geomagnetic storms that affect people's quality of life.

References

Carrington, R. C.: 1859, *MNRAS*, **20**, 13–15.

Hayakawa H., Bechet S., Clette Fr., et al.: 2023, *ApJL*, **954,** L3 (10pp).

Hayakawa H., Ebihara Yu., Mishev A., et al.: 2024, preprint (arXiv:2407.07665).

Hodgson, R.: 1859, *MNRAS*, **20**, 15-16.

Romano P., Elmhamdi A., Marassi A., et al.: 2024, *ApJL*, **973**, L31 (9pp).

https://doi.org/10.18524/1810-4215.2024.37.313466

MACROSCOPIC TURBULENT DIAMAGNETISM OF SOLAR PLASMA

V.N. Krivodubskij

Astronomical Observatory, Taras Shevchenko National University of Kyiv, Kyiv, Ukraine
krivod2@ukr.net

ABSTRACT. Turbulent motions and convection in cosmic plasma play a key role in the processes of magnetic fields evolution in astrophysical conditions. Involvement of turbulent motions in the consideration, when studying the reconstruction of magnetic fields, ended with the creation of the theory of magnetohydrodynamics of mean turbulent magnetic fields, which in the literature was called macroscopic MHD. One of the important effects of macroscopic MHD is called turbulent diamagnetism. The physical essence of the effect of macroscopic turbulent diamagnetism consists in the displacement of global (mean) magnetic fields from areas of increased intensity of turbulent pulsations to places with less developed turbulence along the gradient of turbulent viscosity gradient ν_T with an effective macroscopic velocity $U_\mu = -\nabla\nu_T/2$ ($\nu_T \approx (1/3)ul$, u and l are the effective velocity and the characteristic pulsation scale of the velocity). We considered the role of macroscopic turbulent diamagnetism in the formation of the magnetic field layer in the lower part of the solar convection zone (SCZ). We calculated the radial distribution of the turbulent viscosity ν_T along the depth z for the SCZ model of Stix (2002). It was found that the radial distribution of this parameter has the form of a convex function $\nu_T(z)$ with a maximum approximately in the middle of the SCZ ($z \approx 140{,}000$ km). Noticeable positive radial gradient of the turbulent viscosity $\nabla\nu_T$, which is found in the lower part of the SCZ, causes a downward intense diamagnetic displacement of the toroidal magnetic field, the velocity of which reaches the value $U_\mu \approx 4\text{x}10^3$ cm/s near the lower base of the SCZ ($z \approx 180{,}000$ km). Therefore, macroscopic turbulent diamagnetism in deep layers plays the role of negative magnetic buoyancy. Macroscopic diamagnetism acts against magnetic buoyancy, the velocity of which is $U_B(B) = B/(4\pi\rho)^{1/2}$ (B is the magnetic induction, ρ is the density of plasma), and contributes to the formation of a magnetic layer of a steady state toroidal magnetic field with a strength of $B_S = (4\pi\rho)^{1/2}\,\nu_T/2 \approx 3000$–$4000$ G.

Keywords: magnetic fields, turbulence, magnetic buoyancy, macroscopic MHD, macroscopic turbulent diamagnetism.

АНОТАЦІЯ. Турбулентні рухи і конвекція в космічній плазмі відіграють ключову роль у процесах еволюції магнітних полів в астрофізичних умовах. Залучення до розгляду турбулентних рухів при вивченні реконструкції магнітних полів завершилося створенням теорії магнітогідродинаміки середніх турбулентних магнітних полів, яка в літературі отримала назву макроскопічної МГД. Один із важливих ефектів макроскопічної МГД називається турбулентним діамагнетизмом. Фізична суть ефекту макроскопічного турбулентного діамагнетизму полягає у зміщенні глобальних (середніх) магнітних полів із областей підвищеної інтенсивності турбулентних пульсацій у місця з менш розвиненою турбулентністю вздовж градієнту турбулентного градієнта в'язкості ν_T з ефективною макроскопічною швидкістю $U_\mu = -\nabla\nu_T/2$ ($\nu_T \approx (1/3)ul$, u та l – ефективна швидкість та характерний масштаб пульсацій). Розглянуто роль макроскопічного турбулентного діамагнетизму у формуванні магнітного шару в нижній частині сонячної конвективної зони (СКЗ). Ми розрахували радіальний розподіл турбулентної в'язкості ν_T по глибині z для моделі SCZ Стікса (2002). Встановлено, що радіальний розподіл цього параметра має вигляд опуклої функції $\nu_T(z)$ з максимумом приблизно по середині СКЗ ($z \approx 140\,000$ км). Помітний позитивний радіальний градієнт турбулентної в'язкості $\nabla\nu_T$, який знаходиться в нижній частині СКЗ, викликає низхідне інтенсивне діамагнітне зміщення тороїдального магнітного поля, швидкість якого досягає значення $U_\mu \approx 4\text{x}10^3$ см/с біля нижньої основи СКЗ ($z \approx 180\,000$ км). Тому макроскопічний турбулентний діамагнетизм у глибоких шарах відіграє роль *негативної магнітної плавучості.* Макроскопічний діамагнетизм протидіє магнітній плавучості, швидкість якої становить $U_B(B) = B/(4\pi\rho)^{1/2}$ (B – магнітна індукція, ρ – густина плазми), і сприяє утворенню магнітного шару усталеного тороїдального магнітного поля напруженістю $B_S = (4\pi\rho)^{1/2}\,\nu_T/2 \approx 3000$ – 4000 Гс.

Ключові слова: магнітні поля, турбулентність, магнітна плавучість, макроскопічна МГД, макроскопічний турбулентний діамагнетизм.

1. The necessity to find "anti-buoyancy" effects

According to modern ideas, the global magnetic field of the Sun contains two components. The first component is a weak poloidal (meridional) magnetic field, the lines of force of which cross the solar surface at high heliolatitudes and are therefore clearly observed in the polar regions of the Sun. The second component is a strong toroidal (azimuthal) magnetic field hidden in the

deep layers, fragments of which, when floating on the solar surface in some places, cause the appearance of sunspots. Both magnetic components change cyclically in time in magnitude and polarity in antiphase with a period of about 22 years, called the Hale magnetic cycle. When explaining the magnetic cycle of the Sun, the so-called αΩ dynamo model, which is based on the joint action of helical turbulence (α effect) and differential rotation (Ω effect) in the solar convective zone (SCZ), became the most popular among researchers.

For effective excitation of the toroidal field of the Sun as a result of the effect of differential rotation on the poloidal field (Ω effect), it is necessary that the magnetic power tubes stay in the generation area for a long time. However, due to the magnetic buoyancy of Parker (1979), it is difficult to ensure significant amplification and storage of strong fields in the entire volume of the SCZ for a long time. The rate of magnetic emergence of the *B* field according to Parker is determined by the expression

$$U_B(B,\rho) \approx B/(4\pi\rho)^{1/2}, \quad (1)$$

is determined by the expression from which it can be seen that the value of magnetic buoyancy velocity is inversely proportional to the plasma density ρ, which leads to a limitation on the amplitude of the excited toroidal field. In view of this, the most favorable conditions for maintaining strong magnetic fields in the solar depths exist near the bottom of the SCZ, where the plasma density is the highest. And therefore, this is where the velocity of magnetic buoyancy will be the lowest.

But even near the bottom of the SCZ, it is difficult to ensure the strengthening and maintenance of fields with a magnitude of more than 100 G for a time comparable to the period of the solar cycle (due to the rapid evacuation of strong magnetic fields from the generation zone) (Parker, 1979). Therefore, the problem of compensating the magnetic buoyancy of strong fields and maintaining them for a long time in the dynamo area comes to the fore with special need. Considering this, there is an urgent need to search for mechanisms of magnetic "anti-buoyancy" ("negative magnetic buoyancy"). As it turned out, the macroscopic turbulent plasma diamagnetism can play the role of such a mechanism in SCZ.

2. Macroscopic turbulent diamagnetism of solar plasma - against magnetic buoyancy

The effect was discovered by Zeldovich (1956) for the case of two-dimensional turbulence and later named macroscopic turbulent diamagnetism by Rädler (1968). The physical meaning of the latter consists in the displacement of the initially uniform magnetic field from areas with increased intensity of turbulent motions to places with less developed turbulence (along the turbulent viscosity gradient $\nabla\nu_T$) with an effective velocity U_μ

$$U_\mu = -\nabla\nu_T/2. \quad (2)$$

In the work (Krivodubskij, 2024) we calculated the radial profile of turbulent viscosity $\nu_T(z) \approx (1/3)\, ul$ (u and l are the effective velocity and characteristic size of the turbulent convective motions, respectively). It was found that the parameter $\nu_T(z)$ has the form of a convex function with a maximum $\nu_T \approx 10^{13}$ cm/s approximately in the middle of the SCZ of z = 120000 – 140000 km (Fig. 1).

Thus, the vertical inhomogeneity of the parameter ν_T that we discovered indicates the diamagnetic properties of the solar turbulent plasma. The qualitatively physical content of the phenomenon of macroscopic diamagnetism is as follows. Due to the radial inhomogeneity of the turbulence, the percolation (seepage) of the turbulent pulsations occurs from areas of high pulsation intensity in the directions of their lower intensity. As a result of the freezing of magnetic lines of force in the plasma, magnetic fields will be transferred in a similar way.

Therefore, the global azimuthal field must be pushed out of this area in the radial direction, namely: in the upper half of the SCZ, the magnetic field will be transferred upwards to the solar surface, while in the lower half of the SCZ the magnetic field transfers down to the bottom of the SCZ.

It is relevant that the noticeable positive radial gradient of the turbulent viscosity $\nabla\nu_T$, which is located in the lower part of the SCZ, should cause a downward intensive diamagnetic displacement of the toroidal magnetic field. Indeed, according to our calculations, the velocity of downward diamagnetic displacement of the horizontal field near the bottom of the SCZ reaches $U_\mu \approx 2\cdot10^3$ cm/s (Fig. 2).

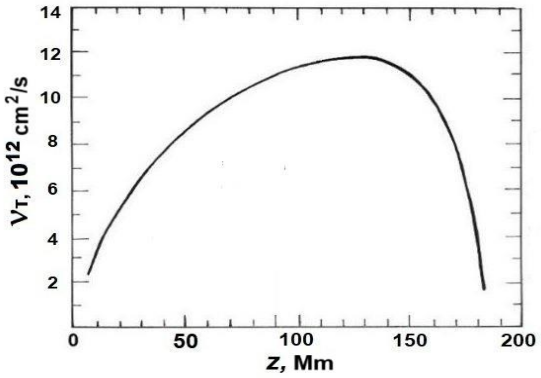

Figure 1: Radial distribution of the value of the turbulent viscosity coefficient $\nu_T(z) \approx (1/3)\, ul$ at the depth z, calculated for the physical parameters from the SCZ model by Stix (2002).

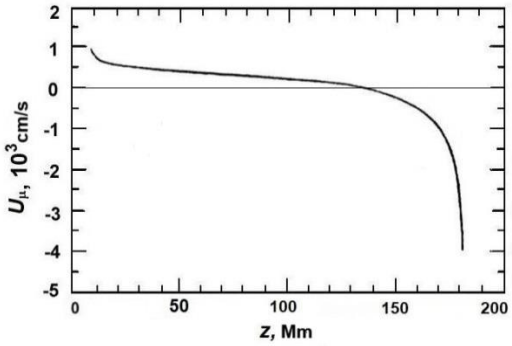

Figure 2: Radial distribution along the depth z of the velocity U_μ of the macroscopic diamagnetic transfer of the global toroidal magnetic field, calculated for the physical parameters from the SCZ model by Stix (2002).

Therefore, in the lower part of the SCZ, the macroscopic turbulent diamagnetism acts against magnetic buoyancy, i.e., here it performs the role of "negative magnetic buoyancy". Since the velocity of magnetic buoyancy depends on the magnitude of the field B, then from the condition of mutual compensation of the processes of buoyancy with velocity U_B (see expression (1)) and diamagnetic downward displacement with velocity U_μ (expression (2))

$$\uparrow U_B + \downarrow U_\mu = 0, \quad (3)$$

the value of the stationary toroidal field can be found

$$B_S \approx U_\mu (4\pi\rho)^{1/2}, \quad (4)$$

the buoyancy of which will be completely compensated by macroscopic turbulent diamagnetism (Fig. 3).

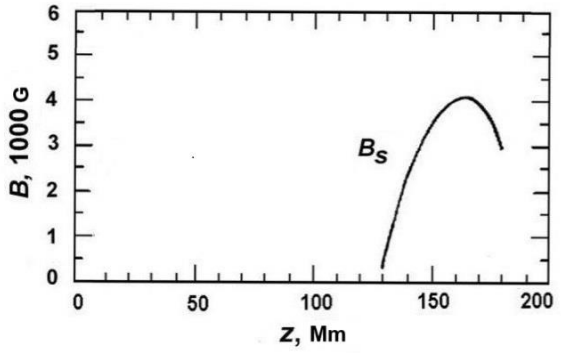

Figure 3: Distribution by depth z in the SCZ model by Stix (2002) of the steady horizontal field $B_S = (4\pi\rho)^{1/2}\,\nu_T/2$, the magnetic buoyancy of which is compensated by the macroscopic diamagnetic effect.

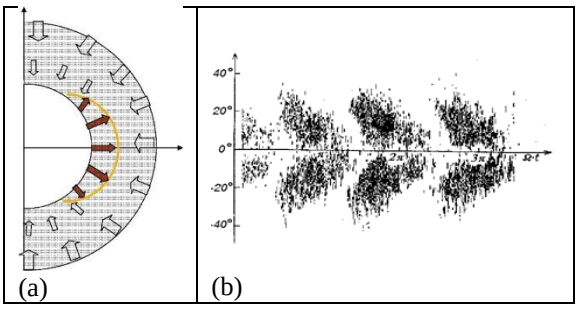

Figure 4: (a) – A meridional cross-section of the SCZ, which demonstrates the direction of the radial transfer of the toroidal magnetic field according to our calculations. Arrows show the direction of field transfer. (b) – Maunder butterfly diagram ("royal sunspots zone"), according to observations from 1874 to 1913, showing areas of sunspot existence depending on heliographic latitude and phase of the solar cycle, Ωt. The area of upward transfer of the toroidal field is localized in the range of heliolatitudes (a), which coincides with the observed latitudinal "royal zone" of sunspots (b).

As a result of "negative magnetic buoyancy" caused by macroscopic diamagnetism, the concentration of a powerful toroidal magnetic field $B_S \approx 3000$–4000 G occurs near the bottom of the SCZ. At the same time, thanks to the continuous action of the Ω effect, further strengthening of the toroidal field continues. Therefore, over time, fragments of the toroidal field, where $B > 4000$ G, will rise to the surface in the "royal latitude zone" and thereby generate sunspots here (Fig. 4).

3. Conclusion

Thus, the noticeable positive radial gradient of the turbulent velocity $\nabla\nu_T$ near the bottom of the SCZ, revealed as a result of our calculations, causes an intense downward macroscopic diamagnetic displacement of the toroidal magnetic field with the velocity $U_\mu = \nabla\nu_T/2$. Acting against the magnetic buoyancy, the macroscopic turbulent diamagnetism in the SCZ performs the role of "negative magnetic buoyancy" and thereby contributes to the long-term maintenance of strong fields ($B_S \approx 3000 - 4000$ G) in the generation zone near the bottom of the SCZ.

Due to the continuous action of the Ω effect, in the future, fragments of the enhanced toroidal field, where $B > 4000$ G, will rise to the surface in the "royal latitude zone" and thereby generate sunspots here. At the same time, in the polar domain, such fields remain blocked near the bottom of the solar convective zone (there is another effect of "negative magnetic buoyancy" (Krivodubskij, 2005). And that is why deeply rooted strong toroidal fields in the polar domains cannot break through to the surface to be observed at high latitudes in the form of sunspots (Krivodubskij, 2021).

Acknowledgements. The work was carried out with the support of the Ministry of Education and Science of Ukraine, state budget grant number 22BF23-03 under the program "Astronomy and space physics" of Taras Shevchenko National University of Kyiv.

References

Krivodubskij V.N.: 2024, *KPCB*, **40**, No. 3, 53.
Krivodubskij V.N.: 2005, *AN*, **326**, No. 1, 61.
Krivodubskij V.N.: 2021, *AdSR*, **68,** Iss. 9, 3943.
Parker E.N.: 1979, Cosmical Magnetic Fields, (Clarendon Press, Oxford).
Rädler K.-H.: 1968, Z*NatA.*, **23a**, 1841.
Stix M.: 2002, *The Sun: An Introduction (2nd ed.)*. (Springer-Verlag, Berlin).
Zeldovich Ya.B.: 1956, *JETP*, **31**, 154.

https://doi.org/10.18524/1810-4215.2024.37.313647

DIAGNOSTICS OF THE SOURCES OF GEOMAGNETIC VARIATIONS FOR THE SUPERSTORM OF MAY 10–13, 2024

T.P. Sumaruk[1], J. Reda[2]

[1] Institute of Geophysics of the National Academy of Sciences of Ukraine, Kyiv, Ukraine, *taras.sumaruk@gmail.com*

[2] Institute of Geophysics, Polish Academy of Sciences, Warsaw, Poland, *jreda@igf.edu.pl*

ABSTRACT. The paper presents the results of the analysis of magnetospheric-ionospheric sources of geomagnetic variations for the superstorm of May 10-13, 2024. This event occurred at the maximum of the 25th cycle of the Wolfe solar activity and at the beginning of the 100-year cycle of geomagnetic activity. During this period, superstorms similar to the storms of October-November 2003 will occur.

To analyze the sources of variations, 1-minute values of Polish and Ukrainian geomagnetic observatories (Table 1) were used. The sources of geomagnetic variations were identified based on the data on the indices of geomagnetic activity D_{st}, $K_{p,}$ AL, AU, AE and model calculations. The influence of magnetospheric sources and auroral ionospheric electric currents in the middle latitudes is diagnosed. The contribution of each source is calculated.

Keywords: solar and geomagnetic activity, solar cycle, magnetospheric-ionospheric current system.

АНОТАЦІЯ. У роботі викладено результати аналізу магнітосферно-іоносферних джерел геомагнітних варіацій для супербурі 10–13 травня 2024 року. Дана подія відбулась у максимумі 25 циклу сонячної активності Вольфа та на початку 100 річного циклу геомагнітної активності. У даний період будуть відбуватися супербурі подібні до бур жовтня-листопада 2003р. Оскільки геомагнітна активність відстає від сонячної на 1–2 роки, її максимум очікується біля 2026 року.

Для аналізу зовнішніх джерел варіацій використано одномінутні значення польських та українських геомагнітних обсерваторій найбільш інформативної сітки INTERMAGNET.

Ідентифікацію джерел геомагнітних варіацій проведено за даними про зміну горизантальної (східної) компоненти вектора напруженості магнітного поля Землі, спокійної сонячно-добової варіації. Індекси геомагнітної активності D_{st}, AL, AU, AE взяті з міжнародних центрів даних та за модельними розрахунками.

У даній роботі нами використано модель Міда для визначення впливу струмів на магнітопаузі (інші моделі дають співмірні значення). Вплив системи кільцевого магнітосферного струму, струму в хвості магнітосфери і ін. в першому наближенні обчислювався за допомогою D_{st} – індекса та його широтної залежності (у нашому випадку використано закон косинуса широти).

Діагностовано вплив магнітосферних джерел та авроральних іоносферних електроструменів та струмів їх розтікання у середні широти. Вичислено величину вкладу кожного джерела: величина магнітосферної складової для даної бурі становить близько 80%, іоносферної – 20%.

Ключові слова: сонячна і геомагнітна активність, сонячний цикл, магнітосферно-іоносферна система струмів.

1. Introduction

On May 8, 2024, solar flares from sunspot region 3664, solar flare X1.0, which peaked at 05:09 UTC, and solar flare M8.6, which peaked at 12:03 UTC on May 8, 2024 caused asymmetric full halo coronal mass ejections that triggered a large geomagnetic storm on May 10–13, 2024, with a storm sudden commencement (SSC) of (Dst = – 412 nT and Kp = 9).

The diagnostics of the sources of geomagnetic variations has been carried out by many authors (Sumaruk, 2006, Laba, 2010, Grandin, 2024), since each event in the geomagnetic field characterizes a different influence of all sources and takes place in a special way. The superstorm of May 2024 occurred at a time close to the maximum of the 25th 11-year Wolfe cycle, but in our opinion it is not the largest in this cycle, since according to our forecasts (Sumaruk, 2023), the maximum of the cycle is expected in 2025–2026, and superstorms occur at the maximum and at the beginning of the decline of cycles, for example, the superstorm of 2003–2004. One of the reasons for this is the possible coincidence of the directions of the Sun's and Earth's magnetic field in odd solar cycles, the increase in recurrent geomagnetic disturbances (Sumaruk, 2009, Orlyuk 2023) and the beginning of the 100-year cycle (Sumaruk, 2023).

2. Magnetospheric-ionospheric current system

To diagnose the sources of the magnetospheric-ionospheric current system, we used one-minute data of the horizontal (north) component H(X) of the Earth's magnetic field induction vector (*B*) of the Ukrainian and Polish INTERMAGNET observatories (data are presented in Table 1).

Table 1: Observatories whose data were used

IAGA code	*Name*	*Geomag. lat. [deg]*	*Geomag. long. [deg]*
ODE	Odesa	43.720	112.430
LVV	L'viv	47.84	106.8
BEL	Belsk	50.18	104.750
HLP	Hel	53.16	104.060

The horizontal component best reflects variations caused by external sources. The value of irregular field variations can be defined as (Sumaruk, 2006):

$$\Delta = X - S_q, \quad (1)$$

where X – value of the horizontal component of the geomagnetic field. S_q – solar diurnal variation of the horizontal component of the geomagnetic field characterizes the wave radiation of the Sun. Since the amplitudes of S_q – variations change with the season and activity. Seasonal variations of activity caused by changes in the ionospheric conductivity. (Sumaruk, 2004). As a reference level for the field of irregular magnetic variations in middle latitudes, we chose the quiet solar diurnal variation calculated by five internationally quiet days (Sumaruk, 2004; Sumaruk, 2005).

The irregular variation of the geomagnetic field caused by the magnetospheric-ionospheric current system is described by the equation (Fukushima and Kamide, 1973):

$$\Delta = DR + DRP + DT + DCF + DP, \quad (2)$$

where *DR* – the variation from the ring magnetospheric current (including the partial ring current);

DRP – the variation due to the partial ring current;

DT – variation from currents in the magnetosphere tail;

DCF – variation with currents at the magnetopause;

DP – variation from the ionospheric currents in the aurora zone and their reverse currents of spreading to the middle latitudes.

Magnetospheric sources (DR, DT, DRP) are well reflected by the D_{st} index of magnetic activity (Campbell, 1996). D_{st} data are taken from the website *(https://wdc.kugi.kyoto-u.ac.jp).* As a first approximation, the magnitude of the variation from magnetospheric sources (Δ_m) can be calculated by the formula:

$$\Delta_m = D_{st} \cdot \cos\Phi, \quad (3)$$

where Φ –the geomagnetic latitude of the observatory.

3. DCF and DP currents

The magnitude of the variation from the currents at the DCF magnetopause is calculated by model calculations. The most commonly used models are the paraboloidal magnetosphere model, the T02 Tsyganenko magnetosphere model, and the Mead magnetosphere model. The magnitude of DCF variations calculated by different models is commensurate in magnitude. In this work, we used the Mead model (Mead, 1964).

According to this model, the components of the *DCF* field on the Earth's surface are defined as (nT):

$$DCF_x = (25150 \cdot \cos\varphi)/r_b^3 + 21000 \cdot ((2\sin^2\varphi - 1) \cdot \cos t)/r_b^4$$

$$DCF_y = (21000 \cdot \sin\varphi \cdot \sin t)/r_b^4 \quad (3)$$

$$DCF_z = (25150 \cdot \sin\varphi)/r_b^3 + (21000 \cdot \sin\varphi \cdot \cos\varphi \cdot \cos t)/r_b^4,$$

where r_b – the geometric distance to the sub-solar point of the magnetosphere; t – local time, which is counted from the midnight meridian; φ – geomagnetic latitude.

The first term in the formulas for the DCF_x and DCF_z components represents the symmetric part of the field, and the second term represents the asymmetric part. The contribution from the magnetopause currents can be calculated if the distance of the sub-solar magnetopause point to the Earth (r_b) is known. The value of r_b (in km) can be found from the solar wind plasma parameters using the model (Shue, 1998):

$$rb = \{10.22 + 1.29 \tanh [0.184 (Bz + 8.14)]\} (nv^2)\, 1/6.6 \quad (4)$$

where v – the velocity of solar wind, km/s; n – the density, cm^{-3}; Bz – Z-component interplanetary magnetic field. During magnetically quiet periods, $r_b = (11–12) \cdot R_E$, R_E – the radius of the Earth. We calculated the variations of DCF_X for all the studied observatories (data are given in Table 2).

Table 2: DCF_X – variations

ODE, nT		LVV, nT		BEL, nT		HEL, nT	
Max	Min	Max	Min	Max	Min	Max	Min
71.4	11.8	66.8	10.8	64.0	10.3	60.3	9.57

The variation from the auroral ionospheric currents in the aurora zone and their return currents to the middle latitudes (*DP*) is described by the auroral activity indices *AE*, *AU*, *AL*. As is known (Feldstein, 1999), during very large magnetic storms ($D_{st} \leq -150$ nT), the focuses of auroral ionospheric currents are shifted to the middle latitudes. During the onset of a magnetic storm, mid-latitude observatories are affected by reverse ionospheric currents. With the growth of D_{st}, the observatories come under the direct influence of the eastern (AU) or western (AL) electric currents, depending on the local time.

We have calculated the variation of DP (data are presented in Fig. 1):

$$DP = \Delta - \Delta_m - DCF. \quad (5)$$

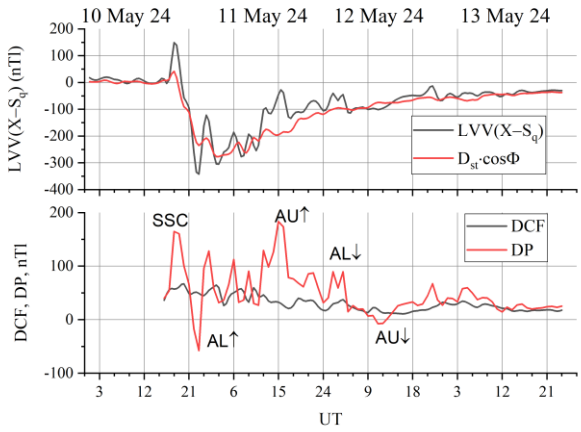

Figure 1 a: Variations of $X - S_q$ and $D_{st} \cdot cos\Phi$ (top diagram) and the variations of DCF and DP variations (bottom diagram) for L'viv geomagnetic observatory.

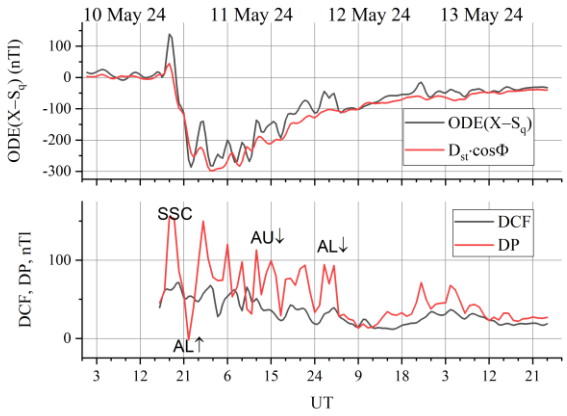

Figure 1 b: Variations of $X - S_q$ and $D_{st} \cdot cos\Phi$ (top diagram) and the variations of DCF and DP variations (bottom diagram) for Odesa geomagnetic observatory.

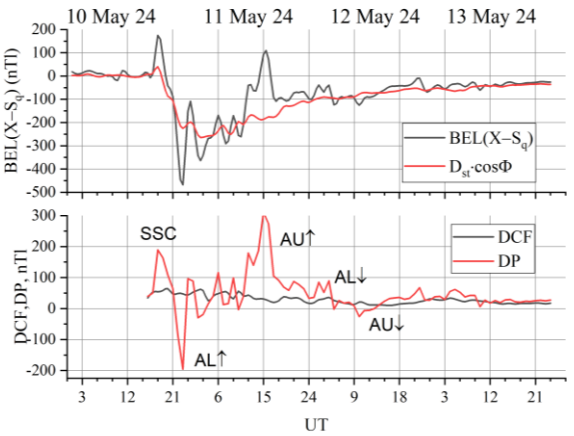

Figure 1 c: Variations of $X - S_q$ and $D_{st} \cdot cos\Phi$ (top diagram) and the variations of DCF and DP variations (bottom diagram) for Belsk geomagnetic observatory.

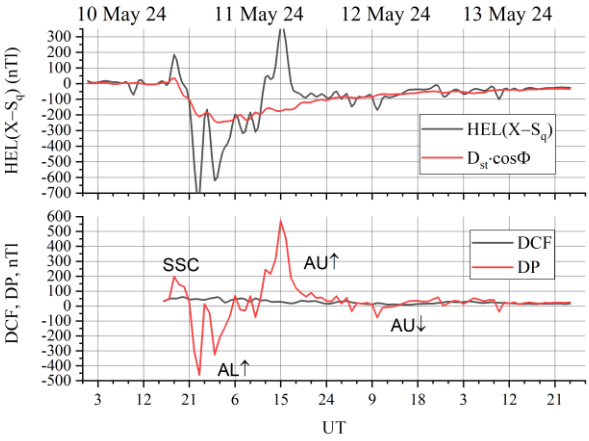

Figure 1 d: Variations of $X - S_q$ and $D_{st} \cdot cos\Phi$ (top diagram) and the variations of DCF and DP variations (bottom diagram) for Hel geomagnetic observatory.

Figure 1

4. Discussion

Fig. 1 shows the variations of $X - S_q$ and $D_{st} \cdot cos\Phi$ (top panel) and the variations of DCF and DP variations (bottom panel). Identification of ionospheric sources is shown by signs: AL – variation from the western auroral electrojet, AU – from the eastern auroral electrojet. The upward arrow indicates the direct effect of the electric currents, the downward arrow indicates the opposite.

At 18 h 50 min UT on May 10, 2024, the DP-variation is positive, associated with SSC and are ODE–138.5 nT, LVV–14.2 nT, BEL–174.4, nT, HEL–185.1 nT. At 00h UT May 11, 2024 the western auroral electric current sharply increases, the ring magnetospheric current develops, the AL-index increases, and the ring magnetospheric current develops. The D_{st}-variation for the studied observatories are ODE–297.7 nT, LVV–276.5 nT, BEL–263.8 nT, HEL–247.1 nT. The increase in the AL-index means that the currents from the western ionospheric electrojet increased and negative DP values were recorded at the observatories. Further enhancement of the ring current resulted in the movement of the auroral electric currents to mid-latitudes and 15 UT on May 11, 2024, and we observe positive sub-storms (indicated by AU with a upward arrow). On 12–21 UT May 11, 2024, we observe a large positive substorm – generated by the direct action of the eastern auroral jet (AU with an upward arrow). But at this time, the tabulated values of the AE, AL, and AU indices decrease sharply. This decrease is not due to a decrease in the strength of the eastern electrojet but to its shift to subauroral latitudes ($D_{st} \leq -150$ nT), the chain of observatories from which the indices are calculated does not record the maximum current, because the electrojet is located in lower latitudes. Subsequently, the ring magnetospheric current weakens, the auroral electric jets move to the north and the magnetometer registers positive and negative bays caused by the reverse currents of the spreading of the eastern and western electrojet and on May 12–13, 2024.

5. Conclusions

1. We diagnosed the sources of geomagnetic variations, calculated the contribution to the variation of each source, and divided it into components relative to the sources that generate them.

2. It is shown that for the superstorm of May 10–13, 2024, at the studied observatories, magnetospheric sources of variations – the ring magnetospheric current together with the current in the tail of the magnetosphere and the current at the magnetopause during a magnetic storm – give the largest contribution to the field variation of 80%, ionospheric – auroral currents and their reverse currents in the field variation of medium latitudes do not exceed 20%.

3. For diagnostics of irregular geomagnetic variations in the middle latitudes, the S_q-variation can be used as a reference level, taking into account its change with the season and the solar activity cycle, calculated by five internationally quiet days.

4. The geomagnetic variations in the middle latitudes can be divided into components with respect to the sources that generate them.

References

Campbell, W.H.: 1996, *EOSTr*, **77** (30), 283.

Feldstein Ya.I., Gromova L.I., Grafe A. et al.: 1999, *AnGeo,* **17**, 497.

Fukushima, N. and Y. Kamide.: 1973, *RvGSP*. **11**, 795.

Grandin M., Bruus E., Ledvina V. E. et al.: 2024, Citizen science observations, *EGUsphere [preprint]*, https://doi.org/10.5194/egusphere-2024-2174.

Laba I. S., Pidstryhach I. Ya., Sumaruk Yu. P., et al.: 2010, *JPhSt,* **14**, №3, 3902(13).

Mead G. D.:1964, *JGR,* **69**, №**7**, 1181.

Orlyuk M.I., Romenets A.A.: 2023, *in Proc. 15-th Workshop "Solar Influences on the Magnetosphere, Ionosphere and Atmosphere",* Primorsko, Bulgaria, June 05-09, P. 30. Solar Cycle progression https://www.swpc.noaa.gov/products/solar-cycle-progression.

Shue J.-H., Song P., Russel C. T., et. al.: 1998, *JGR*, **103**, 17691.

Sumaruk T.P., Sumaruk Yu.P.:2004, *Geophys.J.,* **26**, №**6**, 139. (in Ukrainian)

Sumaruk P.V., Sumaruk T.P.: 2006, *Kosm. nauka tehnol.*, **12**, №**1**, 76.

Sumaruk T.P., Sumaruk P.V.: 2009, *Kosm. nauka tehnol.*, **15**, № **1**, 56.

Sumaruk T.P., Sumaruk P.V., Neska A.: 2023, *OAP,* **36**, 188.

MEMORIAL

https://doi.org/10.18524/1810-4215.2024.37.316659

GAMOW CONFERENCE IN WASHINGTON UNIVERSITY AND 30-TH ANNIVERSARY OF GAMOW'S CONFERENCE IN ODESA UNIVERSITY

M.I. Ryabov

URAN-4 Observatory of the Institute of Radio Astronomy of the NAS of Ukraine, Odesa, Ukraine

ABSTRACT. George Gamow, the eminent physicist and astrophysicist was born in Odesa in 1904. He was educated at the Odesa University (1922–23) and at the University of Leningrad (1923–1929).

He started at Odesa University and during the period of his studies worked at the Astronomical observatory of the University. Later, after he created the theory of alpha decay (1928), he joined the first ranks of leading physicists and took part in the conferences of Niels Bohr.The outbreak of World War II in Europe made their implementation impossible. The Gamow's conferences at the University of Washington were held between 1935 and 1947. Ten conferences were held during this period. Gamow's conferences at Odesa University began in the year of its 90th anniversary in 1994. From the beginning, they were held once every five years. However, due to their popularity (since 2000), conferences have become annual. In 2024 the Gamow's conferences in Odesa will celebrate. This year, the 24th annual Gamow's conference, dedicated to the 120th anniversary of the birth of George Gamow, successfully held its work. Even during the COVID epidemic and wartime, Gamow's conferences continued, switching to an online mode of operation.

Keywords: Gamow, Gamow's Conferences, history of astronomy.

АНОТАЦІЯ. 120 років тому, у 1904 році, в Одесі народився видатний фізик та астрофізик Георгій Гамов. Він навчався в Одеському університеті та в період навчання працював обчислювачем в астрономічній обсерваторії університету. Надалі, після створення ним теорії альфа розпаду (1928 рік) він опинився у перших рядах провідних фізиків і брав участь у конференціях Нільса Бора. Початок Другої світової війни в Європі унеможливив їх подальше проведення. Після переїзду до США та роботи у Вашингтонському університеті Георгію Гамову вдалося організувати продовження конференцій з теоретичної фізики, що проводились раніше Нільсом Бором у Копенгагені. Загалом у період із 1935 по 1947 рік було проведено десять конференцій. У 2024 році відзначається 30 років від часу проведення Гамовських конференцій в Одесі. Гамовські конференції в Одеському університеті розпочалися на рік 90-річчя Г. Гамова в 1994 році. Спочатку вони проводилися один раз на п'ять років. Однак, у зв'язку з їхньою популярністю, починаючи з 2000 року, конференції стали щорічними. Цього року успішно провела свою роботу 24-а Міжнародна Гамовська конференція, присвячена 120-річчю від дня народження Георгія Гамова. Навіть у періоди епідемії Ковіду та воєнного часу гамовські конференції продовжувались, перейшовши на он-лайн режим роботи.

Ключові слова: Гамов, Гамовські конференції, історія астрономії.

2024 is the year of the 120th anniversary of the birth of George Gamow. George Gamow was one of the most influential physicists and cosmologists of the 20th century. He made significant and decisive contributions to modern physics, cosmology, and biology. His three most notable contributions include:

1. Discovery of the quantum nature of alpha decay in nuclear physics (1928).
2. Proposal of the Hot Universe theory (1946-1953).
3. Deciphering the genetic code in biology (1954).

George Gamow was born in Odesa on March 4, 1904. He completed his secondary education there and was a student at the Odesa (Novorossiysk) University for two years. Gamow studied at Odesa University from 1921 to 1922. At the same time he worked as an evaluator at the astronomical observatory. In his book "*My World Line"*, Gamow outlined his journey in science, which began in Odesa. His academic pursuits and the start of his scientific career continued in Leningrad. Later, his work and travels took him across Europe, including to world-renowned centers of theoretical physics such as Copenhagen and Cambridge. A significant part of his "world line" took place in the United States, where he arrived in 1934 and stayed there the end of his life.

Gamow Conferences in George Washington University. When George Gamow was offered a position at George Washington University in 1934, he set one condition for accepting the offer: the establishment of an annual physics conference at the university, co-sponsored by the Carnegie Institution. At that time, Foggy Bottom, the Washington neighborhood where GWU is located, was not particularly known for physics. However, Gamow aimed to bring the "spirit of Copenhagen" to this location and to attract an international group of theorists. The Washington Conference on Theoretical Physics was first held in 1935 and then annually until 1947. After the tenth meeting in 1947, Gamow's focus shifted from nuclear physics to cosmology, and he began working more closely with graduate students and local collaborators. As a result of diminished interest, the conference was no longer held.

Figure 1: Participants conference organized by Gamow (1937, the 3-rd Conference)

Figure 2: Participants Gamow's conference (1947, 10-rd Conference)

Topics of the Gamow Conferences:

- 1935: First Washington Conference on Theoretical Physics: Nuclear Physics.
- 1936: Second – Molecular Physics.
- 1937: Third – Problems of Elementary Particles and Nuclear Physics.
- 1938: Fourth: Stellar Energy and Nuclear Processes.
- 1939: Fifth – Low Temperature Physics and Superconductivity.
- 1940: Sixth – Geophysics and the Interior of the Earth.
- 1941: Seventh – Elementary Particles.
- 1946: Ninth – Physics of Living Matter.
- 1947: Tenth – Gravitation and Electromagnetism.

Attached are photographs (Fig. 1-2) of participants in the Gamow Conferences at the University of Washington in 1937 (3rd Conference) and the 1947 Conference (10th Conference, Halpern, 2010). Detailed information about all Gamow conferences at the University of Washington is available on the website: Washington Conferences on Theoretical Physics (https://www.britannica.com/topic/Washington-Conference-on-Theoretical-Physics).

Figure 3: Participants Odesa Gamow's conference (2004)

Figure 4: Participants of the Odesa Gamow's conference (2019)

Gamow's Conferences in Odesa University. This year marks the 7th Gamow Memorial Conference in Odesa, following those held in 1994, 1999, 2004, 2009, 2014, and 2019. These conferences are held every five years. Since 2000, annual Gamow's conferences have also been held. In 2024, this will be the 24th Gamow's conference. Our goal is to bring together experts in modern astrophysics, cosmology, high-energy physics, and biology, along with enthusiastic scientists and students, to discuss the latest developments and challenges related to these topics, exchange ideas, and review major experimental and theoretical efforts.

We as followers were inspired by the "spirit of the Gamow's conferences" at George Washington University,

so the topics of the Odesa Gamow's conferences are also quite diverse. On the wall of the main building of the university there is a memorial plaque dedicated to Gamow. Following the appeal of participants of the First Gamow's Conference in 1994 and the rector of Odesa University to the Mayor of Odesa, a decision was made to name one of the city's beautiful squares after Gamow. As a result of the work of the Gamow's conferences, the Jubilee Gamow Medal and scholarships for students of physics and astronomy were established at Odesa University. More information about the Gamow Conferences is available on the website: *www.gamow.odessa.ua*. Publications of the history of the Gamow conferences in Odesa in publications (Ryabov, 2004, 2006, 2010, 2020). The page of materials of all Gamow's conferences at Odesa University on the website of the Scientific Library: *lib.onu.edu.ua*.

Gamow's conferences in Odesa have been held for 30 years (since 2000 without a break!) thanks to the dedicated efforts of the members of the Scientific and Local Organizing Committee, representing the Astronomical observatory of Odesa I.I.Mechnikov National University, the Institute of Radio Astronomy of the National Academy of Sciences of Ukraine, with the unwavering support of the Ukrainian Astronomical Association, and the active participation of the Odesa Astronomical Society.

References

Halpern Paul: 2010, *APS.APR*, **55**, 1, abstract id. H10.004.
Ryabov M.I.: 2004, *OAP*, **17**, 5.
Ryabov M.I.: 2006, *A&AT*, **25**, N 5-6, 359.
Ryabov M.I.: 2010, AIP Conference Proceedings, https://lib.onu.edu.ua/wp-content/uploads/2019/09/2.-Gamow-and-Odessa.pdf
Ryabov M.I.: 2020, *A&AT*, **31**, 407.
Washington Conferences on Theoretical Physics: https://www.britannica.com/topic/Washington-Conference-on-Theoretical-Physics.

https://doi.org/10.18524/1810-4215.2024.37.316661

ONOMASTICS AND NAMES OF THE STARRY SKY

To the 95th anniversary of Professor, Corresponding Member of the Academy of Sciences of Ukraine Yu. O. Karpenko – the author of the book "Names of the Starry Sky"

O.Yu.Karpenko [1], M.I.Ryabov [2]

[1] Odesa I. I. Mechnikov National University, Odesa, Ukraine

[2] URAN-4 Observatory of the Institute of Radio Astronomy of the NAS of Ukraine, Odesa, Ukraine

ABSTRACT. In 2024, the 95th anniversary of the outstanding scientist, encyclopedist, Professor Yuriy Olexandrovich Karpenko is celebrated. Yu. O. Karpenko taught for many years at the Faculty of Philology Odesa Mechnikov National University. Yuriy Olexandrovich Karpenko, being a philologist, expanded the object of his research to include the entire Universe. The results of his research are reflected in the book "Names of the Starry Sky", which is still unique today. In the words of Yu. O. Karpenko himself: "The human path of knowledge has always been accompanied by words. Man denoted all his discoveries and victories by means of language – he named them. Without this, without such names, there would be no point in thinking about the accumulation of knowledge, about passing it on to subsequent generations." The authors of the report hope that the life of the wonderful book by Yu. O. Karpenko "Names of the Starry Sky" will be continued by its translation into English and Ukrainian.

Keywords: onomastics, history of astronomy, "Names of the Starry Sky".

АНОТАЦІЯ. У 2024 році відзначається 95-річчя з дня народження видатного вченого енциклопедиста професора Юрія Олександровича Карпенка. Ю. О. Карпенко багато років викладав на філологічному факультеті ОНУ імені І. І. Мечникова. Він є яскравим представником науки ономастики, що досліджує таємниці походження слів, які описують навколишній світ. Юрій Олександрович Карпенко, будучи філологом, розширив об'єкт своїх досліджень, включивши до нього весь Всесвіт. Результати його досліджень висвітлено у книзі «Назви зоряного неба», яка і до сьогодні є унікальною. За словами самого Ю. О. Карпенка, «Людський шлях пізнання завжди супроводжувався словом. Всі свої відкриття та перемоги людина позначала засобами мови – іменувала. Без цього, без таких імен не було чого б і думати про накопичення знань, про передачу їх наступним поколінням». Автори сподіваються, що життя чудової книги Ю. О. Карпенка «Назви зоряного неба» буде продовжено її перекладом англійською та українською мовами.

Ключові слова: ономастика, історія астрономії, «Назви зоряного неба».

Introduction

Yuriy Olexandrovych Karpenko would have turned 95 this year. He was born in 1929 and lived a full and mostly happy life despite the hardships of his wartime childhood. He got his master's degree from Lviv University, completed his PhD and doctoral programs in Chernivtsy University, many years taught students in Odesa University, was elected as a full member of the National Academy of Sciences of Ukraine.

Karpenko's onomastics

The scientific contributions of Yuriy Karpenko are impressive: he is the author of about 500 works (http://karpenko.in.ua), and under his supervision, 62 PhD and 5 doctoral dissertations have been defended. He initiated the publication of many scientific collections, including the annual collection of onomastic papers Opera in onomastica (http://zzo.onu.edu.ua). The Odesa Onomastic School, founded by Yuriy Olexandrovych, continues to actively develop. Onomastics gradually became the main interest of Yuriy Karpenko's scientific research. Yu. O. Karpenko developed the concept of the toponymic system, the ratio of proper and common names; the methodology of the futurological study of proper names, the theory of literary onomastics, the typology of literary proper names. He was drawn to humorous onomastics. He was the author of the concept of Ukrainian ethnology, including the origin of the Ukrainian language, developed the theory of general phonology and the phonology of the Ukrainian language.

Onomastics of the Universe

Possessing outstanding knowledge in the field of onomastics, he wrote an unique book «Names of the Starry Sky» (Karpenko, 1981), which has no analogues to this day. According to the author, "the cosmos is not only other physical states and other worlds. From galaxies and constellations to minor planets and even meteorites, man-made space objects have their own names. The human path of knowledge has always been accompanied by words. Man denoted all his discoveries and victories by means of language – he named them. Without this, without such names, there would be no point in thinking about the accumulation of knowledge, about passing it on

to subsequent generations". The coverage of topics reflected in the book is enormous: star names, galaxies, constellations, asterisms, stars, planets, satellites of planets, asteroids, comets, the surface of the Moon. The time has come to publish an edition of this book in Ukrainian and English.

Reference

Karpenko Yu.A.: 1981, Nazvaniya zvezdnogo neba (Names of the starry sky), M., Nauka, 184.

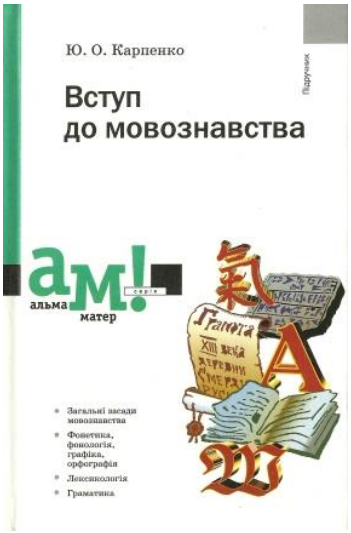

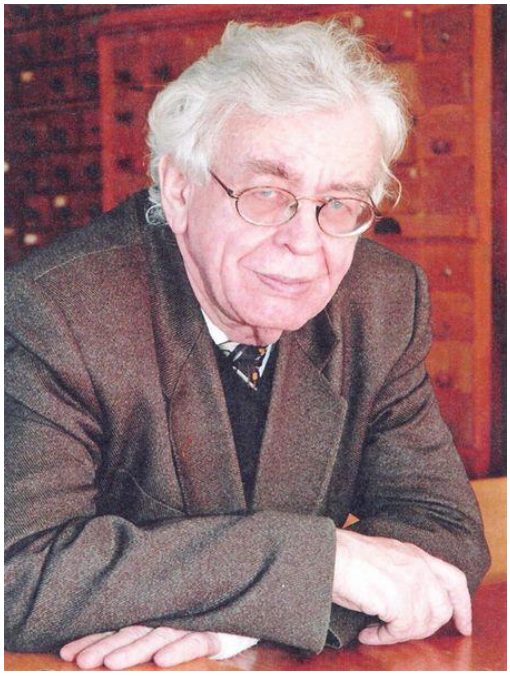

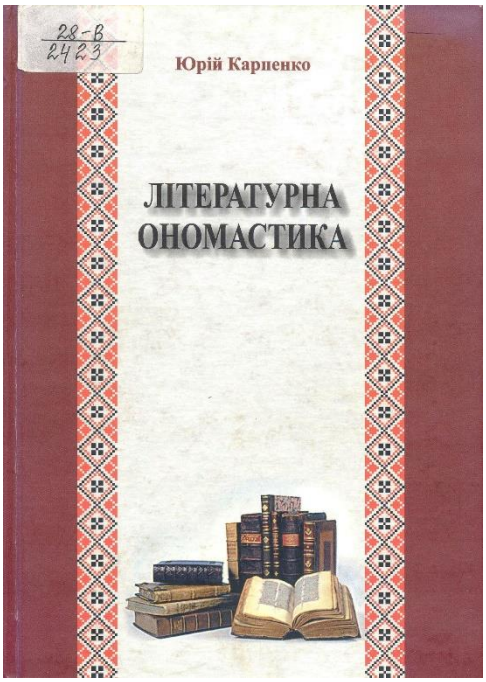

Наукове видання

Одеські Астрономічні Публікації

том 37 (2024)

Англійською мовою

Технічний редактор та комп'ютерна верстка *С. Л. Страхова*

Підписано до друку 27.11.24. Формат 60x84/8.
Ум. друк. арк. 15,11. Тираж 50 прим. Зам. №

Видавець і виготовлювач
Одеський національний університет імені І. І. Мечникова
Свідоцтво суб'єкта видавничої справи ДК № 4215 від 22.11.2011 р.
65082, м. Одеса, вул. Єлісаветинська, 12, Україна
Тел.: (048) 723 28 39
e-mail: druk@onu.edu.ua